

Compact binary coalescences: gravitational-wave astronomy with ground-based detectors

K. Chatziioannou · T. Dent ·
M. Fishbach · F. Ohme · M. Pürrer ·
V. Raymond · J. Veitch

Received: date / Accepted: date

Abstract The era of gravitational wave astronomy began in 2015 with the observation of the signal from the merger of two black holes by the LIGO detectors; by 2021, almost 100 more such transient signals from coalescences of compact binaries of black holes and neutron stars were catalogued. With improvements to the ground-based interferometer network consisting of LIGO, Virgo, and KAGRA now promising to bring the total number of detections into the hundreds, we review the observational signatures and analysis methods for the most prolific gravitational-wave source: the coalescence of compact binaries.

Keywords Gravitational Waves · Compact Binaries · Data Analysis

K. Chatziioannou
Department of Physics, California Institute of Technology, Pasadena, California 91125, USA

T. Dent
IGFAE, University of Santiago de Compostela, E-15782, Spain

M. Fishbach
Canadian Institute for Theoretical Astrophysics, 60 St George St, University of Toronto,
Toronto, ON M5S 3H8, Canada

F. Ohme
Max-Planck-Institut für Gravitationsphysik, Albert-Einstein-Institut, Callinstr. 38, D-30167
Hannover, Germany
Leibniz Universität Hannover, D-30167 Hannover, Germany

M. Pürrer
Department of Physics and Center for Computational Research, University of Rhode Island,
Kingston, RI 02881, USA

V. Raymond
Cardiff University, Cardiff CF24 3AA, United Kingdom

J. Veitch
Institute for Gravitational Research, School of Physics and Astronomy, University of Glas-
gow, Glasgow G12 8QQ, United Kingdom

Contents

1	Introduction	5
1.1	(Pre-)history of compact binary GW sources	5
1.2	The Era of Interferometric Detectors	6
2	Compact binary signals	8
2.1	Emission of compact binaries: the quadrupole formula	8
2.2	Post-Newtonian signal calculation	14
2.2.1	Tidal effects	17
2.2.2	Precessing binaries	18
2.2.3	Cosmological effects	18
2.3	Signal characteristics	20
2.3.1	Description of binary parameters	20
2.3.2	The effect of binary parameters on the gravitational wave (GW) strain	22
2.4	Numerical relativity simulations	27
2.5	Quasi-normal modes	31
2.6	Modeling the signal from inspiral to ringdown	32
2.7	Reduced-order and surrogate models	36
2.8	Comparison of waveform accuracy and efficiency	39
3	Statistical framework	41
3.1	Likelihood function for detector noise	41
3.2	Likelihood for a signal model	44
3.3	The Fisher information metric	44
3.4	Detector response	46
3.5	Measurement precision of signal parameters	47
3.6	Multiple detectors	49
3.7	Normalized signals and similarity measures	50
4	Detection	52
4.1	Theory of transient signal detection	53
4.1.1	Signal with unknown parameters: composite hypotheses	54
4.2	Matched filtering for single-mode CBC signals	55
4.3	Signal manifolds and template banks	56
4.3.1	Optimizing searches for a target signal population	59
4.4	Computational optimization and low latency search	60
4.5	Searches beyond a single GW emission mode	60
4.6	Non-ideal data	63
4.6.1	Noise spectrum drift and calibration	63
4.6.2	Transient excess noise: glitch suppression	63
4.7	Multi-detector searches: coherent, coincident & externally triggered	67
4.7.1	Co-located detectors and composite data streams	67
4.7.2	General networks	68
4.7.3	Coincident search and multi-detector consistency	70
4.8	Statistical methods for significance and search sensitivity	71
4.8.1	Detection significance in non-ideal data	72
4.8.2	Search sensitivity, merger rate and probability of astrophysical origin	72
4.9	Machine learning applications	74
5	Parameter Estimation	76
5.1	Introduction to Bayesian Inference	76
5.2	Priors	78
5.2.1	Prior from astrophysics	78
5.2.2	Computational considerations	78
5.2.3	Change of priors via reweighting	79
5.2.4	Other considerations on priors	79
5.3	Likelihood function	80
5.4	Exploring parameter space	81
5.4.1	Markov Chain Monte Carlo	82
5.4.2	Nested Sampling	84

5.4.3	Hybrid grid-sampler exploration	85
5.4.4	Machine Learning methods	86
5.5	Degeneracies of the likelihood	87
5.5.1	Distance - inclination	88
5.5.2	Sky localization	89
5.5.3	Phase and polarisation angle	90
5.5.4	Masses and spins	91
5.6	Optimization	93
6	Combining Information	95
6.1	From one to many: Hierarchical inference	95
6.1.1	Astrophysical events as a Poisson process	97
6.2	Accounting for selection biases	97
6.3	Inference on astrophysical populations	100
6.3.1	Population model comparisons and checking	106
6.4	Matter effects and equation of state of dense matter	107
6.5	Tests of General Relativity with multiple sources	109
7	Outlook	113
7.1	Current and upcoming generations of compact binary observations	113
7.2	Next generation challenges	114
7.3	Conclusion	116

Definitions and conventions

Except where other units are specified, we use “geometric units” where $c = G = 1$. The following symbols and definitions are used throughout:

- $d, d(t)$: detector strain data stream
- $n, n(t)$: noise component of data stream
- $h, h(t)$: gravitational-wave induced strain on the detector
- $\tilde{d}, \tilde{d}(f)$: Fourier transform of d , etc.
- h_+, h_\times : gravitational-wave plus and cross polarizations
- $H \equiv h_+ - ih_\times$: complex combination of gravitational-wave polarizations
- $\tilde{x}(f) \equiv \int x(t) \exp(-i 2\pi ft) dt$: forward Fourier transform
- $x(t) \equiv \int \tilde{x}(f) \exp(i 2\pi ft) df$: inverse Fourier transform
- $\tilde{x}_k \equiv \sum_{j=0}^{N-1} x_j \exp(-i 2\pi jk/N)$: forward discrete Fourier transform
- $x_j \equiv \frac{1}{N} \sum_{k=0}^{N-1} \tilde{x}_k \exp(i 2\pi jk/N)$: inverse discrete Fourier transform
- S_n : power spectral density (units Hz^{-1}) of noise; we use the one-sided density unless otherwise noted
- $\langle a|b \rangle \equiv 4 \text{Re} \int_0^\infty \tilde{a}^*(f) \tilde{b}(f) S_n(f)^{-1} df$: noise-weighted inner product
- $P(A|B)$: probability of a logical proposition A given information B
- $p(a|B)$: probability distribution over a parameter a given information B
- H_N, H_S : noise hypothesis and signal-plus-noise hypothesis
- $\boldsymbol{\theta}$: vector of source parameters
- \mathbf{C} : a matrix named C
- m_1, m_2 : primary and secondary component masses, $m_1 \geq m_2$ by convention
- $M \equiv m_1 + m_2$: total mass
- $\eta \equiv m_1 m_2 / M^2$: symmetric mass ratio
- $q \equiv m_2 / m_1 \leq 1$: mass ratio
- $\mathcal{M} \equiv M \eta^{3/5}$: chirp mass
- M_\odot : solar mass
- $\mathbf{S}_1, \mathbf{S}_2$: dimensionful component spin vectors
- $\boldsymbol{\chi}_1 \equiv \mathbf{S}_1 / m_1^2$: dimensionless spin vector
- $\chi \equiv |\boldsymbol{\chi}|$: dimensionless spin magnitude
- \mathbf{L} : Newtonian orbital angular momentum vector
- $\cos \theta_1 \equiv (\mathbf{S}_1 \cdot \mathbf{L}) / (|\mathbf{S}_1| |\mathbf{L}|)$: spin tilt
- ϕ_1 : spin azimuthal angle in the \mathbf{L} frame
- $\chi_{\text{eff}} \equiv (m_1 \chi_1 \cos \theta_1 + m_2 \chi_2 \cos \theta_2) / M$: effective aligned spin
- $\chi_p \equiv \max[\chi_1 \sin \theta_1, q(4q + 3) / (4 + 3q) \chi_2 \sin \theta_2]$: effective precessing spin

1 Introduction

1.1 (Pre-)history of compact binary GW sources

Coalescences of compact binaries involving neutron stars and black holes – their inspiraling evolution due to GW emission, and ensuing merger to form a remnant object – are some of the most extreme astronomical phenomena known. Each event can convert a few percent of the total binary mass to gravitational radiation, typically a few times the solar mass for coalescences involving $\sim 30 M_{\odot}$ black holes [31], and the peak GW luminosity at merger can reach $\gtrsim 10^{56}$ erg/s [35]. Coalescences involving neutron stars, in addition to their GW signature, can eject debris from the merger site that emits electromagnetic radiation across the spectrum, enabling spectacular multi-messenger observations [28, 30]. However, while the calculation of GW emission from gravitationally bound systems was promptly performed within Einstein’s General Relativity [467, 256, 252, 257, 556], for decades it was thought that the effects would be too weak to ever be of observational interest. This pessimistic estimate was based partly on considering astrophysical sources known at the time, i.e. planets and stars, and partly on the extremely weak expected effects, of order 10^{-20} or less even for optimistic assumptions.

The order of magnitude of the GW strain h from a gravitationally bound binary of masses m_1 , m_2 with orbital radius r , at distance D from Earth, is

$$|h| \sim \frac{1}{r} \frac{1}{D} \frac{2Gm_1}{c^2} \frac{2Gm_2}{c^2} \equiv \frac{R_{S,1}R_{S,2}}{rD}, \quad (1)$$

where $R_{S,*}$ denotes the component Schwarzschild radius. For planetary or binary star systems at realistic distances, the strain is thus vanishingly small. Furthermore, a bound system with total mass M and size R has a maximum dynamical frequency $\omega_d \sim \sqrt{(GM/R^3)} \sim (G\rho)^{1/2}$, where ρ is the system’s average density, and we expect the frequencies of GW emission to be comparable. Considering “non-compact” objects, this dynamical frequency may attain $\sim 10^{-3}$ Hz for rocky planets, a range impractical for terrestrial detector operation due to overwhelming seismic disturbances. The discovery of white dwarfs – coincidentally close in time to the formulation of General Relativity [65] – provided a source whose dynamical frequency could reach the decahertz to Hz range; indeed, white dwarf binaries are a major source for the future space-based detector LISA [86]. Only with the discovery of Galactic neutron stars (NSs) [101, 385], as both isolated rotating (non-axisymmetric) sources and as binaries with emission frequencies up to $\sim 10^3$ Hz, was a credible GW source for Earth-based detectors known to exist [250, 312, 635].

A major impetus was given to the investigation of compact binaries by the discovery of a double NS binary [394] and subsequent confirmation that its orbit decays as expected due to GW emission, including post-Newtonian (PN) corrections to the lowest order of GW emission [669]. While known Galactic binary neutron stars (BNSs) are very far from the point of merger, their existence puts a lower limit on the rate of detectable coalescences in the local uni-

verse [557, 416]. Furthermore, the mass- and spin-dependence of PN emission contributions carry nontrivial information about the properties of the source binary [216]. This combination of detectability and science potential confirmed BNS as a prime source for the first generation of interferometric detectors. Binaries of black holes (BHs) or mixed neutron-star–black-hole (NSBH) binaries were also considered as possible sources, but with much more uncertain merger rates [7].

1.2 The Era of Interferometric Detectors

While resonant bar GW detectors are sensitive at specific frequencies (see [69] for a review), a broad-band antenna is necessary both to detect and characterize chirping compact binary coalescence (CBC) signals [54]. The initial detector network of LIGO, GEO 600 and Virgo, as essentially Michelson interferometers with many enhancements that are beyond the scope of this review, realized a first technical sensitivity goal in their observations up to 2007 [13, 356, 56]. CBC searches covering Initial data up to 2010 obtained null results [11, 5], as expected under all but the most optimistic rate predictions. At the same time, a revolution in numerical methods for solving the Einstein equations for black-hole spacetimes enabled the full merger-ringdown GW emission from binary black hole (BBH) systems to be investigated [570, 169, 106] and combined with previous detailed knowledge of the PN inspiral [155, 156, 73]; thus, in addition to searches for CBC inspirals, higher-mass BBH mergers could also be targeted [9].

With the upgraded Advanced detectors coming online from 2015 onward [6, 57], improvements both in the response to GW, and in suppression of noise over the full ~ 10 – 1000 Hz band [21], as shown in Fig. 1, were immediately rewarded with the discovery of a merging stellar-mass BBH via its GW signal, GW150914 [19]. Not only was this system the first of its kind observed, it also contained stellar-mass BHs more massive than any confirmed via electromagnetic emission [14]. Within two years, the first joint detection of a BNS coalescence through both GW [29] and electromagnetic emission confirmed the exceptionally broad science potential of multimessenger astronomy with GWs: yielding, among other results, confirmation that BNS mergers source short gamma-ray bursts (GRBs) and kilonovae, and that GW propagate at the speed of light [28, 30]. These overnight astrophysical revolutions were enabled by advances both in our understanding of GW emission and in analysis methods, as we will review in detail.

After the gamut of stellar-mass compact binary types was completed with the discovery of mixed NS-BH binaries [46] thanks again to increased detector sensitivities [151], with the Advanced era O4 run now underway, and as the community is designing future detectors to reach compact binary sources at the edge of the observable universe, this review revisits the basics of CBCs and of current data analysis techniques. We discuss the theory behind the signals we observe in Sec. 2; then in Sec. 3 we describe how we can use GW signals

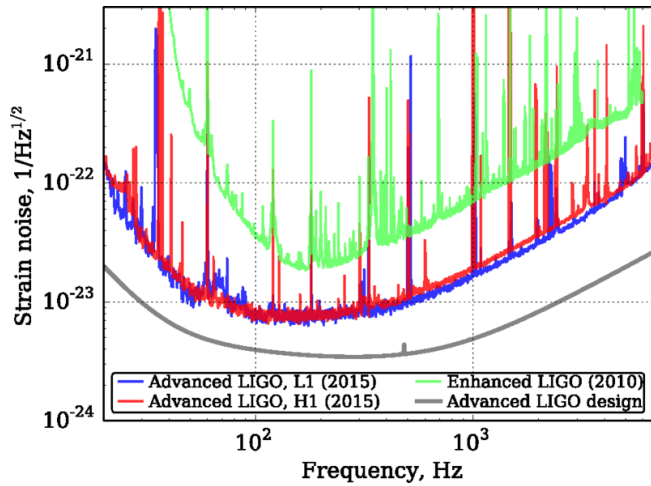


Fig. 1: The strain sensitivity for the LIGO Livingston detector (L1) and the LIGO Hanford detector (H1) during the first observing run, O1. Also shown is the noise level for the Advanced LIGO design (gray curve) and the sensitivity during the final data collection run (S6) of the initial detectors. Figure reproduced from [21].

recorded in detector data to make statistical statements on the presence and properties of possible sources. Based on this framework, we consider methods for CBC signal detection in Sec. 4, and parameter estimation in Sec. 5. In Sec. 6 we generalize from one signal to the catalog of all detections, and describe how large sets of events can be analyzed while taking into account their uncertainties and the instrument selection effects. We conclude in Sec. 7 with an outlook over upcoming CBC observations in the near and medium term and discussion of the associated challenges for data analysis.

2 Compact binary signals

Data analysis techniques for compact binaries consisting of BHs and NSs require detailed knowledge of the GW signal. In principle this can be achieved by calculating the orbital dynamics and waveform by solving Einstein's equations for a source binary. This section starts out by providing an overview of the generation and emission of GWs under Newtonian and post-Newtonian assumptions in Secs. 2.1 and 2.2, including tidal effects and precession, as well as relevant cosmological effects on GW propagation; we then discuss salient characteristics of GW signals in terms of the parameters describing compact binary sources and the effect of these parameters on the GW strain in Sec. 2.3.

The coalescence of compact binaries and the emitted GWs consist of several stages: (i) inspiral, where the orbital velocity is much smaller than the speed of light, and which is well described by post-Newtonian theory, (ii) the highly non-linear merger which requires full numerical solutions of Einstein's equations (see Sec. 2.4), and, (iii), for BBHs, the ringdown stage which is governed by quasi-normal modes emitted from a perturbed final BH (see Sec. 2.5). Modern waveform models may rely on semi-analytical techniques to model the complete GW signal from these stages, as exemplified by the effective-one-body and phenomenological modeling frameworks discussed in Sec. 2.6, or follow a full data-driven approach as used by surrogate models summarized in Sec. 2.7. We close out with a comparison of the accuracy and efficiency of waveform models in Sec. 2.8.

2.1 Emission of compact binaries: the quadrupole formula

We introduce the basic structure of the gravitational wave (GW) signal from compact binaries by considering a weak perturbation of Minkowski space:

$$g_{\alpha\beta} = \eta_{\alpha\beta} + h_{\alpha\beta}, \quad (2)$$

where $\eta_{\alpha\beta} = \text{diag}(-1, 1, 1, 1)$ is the Minkowski metric in Cartesian coordinates, and $|h_{\alpha\beta}| \ll 1$ is a small perturbation.¹ This perturbation tensor will represent GWs on a Minkowski background. The trace-reversed perturbation tensor

$$\bar{h}_{\alpha\beta} \equiv h_{\alpha\beta} - \frac{1}{2}\eta_{\alpha\beta}h_{\sigma}{}^{\sigma}, \quad (3)$$

satisfies a simple wave equation if an appropriate coordinate system (gauge) is chosen in which $\partial_{\beta}\bar{h}_{\alpha}{}^{\beta} = 0$. This choice is commonly referred to as Einstein-de Donder gauge, or Lorenz gauge.² With this choice of coordinates, the Einstein

¹ In the following we assume geometric units in which the gravitational constant and the speed of light are set to one, $G = c = 1$. In these units, lengths and times are measured in units of the total mass of the spacetime M . Conversion to SI units is discussed at the end of this section.

² Named for Ludvig Lorenz in analogy to the gauge choice in electrodynamics.

equation expanded to first order in $\bar{h}_{\alpha\beta}$ becomes a flat-space wave equation,

$$\square \bar{h}_{\alpha\beta} \equiv \left(-\frac{\partial^2}{\partial t^2} + \frac{\partial^2}{\partial x^2} + \frac{\partial^2}{\partial y^2} + \frac{\partial^2}{\partial z^2} \right) \bar{h}_{\alpha\beta} = -16\pi T_{\alpha\beta}, \quad (4)$$

with the stress-energy tensor $T_{\alpha\beta}$ as source term; see, e.g., [376, 633] for a more detailed derivation and discussion. The solution to Eq. (4) for the spatial components of the metric perturbation can be approximated far away from the source as

$$\bar{h}_{ij}(t, d) = \frac{2}{d} \frac{d^2}{dt^2} \int_{\mathcal{S}} x^i x^j \rho(t - d, \mathbf{x}) d^3 \mathbf{x}. \quad (5)$$

Here \mathbf{x} are the spatial coordinates, d is the distance between the observer and the source, ρ is the mass density, and the integral covers a three-dimensional space \mathcal{S} that fully contains the source. The time components of $\bar{h}_{\alpha\beta}$ can be set to zero in an appropriate gauge, as we discuss next.

The Einstein-de Donder gauge does not define a unique coordinate system. The additional gauge freedom can be used to impose further constraints on $\bar{h}_{\alpha\beta}$. A common choice is the transverse-traceless gauge, which can only be imposed in vacuum away from the source. In this gauge, all time components $\bar{h}_{0\beta}$ and the trace $\bar{h}_{\alpha}^{\alpha}$ vanish. Therefore, if one has transformed to this gauge (a discussion on how to do that follows below), Eq. (5) specifies the complete metric perturbation and we can ignore the time components. In addition, we can drop the distinction between $h_{\alpha\beta}$ and its trace-reversed counterpart $\bar{h}_{\alpha\beta}$.

Equation (5), often referred to as the quadrupole formula of GW emission, states that the GW tensor h_{ij} originates from the second time derivative of the mass quadrupole

$$I^{ij}(t) = \int_{\mathcal{S}} x^i x^j \rho(t, \mathbf{x}) d^3 \mathbf{x}. \quad (6)$$

We now consider a binary system in a circular orbit in the x - y plane, see Fig. 2. Due to energy being carried away by the emitted gravitational radiation, the binary orbit cannot remain perfectly closed and circular; but considered as an idealized example, the quasicircular case serves as a good starting point. The system is characterized by the two masses $m_1 \geq m_2$, which correspond to the gravitational (rest) masses of the individual binary components in isolation. As we consider widely separated orbits, the size of the objects is negligible. For binary components orbiting with a separation r and an orbital frequency ω , the location of each object in the center-of-mass coordinate system is

$$\mathbf{x}_1 = \frac{m_2 r}{M} (\cos(\omega t), \sin(\omega t), 0), \quad \mathbf{x}_2 = -\frac{m_1}{m_2} \mathbf{x}_1, \quad (7)$$

where $M = m_1 + m_2$ is the total mass. With the simplifying assumption of point masses, the mass density is

$$\rho(t, \mathbf{x}) = m_1 \delta[\mathbf{x} - \mathbf{x}_1(t)] + m_2 \delta[\mathbf{x} - \mathbf{x}_2(t)]. \quad (8)$$

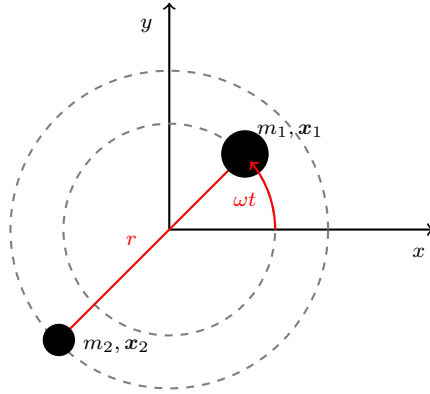


Fig. 2: Illustration of a binary in an idealized circular orbit of radius r . The two orbiting (point) masses are defined by their mass m_i and coordinates \mathbf{x}_i .

The mass quadrupole moment and its second derivative are then

$$I^{ij}(t) = m_1 x_1^i(t) x_1^j(t) + m_2 x_2^i(t) x_2^j(t), \quad (9)$$

$$\frac{d^2 I^{ij}}{dt^2} \equiv \ddot{I}^{ij} = m_1 \left(\ddot{x}_1^i x_1^j + x_1^i \ddot{x}_1^j + 2\dot{x}_1^i \dot{x}_1^j \right) + (1 \leftrightarrow 2). \quad (10)$$

Using the explicit coordinates of the binary given in Eq. (7), one can calculate the GW tensor from Eq. (5) as

$$h_{ij}(t, d) = -\frac{4M\omega^2 r^2 \eta}{d} \begin{pmatrix} \cos(2\omega t') & \sin(2\omega t') & 0 \\ \sin(2\omega t') & -\cos(2\omega t') & 0 \\ 0 & 0 & 0 \end{pmatrix}, \quad (11)$$

where we use t' to denote the retarded time,

$$t' = t - d, \quad (12)$$

and the symmetric mass ratio, η , is defined by

$$\eta = \frac{m_1 m_2}{M^2}. \quad (13)$$

The GW tensor in the transverse-traceless gauge only has two independent components. In our example, we oriented the coordinate system such that the binary orbits in the x - y plane. This leads to the structure of h_{ij} that can be observed in Eq. (11). The tensor is traceless, because $h_{xx} = -h_{yy}$. For waves traveling along the z -direction, the “transverse” condition of the transverse-traceless gauge is also satisfied as only spatial components perpendicular to the direction of propagation contain non-zero values.

Because h_{ij} is a metric perturbation, it has to be symmetric, i.e., $h_{xy} = h_{yx}$. The two independent components are identified as the two polarizations of the GW, $h_{xx} = h_+$, $h_{xy} = h_\times$. In this idealised case of a circular binary,

the polarizations are harmonic oscillation whose frequency is twice that of the orbital motion; h_+ and h_\times differ only by a phase offset of $\pi/2$.

An observer (e.g. a GW detector such as a LIGO or Virgo) will not necessarily be located along the z -axis (i.e., exactly above or below the orbital plane). For more general scenarios, one has to project h_{ij} to the two-dimensional subspace perpendicular to the direction of propagation to remain in the appropriate transverse-traceless gauge. If $\hat{\mathbf{N}}$ is the unit vector from the source to the detector, then we can find the projection operator P_{kl} and the appropriately transformed GW perturbation in the transverse-traceless gauge as

$$P_{kl} = \mathbb{I}_{kl} - \hat{N}_k \hat{N}_l, \quad (14)$$

$$h'_{kl} = P_k^i P_l^j h_{ij} - \frac{1}{2} P_{kl} P^{ij} h_{ij}. \quad (15)$$

Here, \mathbb{I} denotes the three-dimensional identity matrix. The first term in Eq. (15) projects the components of h_{ij} to the subspace perpendicular to \hat{N} . The second term removes the trace.

The two polarizations can be read off the transformed GW perturbation tensor. An L-shaped interferometer will only be sensitive to a linear combination of the two polarisations, depending on its orientation. We denote this observable signal by h and provide more details in Sec. 3.4. For the case of a binary signal in the form of Eq. (11), any linear combination of both polarizations can be expressed by introducing an amplitude factor \mathcal{A} and a phase offset ϕ_0 that each depend on the geometry of the source and the detector. Using the relative velocity $v = \omega r$ we may then express the GW strain due to stationary circular binary motion as

$$h(t, \boldsymbol{\theta}) = -\mathcal{A} \frac{4Mv^2\eta}{d} \cos(2\omega t + \phi_0). \quad (16)$$

Here, $\boldsymbol{\theta} = \{M, v, \eta, d, \omega, \phi_0, \mathcal{A}\}$ is the vector of parameters that characterizes the orbital motion and orientation of the source.

Not all of those parameters are independent. According to Kepler's third law, the total mass, velocity and orbital frequency of a system in a stable, circular orbit are related by

$$v^2 = \frac{M}{r} \quad \Rightarrow \quad v^3 = M\omega. \quad (17)$$

This relation will enable us to heuristically estimate the rate of change of the binary velocity and separation. Although we started by assuming a stable, perfectly circular orbit, the GW signal will carry energy away from the system. The GW flux is proportional to the square of the time derivative of GW tensor in the TT gauge, $\dot{h}^{ij} \dot{h}_{ij}$. The luminosity, \mathcal{L} , is the flux averaged over an orbit and integrated over a sphere of radius d . For our binary system, it is proportional to

$$\mathcal{L} \propto |d\dot{h}|^2 \propto M^2 v^4 \eta^2 \omega^2 = \eta^2 v^{10}. \quad (18)$$

Deriving a general expression for the energy carried by a GW is beyond the scope of this introduction. It can be found in many excellent textbooks, e.g., [183,376]: the result reads

$$\mathcal{L} = \frac{32}{5}\eta^2 v^{10}. \quad (19)$$

The orbital energy of the binary system can be written using Kepler's third law as

$$E = -\frac{M\eta}{2}v^2. \quad (20)$$

Given the energy loss of the system due to GW luminosity, Eq. (19), and taking the mass parameters M and η to be constant, one can use energy balance to calculate how the velocity is changing over time:

$$\frac{dE(t)}{dt} = -\mathcal{L}(t), \quad (21)$$

$$\Rightarrow \frac{dv(t)}{dt} = -\frac{\mathcal{L}(t)}{dE(v)/dv} = \frac{32}{5M}\eta v^9(t) \quad (22)$$

$$\Rightarrow v(t) = \frac{1}{2} \sqrt[8]{\frac{5M}{\eta(t_c - t)}}. \quad (23)$$

Thus, the relative velocity of the binary increases over time as $(t_c - t)^{-1/8}$, apparently diverging at the so-called coalescence time t_c , although the simplifying assumptions made here are not valid all the way up to the time of the binary's merger. Following Eq. (17), the separation is

$$r(t) = 4M \sqrt[4]{\frac{\eta(t_c - t)}{5M}}. \quad (24)$$

Thus, the approximate time to coalescence for a binary with an initial separation of r_0 is

$$T = \frac{5r_0^4}{256M^3\eta}. \quad (25)$$

Finally, the orbital frequency, using Eq. (17) again, behaves as

$$\omega(t) = \frac{v^3(t)}{M} = \frac{1}{8} \left(\frac{5}{M^{5/3}\eta(t_c - t)} \right)^{3/8} = \frac{1}{8\mathcal{M}^{5/8}} \left(\frac{5}{t_c - t} \right)^{3/8}, \quad (26)$$

where we have introduced the *chirp mass*

$$\mathcal{M} = M\eta^{3/5} = \frac{(m_1 m_2)^{3/5}}{(m_1 + m_2)^{1/5}}. \quad (27)$$

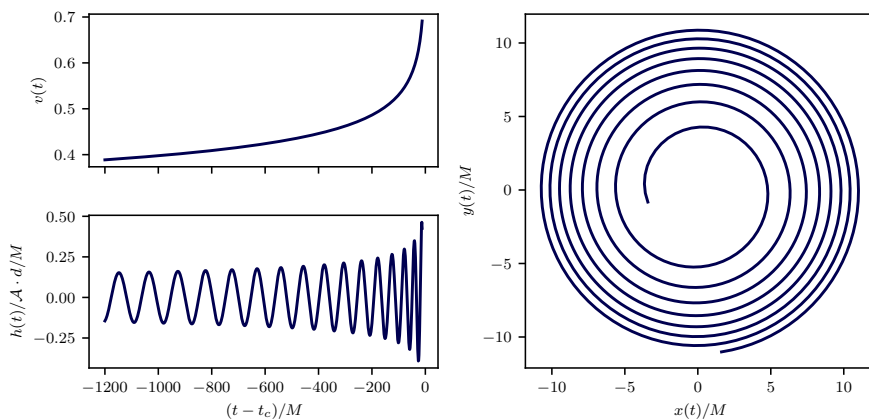


Fig. 3: The evolution of the relative velocity $v(t)$, the (re-scaled) GW signal $h(t)$ and the inspiral track of a Newtonian binary in quasi-circular orbits that evolve only due to the energy carried away by the GW.

With an explicit expression for the orbital frequency, we can also calculate the orbital phase

$$\phi(t) = \int \omega(t) dt = \phi_c - \left(\frac{t_c - t}{5\mathcal{M}} \right)^{5/8}. \quad (28)$$

Here, we label the integration constant ϕ_c as it turns out to be the orbital phase at the divergence time t_c .

This is a remarkable result: the inspiral of a binary under the emission of GWs is predominantly governed by one combination of the component masses, the chirp mass \mathcal{M} . The functions $v(t)$, $h(t)$, as well as the binary separation vector $(r \cos \phi, r \sin \phi)$ in the plane of the orbit are shown in Fig. 3.

The total mass M acts as a trivial scale factor in the binary's dynamics and GW signal. The signal amplitude scales with M/d , and the time, frequency, and separation (at fixed velocity) are proportional to M . This will have important consequences when considering binary sources at cosmological distances, as we will discuss in Sec. 2.2.3. The values in units of M shown in Fig. 3 may be converted to physical (SI) units via

$$t - t_c = \left(\frac{t - t_c}{M} \right) \times M \frac{G}{c^3} \approx \left(\frac{t - t_c}{M} \right) \times 4.9 \text{ ms} \frac{M}{M_\odot}, \quad (29)$$

$$x^i(t) = \left(\frac{x^i(t)}{M} \right) \times M \frac{G}{c^2} \approx \left(\frac{x^i(t)}{M} \right) \times 1.5 \text{ km} \frac{M}{M_\odot}, \quad (30)$$

explicitly reintroducing the gravitational constant G and speed of light c .

PN	0	0.5	1	1.5	2	2.5	3	3.5	4	4.5	5	5.5	6
k	0	1	2	3	4	5	6	7	8	9	10	11	12
energy	✓	✓	✓	✓	✓	✓	✓	✓	✓	×	×	×	×
flux	✓	✓	✓	✓	✓	✓	✓	✓	×	×	×	×	×
chirp mass	■												
mass ratio													
spin-orbit													
spin-spin													
tidal													
references		[710]	[425, 722]	[130, 133, 134]	[222, 424]								

Table 1: Overview of PN orders and effects that enter the gravitational waveform at this order. Here, k is the exponent of the orbital velocity above leading order, as used in Eqs. (31) and (32). PN terms marked with an “x” are only partially unknown. Solid gray boxes indicate which binary parameters or physical effects contribute at the corresponding PN order.

2.2 Post-Newtonian signal calculation

The calculation presented above illustrates the basic behaviour of a compact binary inspiral under the emission of GWs. Although General Relativity is a complex, non-linear theory, for which even approximate solutions require much careful work, the strategy used in Sec. 2.1 to calculate the GW emission of a binary can be generalized to include non-linear effects by means of a series expansion.

Considering energy and luminosity as functions of the binary’s source parameters $\boldsymbol{\theta} = \{M, \eta, \dots\}$ and of the orbital velocity v , the *post-Newtonian (PN)* framework may be applicable,³ allowing us to express these quantities as a series in v (assumed much smaller than the speed of light), thus:

$$E(v, \boldsymbol{\theta}) \approx -\frac{M\eta}{2}v^2 \left(1 + \sum_{k=2}^n E_k(\boldsymbol{\theta})v^k + \ln v \sum_{k=8}^n E_k^{(l)}(\boldsymbol{\theta})v^k \right), \quad (31)$$

$$\mathcal{L}(v, \boldsymbol{\theta}) \approx \frac{32}{5}\eta^2v^{10} \left(1 + \sum_{k=2}^n \mathcal{L}_k(\boldsymbol{\theta})v^k + \ln v \sum_{k=6}^n \mathcal{L}_k^{(l)}(\boldsymbol{\theta})v^k \right). \quad (32)$$

The leading-order term in those expressions is often referred to as the *Newtonian order* term, while each additional contribution is known as the $k/2$ PN order. In General Relativity, the 0.5PN order term (i.e., $k = 1$) vanishes, and higher-order corrections include specific physical effects that may not be present at lower orders. The energy also contains logarithmic terms $\propto \ln v$ at 4PN order and beyond, and starting from 3PN order in the flux.

Examples of higher-order effects include the coupling of the individual objects’ spins with the orbital motion, which enters at 1.5PN order ($k = 3$);

³ For an introductory review of PN theory see Ref. [132] and Ref. [131, 628] for a detailed discussion.

non-linear tail terms, also entering at 1.5PN; the self-spin and spin-spin coupling entering at 2.5PN; horizon absorption effects starting at 2.5PN; and tidal effects for compact objects that are not black holes, entering with a v -dependence corresponding to 5PN order (see Sec. 2.2.1). A list of effects and references is given in Table 1.

We conclude our brief introduction to the PN framework by focussing on how the expressions of energy in Eq. (31) and flux in Eq. (32) can be used directly to model the GW signal of an inspiralling compact binary. Various strategies have been developed to calculate the GW strain h , written via a generalisation of Eq. (16) as

$$h(t, \boldsymbol{\theta}) = \mathcal{A} \frac{4Mv(t)^2 \eta}{d} \cos[\phi_{\text{GW}}(t) + \phi_0]. \quad (33)$$

Here, we restrict the amplitude to the leading order term that is proportional to v^2 . However, higher PN corrections are included in the GW phase and velocity as we discuss next.

The GW phase, $\phi_{\text{GW}}(t) = 2\phi(t)$, is twice the orbital phase, which in turn can be calculated from the integrated orbital frequency ω ,

$$\frac{d\phi}{dt}(t) = \omega(t) = \frac{v^3(t)}{M}, \quad (34)$$

cf., Eq. (26). Finally, as in the Newtonian case, the relative velocity is given by an ordinary differential equation,

$$\frac{dv}{dt}(t) = -\frac{\mathcal{L}(t)}{dE(v)/dv}. \quad (35)$$

Unlike the Newtonian case, we now think of the energy E and flux \mathcal{L} as series expansions up to a given PN order.

Different strategies to solve this system of equations are commonly referred to as PN *approximants*: we name and summarize each such strategy below, see Ref. [157] for a more detailed discussion and comparison.

TaylorT1 Integrate Eqs. (35) and (34) numerically.

TaylorT2 Solve the inverse of Eq. (35),

$$\frac{dt}{dv}(v) = -\frac{dE(v)/dv}{\mathcal{L}(v)}, \quad (36)$$

by re-expanding the expression into a series truncated at the same order as E and \mathcal{L} and integrate analytically to obtain $t(v)$. Equation (34) is solved in a similar way, by re-expanding

$$\frac{d\phi}{dv}(v) = \frac{v^3(t)}{M} \frac{dt}{dv}(v), \quad (37)$$

into a series in powers of v and integrating analytically. One then has analytical descriptions of time and phase, both parameterized by the relative velocity. Finding $\phi(\hat{t})$ for a particular time \hat{t} requires a root-finding algorithm to solve $t(v) = \hat{t}$.

TaylorT3 This approach starts with the same steps as TaylorT2, but inverts $t(v)$ analytically (as a series expansion to consistent order) to obtain a series expression for $v(t)$. This is then used in $\phi(v)$ to obtain an analytical, closed-form series expansion for $\phi(t)$.

TaylorT4 This approach is similar in spirit to TaylorT1 in that it integrates both differential equations numerically. However, Eq. (35) is first re-expanded and truncated, and this form is then integrated.

TaylorF2 Under the *stationary phase approximation* [248] the GW phase in the Fourier domain can be derived from the time domain phase. A simplified expression for the dominant mode is given by [563, 96, 223, 224, 152, 157, 70]

$$\tilde{h}(f) = \mathcal{A} f^{-7/6} e^{-i\psi(f)}, \quad (38)$$

where the amplitude

$$\mathcal{A} \propto \mathcal{M}^{5/6} Q(\text{angles})/d, \quad (39)$$

includes the response of the detector which depends on the location of the source with respect to the reference frame of the GW detector and the inclination angle under which the source is observed. The TaylorF2 phasing is fully known up to 3.5PN for the sake of illustration we only highlight the most important terms ⁴

$$\begin{aligned} \psi(f) = & 2\pi f t_c - 2\phi_c(\text{angles}) - \frac{\pi}{4} + \frac{3}{128\eta v^5} \left\{ 1 + v^2 \left[\frac{3715}{756} + \frac{55}{9}\eta \right] \right. \\ & - v^3 \left[16\pi - \left(\frac{113}{3} - \frac{76}{3}\eta \right) \chi_s - \frac{113}{3} \delta_{\text{PN}} \chi_a \right] \\ & \left. + v^4 [g(\eta) + \sigma] + \dots - v^{10} \frac{39}{2} \tilde{A} + \dots \right\}, \end{aligned} \quad (40)$$

where $v = (\pi M f)^{1/3}$ is the expansion parameter (assuming $c = 1$, we expand in powers of v/c). The Newtonian term (0PN) only depends on binary parameters through the chirp mass \mathcal{M} as $1/(\eta v^5) = (\pi \mathcal{M} f)^{-5/3}$. At 1.5PN order (v^3 term *within* the braces) spin-orbit contributions enter the phase which we write as symmetric and anti-symmetric dimensionless spins aligned with the orbital angular momentum⁵, $\chi_s = (\chi_1 + \chi_2)/2$ and $\chi_a = (\chi_1 - \chi_2)/2$, as well as $\delta_{\text{PN}} = (m_1 - m_2)/M$ and $g(\eta)$ is an unspecified function. Similarly, σ represents the spin-spin contribution at 2PN order. The v^{10} term describes tidal effects which we discuss below.

⁴ Formally the coalescence is reached at infinite frequency. In practice, a finite termination frequency and therefore a finite termination time and phase have to be used. Here, we stick to the usual notation t_c, ϕ_c which refers to the coalescence.

⁵ In the notation of Sec. 2.3 $\chi_i = c \mathbf{S}_i / (G m_i^2) \cdot \hat{L}_N$.

All these approximants correspond to different ways of obtaining expressions for the GW given truncated series expressions for the binding energy and luminosity. In essence, they differ by the order in which they (numerically or analytically) solve the equations vs. re-expand the series. Given the truncated nature of the PN series, no method is *a priori* preferred and their relative strengths and weaknesses are determined by how well they approximate the full non-linear GW calculation.

2.2.1 Tidal effects

An extended body in a spatially inhomogeneous external field will experience varying forces throughout its extent. This is an example of a tidal interaction which is well understood in Newtonian gravity. In the following we define the tidal deformability of a NS which quantifies how easily the star is deformed in an external field. A static, spherically symmetric star of mass m and radius R in an external quadrupolar field \mathcal{E}_{ij} will develop an induced quadrupole moment Q_{ij} . The (dimensionful) *tidal deformability* of the star is given by the ratio [307, 188]

$$\lambda = -\frac{Q_{ij}}{\mathcal{E}_{ij}}, \quad (41)$$

which can be shown to be proportional to R^5 . Hence, the *dimensionless tidal deformability* is defined as

$$\Lambda = \frac{\lambda}{m^5} = \frac{2}{3}k_2 \frac{R^5}{m^5}, \quad (42)$$

where k_2 is the dimensionless *Love number*; typically $k_2 \sim 0.2 - 0.3$. For given m , both k_2 and R depend on the *equation of state* which relates the interior pressure to the energy density and temperature of the NS; the tidal deformability of a BH is zero [118].

In the TaylorF2 phase of Eq. (40) we included the leading-order tidal contribution, which, though a Newtonian physical effect, has a velocity dependence equivalent to 5PN expansion order, with a prefactor given by the effective tidal parameter [307, 291]

$$\tilde{\Lambda} = \frac{16}{3} \frac{(m_1 + 12m_2)m_1^4 \Lambda_1 + (m_2 + 12m_1)m_2^4 \Lambda_2}{(m_1 + m_2)^5}, \quad (43)$$

where Λ_i are defined for each binary component via Eq. (42). Although this tidal term enters at very high PN order we include it here, since it enables the measurement of the neutron star equation of state from binary inspiral signals; this is possible for moderate signal-to-noise ratios due to the large, $\mathcal{O}(100)$, value of $\tilde{\Lambda}$. A detailed discussion of measuring tidal effects and the neutron star equation of state is given in Sec. 6.4.

2.2.2 Precessing binaries

If the compact objects have spin vectors \mathbf{S}_i that are not perfectly aligned with (equivalently, they have components orthogonal to) the Newtonian orbital angular momentum of the binary, then the spin vectors and the orbital angular momentum will change direction in space. The resulting motion resembles *precession* around the total angular momentum, whose direction is approximately fixed when averaged over the timescale of precession. This spin-precession effect enters through a combination of the 1.5PN spin-orbit and 2PN spin-spin (and higher) interaction terms [476]. The equation of motion for the spin of BH a is

$$\frac{d\mathbf{S}_a}{dt} = \boldsymbol{\Omega}_a \times \mathbf{S}_a, \quad (44)$$

with $a \in 1, 2$ denoting each binary component. The angular velocity of the precessional motion for the two BHs labelled a and b is

$$\boldsymbol{\Omega}_a = \frac{1}{r^3} \left[\left(2 + \frac{3m_b}{2m_a} \right) \mathbf{L}_N - \mathbf{S}_b + 3(\hat{\mathbf{x}} \cdot \mathbf{S}_b)\hat{\mathbf{x}} \right], \quad (45)$$

where \mathbf{L}_N is the Newtonian orbital angular momentum, \mathbf{x} the relative separation vector of the two BHs, and $r = |\mathbf{x}|$, and $\hat{\mathbf{x}} = \mathbf{x}/r$.

The typical timescale of precession

$$t_{\text{pr}} \equiv \frac{|\mathbf{S}_i|}{|\dot{\mathbf{S}}_i|} \sim r^{5/2} \sim v^{-5}, \quad (46)$$

is shorter than the radiation reaction timescale

$$t_{\text{r}} \equiv \frac{E}{\dot{\mathcal{L}}} \sim v^{-8}, \quad (47)$$

by 1.5PN orders [191, 192]. In the adiabatic limit we can approximately ignore radiation reaction over one precession cycle. Then the total angular momentum $\mathbf{J} \simeq \mathbf{L}_N + \mathbf{S}_1 + \mathbf{S}_2$ is conserved, $d\mathbf{J}/dt = 0$, and therefore $d\mathbf{L}_N/dt = -d(\mathbf{S}_1 + \mathbf{S}_2)/dt$. This implies that the orbital plane precesses with the same angular velocity as the total spin. In practice the total angular momentum direction is conserved when averaged over spin-precession, while its magnitude shrinks due to radiation reaction [94].

2.2.3 Cosmological effects

So far, we have assumed that our signal is propagating on Minkowski spacetime. However, CBC sources can be observed at large enough distances (on the order of Gpc) that the effect of the cosmological expansion of the Universe becomes important. Just as for electromagnetic radiation, the GW signal is redshifted, reducing the instantaneous frequency observed at the detector by a factor $1/(1+z)$ relative to frequencies in the source reference frame, where z is the redshift. As we have seen in Sec. 2.1, the phase evolution of a signal from a BBH system (or any compact binary, in the point mass approximation)

is determined by the combination t/M , thus a rescaling of the time coordinate is equivalent to rescaling the binary mass: for an observer with time coordinate defined by $dt_{\text{obs}} = dt(1+z)$, the phase is a function of $t_{\text{obs}}/(M(1+z))$. This scaling property also holds for numerical solutions of the full Einstein equations in vacuum (Sec. 2.4), although it is broken by finite-size effects of neutron-star matter, which are strongly dependent on the NS mass (Sec. 2.2.1, see also [496]). If such effects can be neglected, there is a complete degeneracy in phase between a source at nonzero redshift and one with a mass $(1+z)$ times greater [437].

The amplitude or power of radiation propagating in cosmological models is described by the luminosity distance: a source’s measured bolometric flux F is to be related to an intrinsic bolometric luminosity L , which for an isotropically emitting source gives $d_L = \sqrt{L/(4\pi F)}$. The luminosity distance may be derived as a function of redshift for any given model; for cosmologies with a spatially flat metric, it is related to the comoving distance d_c by $d_L(z) = (1+z)d_c(z)$ [388]. It can then be shown that the GW signal received at Earth from a binary of masses $m_{1,2}$ at redshift z and luminosity distance $d_L(z)$ is identical (again neglecting NS matter effects) to a signal propagating in flat spacetime from a binary with masses $m_{1,2}(1+z)$ at distance d_L , e.g. [308]. A physical interpretation of luminosity distance is given in Sec. 2.3.2.

For convenience, it is common to define ‘detector frame’, i.e. redshifted mass $M_z = M(1+z)$ as the parameter determining the observed phase of a signal. This parameter and d_L then suffice to determine the amplitude. Unless otherwise noted (e.g. in Sec 6.3), we will take masses, considered as waveform parameters in the context of data analysis, to be redshifted masses, but drop the z subscript for simplicity.

Gravitational lensing The previous discussion assumed that GW propagate through a homogeneous and isotropic Universe (for some choice of spatial slicing): in reality, this is not a perfect approximation. Inhomogeneities in the distribution of matter along the line of sight to a source, and the associated perturbations in the cosmological metric, will affect the propagation of GW. The resulting effects go under the name of “gravitational lensing”, by analogy with the distortion or magnification of optical images. Such effects may be broadly classified as “weak” lensing, relatively small (perturbative) changes to the GW signal caused by the inhomogeneous large-scale structure of matter; and “strong” lensing, large but rare effects caused by the presence of a massive body – most often considered as a galaxy or cluster of galaxies – aligned with the source binary [711, 524], which can significantly alter the signal morphology as well as the amplitude, and even give rise to multiple copies of a given transient, in analogy to multiple lensed optical images (e.g. [536]).

The effects of weak lensing, as a perturbation to the GW signal amplitude which averages to zero over many events, have generally been neglected for the ground-based network, though becoming significant for future observations [386, 201]. The presence of strong lensing, while *a priori* rare (e.g. [527]), will imply specialized strategies, models and methods, both for signal detection

and parameter estimation as well for astrophysical and cosmological interpretation (see [367, 47, 53] and references therein). Details of such analyses are beyond the scope of this review, thus unless otherwise stated we will consider only cases where strong lensing is absent.

2.3 Signal characteristics

2.3.1 Description of binary parameters

A BBH undergoing quasi-circular inspiral can be described by the two component masses m_i and the spin vectors \mathbf{S}_i (or angular momenta) of its component Kerr black holes. We refer to these eight parameters as *intrinsic* parameters. The mass space can alternatively be parametrized by the total mass M or chirp mass $\mathcal{M} = M\eta^{3/5}$ and the (asymmetric) $q = m_2/m_1 \leq 1$ or symmetric mass-ratio $\eta = m_1 m_2 / M^2$. Since the maximum spin a Kerr black hole of mass m can reach is $|\mathbf{S}_{\max}| = (Gm^2)/c$ it is customary to work with *dimensionless* spin vectors $\boldsymbol{\chi}_i = c\mathbf{S}_i/(Gm_i^2)$. These dimensionless spin vectors are usually projected onto the (Newtonian) orbital angular momentum unit vector \hat{L}_N of the binary in order to separate the spin vectors into parallel and orthogonal components. As described in Sec. 2.2.2, non-zero components in the orbital plane give rise to spin-precession of the orbital plane and the spin vectors around the total angular momentum $\mathbf{J} = \mathbf{L} + \mathbf{S}_1 + \mathbf{S}_2$ [94, 424]. For precessing binaries the spin vectors and derived quantities evolve with time and therefore they are defined at a reference frequency (e.g. the time at which the dominant mode GW frequency reaches the reference frequency).

Often, only the dominant dependence of the spins is of interest, motivating the use of the effective aligned spin $\chi_{\text{eff}} = (m_1\boldsymbol{\chi}_1 + m_2\boldsymbol{\chi}_2) \cdot \hat{L}_N / M$ [74, 624] which is approximately constant during the inspiral to at least the 2PN order [581]. In a similar vein, the effective precession parameter [631]

$$\chi_p = \max \left\{ \chi_1^\perp, \frac{q(4q+3)}{4+3q} \chi_2^\perp \right\}, \quad (48)$$

averages the in-plane spins (with χ_i^\perp being their magnitudes) over a number of precession cycles and assigns the effective precession spin to the primary BH; this is done because spins on the primary have a larger impact on the waveform than spins on the secondary when the binary has unequal masses. Generalizations of the χ_p definition have also been proposed [336, 676]. In parameter estimation, the spin vectors are often expressed in spherical polar coordinates with respect to \hat{L}_N by spin magnitudes χ_i and polar (“tilt”) angles θ_i along with an appropriate choice of the inclination angle for precessing binaries (see below) [283]. Instead of the azimuthal angles ϕ_i , the angle ϕ_{12} between ϕ_2 and ϕ_1 and the angle ϕ_{JL} (the difference between the total and orbital angular momentum azimuthal angles) are used.

In addition to the above set of eight intrinsic parameters seven more *extrinsic* parameters are needed to describe a quasi-circular BBH in relation

to a GW detector. These are the sky location (right ascension α and declination δ defined in the equatorial celestial coordinate system), polarization angle ψ , luminosity distance d_L , an orbital inclination angle, and the time t_c and phase ϕ_c at coalescence. The inclination of the binary's orbit as seen from the observer is traditionally parametrized by an angle ι , the angle between \mathbf{L} and the direction toward the observer. Because \mathbf{L} is not a stable direction for precessing binaries and the direction of the total angular momentum $\hat{\mathbf{J}}$ is approximately fixed throughout the inspiral (except in the unusual case of binaries undergoing transitional rather than simple precession [94]) we prefer to instead use θ_{JN} , the angle between the total angular momentum and the unit vector \hat{N} directed toward the observer as a measure of inclination. Transitional precession [94, 740] happens when the total angular momentum \mathbf{J} goes through zero during inspiral, because $\mathbf{S}_1 + \mathbf{S}_2 \simeq -\mathbf{L}$, and thus flips its direction. This can happen for sufficiently asymmetric precessing binaries with mass-ratios of $q \lesssim 0.3$.

BBHs do not necessarily undergo quasi-circular inspiral where the BHs trace out a sequence of shrinking circular orbits. Instead, the orbit is in general tangent to an ellipse at any one point. Of course, the orbit is not a closed elliptical orbit because of gravitational radiation. There is no unique definition of eccentricity in General Relativity. Locally we can choose a Keplerian parametrization of the binary's orbit $r = p/(1 + e \cos \nu)$, where r is the radius, p the semi-latus rectum, and we have introduced an eccentricity parameter e and a radial phase parameter ν which describes the position of a point on an elliptical orbit. Eccentricity is radiated away during the inspiral and merger and most binaries are expected to circularize by the time they enter the frequency band of a GW detector [555]. Therefore, the eccentricity parameters must be defined at a reference frequency in a similar way as for spin parameters.

For a generic, possibly eccentric and precessing, compact binary the relationship between the binary's *source frame* (x, y, z) (spanned by the instantaneous orbital angular momentum vector and the orbital plane at a reference frequency) and a *wave frame* (X, Y, Z) in which the emitted GW propagates toward a GW detector is illustrated in Fig. 4 and the documentation of the LALSimulation package [459]. The Z -axis of the wave frame points toward Earth. Therefore, the $X - Y$ plane is the plane of the sky. The angle between the Z -axis of the wave frame and the z -axis of the source frame is the inclination ι . To describe generic binaries we need to introduce three more (positional) *orbital elements* [564] in addition to the inclination and reference phase. The *longitude of the ascending node* is the angle on the plane of the sky from the X -axis of the reference direction in the wave frame to the *ascending node*, which is the point at which the binary's orbit cuts the plane of the sky from below. The *true anomaly* is the angle ν (introduced above) along the orbital plane from the periapsis or pericenter (the point of closest approach in the orbit) to the present position of the primary orbiting body. In addition, the *argument of the periapsis* needs to be specified to define the orientation of an elliptical orbit in the orbital plane. For non-eccentric orbits it is degenerate with the reference phase. It is also worth mentioning that the longitude of the

ascending node parameter is degenerate with the polarization angle (as both effect rotations on the plane of the sky).

For binaries containing NSs we need to take into account additional degrees of freedom related to their response to a tidal field as discussed in Sec. 2.2. The dominant quadrupolar ($\ell = 2$) tidal deformation is described by the dimensionless tidal deformability of each neutron star $\Lambda_i = (2/3)k_2[(c^2/G)(R_i/m_i)]^5$ and the effective parameter $\tilde{\Lambda}$ is a mass-weighted linear combination of tidal deformabilities.

For reference we have collected all of the above intrinsic and extrinsic binary parameters discussed in Table 2. For an extended table of parameters used by the `bilby` inference code see App. E of Ref. [603].

2.3.2 The effect of binary parameters on the GW strain

Masses and mass-ratio A change in the total mass M of a binary while holding all other parameters fixed results in a reciprocal change in the binary's frequency evolution, so that the dimensionless product $M\omega(t)$ or Mf is unchanged. Therefore, an increase of M is equivalent to shifting the GW strain in the Fourier domain to lower frequencies by the same factor, which makes the observable signal in the sensitive frequency band of a GW detector shorter.

For fixed total mass the symmetric mass-ratio enters the phasing at 0PN order (see Eq. (40)). A binary becomes more and more asymmetric as the mass-ratio q decreases from its maximum $q = 1$ (equal mass) and this also decreases the symmetric mass-ratio η from its maximum $1/4$ to lower values. The main effects of decreasing η for a GW signal with constant total mass starting from a fixed initial frequency are: (i) a steep increase in the time it takes for the binary to merge; as in Eq. (25) the so-called *chirp time* [627] is inversely proportional to η , and (ii) an increase in the number of GW orbits or cycles until merger, as the 0PN phase term is inversely proportional to η .

The chirp mass depends both on total mass and symmetric mass-ratio. An increase of the chirp mass has two main effects: (i) the GW signal from a binary becomes brighter as its Fourier domain amplitude in Eq. (39) scales as $\mathcal{M}^{5/6}$, and (ii) the number of GW orbits or cycles from a fixed initial frequency until merger are reduced because the 0PN phase term in Eq. (40) goes as $\mathcal{M}^{-5/3}$.

We have seen in Sec. 2.2 that the chirp mass \mathcal{M} enters the phase evolution of Eq. (40) at leading order, while the mass-ratio q and effective aligned spin χ_{eff} appear in the phasing at higher orders. It would not be unreasonable to expect that terms at lower PN order which make larger contributions to the phasing will be easier to measure than terms entering at higher PN order, although this is not always true. See Sec. 5.5.4 for a discussion. Similarly, we expect that the two component masses m_1, m_2 will be harder to constrain than the chirp mass and symmetric mass-ratio because they will involve correlations between chirp mass and mass-ratio.

Aligned spins The dominant effect for spins aligned with the orbital angular momentum of the binary is captured by an effective aligned spin parame-

Mass parameters			
m_1	primary mass	the larger of two binary masses	unit M_\odot
m_2	secondary mass	the smaller of two binary masses	unit M_\odot
M	total mass	$m_1 + m_2$	unit M_\odot
η	Symmetric mass ratio	$m_1 m_2 / M^2$	dimensionless
q	Mass ratio	$m_2 / m_1 \leq 1$	Defined to be ≤ 1 to avoid unbounded parameters
\mathcal{M}	Chirp mass	$M\eta^{3/5}$	unit M_\odot
Spin parameters			
\mathbf{S}_i	spin vector	$i = 1, 2$	at reference frequency dimensionful
χ_i	spin vector	\mathbf{S}_i / m_i^2	dimensionless
$\chi_{i,z}$	aligned spin	$\chi_i \cdot \hat{L}_N$	dimensionless
χ_i	spin magnitude	$ \chi_i $	dimensionless
θ_i	polar angle of χ_i	$\arccos(\chi_{i,z}/a_i)$	spin ‘‘tilt’’ angles
ϕ_i	azimuthal angle of χ_i		
ϕ_{JL}	azimuthal angle of \hat{L}_N on its cone about \mathbf{J}		
ϕ_{12}	difference between azimuthal angles	$\phi_2 - \phi_1$	
χ_{eff}	effective aligned spin	$(m_1 \chi_{1,z} + m_2 \chi_{2,z}) / M$	dominant spin effect
χ_p	precession spin	See Eq. (48)	avg. over precession cycles
Tidal parameters			
Λ_i	dimensionless tidal deformability of object i	$\frac{2}{3} k_2 (R_i / m_i)^5$	non-zero for neutron stars
$\tilde{\Lambda}$	effective dimensionless tidal deformability	See Eq. (43)	dominant tidal effect
Extrinsic parameters			
d_L	luminosity distance	unit Mpc	
z	redshift	can be computed from d_L assuming a cosmological model	
θ_{JN}	inclination angle	angle between total angular momentum \mathbf{J} and direction to observer \mathbf{N}	
ι	inclination angle	angle between orbital angular momentum \mathbf{L} and direction to observer \mathbf{N}	
t_c	time of coalescence	GPS reference time at the geocenter	
ϕ_c	phase of coalescence	at reference frequency	
α	right ascension	celestial equivalent of terrestrial longitude	
δ	declination	celestial equivalent of terrestrial latitude	
ψ	polarization angle	rotates polarizations in plane orthogonal to propagation of GW	

Table 2: Commonly used parameters to describe compact binary coalescences, as found in LIGO-Virgo-KAGRA parameter estimation releases. Mass parameters can be defined either as *redshifted* (‘detector frame’) or *source frame* masses, related by $m_{zi} = m_i^{\text{src}}(1+z)$. Spins are labeled with an index $i = 1, 2$ indicating the primary or secondary object. Most spin quantities evolve during the coalescence and are therefore defined at a reference frequency f_{ref} .

ter. The parameter χ_{eff} is a simplified version of the combination which appears in the spin-orbit term of the PN phasing in Eq. (40). The full term is $\chi_{\text{eff}} - \frac{76}{226}\eta(\chi_1 + \chi_2)$ [563, 70]. The fact that the phasing depends on such a combination implies that it is in general difficult to measure the aligned spins on the individual BHs; for very unequal mass binaries only the spin on the primary will be measurable [575, 193]. In a similar way as for the symmetric mass-ratio, increasing the aligned spin relative to a non-spinning compact binary (i.e. positive χ_i) starting from a fixed initial frequency, and holding other parameters constant, increases the time and the number of GW cycles until merger. If the spins are anti-aligned with the orbital angular momentum (i.e. negative χ_i) the time to merger is decreased relative to the spinless case. The

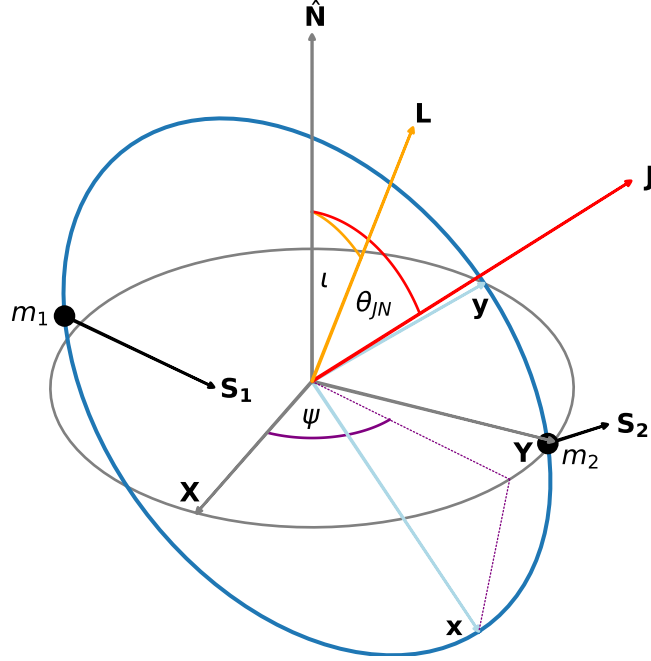


Fig. 4: The orientation of the binary system, defined by the parameters \mathbf{L} , the orbital angular momentum; \mathbf{J} the total angular momentum; $\mathbf{S}_{1,2}$ the spin angular momentum vectors for the two bodies with masses $m_{1,2}$; ψ the polarisation angle; θ_{JN} the angle between the direction to the observer \hat{N} and the total angular momentum. Also shown are the binary's *source frame* (x, y, z) with \mathbf{L} pointing in the z -direction and *wave frame* (X, Y, Z) where \hat{N} coincides with the Z -axis. Figure generated using [719].

slower merger process of binaries with positive aligned spins is due to additional angular momentum that needs to be shed before the binary can settle down into a stationary Kerr black hole. This effect has been called “orbital hang up” [170].

Luminosity distance We saw in Eq. (33) that the GW strain in Minkowski space depends inversely on the distance: GW signals from closer binaries are

stronger, as well as “louder” in a given detector. We also saw in Sec. 2.2.3 that cosmological effects can be expressed by using the Minkowski space signal model but defining ‘redshifted’ masses larger by a factor $(1+z)$, and with d_L taking the place of d .

The phase evolution of a coalescing compact binary which radiates GWs determines the redshifted masses, and, together with the measurement of the GW signal amplitude, the source luminosity distance can thus be deduced [634, 627, 642]; however the effects of angular parameters, particularly inclination as discussed below, on signal amplitude can induce large uncertainties in this measurement.

Sky location and polarization angle As will be discussed in Sec. 3.4, the GW strain recorded by a GW detector is a weighted linear combination of the GW polarizations $h = F_+ h_+ + F_\times h_\times$, where the (real) detector pattern functions F_+, F_\times depend on the sky position (α, δ) and the polarization angle ψ . The GW polarizations are defined with respect to a system of axes in the plane perpendicular to the propagation direction of the wave. The polarization angle effectively rotates this system of axes (see Fig. 4). The triple (α, δ, ψ) defines the location of the source with respect to the frame of a GW detector on Earth.

Spherical harmonic modes and inclination In the wave-zone, far away from the coalescing binary, it is customary to expand the complex combination of gravitational-wave polarizations $H = h_+ - ih_\times$ on a space-like 2-sphere centered on the source in terms of appropriate basis functions for metric perturbations around Minkowski space. These basis functions are spin-weighted spherical harmonics [344] ${}_{-s}Y^{\ell m}$ (of spin weight $s = -2$) which depend on the usual spherical polar angles (θ, φ)

$$h_+ - ih_\times = H(t; \theta, \varphi) = \sum_{\ell=2}^{\infty} \sum_{m=-\ell}^{\ell} h^{\ell m}(t) {}_{-2}Y^{\ell m}(\theta, \varphi), \quad (49)$$

where $h^{\ell m}(t)$ are the GW *modes* or *harmonics*. At leading order, for the dominant $(\ell, m) = (2, \pm 2)$ modes in the GW signal, we have

$$H(t; \theta, \varphi) = h^{22}(t) {}_{-2}Y^{22}(\theta, \varphi) + h^{2,-2}(t) {}_{-2}Y^{2,-2}(\theta, \varphi), \quad (50)$$

where

$${}_{-2}Y^{2,\pm 2}(\theta, \varphi) = \sqrt{\frac{5}{64\pi}} (1 \pm \cos \theta)^2 e^{\pm 2i\varphi}$$

with $h^{22}(t) = A^{22}(t)e^{-i\phi_{\text{GW}}(t)}$, and, assuming equatorial symmetry of the binary, $h^{2,-2} = (h^{22})^*$. This can be simplified to

$$H(t; \theta, \varphi) = \sqrt{\frac{5}{4\pi}} A^{22}(t) \left[\frac{1 + \cos^2 \theta}{2} \cos(\phi_{\text{GW}}(t) - 2\varphi) - i \cos \theta \sin(\phi_{\text{GW}}(t) - 2\varphi) \right]. \quad (51)$$

The angles θ and φ are related to the direction under which the observer sees the orbital plane defined in the source frame of the binary. In general the orbital plane of the binary will be inclined with respect to the plane perpendicular to the direction of wave propagation \hat{N} , which is described by an inclination angle ι (θ_{JN} for precessing binaries). This inclination angle takes the place of the angle θ in the spherical harmonics. The angle φ can be substituted by the phase of the binary at coalescence ϕ_c at time t_c . The effect of changing these parameters ϕ_c, t_c is a simple offset in phase and shift in the time of the GW strain, say the time at which the signal reaches its maximum amplitude. An expansion into spin-weighted spherical harmonic modes allows us to separate the dependence of the waveform on inclination and a phase angle so that the modes $h^{\ell m}(t)$ only depend on the remaining binary parameters.

As can be seen from the above expression for the GW strain (substituting ι for θ), if the source is seen “face-on” ($\iota = 0$) or “face-off” ($\iota = \pi$) the GW signal leads to a much stronger response than if the inclination tends towards “edge-on” ($\iota = \pi/2$) where the response is weakest. Moreover, for $\iota = 0$ the strain is a linear combination $h_+ - ih_\times \propto A^{22} \exp[-i(\phi_{\text{GW}} - 2\varphi)]$ and the GW is circularly polarized, whereas for $\iota = \pi/2$ only $h_+ \propto (A^{22}/2) \cos(\phi_{\text{GW}} - 2\varphi)$ is non-zero and the GW is linearly polarized.

Adapted reference frames for precessing binaries Figure 5 illustrates how waveform modes of a precessing binary exhibit modulations when analyzed in the inertial reference frame of the binary. The modes simplify greatly when one switches to a non-inertial, rotating reference frame which tracks the time-dependent motion of the precession: the co-precessing frame. There, the $(2, 2)$ mode is clearly dominant over the weaker higher order modes shown. Mathematically, the transformation law for spin-weighted spherical harmonics ${}_s Y^{\ell m}$ under arbitrary rotations can be used to find that the inertial GW modes $h_{\ell m}^I$ transform to the co-precessing modes $h_{\ell m}^{\text{copr}}$ as follows [630, 142, 366]

$$h_{\ell m}^{\text{copr}}(t) = e^{im\alpha(t)} \sum_{\ell=2}^{\ell_{\text{max}}} \sum_{m'=-\ell}^{\ell} e^{im'\gamma(t)} d_{m',m}^{\ell}(-\beta(t)) h_{\ell, m'}^I(t), \quad (52)$$

where $d_{m',m}^{\ell}$ denote Wigner d-matrices, and the time dependent Euler angles $\alpha(t), \beta(t), \gamma(t)$ parametrize the evolution of \hat{L}_N in a frame with $\hat{z} = \hat{J}$. An arguably superior representation of time-dependent frame rotations is given by quaternions [142].

In the co-precessing frame the precessing waveform is fairly well approximated by the waveform which has spin components in the orbital plane set to zero, a binary with spins aligned with the orbital angular momentum. However, in general $h_{\ell, m}(t) \neq (-1)^{\ell} h_{\ell, -m}^*(t)$ and this approximation therefore discards asymmetry in the waveform modes [143, 695, 678, 432]. A further simplification can be achieved by taking out the orbital phase times the m number of each mode, $h_{\ell m}^{\text{coorb}}(t) = h_{\ell m}^{\text{copr}}(t) e^{im\phi_{\text{orb}}}$, where a quantity that approximates the orbital phase is defined as the average of the dominant mode phases in the co-precessing frame $\phi_{\text{orb}} = (\arg[h_{2,-2}^{\text{copr}}(t)] - \arg[h_{2,2}^{\text{copr}}(t)])/4$.

An example of the waveform emitted by a strongly precessing binary decomposed into modes is shown in Fig. 5 and the precession cones traced by the orbital angular momentum and spin vectors for the same binary are displayed in Fig. 6. In this configuration both spin vectors have non-zero projections in the orbital plane, and the binary has unequal masses which amplifies the effect of precession on the waveform.

The impact of sizable precessing spins as subsumed in the effective precession parameter χ_p is mainly visible in strong modulations in the inertial frame waveform as seen in the modes shown in the top left panel of Fig. 5. The strength of these modulations increases as the binary becomes more unequal in mass-ratio and becomes more prominent for an inclination angle tending towards edge-on rather than face-on inclination. Precession also has more subtle effects on the phasing which are not visible in Fig. 5.

Eccentricity The waveform emitted from a highly eccentric binary is highly deformed and resembles bursts of radiation compared to a quasi-circular inspiral. The binary alternates orbital passages by the periastron (where the two bodies have their closest approach) and the apastron (where they are the furthest apart within one orbit). Contrary to quasi-circular binaries, waveforms emitted from eccentric binaries (even if they have aligned spins) have oscillatory amplitudes and frequencies. The periastron of the orbit is also no longer fixed and instead precesses or advances during the inspiral. The emitted gravitational radiation is enhanced for highly eccentric binaries and radiates peak power in the higher harmonics in the inspiral regime. The increased GW emission also radiates away eccentricity during the inspiral of an eccentric binary so that the orbit eventually circularizes [555]. Therefore, as the binary approaches the merger, the higher harmonics become subdominant. The time to coalescence for eccentric binaries is shortened compared to quasi-circular binaries. A radial phase parameter l fixes where in the orbit a binary finds itself at a reference frequency and so this parameter will shift the oscillation pattern in the waveform in time.

2.4 Numerical relativity simulations

As a coalescing binary approaches merger, the orbital velocity reaches a sizable fraction of the speed of light. In this regime the PN expansion breaks down and the solution of Einstein's equations can only be approximated by full numerical simulations. Simulations of the merger of BBHs have become routine since the breakthroughs by several independent groups in 2005 [570, 169, 106]. The Einstein equations formally depend on the ten degrees of freedom in the metric tensor $g_{\alpha\beta}$ ⁶. The introduction of a coordinate system (usually one time-like and three space-like coordinates) allows us to separate Einstein's equations

⁶ Here we do not assume a weak perturbation around Minkowski space as in Sec. 2.1, but a general metric.

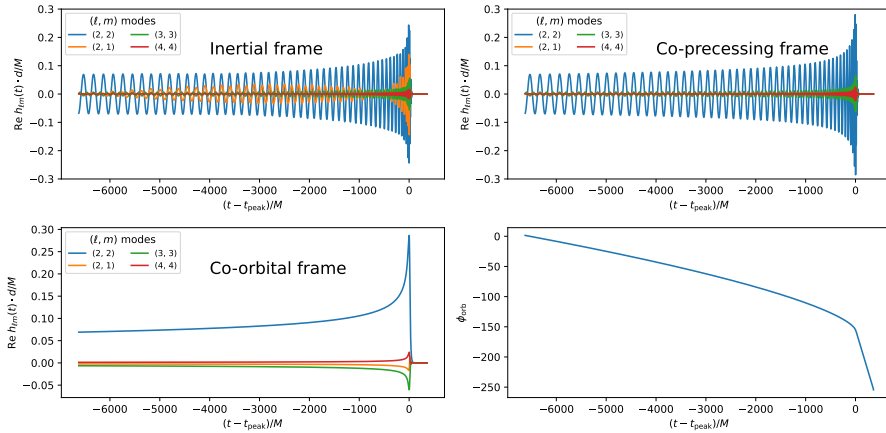


Fig. 5: Selected spherical harmonic modes $((2, 2), (2, 1), (3, 3), (4, 4))$ of the GW signal emitted by a precessing black hole binary. Shown is the real part of the modes in three reference frames. *Top left*: inertial frame, *top right*: co-precessing frame, *bottom left*: co-orbital frame, *bottom right*: one half the averaged phase of the co-precessing frame $(2, \pm 2)$ modes. The binary has mass-ratio $q = 1/4$, and spin vectors $\chi_1 = (0.2, 0.3, 0.35)$, $\chi_2 = (0.5, 0.05, 0.42)$ defined at a reference frequency of 20 Hz for a total mass of $50 M_\odot$. The waveform model used is SEOBNRv5PHM [583].

into six dynamical and four constraint equations of second order. The dynamical equations describe the time evolution of the spatial metric tensor and its time derivative (or, equivalently, the extrinsic curvature variable) given some initial data on an initial hypersurface which in turn needs to satisfy the elliptic constraint equations. To stably evolve the Einstein equations numerically it is important to choose a formulation of Einstein's equations which makes the dynamical equations hyperbolic of a strong enough degree so that the system is well-posed⁷. This is satisfied by the BSSN and the generalized harmonic formulations [108, 78]. To fix the coordinate or gauge freedom four variables need to be specified. For instance, they can describe the proper time of an observer's normal to the current spatial hypersurface (lapse function) and how the timeline of an observer deviates from the normal to the hypersurface (shift vector).

Starting from a numerical solution of the constraint equations for a BBH system, one can evolve the system in time until the merger with the help of special techniques to deal with the curvature singularity inside each BH: either the BH interior inside the *apparent horizon* (a quasi-local definition of the BH horizon which is based on the spatial locations where outgoing light rays

⁷ Well-posedness requires that a unique solution exists and the solution depends continuously on the initial conditions.

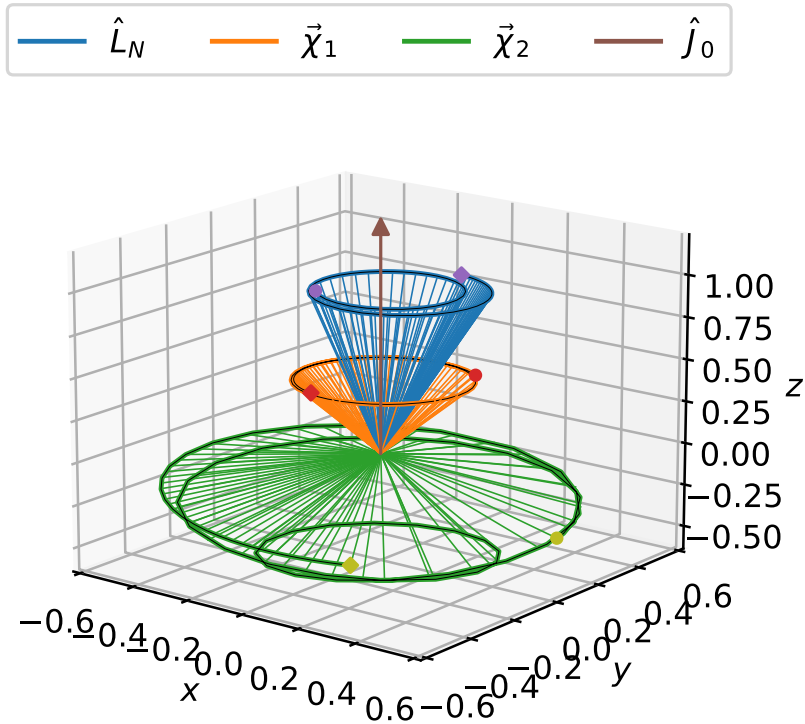


Fig. 6: Evolution of Newtonian orbital angular momentum \hat{L}_N and spin vectors χ_i over time for the precessing binary with waveform shown in Fig. 5. The initial point is indicated by a filled circle and the end point (merger) by a diamond. The evolution of each vector traces out a separate precession cone about the direction of the total angular momentum \hat{J}_0 at the initial point (slightly scaled).

cannot escape the BH ⁸) is excised from the computational domain and the excision surface carefully follows the BH motion, or one can use the so-called “moving puncture” method which places the singularity in-between points of the numerical grid. Special prescriptions for the gauge conditions are also used to avoid singularities. The spatial derivative operators in the dynamical equations are usually discretized with high order finite difference stencils or

⁸ Apparent horizons, when they exist, always lie in the interior of the globally-defined event horizon. NR simulations rely on quasi-local quantities for the positions and properties of BHs in each spatial hypersurface.

spectral methods. The spatial resolution is set by the size of the apparent horizons of the BHs and therefore scales with the size of the smaller BH if the masses are unequal, while the total mass can be scaled out. Time evolution is performed by methods for numerically solving ordinary differential equations. The spatial discretization scale then determines the size of the largest time step for which the system can be stably evolved. Furthermore, BBH simulations need to resolve both the small scales of the BH horizons, and extract the GWs in the wave zone, sufficiently far away from the binary. Covering these disparate scales with a single uniform grid is infeasible; instead, practical simulations require the use of fixed or adaptive mesh refinement methods. Errors due to extraction of the waves at finite distances from the source can be mitigated by extrapolation methods or, ideally, by transporting the radiation to future null infinity.

A non-eccentric binary black hole coalescence can be divided into three regimes: (i) *inspiral* where the orbital velocity is low, $v \ll c$, and the system undergoes quasi-circular inspiral, (ii) *merger* where the two separate BH horizons combine to form a single distorted potato-like horizon and orbital velocities reach $v \simeq 0.5c$ or more in this highly nonlinear regime, and (iii) *ringdown*, where the final black hole radiates away excess energy in terms of quasinormal modes (QNMs) and settles down to a stationary Kerr black hole solution. This last stage can be well described by BH perturbation theory. The emitted waveform is a chirp signal that peaks in amplitude and frequency at the merger, before decaying exponentially in the ringdown. The mass and spin (angular momentum) of the BHs can be determined numerically from their apparent horizon properties.

For an equal-mass non-spinning BH binary, about 5% of the total mass of the system is radiated away in GWs and therefore the mass of the final Kerr black hole is about $M_f/M \simeq 95\%$ of the initial mass of the binary. The final Kerr black hole of an equal-mass non-spinning binary turns out to have a spin of about $\chi_f \simeq 0.7$ acquired from remaining angular momentum of the binary that has not been radiated away during the coalescence. For unequal mass binaries the radiated energy is lower than for the equal mass case. In general, the dependence of the final mass and the final spin is a function of the initial binary masses and spins which is needed for waveform models that include a description of the merger and ringdown parts of the signal. This information can be fitted from numerical relativity (NR) simulation data available over the binary parameter space.

NR simulations can produce highly accurate waveforms (with phase errors a fraction of a radian required by data analysis applications), but the high computational cost limits the number of simulations and their length in time which can be carried out in practice. Moreover, the cost of simulations also varies strongly over the binary parameter space and, in particular, increases steeply the more unequal the mass-ratio and the higher the aligned spin are, based on the induced size of the apparent horizons to be resolved and the allowed time step. A single simulation can take several months on a supercomputer while running in parallel on hundreds of CPU cores. Over 4000 publicly available

BBH NR simulations have been performed so far and have been collected in several catalogs for use in modeling and GW data analysis [1, 518, 145, 2, 381, 380, 378, 379, 3, 405, 4, 361].

2.5 Quasi-normal modes

After the apparent horizons of the two individual BHs in a binary have merged, the BH can be treated as a deformed Kerr BH in linear perturbation theory. It is therefore natural to seek to describe the gravitational radiation emitted by this object by metric perturbations of an analytical BH solution. The linear perturbations around a Schwarzschild black hole are described by the Regge-Wheeler (RW) and Zerilli equations and perturbations of a Kerr black hole by the Teukolsky equation [476]. Perturbations are in general decomposed into spheroidal harmonics of spin-weight -2 which depend on quantum numbers ℓ, m and the (complex) mode frequency ω . In the Schwarzschild case, for a fixed ℓ mode, these equations are formally of the form

$$\frac{d^2\phi}{dx^2}(\omega, x) + [\omega^2 - V(x)] \phi(\omega, x) = 0, \quad (53)$$

with $x \in \mathbb{R}$ a rescaled version of the Schwarzschild tortoise coordinate, $\phi(\omega, x)$ the Fourier transform with respect to time of the RW or Zerilli function, and $V(x)$ the RW or Zerilli potential. These potentials have a peak in the vicinity of small and positive x and fall off smoothly to zero as $x \rightarrow \pm\infty$.

Consider for a moment perturbations of a one-dimensional string with fixed endpoints. In this case, a general perturbation can be expressed as a sum over normal modes $\phi_n(t, x) = e^{i\omega_n t} \psi_n(x)$, which form a complete set. In contrast to the fixed (Dirichlet) boundary conditions used in the string example, the metric perturbations of a BH are not describing a stationary system, but will either escape into the BH horizon or towards infinity with radiation boundary conditions $\phi(\omega, x) \propto e^{i\omega|x|}$ as $x \rightarrow \pm\infty$. We will obtain a discrete set of complex frequencies $\omega_{\text{QNM}} = \omega_R + i\omega_I$ belonging to the so-called *quasi-normal mode* (QNM) solutions of the system. The QNMs vanish in time as damped oscillations of the form

$$e^{\omega_I t} [a \sin(\omega_R t) + b \cos(\omega_R t)], \quad (54)$$

where $\omega_I < 0$. For a Schwarzschild black hole, QNM solutions depend on the azimuthal quantum number ℓ which scales the frequency ω_R , and the overtone index n which increases ω_I and therefore determines how quickly the mode is damped in time. QNMs for Kerr also depend on the (magnetic) quantum number m . The Kerr QNM modes can co-rotate ($m > 0$) or counter-rotate ($m < 0$) with the Kerr BH. We are most interested in the least-damped QNM modes which will dominate the emitted GW signal. The least-damped mode for a non-spinning black hole has $\omega_{n=1, \ell=2} \approx (0.75 - i0.18)c/R_S$, with the Schwarzschild radius $R_S = 2GM/c^2$. This yields a frequency $f \simeq 12 \text{ kHz}(M_\odot/M)$ and a damping time $\tau = 1/|\omega_I| \simeq 55 \mu\text{s}(M/M_\odot)$.

Perturbations of the Kerr metric have been analyzed in terms of curvature perturbations in the Newman-Penrose null tetrad formalism which leads to the Teukolsky equation. The QNMs of Kerr BHs are denoted as $\omega_{n\ell m}$, with ω_{122} being the least-damped mode, now depend on the Kerr parameter of the background BH around which we are perturbing.

2.6 Modeling the signal from inspiral to ringdown

We next discuss two approaches that are used to construct accurate waveform models covering all regimes of GWs emitted in a black hole binary coalescence: the phenomenological (Phenom) and effective-one-body (EOB) frameworks. Both combine theoretical understanding from PN and perturbation theory with NR simulations, and both have also been modified to model waveforms from binaries which include NSs. Another approach that builds a direct surrogate to numerical simulations is discussed in Sec. 2.7.

In the data-driven Phenom and surrogate approaches, and to a lesser degree for EOB, the waveform is usually decomposed to simplify modeling. This is informed by physical intuition about the class of binaries to be modeled, in particular taking into account the effect of certain parameters on the signal as described in Sec. 2.3. For non-precessing binaries the dominant $(\ell, m) = (2, \pm 2)$ spherical harmonic mode of the GW signal can be well represented by its amplitude and phase $h(t) = A(t)e^{i\phi(t)}$. If higher harmonics are included in the model the amplitude - phase decomposition can lead to zero-crossings which are hard to model and it is advantageous to extract the orbital motion of the two bodies by multiplying the complex modes with an exponential of half the phase of the $(2, 2)$ mode. In the resulting “co-orbital frame” [695] the real parts of the modes become non-oscillatory and amplitude-like, while the imaginary parts add some fine structure. If the signals include precession effects, one can transform into a time-dependent reference frame in which the orbital plane of the binary is fixed. In this “co-precessing frame” [630, 540, 144], precession-induced modulation effects are significantly reduced. Both the motion of the reference frame and the signal in the precession-adapted frame need to be modeled.

Effective-one-body framework In the late inspiral the PN approximation deteriorates and eventually breaks down as the orbital velocity becomes a sizable fraction of the speed of light. This difficulty can be addressed by the effective-one-body (EOB) framework [155, 156]. In the following we qualitatively describe the main idea of EOB following Ref. [476]. We start by considering the equations of motion of a two-body system. Up to 2PN order and assuming zero spins, no radiation reaction force is present and the system is conservative. After introducing a particular set of coordinates (ADM coordinates) we can write the equations of motion in terms of a Hamiltonian in the center-of-mass frame of the binary, using relative position and conjugate momentum coordinates (\mathbf{q}, \mathbf{p}) . Due to the invariance of the Hamiltonian under time translations and

rotations, energy and angular momentum are conserved. We write energy as a function of the angular momentum and a radial action variable which is an adiabatic invariant.

The basic idea of EOB is to find a one-body problem in an external space-time that reproduces the solution of the given two-body problem (written in a gauge invariant form). We can consider a test particle of reduced mass $\mu = m_1 m_2 / (m_1 + m_2) = \eta M$ which moves along the geodesic of a static spherically symmetric metric $g_{\text{eff}}^{\mu\nu}$ written in terms of some effective coordinates. At the Newtonian level this is the Schwarzschild metric which describes the gravitational potential of a mass $M = m_1 + m_2$. The EOB line element is

$$ds_{\text{eff}}^2 = g_{\text{eff}}^{\mu\nu} dx_{\text{eff}}^\mu dx_{\text{eff}}^\nu = -A(R)dt_0^2 + B(R)dR^2 + R^2(d\theta^2 + \sin^2\theta d\phi^2), \quad (55)$$

where the functions $A(R)$ and $B(R)$ need to be determined. The EOB approach then defines a natural mapping between the real two-body problem and the effective one-body problem. This can be motivated by a quantum mechanical analogy (the Bohr-Sommerfeld quantization condition of the hydrogen atom). Adiabatic invariants corresponding to the principal and angular momentum quantum numbers can be directly related between the two descriptions, whereas the mapping of the energy is nontrivial. One arrives at the following result at 2PN order:

$$A(R) = 1 - \frac{2M}{R} + 2\eta \left(\frac{M}{R}\right)^3, \quad (56)$$

$$B(R) = 1 + \frac{2M}{R} + (4 - 6\eta) \left(\frac{M}{R}\right)^2, \quad (57)$$

along with an energy mapping. Therefore, within this approximation we can substitute the original two-body problem by an easier to solve effective one-body problem and solve it for $\eta > 0$.

Considering the conservative dynamics of the system one finds that, as is the case for the Schwarzschild metric, the EOB metric has a horizon (because $A(R)$ has a simple zero at $R > 0$ for all η) and an *innermost stable circular orbit* (ISCO). Similarly, one can define the *light ring*: the smallest possible (unstable) circular orbit for a massless particle. For very unequal masses a small mass inspirals through a sequence of quasi-circular orbits until it reaches the ISCO and suddenly starts to plunge toward the central BH. In contrast, for comparable masses, there is no sharp transition between inspiral and plunge.

The effect of the emission of GWs (first entering at 2.5PN order) can be expressed as a radiation reaction force $\hat{\mathcal{F}}_\varphi$ which can be added into the Hamiltonian equations of motion for the conservative dynamics. Written in

polar coordinates in the orbital plane these equations read

$$\frac{dr}{d\hat{t}} = \frac{\partial \hat{H}}{\partial p_r}, \quad (58)$$

$$\frac{d\varphi}{d\hat{t}} = \frac{\partial \hat{H}}{\partial p_\varphi}, \quad (59)$$

$$\frac{dp_r}{d\hat{t}} = -\frac{\partial \hat{H}}{\partial r}, \quad (60)$$

$$\frac{dp_\varphi}{d\hat{t}} = \hat{\mathcal{F}}_\varphi(r, p_r, p_\varphi), \quad (61)$$

where

$$\hat{H}(r, p_r, p_\varphi) = \frac{1}{\eta} \sqrt{1 + 2\eta \left[\sqrt{A(R) \left(1 + \frac{p_r^2}{B(r)} + \frac{p_\varphi^2}{r^2} \right)} - 1 \right]}, \quad (62)$$

and $r = R/M$, $\hat{t} = t/M$.

After solving these equations of motions numerically to obtain the inspiral and plunge dynamics, we can compute the emitted GWs via the quadrupole formula. To complete the waveform, a merger part needs to be smoothly attached after the plunge. This ringdown waveform consists of a superposition of damped sinusoids which results from the oscillation of the final Kerr BH in its quasi-normal mode oscillations. This yields a qualitatively correct waveform of the inspiral, merger and ringdown. The above EOB construction can be extended up to higher PN orders (4PN is used in practical models) and can be generalized to include spin effects. In practice, EOB models also add corrections for neglected non quasi-circular effects and introduce unknown higher order PN terms in the Hamiltonian which are then tuned or calibrated to NR simulations to increase the accuracy of the model.

EOB models from two different groups have been used for LVK analyses. This includes the ‘‘SEOBNR’’-type models for aligned spin and the dominant mode [667, 668, 135], models including higher harmonics [207, 565] and precession [548, 103, 541, 583], as well as prescriptions for tidal models [654, 490], and models incorporating further optimizations [233, 430]. Of these, the most complete recent model for BBHs is ‘‘SEOBNRv5PHM’’ [583] for generically precessing binaries which includes higher harmonics. ‘‘TEOBResum’’-type models have been constructed for non-precessing binaries including tidal effects [522, 520, 75], and for precessing binaries [76, 327].

Phenomenological waveform model framework The class of phenomenological models takes a very practical approach at constructing models of the GW signal emitted from compact binaries. This approach matches a post-Newtonian inspiral to a phenomenological description of the merger and ringdown which aims at encapsulating the waveform morphology from numerical-relativity simulations. The method posits ansatz functions in the Fourier domain for

different regimes of the coalescence along with a polynomial dependence on mass-ratio and spins. Hybrid inspiral - NR waveforms are created by stitching together NR simulations with inspiral waveforms produced by an uncalibrated EOB model (evaluated at the same binary parameters as the respective NR simulation). These “hybrids” are created for all mass-ratios and aligned spins where accurate NR simulations are available and are used to calibrate the model. The resulting phenomenological models focus on computational efficiency by avoiding the numerical solution of systems of complicated ODEs (as used in EOB) and instead provide analytical expressions that can be directly evaluated.

Traditionally, phenomenological models have been constructed in the Fourier domain [74], so that inner products between waveforms used in data analysis can be directly computed. Therefore, modeling starts by considering the morphology of waveforms in the Fourier domain in contrast to the EOB time domain method. Ansatz functions are picked in three frequency regimes: inspiral, an intermediate late-inspiral regime, and merger-ringdown. In the following we describe some elements of the “IMRPhenomXAS” waveform model [568].

In the inspiral regime the phase model is written as the 3.5PN TaylorF2 approximant plus higher order “pseudo-PN” terms

$$\varphi_{\text{Ins}}(f) - \varphi_{\text{TF2}}(f) = \frac{1}{\eta} \left[\sigma_0 + \sum_{i=0}^4 \sigma_{i+1} f^{(i+3)/3} \right], \quad (63)$$

where the σ_i are unknown PN coefficients that have not yet been calculated. The σ_i are determined by fitting a rescaled difference between frequency derivatives of hybrid waveform and TaylorF2 phases $f^{-8/3}(\varphi'_{\text{Hybrid}}(f) - \varphi'_{\text{TF2}}(f))$. A similar PN-based ansatz is made for the inspiral amplitude

$$A_{\text{Ins}}(f) = A_{\text{PN}} + A_0 \sum_{i=1}^3 \rho_i (\pi f)^{(6+i)/3}, \quad (64)$$

with “pseudo-PN” coefficients ρ_i , again determined from the hybrids.

As discussed in Sec. 2.5 the ringdown can be described by BH perturbations in the time domain. It is therefore instructive to consider the Fourier transform of a damped oscillation $h(t) = \Theta(t) e^{2\pi t(i f_{\text{RD}} - f_{\text{damp}})}$, where $\Theta(t)$ is the Heaviside step function. This leads to a Lorentzian function (Cauchy distribution) for the phase derivative and for the square of the Fourier domain amplitude $|\tilde{h}(f)|^2 \propto 1/[(f - f_{\text{RD}})^2 + f_{\text{damp}}^2]$. Since the physical waveform should fall off faster than $1/f$ due to its smoothness, the ansatz for the merger-ringdown amplitude multiplies the Lorentzian by a decaying exponential

$$A_{\text{MR}} = \left[\frac{a_R (f_{\text{damp}} \sigma)}{(f - f_{\text{RD}})^2 + (f_{\text{damp}} \sigma)^2} \right] e^{-\lambda(f - f_{\text{RD}})/(f_{\text{damp}} \sigma)}, \quad (65)$$

with fitting parameters a_R, σ, λ . The merger-ringdown model for the phase derivative consists of a Lorentzian plus terms with negative powers in fre-

quency to capture steep gradients

$$\eta\varphi'_{\text{RD}} = c_{\text{RD}} + \sum_i^n c_i^{-p_i} + \frac{c_0 a_\varphi}{(f - f_{\text{RD}})^2 + f_{\text{damp}}^2}, \quad (66)$$

again introducing a number of new parameters $c_{\text{RD}}, c_i, a_\varphi$. Moreover, the ring-down model depends on a fitting formula that predicts the final BH’s mass and spin from the progenitor BHs. From these one can determine the ringdown and damping frequencies f_{RD} and f_{damp} .

Lastly, an intermediate regime bridges the gap between the inspiral and merger-ringdown parts of the model and uses ansatz functions inspired by the neighboring regimes. For a description of the model in the intermediate regime and details about where in frequency the models in the three frequency regions are situated and how they are matched together, see [568].

With the amplitude and phase ansatz functions defined, one can fix the model coefficients for any given point in parameter space where an accurate NR simulation is available and a hybrid waveform has been computed. To obtain a practical model one posits a polynomial or rational dependence of the model coefficients over parameter space, motivated by the mass-ratio and spin dependence of PN approximants. The model uses hierarchical fits in symmetric mass-ratio, an effective aligned spin parameter, and the difference between the BH’s aligned spins.

This approach leads to fast, closed form models that are convenient to use for data analysis. Examples include the aligned-spin BBH models up to “IMR-PhenomD” [74, 624, 423] and the recent “IMRPhenomXAS” [568]. Newer models are available in versions that include higher-order modes [465, 328]. Models for precessing binaries require additional modeling of the time-dependent rotation of the reference frame, in a similar way as for EOB models. To use this prescription in the Fourier domain, additional approximations are introduced via the stationary phase approximation [366]. An extension to two-spin dynamics is given in [421]. A more accurate solution of the frame dynamics for generically precessing binaries is used in “IMRPhenomXPHM” [569]. A recent model includes tuning against numerical waveforms in the precessing sector [360]. Further models incorporate tidal effects for BNSs [240, 243] or NS - BH binaries [677]. Recently, a family of phenomenological models has been created in the time domain [270, 269, 268] in an effort to avoid some of the approximations used by Fourier domain phenomenological models.

2.7 Reduced-order and surrogate models

Over the past decade, data driven models of GWs have come to prominence in GW data analysis with the promise of delivering high accuracy and fast evaluation speeds. Reduced-order and surrogate modeling aims at creating an efficient and accurate *surrogate*⁹ or substitute model for a given set of gravi-

⁹ “Surrogate model” is the more general term, while “reduced-order model” implies the use of truncated basis expansions in the model construction.

tational waveform data, with the help of numerical methods for decomposing, compressing, and fitting the original data.

Waveform data set and data pieces. A data set $\{h(\mathbf{t}; \boldsymbol{\lambda}_i)\}_{i=1}^N$ can be generated from a GW model $h(\mathbf{t}; \boldsymbol{\theta})$ ¹⁰ (or a set of NR waveforms) at parameter values $\mathcal{T} = \{\boldsymbol{\lambda}_i\}_{i=1}^N$ on a time grid $\mathbf{t} = \{t_j\}_{j=1}^m$. The input data is then a set of waveforms given over the space of relevant intrinsic binary parameters $\boldsymbol{\lambda}$ (a subset of the set of all physical parameters $\boldsymbol{\theta}$). The values \mathcal{T} can form a grid or, more generally, can be scattered data points in the domain of the original model. Each waveform in this input data set is decomposed into a number of *data pieces* $f_k(\mathbf{t}; \boldsymbol{\lambda})$ chosen in such a way as to obtain as simple a function of time and binary parameters as possible as discussed in Sec. 2.6.

Reduced basis. Each waveform data piece $f(\mathbf{t}; \boldsymbol{\lambda})$ in a surrogate model aims to approximate its discrete training data set $\mathcal{H} = \{f(\mathbf{t}; \boldsymbol{\lambda}_i)\}_{i=1}^N$ as closely as possible. Usually, one first computes a discrete orthonormal basis $\{\mathbf{B}_i\}_{i=1}^N$, $\langle \mathbf{B}_i, \mathbf{B}_j \rangle = \delta_{ij}$ with elements $\mathbf{B}_i = B_i(\mathbf{t}) = (B_i(t_1), \dots, B_i(t_m))^T$ from the training data, with $\langle \cdot, \cdot \rangle$ the Euclidean inner product on \mathbb{R}^m . Often a *reduced basis* with $\dim \mathbf{B} = n < N$ is computed which amounts to a truncated basis expansion

$$\mathbf{f}(\boldsymbol{\lambda}) = f(\mathbf{t}; \boldsymbol{\lambda}) \approx \sum_{i=1}^n c_i(\boldsymbol{\lambda}) \mathbf{B}_i(\mathbf{t}), \quad (67)$$

with n chosen according to a desired accuracy threshold. The basis expansion coefficients are given by

$$c_i(\boldsymbol{\lambda}) = \langle \mathbf{f}(\boldsymbol{\lambda}), \mathbf{B}_i \rangle. \quad (68)$$

Two methods have been used in the literature to build a reduced basis for a data piece f : (i) a greedy algorithm which at step k adds waveform data at the point in parameter space where the data piece vector has the highest projection error $\|f(\cdot; \boldsymbol{\lambda}) - \mathcal{P}_k f(\cdot; \boldsymbol{\lambda})\|$; here, $\mathcal{P}_k f(\cdot; \boldsymbol{\lambda})$ is the orthogonal projection of the data piece onto the span of the basis $\{\mathbf{B}_i\}_{i=1}^k$ constructed in the first k steps of the algorithm (see Appendix A of [293] for details), or (ii) a method where the waveform data is suitably downsampled in the independent variable, arranged in a matrix with elements $\mathcal{F}_{ij} = f(t_j; \boldsymbol{\lambda}_i)$ and the (truncated) singular value decomposition [349] $\mathcal{F} = U^T \Sigma V$ is used to compute the basis [573, 574]. If the training set is sufficiently dense and the data are smooth, waveforms inside the domain covered by the training set, but not part of the training set itself will be well approximated by the reduced basis.

Surrogate construction. Given a reduced orthonormal basis $B_i(\mathbf{t})$ for a waveform data piece $f(\mathbf{t}; \boldsymbol{\lambda})$ two contrasting approaches have been used to build

¹⁰ In the following we assume time domain waveforms, but surrogates can also be constructed in the frequency domain.

a surrogate for this piece by fitting or interpolating coefficients over parameter space: (i) one may directly fit or interpolate the coefficients $c_i(\boldsymbol{\lambda})$ ¹¹ as in Ref. [573,574], or (ii) the problem can be recast as interpolation in time by selecting a “good” set of sparse *empirical* time nodes $\{T_1, \dots, T_n\}$ from the full time grid such that the resulting interpolant recovers the waveform data piece exactly at the T_i while minimizing the interpolation error. As discussed in Ref. [293] this is achieved by the so-called *empirical interpolant* [471,187] (EI)

$$\mathcal{I}_n[f](\mathbf{t}; \boldsymbol{\lambda}) = \sum_{j=1}^n \mathcal{B}_j(\mathbf{t}) f(T_j; \boldsymbol{\lambda}), \quad (69)$$

where $\mathcal{B}_j(\mathbf{t}) = \sum_{i=1}^n B_i(\mathbf{t}) (V^{-1})_{ij}$ and $V_{ij} = B_j(T_i)$, $V \in \mathbb{R}^{n \times n}$. The EI time nodes are chosen such that V has a small condition number. This can be accomplished with an algorithmic complexity of $\mathcal{O}(n^3)$ as shown in App. A of Ref. [89]. With this transformation in hand, the data piece $f(\cdot; \boldsymbol{\lambda})$ then needs to be fitted at each of the EI time nodes T_j .

Fitting and interpolation methods. A variety of methods have been used to predict expansion coefficients $c_i(\boldsymbol{\lambda})$ or the waveform data piece at a fixed EI node $f(T_j; \boldsymbol{\lambda})$ at unknown parameter space values $\boldsymbol{\lambda}$ given training data. See Ref. [639] for an introductory review. Interpolation methods enforce that the interpolant coincides with the given data at the training set points, while a fitting method provides no such guarantee and minimizes the residual between the given data and e.g. a polynomial ansatz made by the method. In low dimensional parameter spaces interpolation by tensor-product splines [136] is straightforward and reliable [573,574] whenever a large enough training set can be generated on a regular grid. A combination of radial basis functions with monomials has been used in Ref. [552] which does not require a grid. For moderately large parameter spaces with dimensions $\gtrsim 5$ methods for fitting scattered data must be used. This includes polynomial regression with feature selection such as the greedy forward stepwise regression method with cross-validation error estimates described in Appendix A of Ref. [128], Gaussian process regression (GPR) [585] which can also provide a measure of uncertainty for each fit [245,442,696,695], but is costly for large training sets ($\mathcal{O}(N^3)$), and, more recently, neural networks [351] which have been shown to handle problems of moderate dimensionality with good accuracy and are fast to evaluate [422,632,675].

Available surrogate models. Surrogate models have been built for dominant mode aligned-spin binaries [293,573,574,442], models including higher harmonics [696,208] and precession [128,129,695,323]. Many surrogate models (or ROMs) have been built for EOB models, see Sec. 2.6, which are in general significantly slower to evaluate than phenomenological models, see Sec. 2.6,

¹¹ Note that, in contrast to method (ii), sparseness in time has already been imposed before basis construction.

limiting their applicability for data analysis purposes. Similar to phenomenological models EOB surrogates tend to be built directly in the frequency domain [573, 574, 442, 208]. Over the past several years surrogate models of NR simulations have been successfully constructed including effects of precession, higher harmonics, memory, and eccentricity [128, 129, 695, 696, 730, 404]. As NR simulations are extremely costly and sparse, these studies have worked with carefully designed training sets to keep the number of simulations small without sacrificing high accuracy. Naturally, their parameter space coverage is more restrictive than for semi-analytic models, but where they are available, NR surrogates are arguably more accurate than models based on semi-analytical techniques. Surrogates have also been constructed for remnant properties of BH mergers (final mass and spin, as well as recoil velocity) [697].

The evaluation speed of surrogate models is typically several orders of magnitude faster than it took to generate one of the training space waveforms; the speedup is especially high for NR surrogates. Surrogate models usually achieve accuracies of 10^{-3} (or better) in the *mismatch*, a normalized and maximized inner product between waveforms, (see Eq. (102) and the following discussion in Sec. 3.7) against original data which is in general sufficient for most GW data analysis tasks for current ground based interferometers, but see [576] for estimated accuracy requirements for future ground-based GW detectors.

2.8 Comparison of waveform accuracy and efficiency

Waveform models aim to provide accurate approximations of the true underlying waveform (as a solution to Einstein's equations in GR). Given that the most accurate merger waveforms come from a sparse set of expensive NR simulations, but are too short to cover the frequency sensitivity of ground based GW detectors, practical models invariably need to combine analytical and numerical waveforms in addition to some interpolation or fitting. Therefore, waveform models compound various sources of errors from their constituent parts and model assumptions. Given these imperfections and the undesirable consequences of waveform systematics in data analysis applications (missed signals, bias in binary parameters) it is crucial to study how these models compare among themselves and against NR simulations in an effort to further improve their fidelity.

A detailed comparison of the accuracy of current waveform models is beyond the scope of this review. The following articles provide comparisons between a number of models in terms of mismatch or in terms of a shift (*bias*) in recovered parameters compared to the parameters of a synthetic signal in parameter estimation. For comparisons of aligned spin models see Refs. [423, 135, 568, 696], for models including precessing see Refs. [421, 695, 541, 569, 360]. Tidal models are being compared in Refs. [243, 677].

For data analysis applications the efficiency of waveform models is very important. A comparison of the computational cost of BBH models implemented in the LSC's Algorithm Library Suite [460] is shown in Fig. 7. The evaluation

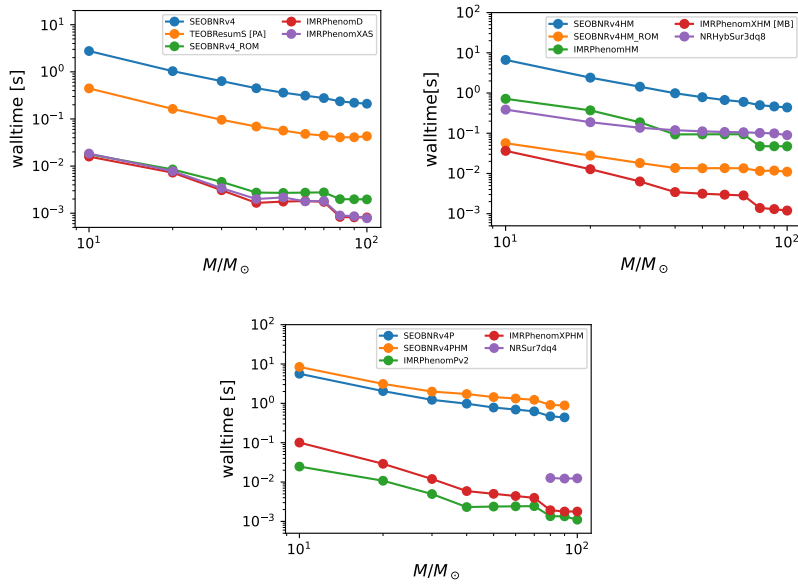


Fig. 7: Evaluation times for Fourier domain polarizations of a number of BBH waveform models as a function of the total mass of the binary. *Top Left:* aligned-spin models for the dominant (2,2) mode, *Top Right:* aligned-spin models including higher harmonics, *Bottom:* models for precessing binaries. The total mass was varied from $10 M_{\odot}$ to $100 M_{\odot}$, while all other parameters were kept fixed (mass-ratio 1:3, all spin components set to zero except $\chi_{1z} = \chi_{2z} = 0.5$ and, for models supporting precession, $\chi_{1x} = 0.5$; the starting and maximum frequencies were set to 20 and 16384 Hz, with the frequency spacing automatically determined by LALSuite’s [460] `SimInspiralFD` function.) PA refers to the post-adiabatic approximation and MB to multi-banding techniques. The NR surrogate model in the precession panel is limited by the number of cycles available, which translates to a lower total mass for which it can be evaluated. In contrast, the NR surrogate in the middle panel has been hybridized with PN waveforms in the inspiral, allowing it to produce longer waveforms.

time increases steeply for low-mass binaries driven by the waveform length. Models including higher harmonics and/or precession are in general slower than simpler models. Phenomenological and surrogate / ROM models are several orders of magnitude faster than time domain EOB models. Further acceleration for frequency domain models is possible with multi-banding techniques as used by IMRPhenomXPHM [703, 329], while time domain EOB models can trade efficiency for accuracy through the post-adiabatic approximation [521, 502].

3 Statistical framework

In this section we develop a statistical model of the GW signal and detector noise, showing how the noise curves from Sec. 1 and the parameter-dependence of the waveforms from Sec. 2 combine to produce a natural geometric structure for the parameter space. This structure gives rise to the typical correlations in the parameter estimation results discussed in Sec. 5, and gives us a method for covering the parameter space with templates for a matched-filter search, discussed in Sec. 4.

Detector noise is generally treated as a stationary Gaussian process with a correlation structure described by a given power spectral density (PSD), resulting in the Whittle likelihood function [717]. The noise PSD used may be estimated from data or predicted via the physics of the detector(s) considered. This noise model was initially applied to GW data analysis studying both detectability and parameter estimation for inspiral signals in [295]. The likelihood ratio of a signal under the Gaussian noise model also gives rise to the classical matched filter for signal detection [689].

More recent works have examined relaxing some of the assumptions behind the Whittle likelihood: for example, the PSD may not be known exactly, so its uncertainty may be marginalised over [609, 463, 190, 663, 121], or the PSD may be jointly estimated along with the signal parameters [189, 561].

3.1 Likelihood function for detector noise

The calibrated output of a GW detector $d(t) = h(t) + n(t)$ contains the GW signal $h(t)$ and additive noise $n(t)$. The noise is a combination of fundamental, environmental and technical noise sources for the particular detector; references in Sec. 1.2 provide more details. Mathematically, we can say that the noise is drawn from a stochastic process, $n \sim N$ described by a statistical model H_N that gives us the probability of observing a particular noise realisation $p(n(t)|H_N)$.

The noise model is chosen in the light of available information, which we can quantify in terms of the moments of the process, written as expectation values integrating over the space of noise realisations.¹² The first moment, the mean, may for simplicity be set to zero by redefining the zero of detector strain output:

$$E_N[n(t)] = \int n(t)p(n(t)|H_N) dn(t) = 0. \quad (70)$$

The second moment of the stochastic process

$$E_N[n(t)n(t')] = \int n(t)n(t')p(n(t)|H_N) dn(t) \equiv C_N(t, t'), \quad (71)$$

¹² Thus, the moments are *not* defined as time-averages for a specific realisation $n(t)$, although knowledge of surrounding data may be used to inform the model, assuming ergodicity of the noise generating process.

specifies a two-point kernel $C_N(t, t')$ known as the auto-covariance function.

We may continue in this fashion to higher-order moments to completely specify the noise stochastic process. However, the common case where we only have constraints for the first and second moments, i.e., the mean and variance, the probability distribution that maximises the entropy, therefore representing the least informed distribution, is the *multivariate Gaussian* distribution. This motivates the use of the Gaussian likelihood function in our analyses, although it is possible to derive a likelihood with higher order information.

Stationarity A stochastic process is said to be stationary if it is invariant under a translation in time,

$$p(n(t)|H_N) = p(n(t + \tau)|H_N), \quad (72)$$

which is satisfied if all its moments are time-invariant. A less restrictive requirement is that of *weak-sense stationarity*, where only the first two moments are required to be invariant. The mean may be set to zero at all times, but for the second moment stationarity implies that

$$C_N(t, t') = C_N(0, t' - t) \equiv C_N(\tau), \quad (73)$$

i.e., the auto-covariance is a function only of the time lag $\tau \equiv t' - t$.

Discretization The noise considered above as a continuous process $n(t)$ is a mathematical idealization of actual detector output, which is a set of discrete samples from the generating process. For data sampled at a finite set of J times, t_j , separated by uniform intervals Δt , the sampled values can be thought of as a vector \mathbf{n} in a J -dimensional space, and the covariance function becomes a symmetric matrix

$$C_{jk} \equiv E[n_j n_k] = \int n_j n_k p(\mathbf{n}|H_N) d^J \mathbf{n}. \quad (74)$$

Neglecting information from higher moments, the probability of a particular noise realisation \mathbf{n} is given by the multivariate Gaussian distribution

$$p(\mathbf{n}|C_N, H_N) = \frac{1}{\sqrt{\det 2\pi \mathbf{C}_N}} \exp \left[-\frac{1}{2} \sum_j \sum_k n_j (C_N^{-1})_{jk} n_k \right]. \quad (75)$$

This time-domain likelihood function requires a double sum over the data, thus its computational cost scales as J^2 . The likelihood may be much more efficiently evaluated in the frequency domain using the discrete Fourier transform (DFT): the frequency-domain noise realization is expressed via a matrix operation as $\tilde{\mathbf{n}} = \mathbf{F} \mathbf{n} \Delta t$, where $F_{jk} = J^{-1/2} \exp(-2\pi i j k / J)$ is a (unitary)

discrete Fourier transformation matrix. Since $\mathbf{F}\mathbf{F}^* = \mathbf{I}$, the time-domain likelihood can be rewritten as

$$\begin{aligned} p(\mathbf{n}|C_N, H_N) &= \frac{1}{\sqrt{\det 2\pi\mathbf{C}_N}} \exp \left[-\frac{1}{2}(\mathbf{n}^T \mathbf{F})(\mathbf{F}^{-1}\mathbf{C}_N^{-1}\mathbf{F})(\mathbf{F}^{-1}\mathbf{n}) \right] \\ &= \frac{1}{\sqrt{\det 2\pi\mathbf{C}_N}} \exp \left[-\frac{1}{2\Delta t^2} \tilde{\mathbf{n}}^T \tilde{\mathbf{C}}_N^{-1} \tilde{\mathbf{n}}^* \right], \end{aligned} \quad (76)$$

where $\tilde{\mathbf{C}}_N = \mathbf{F}^{-1}\mathbf{C}_N\mathbf{F}$.

If the noise is stationary, then \mathbf{C}_N is a circulant matrix, and $\tilde{\mathbf{C}}_N$ is diagonal, allowing us to replace the double sum with a single sum over the diagonal elements. We define the *one-sided* noise PSD $S_N(f)$ via the Wiener-Khinchin theorem as the Fourier transform of the noise auto-covariance function,

$$\frac{1}{2}S_N(f) = \int_{-\infty}^{\infty} C_N(\tau) \exp(-2\pi i f \tau) d\tau, \quad (77)$$

allowing the diagonal of $\tilde{\mathbf{C}}_N$ to be written as $\tilde{C}_{ii} = \frac{J}{2\Delta t} S_N(f_i)$. Therefore, the frequency domain likelihood can be written as

$$\begin{aligned} p(\tilde{\mathbf{n}}|S_N, H_N) &= \det(2\pi\mathbf{C}_N)^{-1/2} \exp \left[-\frac{1}{2J\Delta t} \sum_i \frac{\tilde{n}_i \tilde{n}_i^*}{\frac{1}{2}S_N(f_i)} \right] \\ &= \det(2\pi\mathbf{C}_N)^{-1/2} \exp \left[-\frac{1}{T} \operatorname{Re} \sum_{i>0} \frac{\tilde{n}_i \tilde{n}_i^*}{\frac{1}{2}S_N(f_i)} \right], \end{aligned} \quad (78)$$

using the fact that the original time-series \mathbf{n} is real, implying $\tilde{n}_{-i} = \tilde{n}_i^*$, and we have introduced $T = J\Delta t$. If we further define the noise-weighted inner product

$$\langle \mathbf{a} | \mathbf{b} \rangle \equiv 2 \operatorname{Re} \int_0^\infty \frac{\tilde{a}^*(f) \tilde{b}(f)}{\frac{1}{2}S_N(f)} df, \quad (79)$$

the noise likelihood can be written in terms of the frequency-domain noise realisation $\tilde{n}(f)$ as

$$p(\tilde{n}(f)|S_N, H_N) = \det(2\pi\mathbf{C}_N)^{-1/2} \exp \left(-\frac{1}{2} \langle \mathbf{n} | \mathbf{n} \rangle \right). \quad (80)$$

With this definition the space of data is formulated as an *inner product vector space*, which we will later use to access various (differential)-geometric methods, for example considering distances between neighbouring signals. See [601, 38] for further discussion of the derivation of the Gaussian likelihood and its assumptions.

3.2 Likelihood for a signal model

We now return to the case where the data contains both noise and a signal, which we denote as H_S for signal hypothesis. This hypothesis includes our previous assumptions about the noise \mathbf{n} given by the noise model H_N with PSD S_N , but adds the assumption that the mean of the data is non-zero due to the presence of a signal \mathbf{h} , such that $\mathbf{d} = \mathbf{h} + \mathbf{n}$. Calculating the precise form of the signal requires assuming a particular waveform model; for a given set of source parameters $\boldsymbol{\theta}$, the waveform model yields the signal time series \mathbf{h} , or *signal model*, and, from 80, the likelihood of the residuals $\mathbf{h} - \mathbf{d}$ is

$$p(\mathbf{d}|\mathbf{h}(\boldsymbol{\theta}), H_S) = \det(2\pi\mathbf{C}_N)^{-1/2} \exp\left(-\frac{1}{2} \langle \mathbf{d} - \mathbf{h} | \mathbf{d} - \mathbf{h} \rangle\right). \quad (81)$$

The shape of this function across the parameter space $\boldsymbol{\theta}$ will determine the precision with which we can estimate the physical parameters of the source, see Sec. 5. The likelihood function over $\boldsymbol{\theta}$ is also of importance when searching for a signal, as values of the likelihood close to those at any global or local maximum are generally only obtained over a tiny fraction of the possible parameter space. We therefore need to know how finely to sample the space to avoid missing possible signals, i.e. how to lay out a *template bank*, as discussed in Sec. 4.3.

The inner product in Eq. (81) can be expanded as $\langle \mathbf{d} - \mathbf{h} | \mathbf{d} - \mathbf{h} \rangle = \langle \mathbf{d} | \mathbf{d} \rangle + \langle \mathbf{h} | \mathbf{h} \rangle - 2 \langle \mathbf{d} | \mathbf{h} \rangle$. The quantity $\rho_{\text{opt}}^2 = \langle \mathbf{h} | \mathbf{h} \rangle$ is the square of the optimal signal-to-noise ratio (SNR), a useful measure of the detectability of a signal in a detector with given noise PSD. In the picture where data of fixed length is described as a J -dimensional vector space with the inner product Eq. (79), the optimal SNR is the length of the vector representing a particular signal. We may consider the space of data streams \mathbf{d} to have an associated metric $\boldsymbol{\Sigma}$: for data in the frequency domain, the metric is a diagonal matrix with nonzero elements given by $\Sigma_{ii} = (T/2)S_N(f_i)^{-1}$, indicating that the Fourier frequency bins are orthogonal dimensions of this space. The operation of *whitening* the data – achieved by multiplying a data stream $\tilde{\mathbf{d}}$ by $S_N(f)^{-1/2}$ – can then be seen as the normalisation of these frequency bins, such that the metric becomes the identity matrix.

3.3 The Fisher information metric

The space of possible signals \mathbf{h} can be considered as a sub-manifold of the full vector space of possible data streams \mathbf{d} . This sub-manifold of signals, with dimensionality equal to the number of independent parameters used to describe the signal, is not itself a vector space, since a linear combination of signals in general is not another valid signal. Still, provided the waveform is a smooth function of these parameters we may consider it as a continuous manifold.

We can then use the signal parameters as a coordinate system to identify points on the signal manifold; the flat-space metric restricted to the signal

manifold will induce a metric $\mathbf{\Gamma}$ in the parameter space, determined by the “closeness” of neighbouring signals. Formally, for an infinitesimal change in parameters $d\boldsymbol{\theta}$ we have a change in the waveform $d\boldsymbol{h}(\partial\boldsymbol{h}/\partial\boldsymbol{\theta})$ and a squared interval

$$\begin{aligned} ds^2 = \|d\boldsymbol{\theta}\|^2 &= \left(d\boldsymbol{\theta} \frac{\partial \tilde{\boldsymbol{h}}}{\partial \boldsymbol{\theta}} \right)^T \tilde{\mathbf{C}}_{\mathbf{N}}^{-1} \frac{\partial \tilde{\boldsymbol{h}}}{\partial \boldsymbol{\theta}} d\boldsymbol{\theta} \\ &= d\boldsymbol{\theta}^T \mathbf{\Gamma} d\boldsymbol{\theta}, \end{aligned} \quad (82)$$

where the metric in parameter space is given by

$$\Gamma_{ij} = \left\langle \frac{\partial \boldsymbol{h}}{\partial \theta_i} \middle| \frac{\partial \boldsymbol{h}}{\partial \theta_j} \right\rangle. \quad (83)$$

The matrix $\mathbf{\Gamma}$ is known as the Fisher information matrix, or metric in this context [84].

The Fisher matrix formalism is widely used to determine parameter estimation precision under a Gaussian approximation of the likelihood function [295, 214, 692]. If we have identified the parameter values $\boldsymbol{\theta}_0$ which maximise the log-likelihood at $l_0 = \log L(\boldsymbol{\theta}_0)$, the expansion of the log-likelihood to second order around $\boldsymbol{\theta}_0$ is given by

$$\log L(\boldsymbol{\theta}_0 + \delta\boldsymbol{\theta}) \approx l_0 - \frac{1}{2} \delta\theta_i \Gamma_{ij} \delta\theta_j \equiv l_0 - \frac{1}{2} \|\delta\boldsymbol{\theta}_i\|^2. \quad (84)$$

Neglecting higher order terms results in a Gaussian function on parameter space with covariance matrix $\mathbf{\Gamma}^{-1}$. Assuming a uniform prior distribution, the resulting posterior probability distribution for the parameters is also a multivariate Gaussian. The diagonal elements of $\mathbf{\Gamma}^{-1}$ will then give the variance of the marginal posterior, i.e. the precision at which a given parameter may be measured. In particular, the variance is proportional to $\langle h|h \rangle^{-1}$, i.e. to ρ_{opt}^{-2} .

In practice, this predicted precision may be inaccurate if the prior distribution is not uniform over the scale of the likelihood peak, or if the Gaussian approximation of the likelihood fails, e.g. if there are multiple maxima of comparable height due to symmetries of the likelihood. These limitations restrict the applicability of the Fisher matrix formalism for parameter estimation precision to cases with high SNRs and a single, well-defined peak [599] – though even in the low SNR case where we cannot neglect higher-order terms, it provides the Cramer-Rao bound on the covariance of an unbiased point estimator [692]. One can alleviate these restrictions using a higher order expansion of the likelihood to predict parameter estimation precision [706], but in general the parameters of a signal must be estimated by sampling the posterior probability distribution, as described in Sec. 5.

3.4 Detector response

Having described the generic likelihood function for a transient GW signal, we now introduce some specifics for the CBC case, with the ultimate aim of understanding the design of searches and parameter estimation methods.

The strain from a generic frequency-domain compact binary signal can be written as

$$\tilde{h}_+(f) = A_+(f) \exp(-i\phi_+(f) + \phi_0), \quad (85)$$

$$\tilde{h}_\times(f) = A_\times(f) \exp(-i\phi_\times(f) + \phi_0), \quad (86)$$

for the $+$ and \times polarisations respectively, see Sec. 2.3. A detector, labelled by I , responds linearly to a weighted combination of these,

$$\tilde{h}_I(f) = F_+ \tilde{h}_+(f) + F_\times \tilde{h}_\times(f), \quad (87)$$

where F_+ and F_\times are the *detector response functions* (or *pattern functions*). These are independent of signal frequency in the long-wavelength approximation, but depend on the direction of propagation of the waves with respect to the detector, as parameterised by the right ascension α and declination δ of the source and the GW polarisation angle ψ , as in Sec. 2.3.1 and Table 2. For an interferometric detector with arms along the x - and y -axes, the response functions are given by, e.g. [475],

$$\begin{aligned} F_+(\theta, \phi; \psi = 0) &= \frac{1}{2}(1 + \cos^2 \theta) \cos 2\phi, \\ F_\times(\theta, \phi; \psi = 0) &= \cos \theta \sin 2\phi, \end{aligned} \quad (88)$$

where θ and ϕ are the polar and azimuthal angles in the detector frame; for nonzero polarization angle ψ the responses follow from considering a rotation about the direction of propagation.

In the simplified case of emission in the $l = m = 2$ mode of a binary whose component spins are parallel to the orbital angular momentum vector, the orbital plane will not precess over time and the two polarization phases are related by $\phi_+ = \phi_\times + \pi/2$, thus we have

$$A_+(f) = \frac{1}{2}(1 + \cos^2 \theta_{JN}) \frac{A_0(f)}{d_L}, \quad (89)$$

$$A_\times(f) = \cos \theta_{JN} \frac{A_0(f)}{d_L}, \quad (90)$$

where $A_0(f)$ is a common frequency-dependent amplitude, and other parameters are defined in Table 2.

The response in detector I for a signal whose arrival time and coalescence phase are $t_{c,I}$ and $\phi_{c,I}$ respectively may then be written

$$\tilde{h}_I(f) = A_I(f) \exp(i(\Phi(f) - 2\pi f t_{c,I} - \phi_{c,I})), \quad (91)$$

where the amplitude $A_I(f) = A_0(f)/D_{\text{eff},I}(\alpha, \delta, \psi, \theta_{JN}, t_c)$, with $D_{\text{eff},I}$ being the *effective distance* to the source for detector I , which folds together the dependence on position and orientation angles [82]. Equation (91) implicitly defines $\Phi(f)$; see Eq. (40) as an example of the phase of the TaylorF2 approximant.

3.5 Measurement precision of signal parameters

Now that we have a definition of the notion of “closeness” of two signals or templates via the Fisher matrix, we consider the case of actual compact binary signals. This will let us understand which quantities make the largest contributions to measurable waveform differences, and therefore, about which ones observed signals are expected to yield the most information.

In Sec. 3.3 we saw that the definition of the Fisher matrix, Eq. (83), requires waveform derivatives $\partial\tilde{h}/\partial\theta$. In the frequency domain, considering a single detector, we can write the waveform as Eq. (91), i.e., a product of amplitude and phase factors, to obtain the derivatives with respect to θ :

$$\tilde{h}(f) = A(f) \exp i\Phi(f), \quad (92)$$

$$\begin{aligned} \frac{\partial\tilde{h}(f)}{\partial\theta} &= \frac{\partial A(f)}{\partial\theta} \frac{\tilde{h}(f)}{A(f)} + i \frac{\partial\Phi(f)}{\partial\theta} \tilde{h}(f) \\ &= \left(\frac{\partial \log A(f)}{\partial\theta} + i \frac{\partial\Phi(f)}{\partial\theta} \right) \tilde{h}(f). \end{aligned} \quad (93)$$

From this we can see the relative importance of the signal amplitude and phase to the measurement of parameters: roughly speaking, a change in the phase by the *addition* of one radian (counted over the entire observed bandwidth of the signal) is equivalent to a change in the amplitude by a *factor* of e . Since the waveform may spend many thousands of cycles in the detector’s sensitive frequency band, the signal phase evolution is of primary importance: parameters which affect the phase are typically much more precisely measured than those that vary only the amplitude. The derivative is also proportional to the signal itself: as expected, louder signals provide more information about their parameters.

We can take the post-Newtonian waveform expansion as a starting point to investigate the influence of some key parameters. As detailed in Sec. 2.2 and Eq. (40), the phase is written as a sum over powers of frequency $f^{(k-5)/3}$:

$$\Phi(f) = 2\pi f t_c - \phi_c - \frac{\pi}{4} + \sum_k \psi_k(\mathcal{M}, q, \mathbf{a}_1, \mathbf{a}_2) f^{(k-5)/3} + \dots, \quad (94)$$

omitting terms in $\log f$ for simplicity.¹³ The derivative with respect to the reference phase ϕ_c is trivial; for the other parameters we have

$$\frac{\partial \Phi(f)}{\partial t_c} = 2\pi f, \quad (95)$$

$$\frac{\partial \Phi(f)}{\partial \theta} = \sum_k f^{(k-5)/3} \frac{\partial \psi_k}{\partial \theta}. \quad (96)$$

In Table 1 we show the order at which different parameters appear. At lowest order only \mathcal{M} contributes: we have $\psi_0(\mathcal{M}) = (3/4)(8\pi\mathcal{M})^{-5/3}$, such that $\partial\psi_0(f)/\partial\mathcal{M} \propto \mathcal{M}^{-8/3}$. We therefore expect that only the (redshifted) chirp mass, not the individual masses m_1, m_2 , will be well-measured for inspiral-dominated waveforms. Only by continuing the expansion to higher orders in k will a second combination of masses, the symmetric mass ratio η , enter the expansion; contributing less to the integral of Eq. (83), it will be less well measured. Therefore we should expect the measurement uncertainties in the two component masses to show a high degree of correlation, as for instance in [36].

At higher order still, the spin vectors $\mathbf{a}_1, \mathbf{a}_2$ enter the expansion, and are accordingly less well determined. As with the individual masses, certain combinations of spins appear earlier than others, the most important being the effective aligned spin χ_{eff} , and then the effective precessing spin χ_p . Since the spin orientations are defined on the sphere, the corresponding parameters have nontrivial prior boundaries and/or distributions; for relatively low SNRs, the Fisher matrix expansion is thus less useful in predicting their measurability, and the full apparatus of Bayesian inference should be used, as in Sec. 5. Tidal deformability, finally, enters for systems containing one or more NSs only from 5PN order, as in Sec. 2.2.1, thus requires much higher SNRs for a nontrivial measurement, although the high order is partly counteracted by a large numerical coefficient, compare [36, 707].

Further insights arise by considering the *integrand* of Fisher matrix elements: for a parameter θ , the diagonal matrix element is the frequency integral of $|\partial\tilde{\mathbf{h}}/\partial\theta|^2/S_n(f)$. This may be thought of as a spectral density of information or parameter precision; Fig. 8 illustrates the density over *log* frequency for various parameters of BNS systems. Moreover, for parameters having similar frequency dependence of $\partial\tilde{\mathbf{h}}/\partial\theta$, the off-diagonal matrix elements are expected to be relatively large, implying strongly correlated measurement errors, for instance between orbit-aligned spins and mass ratio [214, 105].

Post-Newtonian coefficient space As the coefficients of many PN expansion terms ψ_k are complicated non-linear functions of physical binary parameters, the Fisher matrix varies strongly over parameter space, leading to additional pitfalls for low- or moderate-SNR signals. While the nonlinearity can be partly addressed by careful choice of parameter basis, e.g. [700], an alternative strategy considers the *space of PN coefficient values*, over which the Fisher matrix is

¹³ See e.g. [95] for closed form expressions to 3.5PN order.

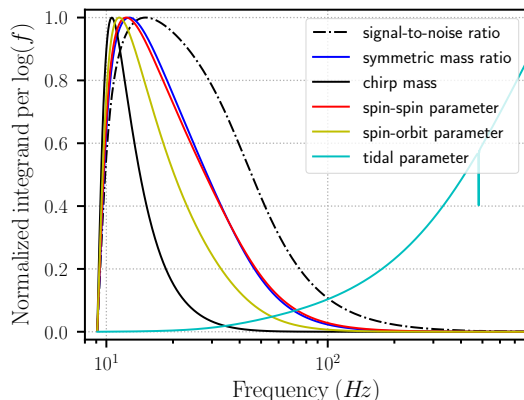


Fig. 8: Frequency dependence of Fisher matrix element integrands, reproduced from [370] (see also [225]). The quantity plotted versus frequency is the density of information about each binary parameter over $\log(\text{frequency})$, $|\partial\dot{\mathbf{h}}/\partial\theta|^2/(fS_n(f))$ where S_n is taken to be the zero-detuned high power Advanced LIGO model PSD; each curve is normalized to peak at unity, except the tidal parameter, normalized to unity at 1 kHz. Although the tidal parameter information appears to increase monotonically towards high frequency, this calculation will become inapplicable by the BNS merger phase, at frequencies beyond the scale of this plot.

(near)-constant [666, 545, 149, 537] for low-mass binaries. Linear combinations of ψ_k may then be found for which the matrix is diagonal, making tasks such as template placement in a multi-dimensional space (Sec. 4.3) significantly simpler.

3.6 Multiple detectors

We can extend the single-detector analysis to the case of multiple detectors by applying the chain rule of probability. For example, if we are analysing data from Hanford (H), Livingston (L) and Virgo (V), the joint likelihood is

$$\begin{aligned} p(\mathbf{d}_H, \mathbf{d}_L, \mathbf{d}_V | H_S) &= p(\mathbf{d}_H | \mathbf{d}_L, \mathbf{d}_V, H_S) p(\mathbf{d}_L | \mathbf{d}_V, H_S) p(\mathbf{d}_V | H_S) \\ &= \prod_{I \in \{H, L, V\}} p(\mathbf{d}_I | H_S), \end{aligned} \quad (97)$$

where the expression reduces to a product over the detectors if the noise in each detector is assumed to be statistically independent.¹⁴ The multi-detector

¹⁴ Schumann resonances could cause correlated magnetic noise in distant detectors, potentially impacting searches for the stochastic background, e.g. [679].

likelihood may then be written as

$$p_{\text{net}}(\{\mathbf{d}_I\}|H_S) \propto \exp\left(-\frac{1}{2} \sum_I \langle \mathbf{d}_I - \mathbf{h}_I | \mathbf{d}_I - \mathbf{h}_I \rangle_I\right), \quad (98)$$

where $\langle a|b \rangle_I$ denotes an inner product using the PSD of detector I and \mathbf{h}_I is the signal as measured at detector I , including the detector responses and time shifts due to propagation time between different sites. This *coherent* likelihood function gives a complete model of the detector network response as a whole: the signals at each detector $\mathbf{h}_I \equiv \mathbf{h}_I(\boldsymbol{\theta})$ are dependent on a *single* parameter vector $\boldsymbol{\theta}$. This form is used in coherent analyses, including for parameter estimation of the signal in Sec. 5.

If we allowed the signal parameters to (unphysically) vary independently in each detector I , which we may write as $\boldsymbol{\theta}_I$, we could use this additional freedom to find a higher maximum of the product of likelihoods: $\prod_I \max_{\boldsymbol{\theta}_I} p(\mathbf{d}_I|\boldsymbol{\theta}_I, H_S) \geq \max_{\boldsymbol{\theta}} p_{\text{net}}(\{\mathbf{d}_I\}|\boldsymbol{\theta}, H_S)$. Thus we can simplify the problem of maximising the likelihood, for the purposes of detection, by maximising the *separate* per-detector likelihoods, at the cost of some inaccuracy if unphysical combinations of parameters are allowed. In practice, constraints are imposed upon maxima to ensure compatible signals in all detectors, for example by enforcing consistent relative arrival times. This approach is referred to as a *coincident* likelihood, as opposed to the fully *coherent* likelihood of Eq. (98), and is commonly applied in matched filter searches, as discussed further in Sec. 4.7.

3.7 Normalized signals and similarity measures

Since CBC sources occur at a wide range of *a priori* unknown distances, the absolute amplitudes of GWs at a detector also have a wide range of uncertainty. We may discuss the properties of signals without specifying an amplitude or distance via *normalized* signals with an optimal SNR (for some notional or real detector sensitivity) of unity,

$$\hat{\mathbf{h}} = \frac{\mathbf{h}}{\langle \mathbf{h} | \mathbf{h} \rangle^{1/2}} \implies \mathbf{h} = \rho_{\text{opt}} \hat{\mathbf{h}}. \quad (99)$$

The Fisher matrix is then

$$\Gamma_{ij} = \rho_{\text{opt}}^2 \left\langle \frac{\partial \hat{\mathbf{h}}}{\partial \theta_i} \left| \frac{\partial \hat{\mathbf{h}}}{\partial \theta_j} \right. \right\rangle, \quad (100)$$

giving an expected inverse relation of parameter estimation accuracy with optimal SNR. For data containing a signal $\rho_{\text{opt}} \hat{\mathbf{h}}$ plus noise n , if we consider a model that is identical to the signal except for an unknown amplitude $\mathcal{A} \hat{\mathbf{h}}$, the likelihood is maximized for $\mathcal{A}_{\text{ML}} = \rho_{\text{opt}} + \langle \hat{\mathbf{h}} | n \rangle$, where the noise term averages to zero over data realizations.

Various *measures of similarity* between different signal models $\mathbf{h}(\boldsymbol{\theta})$ are linked to aspects of parameter estimation and detection. While the amplitude of a predicted signal has an influence on astrophysical interpretation, similarity of signals is generally assessed independently of amplitude: the most basic measure is the *overlap* of two signals $\mathbf{h}_1, \mathbf{h}_2$

$$\mathcal{O}(\mathbf{h}_1, \mathbf{h}_2) = \frac{\langle \mathbf{h}_1 | \mathbf{h}_2 \rangle}{(\langle \mathbf{h}_1 | \mathbf{h}_1 \rangle \langle \mathbf{h}_2 | \mathbf{h}_2 \rangle)^{1/2}} \equiv \langle \hat{\mathbf{h}}_1 | \hat{\mathbf{h}}_2 \rangle. \quad (101)$$

The overlap can be shown to be maximized at unity, when $\mathbf{h}_1 = \mathbf{h}_2$.

Furthermore, the absolute values of the orbital phase of a binary or its time of merger are rarely of astrophysical interest (in the absence of non-GW observations that may depend on these quantities), and detection algorithms do not generally make use of them. Allowing arbitrary differences in phase and coalescence/merger time between signal models, we arrive at a less restrictive measure called the *match*

$$\mathbf{M}(\mathbf{h}_1(t_{c1}, \phi_{c1}, \boldsymbol{\theta}_1), \mathbf{h}_2(t_{c2}, \phi_{c2}, \boldsymbol{\theta}_2)) = \max_{t_{c1}-t_{c2}, \phi_{c1}, \phi_{c2}} \mathcal{O}(\mathbf{h}_1, \mathbf{h}_2), \quad (102)$$

where $\boldsymbol{\theta}$ represents source parameters excluding time and phase.¹⁵ The *mismatch* is simply $1 - \mathbf{M}$, which like \mathbf{M} ranges between 0 and 1.

If, conversely, we are comparing different signal models, for example two approximants discussed in Sec. 2.6, our goal is to assess systematic differences. The comparison between signals for binaries with identical parameter values $\boldsymbol{\theta}'$ (including intrinsic parameters), $\mathbf{M}(\mathbf{h}_1(t_{c1}, \phi_{c1}, \boldsymbol{\theta}'), \mathbf{h}_2(t_{c2}, \phi_{c2}, \boldsymbol{\theta}'))$, is then called the *faithfulness*. This quantity informs how far we expect the models to give the same inferences on such parameters; differences between models will contribute to systematic uncertainties and/or biases in measured source properties (see Sec. 2.8).

¹⁵ In the approximation that the dependence of each signal on orbital phase is via a complex phase $\sim e^{i\phi_{ci}}$, it is only necessary to maximize over the phase difference.

4 Detection

In this chapter we present the problem of detection for compact binary merger signals in the data of a GW detector network, and describe solutions deployed or proposed for real data as well as the principles underlying them.

In the ground-based detector network, sensitive at frequencies of a few Hz and above, CBC signals are comparatively rare and weak relative to the noise. By contrast, future space-based detectors are expected to face the opposite case where signals (not necessarily all from compact binaries) dominate the output stream, see e.g. [85]. Even for 3rd generation detectors with a sensitivity to BBH mergers covering nearly the whole of the observable Universe, the rate of signals is expected to be at most one per tens or hundreds of seconds; while these “chirp” signals will overlap in time within the detector’s frequency band, they will not overlap significantly in the time-frequency plane [591, 493, 409].

Detection thus implies *selecting* the small fraction of data containing distinguishable signals, as opposed to noise or indistinguishably weak signals. This problem is close, but not identical, to classic detection theory with a well-defined “null hypothesis” denoting the lack of signal. In realistic cases, there are important differences from idealized theory.

For one, possible binary signals cover a large parameter space: we do not *a priori* know the true distribution of signals over that space. A theoretically optimal search maximizes the number of detected signals for a given rate of false alarms, but we are unable to evaluate this for an unknown population. We also might choose a figure of merit that differs from simply the expected number of detections.

Second, even for a known signal distribution, the optimal search method depends on the noise content of the data. Since real GW detector data contains transient excess noise events whose rate and morphology cannot be predicted, search optimization requires empirical information on such noise properties, and thus is necessarily limited by the finite statistics of real noise.

Furthermore, searches precede a much more computationally intensive exploration of the properties of candidate signals, see Sec. 5. Thus, beyond the mere presence of a signal, sufficiently accurate point estimates of arrival time and of binary component masses provided by the search algorithm will significantly reduce the cost of subsequent analysis. Searches also provide detailed timing information used to estimate the source’s location for low-latency followup [641, 642].

CBC detection methods are also subject to technical and computational limits. The technical challenges of setting up a (near-)optimal search are currently solved only for signals in the four-dimensional parameter space $\{m_1, m_2, \chi_{1z}, \chi_{2z}\}$ of quasi-circular, non-precessing coalescences neglecting subdominant GW multipoles, see Sec 2. Methods for detection of more complex (and thus more realistic) signals are under active investigation, as discussed below.

In the rest of this chapter we revise standard detection theory, before discussing alterations or extensions for real GW data and reviewing the challenges

of more complex CBC signals, computational issues and different astrophysical search applications.

4.1 Theory of transient signal detection

Given a stretch of data $d(t)$, we want to distinguish between the hypothesis H_S that it contains a signal of known form, and the hypothesis H_N that it contains no signal.¹⁶ For GW data spanning several months, more than one signal may arrive; to begin we consider a short period containing no more than one signal¹⁷, see Sec. 6 for joint analysis of multiple signals. The data are supposed to contain noise with known statistical properties, usually described via the correlation function, which in the simplest case is assumed stationary, see Sec. 3.1. The detection algorithm calculates a scalar ‘test statistic’ $\varrho(d)$ which will as far as possible take a higher value under the H_S hypothesis than under H_N .

Efficiency and false alarm rate The performance of a test statistic may be evaluated by imposing a threshold value ϱ^* : the *efficiency* $\epsilon(\varrho^*)$ is the expected fraction of cases actually containing a signal for which $\varrho > \varrho^*$, *i.e.* $P(\varrho > \varrho^*|H_S)$. The *false alarm rate*¹⁸ $F(\varrho^*)$ is the expected fraction of cases containing no signal for which $\varrho > \varrho^*$, *i.e.* $P(\varrho > \varrho^*|H_N)$. In terms of probability density over the data realization d ,

$$\epsilon(\varrho^*) = \int \Theta(\varrho(d) - \varrho^*) p(d|H_S) dd, \quad (103)$$

$$F(\varrho^*) = \int \Theta(\varrho(d) - \varrho^*) p(d|H_N) dd. \quad (104)$$

Receiver operating curve and likelihood ratio We may calculate $\epsilon(\varrho^*)$ and $F(\varrho^*)$ over a range of ϱ^* values, parameterizing a curve in the (F, ϵ) plane called the “receiver operating curve” (ROC). Any monotonic increasing function of $\varrho(d)$ will yield the same ROC, giving the same ranking of data from noise-like to signal-like; hence $\varrho(d)$ is called a “ranking statistic”.

A “Neyman-Pearson” optimal statistic is one that yields the largest possible ϵ for a given value of F . It may be shown, e.g. [126] that the likelihood ratio Λ_{SN} is an optimal statistic, where

$$\Lambda_{SN}(d) \equiv \frac{p(d|H_S)}{p(d|H_N)}. \quad (105)$$

¹⁶ We sometimes designate the no-signal case as ‘noise’ although noise is present in both hypotheses.

¹⁷ Signals from compact binary mergers arrive at Earth at a rate of one per \sim tens of seconds, although the great majority have an amplitude well below that currently considered detectable [32].

¹⁸ ‘Rate’ here denotes a probability, not a Poisson rate parameter.

If this likelihood ratio can be efficiently and accurately computed for the true GW signal population under all possible data realizations, the problem is solved; however it will not be surprising that in real applications the classic solution, the matched filter, is only the first of many tools required.

The idealized matched filter For a signal of known form $h(t)$, the likelihood of a data set $d(t)$ in a single detector as defined in Sec. 3.2 is

$$p(d|H_S, h(t)) = p(n(t) \equiv d(t) - h(t)|H_N) = \text{const} \cdot e^{-\langle d-h|d-h \rangle/2}, \quad (106)$$

where the inner product $\langle a|b \rangle$ is given by Eq. (79) for Gaussian noise with a known spectrum S_N . The likelihood in the absence of signal is just

$$p(d|H_N) = p(n(t) \equiv d(t)|H_N) = \text{const} \cdot e^{-\langle d|d \rangle/2}, \quad (107)$$

thus the likelihood ratio is $\Lambda_{\text{SN}}(d) = e^{\langle d|h \rangle - \langle h|h \rangle/2}$. For a fixed signal, $\langle h|h \rangle$ is constant, thus $\langle d|h \rangle$ is an equivalent ranking statistic to Λ_{SN} . As a product of the (whitened) data with a whitened template in the frequency domain, $\langle d|h \rangle$ is called a ‘‘matched filter’’.

4.1.1 Signal with unknown parameters: composite hypotheses

In astrophysical applications, some properties of the signal are unknown; we parameterise them by a set of values $\boldsymbol{\theta}$, for instance the amplitude or time of arrival at the detector. Hence, we have a ‘‘composite signal hypothesis’’. We write the signal hypothesis for specific parameter values as $h(\boldsymbol{\theta}), H_S$ or just $\boldsymbol{\theta}, H_S$. In order to determine an optimal detection method, we require the *distribution* over $\boldsymbol{\theta}$, notated as $p(\boldsymbol{\theta}), H_S$; this distribution is analogous to a prior in parameter estimation, see Sec. 5.2. Considering transient signals as an inhomogeneous Poisson process with rate $\lambda(\boldsymbol{\theta})$, the PDF of a single merger’s parameters is proportional to $\lambda(\boldsymbol{\theta})$.

For some parameters, $p(\boldsymbol{\theta})$ is trivial: the distributions over arrival time t_c and coalescence phase ϕ_c are uniform. Since we believe the Earth is not in a special location in the Universe, the distribution of source locations is uniform over spatial volume, up to cosmological effects at high redshift: hence we expect a distribution of luminosity distances $p(d_L) \propto d_L^2$, and of signal amplitudes $p(A) \propto A^{-4}$ [636]. Similarly the orbital axis direction is isotropic, thus for the inclination $p(\iota) \propto \sin \iota$.

For other parameters, in particular binary masses and spins, there is no clear expectation. Published LIGO-Virgo searches generally specify only the boundaries of the region to be searched: for instance in [15] a range of (redshifted) component masses $[1, 99] M_\odot$ and binary total masses $[2, 100] M_\odot$ was considered, with a maximum component spin magnitude $\chi < 0.9895$. However, search methods were not designed for optimal sensitivity to a specific distribution over this space.

For a signal distribution $p(\boldsymbol{\theta})$, the optimal likelihood ratio statistic is

$$A_{\text{SN}}(d; p(\boldsymbol{\theta})) = \frac{\int p(\boldsymbol{\theta}) p(d|\boldsymbol{\theta}, H_S) d^n \boldsymbol{\theta}}{p(d|H_N)}. \quad (108)$$

The numerator here is mathematically identical to the *evidence* for a signal model specified by parameters $\boldsymbol{\theta}$ with prior $p(\boldsymbol{\theta})$, see Sec. 5.

Current search methods treat the signal likelihood $p(d|h(\boldsymbol{\theta}), H_S)$ as a strongly peaked function of $\boldsymbol{\theta}$, and approximate the integral over a finite parameter space Θ by a small region around the global maximum. For a signal of optimal SNR ρ_{opt} as in Sec. 3.2, the peak likelihood is higher by a factor $\sim \exp(\rho_{\text{opt}}^2/2)$ than at parameters far from the peak; thus, such an approximation may be useful for $\rho_{\text{opt}} \sim (5 - 10)$ and above. Approximate evaluation of A_{SN} is also possible if one records only the maxima of $p(d|\boldsymbol{\theta}, H_S)$, or better of $p(\boldsymbol{\theta})p(d|\boldsymbol{\theta}, H_S)$, that exceed a predetermined threshold: these maxima are called *triggers*, a term borrowed from high-energy physics. The threshold value for real (non-ideal) data results from a tradeoff between search sensitivity vs. computational and data storage limits.

4.2 Matched filtering for single-mode CBC signals

For a general merging binary system, the signal has a complicated structure if including effects of precessing component spins and GW emission in non-dominant modes; yet more so if the orbit has non-negligible eccentricity, i.e. is not quasi-circular. We begin, though, with the simple case of dominant mode GW emission from quasicircular binaries with orbit-aligned component spins, where the signal at a given detector has the form of a sinusoid with frequency-dependent amplitude and phase factors, Eq. (91). The likelihood may easily be *maximized* over the signal amplitude parameter and coalescence phase [626]. *Marginalizing* over these parameters yields corrections, which at least for high-SNR signals are small [148, 232].

The maximized likelihood ratio is $\exp(\rho(t_c, \boldsymbol{\theta}^-)^2/2)$, where ρ is the phase- and amplitude-maximized matched filter SNR for a signal with coalescence time t_c and template parameters $\boldsymbol{\theta}^-$ (excluding amplitude, coalescence time and phase). We find [82]

$$\rho(t_c, \boldsymbol{\theta}^-)^2 = \langle d|\hat{h}(t; t_c, \phi_c = 0, \boldsymbol{\theta}^-) \rangle^2 + \langle d|\hat{h}(t; t_c, \phi_c = \frac{\pi}{2}, \boldsymbol{\theta}^-) \rangle^2 \quad (109)$$

$$= \left| 2 \int_0^\infty \frac{\tilde{d}(f) \hat{h}^*(f; \boldsymbol{\theta}^-)}{\frac{1}{2} S_N(f)} e^{2\pi i f t_c} df \right|^2, \quad (110)$$

where $\hat{h}(\boldsymbol{\theta}^-)$ is a normalized template waveform with ϕ_c, t_c set to 0. This “complex matched filter” uses the fact that $\tilde{h}(t_c; \phi_c = \frac{\pi}{2}) = i\tilde{h}(t_c; \phi_c = 0)$. The DFT [82] allows us to straightforwardly evaluate $\rho(t_c, \boldsymbol{\theta}^-)$ as a series over t_c , although time-domain implementations have also been considered [176, 468]. It is appropriate to call ρ a SNR, as each scalar product of the form $\langle d|\hat{h} \rangle$ has

zero mean and unit variance in stationary Gaussian noise; thus in the absence of signal we have the distribution $p(\rho|H_N) = \rho \exp(-\rho^2/2)$, peaking at unity.

For data containing a signal $\mathcal{A}\hat{h}(t; t_c, \phi_c, \theta^-)$ that exactly matches a template, the most probable value of ρ is the optimal SNR $\rho_{\text{opt}} = \mathcal{A}$, see Sec. 3.7. Heuristically, with some fairly large number of independent templates (see discussion below in Sec. 4.3), the rate of noise triggers will fall to a sufficiently low level at high SNRs such that signals with $\rho_{\text{opt}} > 8$ have a high probability of being distinguishable from noise. The *horizon distance* D_h of a detector for a binary with given intrinsic parameters is the largest distance for which $\rho_{\text{opt}} > 8$: this is attained for a system located directly overhead the detector and with zero orbital inclination to the line of sight. Often, D_h for a BNS system with non-spinning components of mass $1.4 M_\odot$ is considered as a “standard candle” to quantify detector sensitivity.

By contrast, the sensitive *range* of a detector is an averaged distance, considering the distribution of angular parameters specifying the binary position and orientation. It can be defined by considering a distribution of mergers with a homogeneous rate density \mathcal{R}_* . The expected rate of mergers having $\rho_{\text{opt}} > 8$, \mathcal{R}_{det} , may then be calculated [296]; the range D_{det} is the radius of a sphere such that $(4\pi/3)D_{\text{det}}^3 \mathcal{R}_* = \mathcal{R}_{\text{det}}$ [82, 658]. Equivalently, drawing a merger with random position and orientation within a distance D_h , the probability that it has $\rho_{\text{opt}} > 8$ is $(D_{\text{det}}/D_h)^3 \simeq 2.26^{-3}$.

These definitions neglect cosmological expansion of space, which affects both the signal seen at the detectors [437], see Sec. 2.2.3, and the geometric relation between luminosity distance and volume of space. While for Advanced detectors the redshift z of detectable BNS is small compared to unity, for more massive and distant source redshift effects must be included [195]. The actual sensitivity of a search over real data will be determined by the detector *network*, and as we discuss in Secs. 4.6 and 4.8, does not correspond to a fixed SNR threshold. The rate of mergers is also likely not constant even in comoving cosmological units [303, 52], implying further corrections to the D_{det} calculation. Sensitive range is, though, still a useful standard measure of broadband detector performance.

4.3 Signal manifolds and template banks

In searching for signals from binaries with unknown parameters (component masses, spins, etc.), in addition to the scientific problem of determining the correct range and distribution of signal parameters, we face a technical challenge of computational cost to evaluate the likelihood at a “densely spaced” set of points in the parameter space. This challenge has a well-defined solution via the construction of template banks, the topic of this section.

Given a desired parameter search region, for data with a given PSD there will be some rate of noise events (maxima of likelihood or matched filter SNR) inside this region. As the rate density of noise events is a rapidly falling function

of SNR, for a statistically confident detection a signal must have SNR above a specific threshold.

The matched filter SNR obtained for a template exactly matching a signal with parameters $\boldsymbol{\theta}$ has a non-central χ^2 distribution with mode equal to ρ_{opt} , as above. For a template $\hat{h}(\boldsymbol{\theta}')$ differing from the signal, the ‘‘match’’ of Eq. (102), i.e. the normalized overlap maximized over arrival time and orbital phase, notated here as

$$\mathbf{M}(\boldsymbol{\theta}, \boldsymbol{\theta}') \equiv \mathbf{M}(h(t_1, \phi_1, \boldsymbol{\theta}'), h(t_2, \phi_2, \boldsymbol{\theta})), \quad (111)$$

is bounded to be ≤ 1 . The most likely value of SNR recovered by $\hat{h}(\boldsymbol{\theta}')$ is then $\mathbf{M}\rho_{\text{opt}}$; thus for a given signal the probability of detection drops progressively with decreasing \mathbf{M} . For a bank, we consider only the maximum of $\mathbf{M}(\boldsymbol{\theta}, \boldsymbol{\theta}'_p)$ over templates $\hat{h}(\boldsymbol{\theta}'_p)$. For a given probability of detection, the optimal SNR required scales as $1/\mathbf{M}$, which for fixed intrinsic parameters $\boldsymbol{\theta}$ implies a maximum source distance scaling as \mathbf{M} . The expected number of detectable signals then scales as the volume of space $\propto \mathbf{M}^3$ (neglecting cosmological effects). If all signals had the same maximum match \mathbf{M} we would lose a fraction $1 - \mathbf{M}^3$ of signals relative to the ideal case of an infinitely dense bank.

In general the match ranges between 1 and the smallest value in the target parameter region, the ‘minimal match’ (MM), i.e. the largest ‘hole’ in the bank. Thus a minimax strategy places templates to obtain a sufficiently high MM value, losing a fraction $1 - \text{MM}^3$ of signals in the worst case. Typical target values are $\text{MM} = 0.965$ (0.97, 0.98), losing at worst $\sim 10\%$ ($\sim 9\%$, $\sim 6\%$). For a broad and smooth distribution of signal parameter values, the *average* match will be significantly higher than MM [81].

For a template $\hat{h}(\boldsymbol{\theta}'_p)$, the region of parameter space ‘‘covered’’ with match $\geq \text{MM}$ is that within a given distance of $\boldsymbol{\theta}'_p$ using the information (Fisher) metric of Sec. 3.3, after projecting out the coalescence time and phase dimensions; the covered region is an approximate ellipsoid in suitable coordinates [542, 543]. To completely cover an extended region, we require overlapping ellipsoids; the larger such overlaps are the more templates are required in total, increasing computational cost. If coordinates can be found with an approximately constant metric, geometrical grid methods will minimize the overlaps [543, 200, 149, 375, 605]: this is the case where the PN parts of the inspiral waveform dominate the SNR. In general for inspiral-merger-ringdown (IMR) signals there is no convenient coordinate basis with a near-constant metric, and stochastic or random methods must be used [102, 373, 477], with a modest increase in computational cost relative to theoretically optimal placement.

Random placement using a uniform distribution over specific coordinates is likely to be inefficient, requiring a large number of templates to cover a given fraction of the space, as first, the ideal density of templates indicated by the metric may vary significantly over the space, and second, due to random fluctuations many templates may be much closer than required for coverage. Stochastic methods address both issues by sequentially proposing new random templates, where a template is added to the bank only if its highest match

over the current template set is below some threshold. The match may either be evaluated via an approximate metric (e.g. [71,413]) or by directly computing the maximized overlap with existing templates. For both methods the computational cost of building stochastic banks can become large: there exist several strategies to limit this cost while maintaining efficiency of coverage, e.g. [178], including combinations of geometric and stochastic placement [611, 218,610]. High-frequency effects arising from tidal deformation of NS components may invalidate the geometric placement framework, as a quadratic approximation of the overlap is insufficient, however stochastic methods are still applicable [371].

For target signals considered as the dominant multipole emission from quasi-circular BBHs with non-precessing spins, which may be written as a single sinusoidal term, the template bank ranges over two masses and two aligned spin components, though in practice only the combination χ_{eff} has a large enough effect on the signal to affect placement [149,71,571,220]. This parameter space is essentially completely covered by banks in use for LVK searches, up to limits imposed by the waveform models. The case of searches for low-mass eccentric binaries may also be treated via this standard route, considering the effect of eccentricity as a correction to the dominant mode PN evolution [532,238], though the larger parameter space leads to severe computational limitations.

Hierarchical search and alternative templated methods The above discussion assumes the use of a single, fixed bank for a given data set; however, alternative schemes may yield computational savings. Hierarchical search first applies a “coarse” bank with lower minimal match, then selectively filters an additional higher-density bank around times and parameter points with high SNR, e.g. [322,649,237]. Fixed banks may also be dispensed with altogether, in favour of time-dependent stochastic selection of template parameters, given a suitable optimization method [365]; thus, particle swarm optimization (PSO) promises to reduce computational cost in cases where a very large fixed bank is required [715,653], as for instance eccentric inspirals [546].

Effectualness and bank robustness We do not expect any real CBC signal to be exactly represented by the template waveforms – real signals will be “outside” the submanifold in signal space over which a bank is placed, even if numerical relativity (NR) waveforms are used directly as templates [440]. The bank’s usefulness is measured by its *effectualness* or *fitting factor* [93] for a given signal $h_{\text{test}}(\boldsymbol{\theta})$, defined as $\max_p \mathbf{M}(h_{\text{test}}(\boldsymbol{\theta}), h(\boldsymbol{\theta}'_p))$, where the phase and coalescence time of the template $h(\boldsymbol{\theta}'_p)$ are maximized over when calculating \mathbf{M} ; for multimodal signals, this is not equivalent to maximizing over the signal phase. In practice, various strategies exist to evaluate the robustness of banks: using h_{test} from different waveform models or approximants, or from NR; taking the test signal’s parameters $\boldsymbol{\theta}$ to lie outside the region covered by the bank; and including the effects of non-dominant multipoles, spin-induced orbital preces-

sion or orbital eccentricity (beyond the leading PN effect). We discuss methods for improving coverage of such general signals below in Sec. 4.5.

4.3.1 Optimizing searches for a target signal population

We now consider implementation of the theoretically optimal search method for a signal of unknown parameters, i.e. the marginalized likelihood ratio of Eq. (108). If sufficient computational resources are available, the likelihood integral may in principle be evaluated by directly sampling the entire search parameter space, using methods adapted to source parameter estimation in place of template filtering, Sec. 5.4; see also [647]. In practice, the integral over parameter space can be approximated by a sum over templates (marginalizing over phase and coalescence time for each template) [232]. In such a sum, the density or distribution of signals over the search parameter space $p(\boldsymbol{\theta})$ is replaced by a signal probability *per template* (at given SNR); this probability will then scale inversely with the density of templates.

The expected behaviour of the likelihood in the neighbourhood of a local maximum is given by the Fisher metric, see Sec. 3.3, thus the marginalized likelihood over a region around the template with maximum SNR may also be approximated analytically. The resulting ranking statistic contains a term for the ratio of the astrophysical signal distribution to the template bank density induced by the Fisher metric [232] (assuming a near constant correlation/match between neighbouring templates). The bank or metric density may be thought of as the *density of independent noise events* over parameter space, yielding an interesting connection between parameter measurability and detection: the more precisely the parameters of a signal can be measured at a given SNR, the higher is the rate of noise events in a matched filter search. Template or noise density is very highly concentrated in the low component mass regions of CBC parameter space, in contrast to signal density which is concentrated mainly over component masses 10–50 M_{\odot} [52]. For a signal density that varies rapidly over the search space, it may also be important to account for the effect of noise, and/or of biases in the search templates relative to expected signal waveforms, on the position of likelihood maxima [309].

While the detection rate is maximized by a ranking where the signal model corresponds to the best current estimate of the astrophysical merger distribution [439], other figures of merit may be optimized by suitable model choices. Specific subpopulations of astrophysical interest may be targeted via a strongly peaked signal density [473, 454]; conversely, search sensitivity may be maintained over a broad parameter space, accounting for template density effects, via a simple monotonic model, for instance a merger rate uniform over $\log m_1$, $\log m_2$ [309, 44, 558].

4.4 Computational optimization and low latency search

The evaluation of matched filter time series via DFT [82] is realized by instruction sets that optimize throughput per CPU or GPU core when processing large batches of data. However, DFT is not immediately adapted to all search applications: as one requires a segment’s worth of samples to be convolved with the template, waiting for a complete input data segment may introduce tens or hundreds of seconds additional latency. In practice, DFT optimization allows for the use of redundant, overlapping data segments to reduce latency to $\leq \mathcal{O}(10\text{ s})$ [529,219].

Significant computational savings may also be realized by exploiting the time-dependence of the inspiral-merger signal: the cost of filtering scales with the sample rate, but the highest rate is only required for the last few template cycles (considering only the dominant sinusoidal mode), the previous cycles being well represented at a lower rate. Thus, separate filter banks operating with different bandwidths may be combined to reconstruct the SNR of the full template at much lower total cost [158,64,100].

An alternative strategy for streaming low latency search is the time domain filter [176,468,389] which introduces negligible latency, at the cost of significantly higher basic computational cost. (Time-domain whitening or overwhitening filters still require a nontrivial data buffer, unless carefully designed [687].) In practice, the number of template filters must be minimized. Given a bank with high minimal match, the outputs of neighbouring templates are highly correlated: one template may be written as a sum of neighbouring templates plus a small (few %) additional term. The number of matched filtering operations can be reduced by *decomposition* of a bank into a smaller number of (near) orthogonal filters having a negligible match with each other, for instance singular value decomposition [173]. However, reconstructing the SNR time series of the original bank from a smaller basis requires a large number of matrix multiplications: careful tuning is required to realize a computationally workable search [498,199].

If our figure of merit for the detection algorithm gives enough weight to how early a signal may be identified, as against sensitivity (probability of detection) at fixed $F(\varrho^*)$, then a low bandwidth filter which can produce an output *before the coalescence time*, even at the cost of underestimating the likelihood ratio, may form part of an optimized strategy [614,533,434]. While such “early warning” filters also imply reduced parameter precision, even a rough indication of sky position and distance may be valuable for guiding initial followup observations.

4.5 Searches beyond a single GW emission mode

The machinery of complex matched filters and matches (overlaps) maximized over phase, which underlies current CBC searches, requires templates with a single sinusoidal component whose phase and amplitude are functions of

either time or frequency. This “dominant mode” assumption is a good approximation over a significant range of parameter space, as the effects of orbital precession or non-dominant emission multipoles on signals seen at the detectors are often small. Furthermore, the actual detected population to date lies predominantly in this range, with mostly near-equal binary masses and small in-plane spins.¹⁹ Nevertheless, the single-component banks have low effectualness for signals whose (optimal) SNR receives large contributions from non-dominant modes: specifically, unequal-mass ($q \lesssim 1/4$) binaries, especially when viewed edge-on [179, 162]; signals with strong amplitude modulation during the inspiral phase due to orbital precession, which likewise implies total angular momentum nearly perpendicular to the line of sight; signals for binaries undergoing transitional precession; and very high mass binaries, for which dominant mode emission is at frequencies below the detector sensitive band. Non-negligible eccentricity within the detectors’ sensitive frequency range will also decrease effectualness and sensitivity, given that the template bank assumes quasi-circular orbits [150, 244, 324].

Low effectualness does not imply such signals *cannot* be detected, but significant losses in sensitivity are expected. Methods to suppress instrumental artefacts in non-ideal data by penalizing signals that deviate from single-component templates, see Sec. 4.6.2, will in general further reduce sensitivity to such signals. As their sources, though rare, are of high interest for both astrophysics and fundamental gravitational physics, there is a strong motivation to improve detection prospects.

Methods to do so fall broadly into two categories. One is to supplant the matched filter by a “weakly modelled” algorithm that places only generic constraints on transient signal morphology – for instance on GW signal duration, frequency range and evolution, and polarization – rather than matching to exact templates. The details of weakly modelled methods are beyond the scope of this review: see for instance [429, 20]. Such methods are expected to approach the detection efficiency of an optimal matched filter for high-SNR signals, regardless of their match to any given template model; their sensitivity to quieter signals will depend on implementation and on the parameter range targeted.

The second basic approach to detection of multi-component signals is to extend the standard matched filtering machinery in order to account for the higher signal complexity, by either maximizing or marginalizing over the extrinsic parameters which control the relative amplitudes and phases of the component modes. These parameters comprise the sky location of the source and its spatial orientation (i.e. the inclination, orbital phase and polarization angle); Ref. [236] gives a general discussion of such marginalization.

Precessing binaries For the inspiral of single-spin precessing binaries, Ref. [547] gives a semi-analytic maximization over these angular parameters, considering the $l = 2$ GW emission formulated as a sum of 5 “harmonic” components.

¹⁹ These trends in the merging binary population persist after accounting for search selection biases: see Secs. 6.2 and 6.3.

A search for precessing binaries along these lines requires a template bank covering spin magnitude and orientation parameters, which so far has only been achieved by imposing strong restrictions on other source parameters [396] in order to reduce the dimensionality of the problem: even then, the size of the bank is significantly larger than the non-precessing case. To circumvent the complexity of signals from generic spinning binaries, approximate search strategies have considered a simpler space of templates that also contains non-physical signals [154], or have maximized over extrinsic parameters without applying all physical constraints [547, 153]. However, the resulting gain in SNR for precessing signals is largely offset by a higher noise level relative to a standard single-component search [693]. Restricting to the physical signal space, [372] demonstrates a method for maximizing likelihood over extrinsic parameters, with the exception of inclination, which significantly affects how precession appears in the detected signal. The resulting search is in principle more sensitive for some precessing systems, particularly unequal-mass BBH and NSBH, despite the higher noise level; however a prohibitively large number of templates is still required.

More recently, the multi-component model of [547] was reformulated as a power law in $\tan(\beta/2)$, where β is the precession cone opening angle (Eq. (52)), equivalent to θ_{JL} in the notation of Sec. 2.3.1. Over most of parameter space where $\tan(\beta/2) \ll 1$, the signal is well approximated by a subset of harmonics, often as few as two [276]. Using this hierarchy, [492] constructed a bank with effectualness over 0.9 for a full range of NSBH spins, without excessive increases in computational cost and noise background, to yield substantially increased sensitivity to highly precessing signals.

Non-dominant multipoles A multi-component search involving multipoles of different l (emission “modes”) is conceptually similar to the precessing inspiral $l = 2$ case, but the component GW frequencies are widely separated and cannot be approximated as a single sinusoid with “sidebands”. The additional complexity of multi-mode templates is expected to increase the noise level in searches [179], requiring targeted strategies to achieve improved sensitivity. In [369] an approach similar to [372], but without analytic maximization over the source orbital rotation angle (corresponding to the coalescence phase) was given, treating both this angle and the inclination as parameters to be covered by a bank of multi-mode templates, in addition to binary masses and spins. The two additional angular parameters control the relative amplitudes and phases of different multipoles. Despite the larger bank, this strategy is more sensitive than the standard dominant mode search for binaries with significantly unequal masses and/or high (redshifted) total mass, and with nearly edge-on inclination [185]. Recently, a general numerical method of likelihood marginalization over extrinsic parameters [606] was used to effectively reduce the multi-mode search to a combination of separate matched filters for each mode, potentially yielding significant efficiency gains [709]. For searches using “higher mode” templates, as for standard single-mode templates, in addition to false alarms caused by Gaussian noise, sensitivity is also impacted by tran-

sient noise artefacts [185, 708]; the next section presents the general problem of non-ideal detector data, before discussing relevant strategies and methods to maintain search sensitivity.

4.6 Non-ideal data

4.6.1 Noise spectrum drift and calibration

The theoretically ideal matched filter assumes stationary noise with a known PSD, but the mere fact that real GW detectors do not observe for indefinitely long times, and are subject to variations in sensitivity, breaks this assumption [38]. Even within segment lengths analyzed in practice, i.e. 10^2 – 10^3 s, PSDs can disagree significantly between shorter stretches of data, typically by a few percent, e.g. [702]. Such drift is not necessarily surprising, as GW interferometers have myriad moving parts, subject to complex and sometimes nonlinear passive isolation and active control systems [21, 151] to suppress low-frequency ground motion; alignment degrees of freedom affecting the strain noise spectrum may then vary on few-second timescales. Mild short-term PSD variations may be accounted for in detection algorithms by suitable moving averages or ad-hoc correction factors [498, 735, 517].

Search sensitivity may also be affected by inaccuracies in detector calibration: specifically, large calibration errors may increase the mismatch of templates with GW signals in the calibrated strain. A constant amplitude or phase calibration error has no effect on search sensitivity in a single detector, though if errors are different between detectors a multi-detector search may be affected, see Sec. 4.7.3. The effect of frequency-dependent errors on single-detector sensitivity scales quadratically with the size of the miscalibration – considered as a fractional amplitude error, or phase error in radians [79, 159] – implying a negligible loss given the scale of current errors [26, 657, 58, 59].

4.6.2 Transient excess noise: glitch suppression

While the great majority of existing data can be well described as quasi-stationary or locally stationary Gaussian noise [38], it has been evident since the first LIGO observing run [12] that multiple, short ($\lesssim 1$ s) stretches of data exist that are highly inconsistent with any Gaussian noise model.²⁰ Significant excess power is observed for short times over some (narrow or wide) frequency range: such noise transients are termed *glitches*, e.g. [16]. These times are in general visible as large deviations in the whitened strain time series. Without a method for subtracting them from the data, glitches invalidate the assumptions of the optimal matched filter and can generate arbitrarily high spurious matched filter SNR and \mathcal{A}_{SN} values.

²⁰ Actual GW signals are also “non-Gaussian”, but in addition are correlated over the detector network, correspond to astrophysical sources, and would not be interpretable as instrumental artifacts.

Implementing an optimal search in the presence of glitches would require an adequate model of their morphology and amplitude and time distributions. For some types of glitch, these parameters may in part be predicted or inferred from detector auxiliary data or environmental monitor data monitoring the physical effects, internal or external to the instrument, that cause excess measured strain power [228, 61]. However, many glitch types remain partly or completely undiagnosed, e.g. “blips” [161]. Hence, glitch suppression strategies have so far been based on more heuristic or empirical methods. These essentially assume that glitch morphology is significantly different from CBC signal morphology, and thus aim to find discriminator statistics which optimally separate the two populations of transient signals. In principle, glitches in a given detector might replicate the form of CBC signals, though this is highly implausible, except for very high-mass systems with only a few signal cycles at detectable frequencies. In this “worst case”, no suppression is possible except within a multi-detector analysis, where a single-detector glitch will be inconsistent with a signal present in the network, see Sec. 4.7. Discriminators based on multi-detector signal properties have also been proposed using methods from parameter estimation [701, 403].

Loud glitch removal: gating and inpainting Very loud glitches that are not suppressed or removed may cause severe artefacts in any frequency domain (i.e. Fourier-transform based) analysis, and will also mask real signals if the glitch has even a small overlap with the relevant CBC template. Very high amplitude outliers in whitened strain (10^2 – 10^3 standard deviations) are sufficiently unlikely to be caused by GW signals that the affected data can safely be ignored. *Gating* achieves this by zeroing (windowing) out short data segments ($\lesssim 1$ s) around these outliers, at the possible cost of introducing edge artifacts [691, 498, 613]. Searches using gating successfully detected and localized the GW170817 signal, a BNS where one detector’s data contained a loud glitch ~ 1 s before merger [29], see Fig. 9. Gating is restricted to short segments, as zeroing significant fractions of the data would introduce significant biases in PSD estimation which may invalidate the matched filter output (on top of reducing expected signal SNR).

A theoretically better justified but computationally more expensive technique is *inpainting*: rather than zeroing a short segment, it is replaced by a time sequence determined by the condition that the resulting likelihood or matched filter is completely insensitive to template values inside the “hole” [735]; i.e. the inpainted data contributes identically zero to the likelihood. While inpainting removes the issue of gating edge artefacts, it still introduces some SNR bias which requires correction. In practice, the matched filter is not valid or useful if a significant fraction of the template duration is affected by gating or inpainting, thus short duration templates are typically vetoed in times surrounding gates/‘holes’ [735, 186]. While these techniques prevent very loud glitches from raising the overall search noise distribution, they cannot avoid a loss of sensitivity around the glitch time, as they necessarily remove a portion of any GW signal.

Signal consistency: chi-squared and friends Glitches that are not *a priori* too loud to be confused with CBC signals can still produce significant ($\rho \gtrsim 10$) matched filter SNRs. If the morphology of a glitch differs significantly from the template that best matches it, the data will remain inconsistent with Gaussian noise even after subtracting the corresponding signal: i.e. there is excess power orthogonal to the template. In addition, properties of the matched filter apart from the SNR itself are unlikely to be typical of an astrophysical signal. These considerations may be exploited to exclude or suppress triggers caused by glitches.

A classic example is the time-frequency chi-squared test [80]: the template is divided into disjoint frequency bins and the distribution of SNR over the bins (at the supposed merger time of the trigger) is employed to calculate a measure of fit with the expected signal behaviour. Typically, while the matched filter

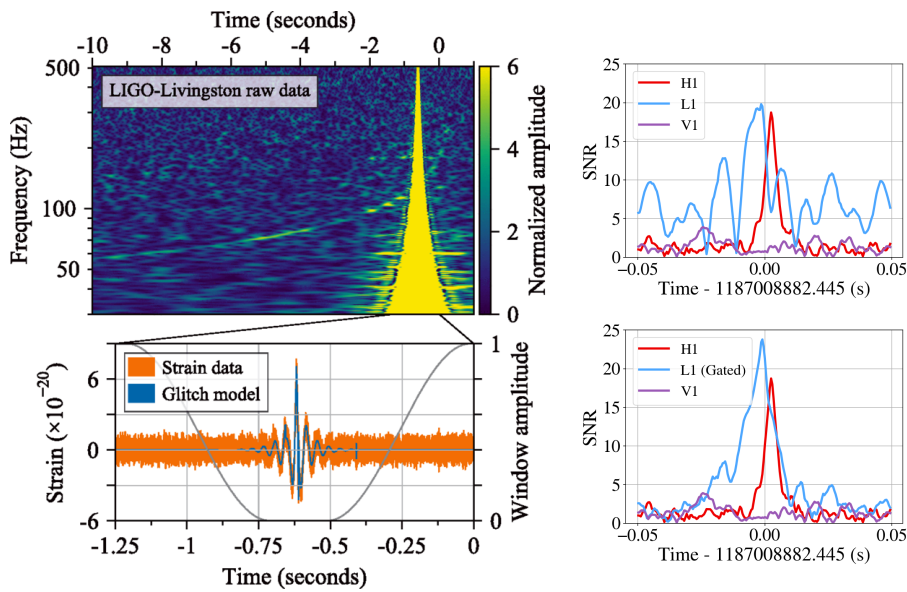


Fig. 9: Mitigation of the glitch in LIGO-Livingston data during the GW170817 signal. Top left: A time-frequency representation of the raw LIGO-Livingston data; the time-frequency track of GW170817 is clearly visible despite the presence of the glitch. Bottom left: Band-passed LLO strain data (orange curve), showing the glitch in the time domain. To mitigate the glitch in rapid reanalysis to produce a 3-detector sky map, the raw detector data were multiplied by an inverse Tukey window (gray curve, right axis) that zeroed out (“gated”) the data around the glitch. The blue curve shows a wavelet-based reconstruction of the glitch [206] which was subtracted from the data for subsequent analysis of the source properties. Figure reproduced from [29]. Right: SNR time series from the PyCBC search, without gating (top) and with gating applied to LLO data (bottom).

integrand of a true signal is supported over the entire template bandwidth, that of glitches is concentrated in a narrow frequency band; this chi-squared test is thus typically most effective for long duration or high bandwidth templates. Comparable signal consistency tests use the expected time dependence of SNR based on the filter template autocorrelation [374,498,363], or the distribution of trigger SNRs over different templates [374], the so-called “bank chi-squared” test [374,688,363].

The above tests consider only the glitch power that matches (is contained within) the search templates. The ability to discriminate glitches can be improved by also measuring power orthogonal to the templates, see [235] for a general discussion. For instance, the “sine-gaussian” veto of [528] deploys additional filters at frequencies higher than the end (ringdown) frequency of the binary template, in order to exclude or suppress very short duration transients with excess power over a wide frequency range [161]. If some assumption is made on the morphology of glitches, or if their morphology can be inferred or “learned” from bulk data, e.g. [651,342], then near-optimal strategies may be designed to distinguish them from binary signals, e.g. [411,495]: the idea is to calculate or approximate the likelihood ratio between CBC signal and glitch hypotheses. The feasibility of such methods depends on the number of parameters or principal components required to model glitches accurately.

Care must be taken when applying signal-based vetoes and discriminators, as true CBC signals do not necessarily match the search templates closely. For current searches that only model the dominant emission mode from non-precessing binaries, GW power orthogonal to the best-matched template may arise from precession and/or “higher modes”, posing a risk of false positives in identifying glitches (see e.g. [528]). Any reduction in sensitivity to signals with such physical effects can be checked via analysis of simulations (as in [178]) and may be mitigated by the design of signal-based tests.

Extended and/or broad-band excess noise Some types of non-ideal detector behaviour violate the assumption that departures from Gaussian-distributed noise take the form of isolated, short glitches. Longer periods of excess noise, for instance “clusters” of glitches correlated with a temporary instrumental problem, may be diagnosed and suppressed by monitoring the time variation of an averaged search trigger rate [100]. More serious noise contamination over extended periods can arise from light scattering off moving optical components into the main beam, lasting several seconds to tens of seconds over specific frequency bands [55,650,714], see Fig. 10. The matched filters for templates intersecting the affected time-frequency region may be invalidated: short of ignoring such data altogether and effectively zeroing search sensitivity, there is at present no clear strategy for tackling these artefacts. They are an increasing concern as detector low-frequency sensitivity improves, and hence the duration of signals in the sensitive frequency band increases: the longer the signal duration, the higher the probability it will intersect an excess noise region. Gating/inpainting may still be applied over small fractions of the template duration, but in general more complex and potentially costly methods are re-

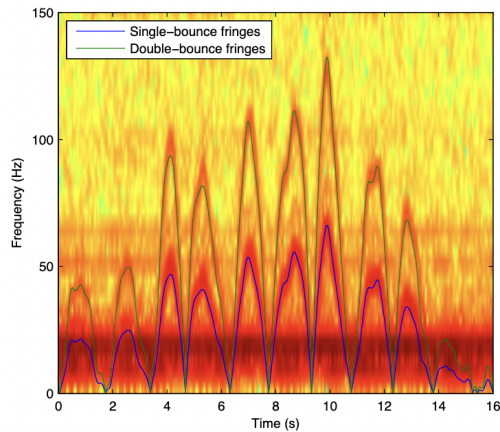


Fig. 10: Spectrogram of the Virgo interferometer output signal during intense microseism activity (logarithmic color scale), showing extended broad-band artefacts due to light scattering. Overlaid are curves predicting the frequency of excess power from the measured velocity of the source of unwanted beam reflection, an optical bench. Figure reproduced from [55].

quired, for instance explicitly modelling and subtracting the excess noise time series [227, 690, 685], currently not adapted for automatic use in searches.

4.7 Multi-detector searches: coherent, coincident & externally triggered

The discussion has, so far, been restricted to data from a single detector, but we now consider strategies for searching global network data. While noise time series in different observatories can be considered as statistically independent (with minor possible exceptions [679]), binary signals will appear consistently in each detector with predictable variations in amplitude, time of arrival and other relevant parameters over the network. Network search methods account for these facts, while respecting constraints from computational cost.

4.7.1 Co-located detectors and composite data streams

The most trivial network consists of detectors with the same location and orientation: in the past, this described the two LIGO Hanford interferometers [449, 313] and it may be relevant for a future Einstein Telescope configuration [316, 572].²¹ The joint likelihood is then a product over detectors, taking the same signal in each. For two co-located detectors with independent noise

²¹ In addition, for a broad range of source directions, the LIGO Hanford and Livingston detectors behave approximately as co-aligned, up to a sign flip of $h(t)$ and a time offset.

processes we have a log likelihood ratio

$$\log \Lambda_{\text{SN}} = \langle d_1|h \rangle_1 + \langle d_2|h \rangle_2 - \frac{1}{2} (\langle h|h \rangle_1 + \langle h|h \rangle_2), \quad (112)$$

where $\langle a|b \rangle_A$ denotes an inner product using the PSD of detector A . The first two terms may be rewritten as $\langle d_{\text{co}}|h \rangle_{\text{co}}$ via a composite or coherent data stream $\tilde{d}_{\text{co}} = S_{\text{co}}(f)(\tilde{d}_1 S_{n,1}^{-1}(f) + \tilde{d}_2 S_{n,2}^{-1}(f))$, where $S_{\text{co}}(f)$ is an initially arbitrary function defining the inner product $\langle \cdot | \cdot \rangle_{\text{co}}$. Requiring that $S_{\text{co}}(f)$ in fact be the PSD of the data stream \tilde{d}_{co} , we obtain $S_{\text{co}}(f)^{-1} = \sum_A S_{n,A}(f)^{-1}$, and the terms in brackets may be rewritten as $-(1/2) \langle h|h \rangle_{\text{co}}$. Thus, co-located and -aligned detectors behave as a single composite detector with a lower noise floor than any individual one. This remains the case if there are significant correlations between the detectors' noise streams, although the resulting expressions are more complicated [449]. In addition to the composite detector, a “null” stream may be derived for which the GW signal vanishes: while under ideal conditions the null stream is not useful for detection, it may be used to diagnose non-ideal behaviour such as glitches and/or calibration systematic error [72, 637, 350].

4.7.2 General networks

For non-co-aligned detectors, we consider two *a priori* independent signals $h_{+,\times}(t)$ with different amplitudes and phases. The signals seen at different detectors are then controlled by the extrinsic parameters of source direction, inclination, and polarization angle, which for the single-detector dominant mode case discussed earlier collapse into a single amplitude factor.²² In general, an optimal search is obtained by marginalizing the joint multi-detector likelihood over these extrinsic parameters given their known priors, as well as over the intrinsic mass and spin parameters. For short transient signals the dependences on extrinsic (“sky”) and intrinsic parameters can be approximately separated [419] such that component masses and (orbit-aligned) spins may be covered by a fixed template bank, as in the single-detector case. The intrinsic space metric is determined by a composite PSD which, as in the co-located case, is the harmonic sum of individual detector PSDs [419].

Currently implemented approaches treat the extrinsic parameter dependence approximately via maximization. For a binary of given masses and spins, the two signals in the radiation frame can be written as, e.g. [374],

$$h_{+,\times} = \mathcal{A}^{1,2} h_0(t) + \mathcal{A}^{3,4} h_{\pi/2}(t), \quad (113)$$

where $h_{0,\pi/2}(t)$ are the two waveform phases for a source at a fixed fiducial distance such that $\langle h_0|h_0 \rangle_A = \langle h_{\pi/2}|h_{\pi/2} \rangle_A \equiv \sigma_A^2$, and the \mathcal{A}^μ ($\mu = 1, \dots, 4$)

²² For co-located but not co-aligned detectors, the likelihood may be simplified considerably [139].

are amplitudes dependent on the source's distance and orientation relative to the given frame.²³ The signal seen by detector A is decomposed as

$$h^A(t) = \sum_{1,2} \mathcal{A}^{1,2} F_{+, \times}^A h_0(t^A) + \sum_{3,4} \mathcal{A}^{3,4} F_{+, \times}^A h_{\pi/2}(t^A) \equiv \sum_{\mu=1}^4 \mathcal{A}^\mu h_\mu^A(t^A), \quad (114)$$

defining the four components $h_\mu^A(t^A)$, where t^A is the signal arrival time at the detector. The multi-detector likelihood ratio generalises from Eq. (112) as

$$\begin{aligned} \log \Lambda_{\text{SN}} &= \sum_A \left(\langle s^A | h^A \rangle_A - \frac{1}{2} \langle h^A | h^A \rangle_A \right) \\ &\equiv \sum_A \left(\mathcal{A}^\mu \langle s^A | h_\mu^A \rangle_A - \frac{1}{2} \mathcal{A}^\mu \mathcal{M}_{\mu\nu} \mathcal{A}^\nu \right), \quad (115) \end{aligned}$$

where $\mathcal{M}_{\mu\nu} = \sum_A \langle h_\mu^A | h_\nu^A \rangle_A$ [374]. Since $\langle h_0 | h_{\pi/2} \rangle \simeq 0$, we take the matrix $\mathcal{M}_{\mu\nu}$ to be block-diagonal. Maximizing Λ_{SN} freely over \mathcal{A}^μ we find a coherent SNR

$$\rho_{\text{coh}}^2 \equiv 2 \log \max_A \Lambda_{\text{SN}} = \sum_A \langle s^A | h_\mu^A \rangle_A (\mathcal{M}_{\mu\nu})^{-1} \sum_B \langle s^B | h_\nu^B \rangle_B. \quad (116)$$

This coherent SNR², comparable to the \mathcal{F} -statistic for continuous wave detection [406] is chi-squared distributed with 4 degrees of freedom [215]. Further redefining the radiation frame via a rotation,²⁴ the cross-terms between + and \times elements in $\mathcal{M}_{\mu\nu}$ can be eliminated, rendering the matrix diagonal. The resulting ‘‘dominant polarization’’ SNR², e.g. Eq. (2.34) of [374], is a sum of independent power terms over the two waveform phases and two polarizations.

For a template of given intrinsic parameters, the signal arrival times in each detector remain to be searched over. As these times are determined by the direction to the source, i.e. sky position, this aspect can be handled by setting up a discrete grid or bank of sky points with spacing determined by a condition on minimal match, based on expected loss of SNR from slightly inaccurate relative arrival times [419, 217, 470]; this sky mismatch contributes in addition to intrinsic parameter mismatch. The computational cost of constructing the coherent SNR from individual matched filters scales directly with the number of sky points, which grows rapidly for larger networks of widely separated detectors (see Chapter 4 of [217]), as expected given the localization accuracy of such networks [274, 716]. It is then the dominant cost except for networks with relatively poor localization, e.g. the initial LIGO configuration with two co-located Hanford interferometers H1 and H2 [470], or the LHO-LLO-Virgo network before reaching Advanced design sensitivity.

Coherent search computational cost is thus strongly dependent on the maximal mismatch (i.e. expected loss in SNR) used to construct both the intrinsic

²³ For transient signals lasting up to several minutes, \mathcal{A}^μ may be taken as constant.

²⁴ This redefinition will depend on the source sky direction via $F_{+, \times}^A$ and on the detector sensitivities and template waveform via σ_A .

and sky banks. At realistic fixed computational cost, one is forced to mismatches higher than the typically considered $\sim 3\%$, implying a nontrivial loss of sensitivity [217]. (This limitation only becomes stronger considering additional searches of time-shifted data for estimating the noise background, see Sec. 4.8.1.) Therefore for covering a complete range of sky directions, rather than coherent search, *coincident search* has been preferred, where triggers are first obtained as peaks in SNR for each separate detector’s data, then combined over detectors in a subsequent stage, see Sec. 4.7.3.

Externally triggered searches If, however, the signal arrival time and source direction are more or less exactly known, such as for sources detected via electromagnetic (EM) transient emission, a coherent search is viable at realistic computational cost with negligible loss of sensitivity [374, 721]. Such *externally triggered* searches have been employed for short GRB counterparts [8, 10, 28, 51], and have also been considered for fast radio bursts (FRBs) [50]. As these searches cover small volumes of parameter space, particularly coalescence time, significantly lower SNRs are required to obtain a high evidence in favour of H_S than in “all-sky” searches, where all source parameters are unknown. Beyond optimizing sensitivity in the ideal Gaussian noise case, the coherent search offers specialized methods for suppressing glitches, for example the presence of excess power or SNR in a null stream; these tests become more powerful if the sky direction, and thus the detector antenna factors, are known. It is believed that GRB are emitted within a narrow cone around the binary orbital axis (so-called “beaming”), thus the range of orientations to be maximized over is significantly reduced, essentially assuming circular GW polarization, which further increases sensitivity relative to the all-sky case [721].

4.7.3 Coincident search and multi-detector consistency

Published searches of LIGO-Virgo data using CBC templates have employed the coincident method, which conducts a single-detector search for each detector and then combines candidate signals over the detector network, e.g. [104]. While coincident search is in general less sensitive than coherent, it is computationally feasible and simpler to implement. The product of the single-detector stage is a set of triggers above a low SNR threshold, typically 4-5; for large template banks and long stretches of data, typically only a subset are stored. For instance, “clustering” may be applied to discard triggers with significantly lower SNR than others in nearby templates within a small time window.

Then, candidate events for the observing network are derived from combinations of single-detector triggers which are sufficiently likely to be generated by the same GW signal [597]. (Depending on detector sensitivities and pattern functions, a signal may also give rise to only one single-detector trigger [167, 613, 531].) Typically, “coincidence” between triggers in different detectors is determined in two stages: initially, triggers are enforced to be generated in the same template and to have consistent merger times, allowing for GW propagation time between observatories plus a small buffer. For multi-detector candi-

dates surviving these cuts, the likelihood of the remaining trigger parameters – SNRs, relative merger times and relative GW phases – is estimated based on the expected signal distribution [175, 530, 364]. As these trigger properties are determined by the putative source’s extrinsic parameters, this step is analogous to maximization over source direction and orientation in the coherent search. However, as the coincident search only considers maxima of single-detector SNR above threshold, it will not in general be able to reproduce the maximum signal likelihood of the coherent search. Instead, the coincident search estimates the likelihood of the *set of single-detector triggers*.

The single-detector SNR threshold, arising from computational limitations, is the main limitation on the sensitivity of coincident search, as compared to an ideal (and computationally infeasible) coherent search. For a 2-detector network the two approaches are expected to be nearly equivalent, but the loss relative to optimal sensitivity increases rapidly with the number of observatories of similar sensitivity in the network from 3 upwards (see e.g. [217]). For networks with many detectors, a signal may have moderate or low SNR in several detectors, thus thresholding may cause an inaccurate estimate of its likelihood ratio.

Hierarchical coherent search A more complicated scheme to obtain some benefits of coherent search with moderate computational cost involves making an initial selection of trigger times using a coincident search, then running the full coherent search only around these trigger times. With careful selection of thresholds, such a hierarchical approach may approach the coherent search sensitivity for large networks at manageable cost [138, 217] although the need for accurate background estimation, to be discussed in the next section, places computational limitations. The complexity of coherent hierarchical search, as well as the status of the Advanced detector network to date, have restricted its implementation in practice, though see [199] for an exception with large scale GPU use to cover a 3-detector sky grid, and [538] for a recent application of hierarchical coherent search to the LHO-LLO network.

4.8 Statistical methods for significance and search sensitivity

Having searched a stretch of data, the remaining task is to interpret the output: have signals actually been detected, and which possible signals *could* have been detected? Given the unpredictable real detector noise and unknown signal distribution, regardless which function of trigger parameters is chosen as detection statistic, the statistic value cannot be directly interpreted in terms of odds, i.e. probability of signal *vs.* noise origin; instead the relation must be estimated empirically. This section will describe statistical methods for interpreting search results, both concerning individual candidate detection and the overall rate of detections, and ultimately the rate of mergers for an astrophysical population of sources. Inference on population properties beyond the rate requires more sophisticated inference, which is treated in Sec. 6.

4.8.1 Detection significance in non-ideal data

The initial objective is to measure the (frequentist) significance of a candidate event, in terms of the probability that noise would generate a comparable event. The *false alarm probability* of an event with ranking statistic ϱ^* , in a search of data with duration T , is the probability at least one event with $\varrho \geq \varrho^*$ would occur if searching this duration of instrumental noise, i.e. in the absence of GW signals. Considering noise events as an inhomogeneous Poisson process with differential rate $\mu_N(\varrho)$, we have

$$\begin{aligned} p(\geq 1 \text{ noise events with } \varrho \geq \varrho^* | T) &= 1 - p(0 \text{ noise events with } \varrho \geq \varrho^* | T) \\ &= 1 - \exp\left(-T \int_{\varrho^*}^{\infty} \mu_N(\varrho) d\varrho\right). \end{aligned} \quad (117)$$

This may be written in terms of false alarm rate (FAR) at a threshold ϱ^* , i.e. $\int_{\varrho^*}^{\infty} \mu_N(\varrho) d\varrho$.

Considering a duration $\sim T$ of noise data, the FAR may only be directly measured with precision $\sim 1/T$. However, the noise rate density $\mu_N(\varrho)$ is estimated in practice via bootstrap resampling of the actual data (although this data may contain signals [174,177]): in order to reach very small false alarm probabilities, resampling schemes must generate much larger durations of notional noise data [175,691]. The most conceptually straightforward method is to apply a large range of relative time-shifts to data or triggers from different detectors, obtaining samples comparable with the actual search but without coincident signals [713,104]; the time-shifts must thus be larger than signal arrival time differences over the network. Additional steps may be taken to remove potential signals for a mean-unbiased estimate of $\mu_N(\varrho)$, e.g. [688,412]; however, to ensure the correct rate of false positive outcomes, i.e. candidates with a very small estimated false alarm probability in the absence of signals, the time-shifted analysis must use the same data selection as the actual search [177]. For events observed only in a single detector, the precision of background estimates is severely limited unless extrapolation beyond the limit $\sim 1/T$ is considered [167,531,226].

Typically, estimates of $\mu_N(\varrho)$ and candidate FAR are produced by resampling hours up to a few weeks of data; on such timescales, detector behaviour (e.g. average rate of glitches) is assumed stable. FAR may be interpreted by comparison with an expected rate of astrophysical signals, as discussed further in Sec. 4.8.2, or by finding the p -value, i.e. the false alarm probability over a total duration of data T , via $p = 1 - \exp(-T \cdot \text{FAR})$ [691,18].

4.8.2 Search sensitivity, merger rate and probability of astrophysical origin

To connect the results of a search with astrophysical processes, its response to GW signals must be estimated: this is achieved by analyzing large sets of simulated signals (“injections”), added to the data searched, or at least data with the same noise properties. The search output for any individual injection

should be the same as for an equivalent astrophysical signal, up to possible waveform systematic errors. Injected signal parameters are drawn randomly from a population distribution which may be intended as astrophysically realistic, or which may be reweighted via importance sampling [681] to represent other distributions of interest.

For relatively low-mass systems in the Initial detector network, the potential sources within a detectable range could not be approximated as homogeneous, thus search results were interpreted using an estimate of the distribution of blue light luminosity over the local Universe, an observable which is assumed to trace compact binary formation [275]. For more recent observations, sources are assumed uniformly distributed in (comoving) volume and time, with random orientations [9]: thus, search sensitivity is described by the fraction of signals ϵ_{det} up to a maximum distance d_{max} that are detected with inverse false alarm rate (IFAR)²⁵ or ranking statistic above a threshold value. If a total time T is searched, the search sensitive volume-time is given by [24, 22]

$$VT = \int_0^{d_{\text{max}}} \frac{T}{1+z(d_L)} \epsilon_{\text{det}}(d_L) \frac{dV_c}{d d_L} d d_L \equiv \mathcal{V}_{\text{max}} \epsilon_{\text{det}}, \quad (118)$$

where $\epsilon_{\text{det}}(d_L)$ is the average probability of detection at a given distance, $V_c(d_L)$ is the comoving volume within a sphere out to distance d_L , and the factor $1/(1+z)$ accounts for time dilation; the total comoving volume-time \mathcal{V}_{max} is defined by evaluating the integral with ϵ_{det} set to 1. If a total of N_{inj} injections are performed with the desired distribution and N_{det} are recovered above threshold, we estimate a detection fraction $\epsilon_{\text{det}} \simeq N_{\text{det}}/N_{\text{inj}}$. The sensitivity VT may be evaluated for an arbitrary distribution of masses and spins: in particular, for a delta function in (source frame) masses and spins, VT is a function of these intrinsic parameters, proportional to the detection probability for a merger with randomly drawn extrinsic parameters within d_{max} .

For a constant (in comoving units) astrophysical merger rate R , the expected number of detections is then $R \cdot VT$. The result of the search is then considered as a counting experiment: how many signals above threshold were actually seen? The likelihood of this outcome given a value of R allows us to infer statistical rate limits or estimates. For this procedure to be consistent, the detection threshold should be set such that, with high probability, any event above it is a true signal; in practice, the threshold choice is somewhat arbitrary, and may bias rate estimates [125]. In addition, the value of V is strongly dependent on the assumed binary mass and spin distribution, causing, in general, large unknown systematic errors in astrophysical rate estimates.

While this dependence on the target distribution will be addressed by astrophysical population inference in Sec. 6.2, the number of detections may be inferred more precisely, and avoiding arbitrary bias, by including potential noise events in the inference [286] (cf. [497]). We consider both the rate density of noise events $\mu_N(\varrho) \equiv r_N b(\varrho)$ and that of signals $\mu_S(\varrho) \equiv r_S f(\varrho)$,

²⁵ IFAR is defined as FAR^{-1} so that higher ranking corresponds to a higher numerical value.

with probability density functions (PDFs) over detection statistic $b(\varrho)$, $f(\varrho)$ respectively. We assume that these rates and PDFs are measured with negligible uncertainty, except for r_S ; $f(\varrho)$ may be estimated via injections. In the resulting Poisson mixture model, the likelihood that a single search trigger has statistic ϱ is $p(\varrho|r_S) \propto r_N b(\varrho) + r_S f(\varrho)$, and the likelihood of the entire set of events obtained in the search $\{\varrho_p\}$ given a value of r_S is [286, 22]

$$P(\{\varrho_p\}|r_S) \propto \exp[-T(r_N + r_S)] \prod_p (r_S f(\varrho_p) + r_N b(\varrho_p)) . \quad (119)$$

Choosing a prior over r_S (e.g. of ‘‘Poisson-Jeffreys’’ form $p(r_S) \propto r_S^{-1/2}$) we obtain a posterior distribution $p(r_S|\{\varrho_p\})$. If r_S were known exactly, the probability that a given event is of astrophysical rather than terrestrial (noise) origin would be $p_{\text{astro}}(\varrho) = r_S f(\varrho)/(r_S f(\varrho) + r_N b(\varrho))$; accounting for rate uncertainty, we find [24]

$$p_{\text{astro}}(\varrho) \equiv 1 - p_{\text{terr}}(\varrho) = \int p(r_S|\{\varrho_p\}) \frac{r_S f(\varrho)}{r_S f(\varrho) + r_N b(\varrho)} dr_S . \quad (120)$$

The signal and noise PDFs may be extended to a multi-dimensional space of search outputs beyond the ranking statistic ϱ , notably template masses and spins; this extension allows for signal model features (for instance a specific mass distribution) which are not included in the ranking ϱ [87]. The method has also been extended to include multiple distinct signal components [418].

The values of p_{astro} obtained in catalogues of CBC events, e.g. [45], are mainly determined by the strongly falling dependence of the background distribution $b(\varrho)$: significant variations appear between different search pipelines for some events with odds $p_{\text{astro}}/p_{\text{terr}} \sim \mathcal{O}(1)$, reflecting both fluctuations in event parameters, e.g. in SNR, and differences in methods used to suppress noise events. The p_{astro} values of past events may also be revisited when new search results enable a more precise determination of the rate and distribution of true signals.

4.9 Machine learning applications

Since CBC searches still face complex issues of implementation, machine learning methods have seen significant interest in recent years, ranging from random forest and similar binary classifiers to convolutional deep neural networks. Among the motivations for such methods are the unpredictable nature of glitches, motivating algorithms which can ‘‘learn’’ glitch properties empirically from data rather than using hand-tuned vetoes. A related problem is finding a near-optimal detection statistic over the multi-dimensional parameter space of multi-detector events, where the ‘‘curse of dimensionality’’ may impede accurate empirical estimation of the noise and signal distributions.

A second broad motivation for applying deep learning techniques is computational speed. Search sensitivity or latency are typically still limited by the

computational cost of matched filtering, or of reconstructing template outputs from a smaller set of filters; in principle, classifiers such as neural networks may be evaluated with very little latency, depending on the compute architecture and constraints such as memory.

Classical machine-learning methods, notably maximum likelihood fitting [530] and kernel density estimation [174], are already employed to characterize noise distributions in LVK searches. Multivariate classifiers such as random forest and simple neural networks have been considered since the Initial detector era [107, 426, 417, 427], though finding limited application due to the complexity of incorporating them into existing analysis pipeline architecture.

More recently, image recognition methods have been applied to time-frequency representations of short data segments, in order to identify and suppress glitches [739] or to directly classify signal vs. noise segments, bypassing matched filtering, e.g. [83]. While such “visual” methods can easily identify contaminated data, they discard the signal phase information and so cannot approach the sensitivity of matched filtering for longer duration signals.

A more fundamental approach that has dominated recent research applies the convolutional neural network (CNN) directly to (whitened) strain data streams, thus preserving their information content [334]. With suitable training, a CNN may reproduce the matched filter’s detection efficiency [321] and could address further search issues, for instance optimizing sensitivity for a given signal population, or in non-ideal data, e.g. [330]. Deep learning training typically optimizes sensitivity at operating FAR thresholds of 1 per ~few hours, leaving a challenge of performance at lower (false) event rates, which requires more complicated schemes [393, 629].

When comparing CNN performance to “classic” templated searches, the large-scale compute resources required for training, as well as hardware for evaluation (typically high-grade GPUs) should be borne in mind – see e.g. [488] for a recent practical application. There is an intriguing similarity between the compute operations in templated (time domain) low latency searches, i.e. fast convolution of filters with the data and reconstruction of physical template outputs via large-scale matrix multiplication, and the steps required to train and evaluate CNNs [729]. Application to longer duration (low mass) signals also appears to be impeded by memory constraints given the large number of waveform cycles, although see [436]. A hybrid approach using aspects of existing templated searches within a deep learning compute architecture may yield further advances.

5 Parameter Estimation

5.1 Introduction to Bayesian Inference

As an observational science, GW astronomy is well suited to the Bayesian probability interpretation, whereby uncertainties resulting from noisy observations are quantified through a probability distribution. This statistical approach stands in contrast to the frequentist methods usually employed in the detection problem, where the significance of a potential signal is estimated through comparison to a large number of noise-generated events. Bayesian inference has been widely employed in astronomy and cosmology where one is often dealing with a small amount of data, or a single realisation of a phenomenon. Historically, its use for anything but simple problems was hindered by computational difficulty, but with the advent of modern computers and the development of algorithms such as Markov Chain Monte Carlo the method has seen a resurgence. We will introduce the building blocks necessary to understand Bayesian analysis of GW signals; many textbooks are available for a more in-depth understanding of relevant techniques [643, 332] and their historical and theoretical underpinnings [408, 407].

Since the binary mergers giving rise to GW signals are unique events rather than repeated trials of the same experiment, statements about their parameters have evidential probability, i.e. corresponding to degrees of belief based on the available evidence. In the usual case where the parameters are continuous (masses, angles, etc.), rather than finite, discrete probabilities, we must use a probability density function (PDF) defined on the parameter space: integrating the PDF over (part of) its domain then gives a finite probability. As a density, the PDF depends on the specific parameterisation used, thus a Jacobian must be applied to transform between different parameterisations (see Sec. 5.5).

In Bayesian inference, we update our state of knowledge about a model by calculating the posterior PDF over the model parameters $\boldsymbol{\theta}$ using Bayes' theorem:

$$p(\boldsymbol{\theta}|d, H_S) = \frac{p(\boldsymbol{\theta}|H_S)p(d|\boldsymbol{\theta}, H_S)}{p(d|H_S)}. \quad (121)$$

The posterior PDF is computed from the prior PDF $p(\boldsymbol{\theta}|H_S)$, the likelihood function $p(d|\boldsymbol{\theta}, H_S)$, and the normalisation constant $p(d|H_S)$. The prior PDF describes our prior knowledge about the parameters, before we consider the observations. For example, without fore-knowledge of the binary's location we use a distribution uniform on the celestial sphere (see Sec. 5.2). The likelihood function is the probability of observing the data d if the parameters are $\boldsymbol{\theta}$, see Eq. (81). H_S denotes the ‘‘signal hypothesis’’, a model of the data that defines what parameters are contained in $\boldsymbol{\theta}$, along with models of the waveform and the residual noise, and any additional information required to completely specify the likelihood function. The constant $p(d|H_S)$ is the ‘marginal likelihood’ of the data given H_S , it is computed by marginalising the likelihood over all

parameters, i.e. integration weighted by the prior density:

$$p(d|H_S) = \int p(\boldsymbol{\theta}|H_S)p(d|\boldsymbol{\theta}, H_S) d\boldsymbol{\theta} \equiv Z_S. \quad (122)$$

This term is also often called the ‘Bayesian evidence’ for a model, and is commonly denoted by the symbol Z in analogy to the partition function of thermodynamics. It serves as a normalisation constant for the posterior probability distribution, being independent of the parameters $\boldsymbol{\theta}$, though varying between one model and another. For a given model, the posterior distribution is often defined only up to a constant of proportionality:

$$p(\boldsymbol{\theta}|d, H_S) \propto p(\boldsymbol{\theta}|H_S)p(d|\boldsymbol{\theta}, H_S). \quad (123)$$

The marginal likelihood is also the expectation value of the likelihood of the data, taken over the prior for a given model: thus, as it quantifies the mean likelihood for a particular model, it can also be used to compare the posterior probability of two models. The ‘posterior odds’ $O_{1,2}$ between two models H_1 and H_2 is given by the ratio of their posterior probabilities

$$\frac{P(H_1|d)}{P(H_2|d)} = \frac{P(H_1)}{P(H_2)} \frac{p(d|H_1)}{p(d|H_2)} \equiv \frac{P(H_1)}{P(H_2)} B_{1,2}, \quad (124)$$

where the Bayes factor $B_{1,2}$ is the ratio of the marginal likelihoods for hypotheses 1 and 2. The prior odds $P(H_1)/P(H_2)$ is the ratio of model probabilities prior to considering an observation, for example the two models might be ‘the source is a binary black hole’ versus ‘the source is a binary neutron star’. Since in this example we might have different prior PDFs for the two models, based on assuming the presence or absence of tidal deformability, we see that the models do not need to have the same number of parameters; in general they do not even need to have any common parameters. Nevertheless, the Bayesian framework allows one to compare different assumptions quantitatively via the posterior odds ratio. To go even further, we can allow the prior PDF to be dependent on model ‘hyper-parameters’, which then may themselves be estimated in hierarchical inference, for which see Sec. 6.

In practical cases, while one seeks to compute a ratio of marginal likelihoods for generic models (e.g. General Relativity versus a particular modified gravity theory), typically the actual computation requires much more precisely specified models, which may define a particular PSD, waveform model, and additional signal processing parameters as required to unambiguously evaluate the likelihood. Since the marginal likelihood is integrated over the model’s priors, it also requires that we fully specify both the parameters of the model, and the form of the prior distribution over these parameters. This makes a Bayesian hypothesis test sensitive to very specific model assumptions, which is desirable when relevant information is available a-priori; such assumptions should be made explicit when reporting such a result.

5.2 Priors

Bayesian inference makes explicit the need for a prior probability distribution over the model parameters, which can be chosen to incorporate any prior information or constraints. For some parameters the prior is determined unambiguously by symmetry arguments: this is the case for the direction of the source on the sky, its spatial orientation relative to Earth, and the polarization angle, assuming that no other information is available. However a model assuming an electromagnetic counterpart to a binary coalescence, such as a gamma-ray burst, may use a prior encoding its (known) sky direction rather than the default prior PDF uniform on the celestial sphere. All parameters present in the model (see Table 2) must have a prior specified before inference can be done; in practice, priors are set using a combination of such symmetry arguments, astrophysical foreknowledge or modelling, and convenience in interpreting the resulting posteriors.

5.2.1 Prior from astrophysics

The prior may be chosen as a functional form derived from studies of independent observations or other physics considerations. A standard example is the a-priori spatial distribution of GW sources. Following the cosmological principle and the Copernican principle, given the very large distances of typical GW sources, a prior uniform in co-moving volume is most commonly used (Eq. (156) in Sec. 6.3). While this forces the analysis to assume a cosmology, the choice can be amended in post-processing (see Sec. 5.2.3 below). A prior uniform in co-moving volume also has the convenient advantage of being normalisable, as the integrated volume is finite.

In some cases parameter estimation (PE) results are obtained for different choices of prior representing different astrophysical assumptions, for example allowing wider or smaller ranges of NS spin magnitude [36]. Another example would involve deriving a prior over the masses of BHs using previous electromagnetic or GW observations (in conjunction with other model assumptions), e.g. [36].

5.2.2 Computational considerations

The computational cost of most parameter-estimation analyses is dominated by calculating the likelihood, not the prior. However, it should still be possible to evaluate the prior quickly, as some sampling strategies (in particular nested sampling based on MCMC, see Sec. 5.4.2) require many evaluations. Furthermore as noted above, the posterior and the prior being probability densities, any change of parametrisation $x_i \rightarrow y_i$ (using generic notation) requires computing a Jacobian,

$$p(\mathbf{y}|H) = p(\mathbf{x}(\mathbf{y})|H) \left| \frac{\partial x_i}{\partial y_j} \right|. \quad (125)$$

This computation is much more convenient for priors of closed (analytic) form.

5.2.3 Change of priors via reweighting

From Eq. (121), it is clear that having calculated the posterior PDF $p_1(\boldsymbol{\theta}|d, H_S)$ for a prior $p_1(\boldsymbol{\theta}|H_S)$ with given data, it is possible to calculate the posterior $p_2(\boldsymbol{\theta}|d, H_S)$ for a different prior $p_2(\boldsymbol{\theta}|H_S)$ over the same parameter space:

$$p_2(\boldsymbol{\theta}|d, H_S) = \frac{p_2(\boldsymbol{\theta}|H_S)}{p_1(\boldsymbol{\theta}|H_S)} p_1(\boldsymbol{\theta}|d, H_S). \quad (126)$$

Thus, provided that the *weight* $p_2(\boldsymbol{\theta}|H_S)p_1(\boldsymbol{\theta}|H_S)^{-1}$ can be computed, it is possible to *reweight* the posterior to accommodate a different prior assumption (even a parametrised one — see Sec. 6 for details). To obtain an accurate result, the estimation of the original posterior $p_1(\boldsymbol{\theta}|d, H_S)$ must have delivered enough information (usually in the form of posterior samples, see Sec.5.4, or an accurate interpolant) where the weight is large, so where $p_2(\boldsymbol{\theta}|H_S)$ is large and $p_1(\boldsymbol{\theta}|H_S)$ small. This is made usually more difficult as most PE schemes are designed to spend most computing resources in regions where $p_1(\boldsymbol{\theta}|d, H_S)$ (and $p_1(\boldsymbol{\theta}|H_S)$) is large.

To enable flexible use of posterior PDF computations, it is thus usually better to avoid priors that exclude part of the parameter-space, and instead be very conservative for the computationally expensive first estimation of the posterior, relying on reweighting for subsequent analyses with different priors. This often leads in practice to adopting priors that are uniform over parameters which are of particular interest for further studies: this choice allows a wide range of reweighting options, and also makes summary statistics easier to interpret.

5.2.4 Other considerations on priors

Another approach involves uninformative priors, or the so-called Jeffreys prior, which is a density proportional to the square root of the determinant of the Fisher information matrix. It is invariant under a change of parametrisation, but can require extra computation to determine its density at points of interest, since the Fisher information matrix depends on the signal and noise models for a particular observation.

As mentioned above, a prior PDF represents a distribution of possible signals over parameter space, thus prior choices are necessarily connected with issues of astrophysical or cosmological population modelling. A systematic treatment of such population models will require Bayesian hierarchical inference, where the goal is to determine properties of the global population, rather than of individual sources; this will be presented in Section 6.

5.3 Likelihood function

In the context of Bayesian PE, the statistical model describes the entire process by which the data is created, including both signal and noise models and all relevant parameters required to predict the signal. In Sec. 3 we modeled the noise as a stationary Gaussian process, giving us a noise likelihood function. We have seen in Sec. 2 how the signal model is defined using a parameter vector $\boldsymbol{\theta}$; together with a stationary Gaussian noise model, this yields the likelihood function in Eq. (81), defined in terms of the data d , signal model $h(\boldsymbol{\theta})$, and the signal hypothesis H_S , which includes the statistical description of the noise via its power spectral density $S_N(f)$:

$$p(\mathbf{d}|\mathbf{h}(\boldsymbol{\theta}), H_S) \propto \exp\left(-\frac{1}{2} \langle \mathbf{d} - \mathbf{h} | \mathbf{d} - \mathbf{h} \rangle\right). \quad (127)$$

The inner product inside the exponential is in practice evaluated with a finite amount of data sampled over time T , with a sampling rate f_s , yielding a discrete sum over $N = T/f_s$ points in the time domain instead of an integral. In this case the maximum frequency that can be represented in this data is the Nyquist frequency $f_s/2$, and since the data time series is real, we have in the frequency domain $\tilde{d}(-f) = \tilde{d}(f)^*$. The (log) likelihood for a GW signal template \tilde{h} is then a sum over a finite range of positive frequencies,

$$p(\mathbf{d}|\mathbf{h}(\boldsymbol{\theta}), H_S) \propto \exp\left(-\frac{2}{T} \sum_{i=0}^{N/2} \frac{|\tilde{d}_i - \tilde{h}_i|^2}{S_N(f_i)}\right). \quad (128)$$

Multiple detectors can be incorporated by simply multiplying their individual likelihood functions, assuming their noise is statistically independent,

$$p(\mathbf{d}|\mathbf{h}(\boldsymbol{\theta}), H_S) \propto \prod_A p(\mathbf{d}_A|\mathbf{h}_A(\boldsymbol{\theta}), H_S, A), \quad (129)$$

where the index A runs over available detectors and its use as conditioning information denotes that the corresponding noise PSD is to be used.

In cases where the waveform is calculated in the time domain, care needs to be taken to transform into the frequency domain. To avoid aliasing, f_s must be chosen so that the maximum frequency of the signal is no greater than the Nyquist frequency $f_s/2$, and a window function is applied before applying a discrete Fourier transform. The window function is used to taper the start and end of the waveform, reducing the spurious high frequency content introduced by the discontinuity between the start and end time if no window is applied. This windowing may lead to an overall loss of the signal's power: the Fourier transform of the data \tilde{d} , after applying a window whose Fourier transform is \tilde{w} , is $\tilde{d}_w = \tilde{d} * \tilde{w}$, and the likelihood needs to be modified to take this into account [665].

For signal models generated natively in the frequency domain, particular care needs to be taken of the waveform's abrupt start and end: such unphysical

features may match against data and lead to artificially precise and biased results [479]. In general with CBC templates including merger and ringdown, the signal model naturally tapers at its end, while the start is in general at low enough frequencies so as not to contribute to the likelihood integral.

The likelihood of Eq. (128) is the most commonly used form, but relies on assumptions of a stationary Gaussian noise process with exactly known PSD and no windowing, damping or correlation effects. Various works have looked at relaxing these assumptions, e.g. [609, 463, 189, 190, 663, 390, 97].

5.4 Exploring parameter space

The posterior PDF contains all the information about the model parameters that can be extracted from the data. However, its domain is the entire prior, which for compact binaries is a high-dimensional space containing in practice 15 parameters or more for a generic quasi-circular coalescing black hole binary. While we can evaluate the density at any point in parameter space using Eq. (121), it is not practical to evaluate the posterior entirely on a grid due to the size of the parameter space. One is often concerned with the *marginal* distributions, given by integrating the posterior over “nuisance” parameters, for example we may only be interested in the chirp mass \mathcal{M} , in which case all the other parameters are nuisance parameters denoted $\boldsymbol{\theta}'$. The marginal posterior is

$$p(\mathcal{M}|d, H_S) = \int p(\mathcal{M}, \boldsymbol{\theta}'|d, H_S) d\boldsymbol{\theta}' = \int \frac{p(d|\mathcal{M}, \boldsymbol{\theta}', H_S)p(\mathcal{M}, \boldsymbol{\theta}'|H_S)}{p(d|H_S)} d\boldsymbol{\theta}' .$$

Evaluating this integral using standard quadrature would be very difficult in high dimensional spaces. Instead, in practice, Monte Carlo methods are often used to compute quantities of interest. These rely on a *sampling* of the posterior distribution at various points, chosen with a particular application in mind.

Final PE results are typically provided as samples from the posterior distribution itself, i.e. a set of points in parameter space, where the density of the samples is proportional to the posterior PDF. With such a sampling, integrals weighted by the posterior probability are easily evaluated by Monte Carlo methods, with each sample given an equal weight in the integrand. For example the marginal distribution above can be approximated by a histogram, where the number of samples in each \mathcal{M} bin would be proportional to the probability density in that bin. Using posterior samples also makes it trivial to produce *credible intervals* for individual parameters, defined to be an interval of one-dimensional parameter space $(\theta_{\min}, \theta_{\max})$ that contains a chosen fraction X of the probability, and therefore posterior samples, i.e.

$$\int_{\theta_{\min}}^{\theta_{\max}} p(\theta|d) d\theta = X . \quad (130)$$

There are however many choices of θ_{\min} and θ_{\max} that satisfy this equation. A common choice of interval to quote is the *minimum credible interval*, which spans the region of highest probability density that contains X .

A number of methods have been developed to draw the posterior samples efficiently, based on a variety of statistical methods, with different degrees of specialisation. We give an overview of the main methods and their historical development below.

5.4.1 Markov Chain Monte Carlo

Markov-Chain Monte-Carlo (MCMC) methods are a class of algorithms that enable efficient exploration of high-dimensional probability distributions. First introduced in 1953 in the context of simulating the behavior of particles in a gas [499], they are often a building block of other sampling algorithms.

MCMC methods work by constructing a Markov chain whose stationary distribution is the desired target distribution: the chain is thus designed to converge to the target distribution after a sufficient number of steps. At each step of the chain, the algorithm proposes a new state, which is accepted or rejected based on a probabilistic criterion that preserves the desired stationary distribution.

One of the most commonly used such methods is the Metropolis-Hastings algorithm introduced in 1953 [500] and extended in 1970 [377]. In order to sample from a target probability distribution $\pi(\theta)$, the algorithm consists of the following steps:

- Start with an initial parameter vector θ_0 , often drawn from the prior.
- At each iteration t , propose a new parameter vector θ' from a proposal distribution $q(\theta'|\theta_{t-1})$, where q is a proposal distribution that depends on the current parameter value θ_{t-1} (also known as a “jump proposal distribution”). A common choice for q is a Gaussian distribution with mean θ_{t-1} and some fixed covariance matrix.
- Calculate the acceptance ratio

$$A = \frac{\pi(\theta')}{\pi(\theta_{t-1})} \frac{q(\theta_{t-1}|\theta')}{q(\theta'|\theta_{t-1})}, \quad (131)$$

where $\pi(\theta)$ is the target distribution and $q(\theta'|\theta_{t-1})$ is the probability of proposing θ' given the current parameter value θ_{t-1} . The ratio of the proposal distributions q cancels out if q is symmetric, but if not it is required to maintain detailed balance.

- Set $\theta_t = \begin{cases} \theta' & \text{with probability } \min(1, A) \\ \theta_{t-1} & \text{with probability } 1 - \min(1, A) \end{cases}$.
- Repeat steps 2-4 for a sufficient number of iterations to obtain a stationary distribution.

In step 3, the acceptance ratio A determines whether the proposed parameter vector θ' is accepted or rejected. If $A > 1$, then θ' is accepted with

probability 1, since the new value has a higher probability density than the current value. If $A < 1$, then θ' is accepted with probability A , which is proportional to the likelihood of the proposed value relative to the current value. This ensures that the chain eventually converges to the target distribution $\pi(\theta)$.

PTMCMC (Parallel Tempering Markov Chain Monte Carlo) is an advanced variant of MCMC that incorporates parallel tempering to improve the exploration of complex probability distributions ([659, 420, 251], and see [645, 700, 282] for examples of GW-specific applications). In PTMCMC, multiple chains, each associated with a specific temperature, are run simultaneously. These different temperatures act as scaling factors, controlling the distribution's "flatness". By having chains at higher temperatures explore the distribution more broadly and chains at lower temperatures focus on regions of higher density, PTMCMC enables a more efficient exploration of the entire parameter space. To achieve this, the PTMCMC chains periodically swap parameters between neighboring temperatures, so that information about the tails of the distribution from the higher temperature chains can percolate to the lower temperature ones. This involves a special jump proposal that exchanges states between adjacent chains, which is accepted or rejected based on the temperatures and the likelihoods of the current states in the chains. This process promotes better chain mixing and facilitates the movement of states between different regions of the distribution. Since different temperature chains can run in parallel when a swap is not taking place, this aspect of PTMCMC can be efficiently parallelised.

There are several other MCMC methods that are commonly used in addition to the Metropolis-Hastings algorithm. One popular method is the Gibbs sampler ([333, 331], and see [700] for examples of GW-specific applications), which is efficient when the joint distribution of the parameters can be factorized into conditional distributions. The Gibbs sampler updates one parameter at a time, by drawing from its conditional distribution given the current values of the other parameters. This can be more efficient than the Metropolis-Hastings algorithm when the conditional distributions are easier to sample from than the full joint distribution.

Another commonly used MCMC method is the Hamiltonian Monte Carlo (HMC) algorithm ([249, 359], and see [567, 315] for examples of GW-specific applications), which is designed to move more efficiently through high-dimensional parameter spaces. HMC generates proposals by simulating the Hamiltonian dynamics of the system, which involves using the gradient of the log-posterior distribution to simulate the motion of a particle in a higher-dimensional space. HMC can be particularly useful for sampling from target distributions with complex geometries or correlations between parameters.

There are also variations of the Metropolis-Hastings algorithm, such as the adaptive Metropolis-Hastings algorithm [358, 88], which adjusts the proposal distribution during the sampling process to improve efficiency. The slice sampling algorithm [221, 526] is another variation, which generates proposals by slicing the target distribution at a random point and using a bounded interval

to select a new value. Slice sampling can be particularly useful when the target distribution is difficult to sample from using other methods.

In general, MCMC methods tend not to suffer as much from the curse of dimensionality as other sampling algorithms, but they can be computationally expensive, and require careful tuning of the proposal distribution to ensure efficient exploration of the parameter space. Problem-specific proposal distributions are almost always required, and in the context of GW astronomy depend on the detector network configuration and the signal properties.

5.4.2 Nested Sampling

Nested sampling is a more recently developed Bayesian inference algorithm, proposed initially in [644]. Its aim is to evaluate the marginal likelihood integral of Eq. (122) through a stochastic sampling of the parameter space. As a by-product, it can also produce samples from the posterior PDF. The method relies on a mapping of the D -dimensional integral to a one-dimensional integral

$$Z = \int p(d|\boldsymbol{\theta}, H)p(\boldsymbol{\theta}|H)d\boldsymbol{\theta} = \int_0^1 L(X)dX, \quad (132)$$

where X is defined as the fraction of the prior mass enclosed by a $(D - 1)$ -dimensional surface at constant likelihood $L(X)$:

$$X(L') = \int_{L(\boldsymbol{\theta}) > L'} p(\boldsymbol{\theta}|H)d\boldsymbol{\theta}. \quad (133)$$

As X decreases from 1 to 0, $L(X)$ becomes progressively higher, so that $L(0)$ is the maximum of the likelihood function. Finding the actual surface that encloses any particular likelihood (i.e. finding $X(L)$) is prohibitively difficult in general, so the method instead uses a statistical estimate of X obtained through nested sampling of the prior distribution. This relies on the fact that the prior is by definition normalised over the entire parameter space, so we can initiate the algorithm with $X_0 = 1$. The algorithm then draws N_{live} samples θ_i from the prior, and evaluates their likelihoods to get L_i . The samples are then ordered by likelihood value, such that $L_i < L_{i+1}$. Since the samples are drawn from the prior, the fraction of the prior mass t contained within a likelihood contour that passes through sample j is given by the beta distribution $p(t_j) = \beta(t_j; N_{\text{live}}, 1)$.

At each iteration of the algorithm the lowest-likelihood sample is removed, and replaced by another drawn from the prior but with a higher likelihood. The number of samples above the current likelihood contour, the *live points*, is then kept constant, and at each iteration the prior mass enclosed by the contour shrinks by a factor t , so $X_{i+1} = t_i X_i$. By repeatedly drawing nested samples, X shrinks geometrically toward 0, and we force the samples into a smaller volume of higher likelihood. Working with logarithms we have the expected shrinkage $\langle \log t \rangle = -N_{\text{live}}^{-1}$, with variance $\sigma_{\log t}^2 = N_{\text{live}}^{-2}$, so after i iterations $\log X \approx -i/N_{\text{live}}$.

The marginal likelihood integral can be approximated using the trapezoid rule,

$$Z \approx \frac{1}{2} \sum_i (L_i + L_{i+1}) w_i, \quad (134)$$

where $w_i = X_{i+1} - X_i$. The algorithm is typically run until a termination condition is met, which is often chosen via an upper bound on the remaining evidence $L_{\max} X_i / Z_i < \exp(0.1)$. The set of samples visited during the run is referred to as the nested sampling chain, and provides a scan of how the parameter values are constrained as the likelihood increases. Once the algorithm is complete, samples from the posterior can be produced by re-sampling the nested sampling chain with weight $L_i w_i / Z$, in a procedure similar to that described in Sec. 5.2.3.

The challenge in nested sampling lies in being able to draw samples efficiently from the likelihood-limited prior distribution. In this regard it shares many common features with the challenge of efficiently sampling the posterior distribution that is encountered in Markov-chain Monte Carlo (MCMC) methods, and can benefit from many of the same techniques to improve efficiency. In initial applications of nested sampling to CBC data analysis, the samples were drawn using a short MCMC chain [701] with customised jump proposals to explore the symmetries of the likelihood function. This was developed further with `LALInferenceNest` [700] which combined the custom jump proposal with adaptive MCMC steps based on the affine-invariant sampling method of [352] (also used in the popular `Emcee` sampler [311]). An alternative method requires modelling the constrained region in such a way that it can be sampled exactly. This has the advantage that the samples can be independently drawn, eliminating the need for a mini-MCMC chain at each iteration of nested sampling. The popular `MultiNest` sampler thus fits the target regions with a set of ellipsoids that can be sampled exactly [292]. However, if the likelihood contour does not match the ellipsoids exactly, rejection sampling will be needed, introducing an inefficiency that can be as bad as running an MCMC chain.

As nested samplers have become more sophisticated, the need for custom CBC-specific jump proposals has reduced somewhat, and many general-purpose sampling algorithms have been applied. The `PyCBC` [127] and `Billby` [99] libraries provide user-friendly python interfaces for Bayesian inference of CBC signals, and can inter-operate with many different sampling algorithms, including `MultiNest` and `Dynesty` [652].

5.4.3 Hybrid grid-sampler exploration

An alternative to the purely stochastic sampling methods described above is a mixed approach, where different parameters are tackled with different methods. This is particularly relevant for the division between intrinsic parameters,

which affect the phase or amplitude evolution of the signal, and extrinsic parameters which only result in an overall amplitude or phase shift. Since exploration of the intrinsic parameter space requires recomputing a potentially costly waveform, there is a strong motivation to use a directed search method for that subspace, while the less costly extrinsic space can still be sampled in a pseudo-random fashion. The RIFT pipeline has adopted such a hybrid grid plus stochastic sampling scheme [551, 445], which has enabled the use of otherwise prohibitively expensive waveform models for PE, and even the direct use of NR waveforms [446, 17].

5.4.4 Machine Learning methods

Recently, the rapid development of machine learning (ML) techniques based on large neural networks has enabled novel approaches to gravitational wave analysis (see e.g. [213] for a review). There are a wide array of methods that have been proposed, which can be broadly categorised as enhancements to existing sampling algorithms, or being complete replacements of more traditional methods. Generally these have the goal of decreasing the time required to obtain a PE result.

Early applications of ML were based around improving a particular aspect of the sampling algorithm. For instance, the difficulty in drawing samples from the likelihood-constrained prior distribution in the nested sampling algorithm. One approach that has been explored by the BAMB sampler was to enhance the efficiency of these draws by training a neural network to approximate the likelihood surface [354], which was available within the LALInference software as far back as the first observing run. More recently, the technique of *normalizing flows* has been used to accelerate both nested sampling [720] and MCMC [98] within the Bilby framework, and can offer at least an order of magnitude speedup over previous samplers.

Normalizing flows are a technique that is particularly well-suited to Bayesian inference problems, see [431] for a recent review. Their goal is to learn an invertible transformation that maps a complicated distribution in physical parameter space $p_{\Theta}(\boldsymbol{\theta})$ to a simple distribution $p_Z(\mathbf{z})$ (often a multivariate normal - hence the name normalizing flow) in a *latent space*. The transformation function is defined by $\mathbf{z} = f(\boldsymbol{\theta}; \boldsymbol{\Phi})$ where $\boldsymbol{\Phi}$ is the output of a neural network, and f is typically built up from multiple layers of simple transformations (for example an affine transformation). Using ML optimization methods such as stochastic gradient descent it is possible to find the optimum $\boldsymbol{\Phi}$ that results in the output of the flow $p_{\Theta}(\boldsymbol{\theta}) = p_Z(\mathbf{z})|J(\boldsymbol{\theta}, \mathbf{z})|$ approximating a desired target distribution, where $J_{ij}(\boldsymbol{\theta}, \mathbf{z}) = \frac{\partial z_i}{\partial \theta_j}$ is the Jacobian matrix of the transformation. The output of the flow can then be used to produce a trainable proposal distribution for use in MCMC and nested sampling algorithms.

Another hybrid application of normalizing flows was explored with a combination of normalising flow jump proposals and Hamiltonian Monte Carlo, using the auto-differentiation tools of modern machine learning packages to accelerate the computation of gradients [723].

A particularly appealing application of machine learning methods is the possibility of completely replacing the stochastic sampling algorithms which require repeated draws, and explicit likelihood calculations which are computationally costly. *Likelihood-free inference* techniques have been applied which completely replace the likelihood and prior in Bayesian inference with a joint distribution of the data and parameters, which is then later conditioned on a specific piece of observed data. Two techniques which have been used for this are conditional variational auto-encoders [320], and normalising flows [229] (in a different configuration from the “enhancements” mentioned above). Both these methods have the advantage of being very low-latency compared to stochastic sampling, as they rely on a neural network that is trained in advance on a large number of simulated signals and noise realisations. This moves the dominant cost of inference up-front, so that when an actual observation is made the network simply conditions its output on observed data. Such methods can be slow to train, especially on large datasets, and so their application to longer BNS signals is still to be fully demonstrated. However there have been recent works showing promising combinations of amortised inference with classical principal component analysis, a technique used elsewhere [173] for reducing data volumes [447].

Another simulation-based inference technique that has been developed for computationally expensive problems is neural ratio estimation [503], which has been shown to reduce the number of likelihood evaluations required to perform full parameter estimation by a factor of ~ 50 [117].

5.5 Degeneracies of the likelihood

Parameter estimation results for CBC signals, and of gravitational waves in general, often exhibit certain characteristic features in the posterior PDF, a classic example being the ‘V’-shaped degeneracy between distance and inclination angle. These degeneracies may result in correlations between parameters, or even in multi-modal posteriors, corresponding to similar waveforms that cannot be distinguished from each other due either to an exact symmetry in the waveform model, or because the noise level is too high to resolve their differences. Understanding these degeneracies is essential to the interpretation of PE results, but it can also help us in the design of PE methods, since these structures can be difficult to sample with a naive approach (for example MCMC with fixed jump scales leads to poor mixing of chains). Several works have proposed specific MCMC jump proposals or transformations of the parameter space to reduce or remove these degeneracies [588, 700, 283, 607].

5.5.1 Distance - inclination

Expanding the logarithm of the likelihood function defined in Eq. (81) results in a quadratic in the waveform \mathbf{h} ,

$$\log L = -\frac{1}{2} (\langle \mathbf{d} | \mathbf{d} \rangle + \langle \mathbf{h} | \mathbf{h} \rangle - 2 \langle \mathbf{d} | \mathbf{h} \rangle) + k \quad (135)$$

where $k = -\frac{1}{2} \log \det 2\pi \mathbf{C}_{\mathbf{N}}$ is a normalisation constant that depends only on the (usually fixed) PSD. (If the noise model is fixed then $\langle \mathbf{d} | \mathbf{d} \rangle$ is also a constant.)

From Eq. (91) we see that the response of a single detector labelled I to the dominant $l = m = 2$ mode of a non-precessing signal can be separated into frequency-dependent and non-frequency dependent parts as

$$\mathbf{h}^I = \frac{A_0(f)}{d_L} \left(\frac{F_+^I}{2} (1 + \cos^2 \theta_{JN}) + F_\times^I \cos \theta_{JN} \right) \exp i [\Phi(f) - 2\pi f t_{c,I} - \phi_{c,I}]. \quad (136)$$

Since the inner product is an integral over frequency, this allows us to move the common non-frequency-dependent factors α_I out of the inner product, to obtain

$$\log L = -\frac{1}{2} (\alpha_I)^2 |A_0(f)|^2 + \alpha_I \langle A_0(f) \exp i [\Phi(f) - 2\pi f t_{c,I}] | d \rangle \cos \phi_{c,I} + \text{const.}, \quad (137)$$

$$\alpha_I = \frac{1}{2d_L} (F_+^I (1 + \cos^2 \theta_{JN}) + 2F_\times^I \cos \theta_{JN}), \quad (138)$$

where $|A_0|^2 = \langle A_0(f) | A_0(f) \rangle$. Since the single parameter α_I incorporates the effect of both d_L and θ_{JN} , as well as the antenna response for a particular detector I , there exists a degeneracy among these parameters where α is held constant. The transformation $\theta_{JN} \rightarrow \pi - \theta_{JN}$, $F_\times^I \rightarrow -F_\times^I$, results in the same signal appearing in the detector, and corresponds to a flip between left-handed and right-handed elliptical polarisations of the gravitational wave, with a change in the polarisation angle. Intuitively we can understand this perfect symmetry as a single detector only sees one of the two polarisation modes of a general waveform. The detector response functions themselves depend on three parameters α , δ and ψ , and it is always possible for a single detector to find a new sky position and polarisation angle that maps $F_\times \rightarrow -F_\times$ while keeping F_+ . This can be achieved by changing the sky location, or by mapping $\psi \rightarrow \pi - \psi$. For a two-detector network, there are two α_I 's, and the sky location can be inferred from the time delay between detectors (see below). However the degeneracy in ψ still exists. A third detector in the network is required to fully break this degeneracy, and therefore infer the polarisation state of the GW, although in the case where detectors are of unequal sensitivity, or where a signal originates near the null of one detector's response function, it may be impossible in practice to do so due to the limited signal-to-noise ratio.

Even in a multiple-detector case, the measurement of the amplitudes α_I is still subject to a statistical uncertainty, therefore there is a anti-correlation between d_L^{-1} and $\cos\theta_{JN}$ when $0 < \theta_{JN} < \pi/2$, which reduces the accuracy to which distance can be determined, unless the inclination angle can be measured in another way (for example by multi-messenger observation). This correlation limits the possible precision of inference on the Hubble constant using GW distance estimates [25].

5.5.2 Sky localization

The localisation of compact binary sources is a highly important output of parameter estimation used to enable multi-messenger followup observations and correlations with other astrophysical transients, e.g. GRBs. The location of the source on the celestial sphere is typically described by the right ascension α and declination δ coordinates. As a single gravitational wave detector is approximately omnidirectional, a network of two or more detectors is required to achieve any reasonable precision. As we have seen, the antenna response functions determine the amplitude of the signal at each detector, and so provide weak information about the probable location; far more information, though, is obtained from differences in signal arrival times between observatories.

Fig. 11 shows the localisation of a $\mathcal{M} = 10 M_\odot$ source by different two-detector networks, illustrating the difference between localisation with timing alone versus that including the true antenna response function. From timing alone, each pair of detectors located at \mathbf{x} is able to localise a source with propagation direction \mathbf{k} to a ring on the sky consistent with a constant time offset between them $\Delta t_{IJ} = (\mathbf{x}_J - \mathbf{x}_I) \cdot \mathbf{k}/c$. The width of the ring is produced by the uncertainty in the difference in the time of arrivals at the two sites, which is inversely proportional to the effective bandwidth of the signal, weighted by the noise PSDs [274].

If we consider the three pairs of detectors possible from a three detector network, the three resulting rings intersect at the true location of the source, but also at the point which is the reflection of the source in the plane containing the detectors, which generates the same times of arrival (see left panel of Fig. 11). There are therefore always two locations on the sky consistent with any observed time of arrival in a three detector network. With the inclusion of the antenna response function, the symmetry of the two modes is broken, since in general only one has a consistent set of antenna response functions that lead to the observed signal in all three detectors. However if one detector has significantly poorer sensitivity than the others, then the signal to noise ratio may be low in one detector, and the degeneracy only weakly broken.

Sampling the sky location posterior can be challenging for algorithms because of the spherical topology of the parameter space and the ring-like structures which even when broken must be explored at lower likelihood levels for nested sampling algorithms, or at higher temperatures for annealed MCMC methods. Local Gaussian jump proposals that are not adaptive to the structure will have difficulty achieving good acceptance rates at all points in the

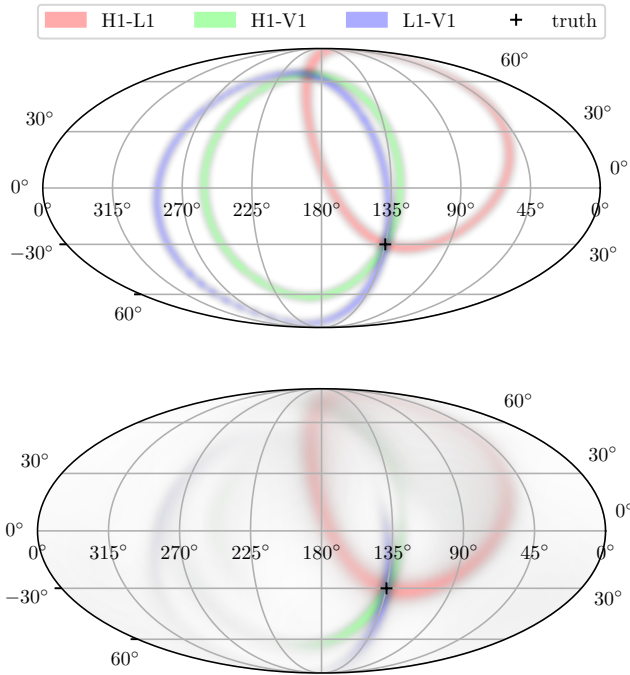


Fig. 11: Localisation of a gravitational wave source by a detector network using (top) only timing information and (bottom) timing and antenna response information. Colours indicate which network is used to perform localisation, and the true location is marked with a +.

space. One solution is to perform a reparameterisation that rotates the sky so the north pole is aligned with the vector separating the detectors. If the dominant pair of detectors is chosen then the posterior ring will align with a constant latitude in the new coordinate system, decoupling the two angular parameters so that they can be sampled more effectively. The time of arrival of the signal can also be remapped as part of this transformation: the time of arrival is typically well measured in each detector individually, but the time of arrival at the geocentre, relative to the detectors, is dependent on the direction of propagation of the signal. Therefore using the common reference position of the geocenter leads to degeneracy between the sky location and the reference time. When performing the sky rotation it is also useful to remap the reference time to that of arrival in the most sensitive detector.

5.5.3 Phase and polarisation angle

The orientation of a quasi-circular binary is given by the three angular parameters, θ_{JN} , ψ and ϕ_c , which completely determine the polarisation content of

the signal through the decomposition into spin-weighted spherical harmonics, as in Eq. (49). For the dominant $\ell = m = 2$ mode, the signal can be written as

$$h_+ - ih_\times = h^{22} {}_{-2}Y^{22}(\iota, \phi_c) + h^{2-2} {}_{-2}Y^{2-2}(\theta_{JN}, \phi_c)$$

where ${}_{-2}Y^{\ell m}(\theta_{JN}, \phi_c) = f^{\ell m}(\theta_{JN})e^{im\phi_c}$, and $f^{\ell m}(\theta_{JN})$ is the inclination-dependent emission pattern determined by the spin-weighted spherical harmonics [491]. The effect of the phase parameter on the $m = 2$ mode is therefore to rotate between the $+$ and \times parts of the waveform when written in this complex format. Recall that the effect of the ψ parameter is also to rotate between $+$ and \times polarisations with angle 2ψ . When the source is viewed directly face-on or face-off ($\theta_{JN} = 0, \pi$), varying the ϕ_c and ψ parameters produces equivalent effects on the $m = 2$ mode, causing a positive or negative degeneracy, $\phi + \psi = \text{const}$ or $\phi - \psi = \text{const}$. Each condition describes a characteristic stripe in the ϕ, ψ parameter space that can be difficult to sample, being periodic in both parameters and potentially quite narrow. For a generic orientation θ_{JN} , the posterior exhibits a combination of both positive and negative degeneracies.

5.5.4 Masses and spins

As discussed in Sec. 3.5, those parameters which most influence the phase evolution of the signal tend to be the best measured. These are referred to as intrinsic parameters, including both the masses and spins of the binary components, combinations of which enter into the phasing formulae at different PN orders for the inspiral (see Tab. 1). Generally, the lower the order, the more effect the parameter has on the phasing, and the easier it will be to measure it for lower-mass signals. Unfortunately the parameter combinations that enter into the PN expansion are not necessarily those of the greatest astrophysical interest. The chirp mass, entering the PN expansion at lowest order, is by far the best determined intrinsic parameter for inspiral-dominated signals. As a consequence, the posterior on component masses is constrained to lie on a line of approximately constant chirp mass. The length of the line in the direction perpendicular to chirp mass is determined by the uncertainty in the second mass combination, which can be taken to be the symmetric mass ratio η which enters at 1PN order.

High-mass signals, though can have a significant or even dominant contribution from the merger and ringdown parts. Since the quasi-normal mode frequencies of the ringdown signal scale inversely with the final mass, in these cases the final mass measurement may be as effective as the chirp mass measurement [699].

Sampling the highly correlated (m_1, m_2) joint distribution can be challenging, especially for binary neutron star signals where the chirp mass is extremely well measured. It is therefore common to use the (\mathcal{M}, q) parameterisation of the mass space, where $q = m_2/m_1 < 1$ provides a naturally bounded domain that is still easily interpretable.

Turning to the spin parameters, the first combination that enters the PN expansion is the χ_{eff} parameter, a mass-weighted combination of the aligned spin components that determines the spin-orbit coupling and has a dominant effect on the rate of inspiral in the near-equal-mass regime [74]. It is conventionally defined as

$$\chi_{\text{eff}} \equiv \frac{(m_1 \boldsymbol{\chi}_1 + m_2 \boldsymbol{\chi}_2) \cdot \hat{\boldsymbol{L}}}{m_1 + m_2}. \quad (139)$$

As χ_{eff} enters at 1.5PN order, it is typically poorly measured for near-threshold signals. Furthermore, the prior on this parameter is not trivial: if one assumes that the spin vectors $\boldsymbol{\chi}_1, \boldsymbol{\chi}_2$ have a uniform prior within the 3-ball $|\boldsymbol{\chi}| < 1$, the marginal prior on the z -components of the spin vectors contains an integrable singularity at $\chi_z = 0$, $p(\chi_z) = \frac{1}{2\chi_{\text{max}}} (-\ln |\chi_z/\chi_{\text{max}}|)$ [445]. This in turn creates a singularity in the marginal prior at $\chi_{\text{eff}} = 0$ since it is the weighted sum of the χ_z 's. This makes interpreting the results of parameter estimation difficult: typically one is looking primarily for evidence that the posterior is significantly shifted compared to the prior (see for example the χ_{eff} analysis in [484]).

Further spin measurements enter at even higher PN order in the phasing, although the non-aligned parts of the spin vectors can be measured by another means: through the precession of the orbital plane that occurs due to spin-orbit coupling, introduced in Sec. 2.2.2. This effect produces an amplitude and a phase modulation of the signal, as the system's orbital angular momentum vector tips toward and away from the observer. The measurability of this effect is dependent on the rate of change of the emission pattern ${}_{-2}Y_{lm}(\iota, \phi_c)$ with respect to the instantaneous inclination angle $\iota = \tan^{-1} \hat{\boldsymbol{L}} \cdot \hat{\boldsymbol{N}}$, which determines the size of the amplitude modulation seen by an observer viewing the system along the N vector. This time-dependence of ι for a precessing binary makes the choice of angular parameter θ_{JN} a more useful choice in parameter estimation, since the total angular momentum of the source, J is more closely conserved during the merger process. To encode the dominant information about the precession, the χ_p parameter has been introduced, which measures the relevant in-plane spin combination [366, 631]. This too has a non-uniform prior induced by the uniform component spins, which complicates the interpretation of its posterior distribution. See [163] for a detailed comparison of spin priors under different constraints.

The use of these two dominant parameters is also complicated in practice by the need to specify 4 additional spin degrees of freedom to fully determine the source properties. It is therefore more common to use an angular coordinate system determined by the spin magnitudes $a_{1,2}$, tilts $\theta_{1,2}$, and the azimuthal angles ϕ_{JL} and ϕ_{12} which measure the difference between J and L and between the component spin vectors respectively [283].

Results on the spin angular can be visualised by the marginal posteriors on the various parameters of interest, particularly χ_{eff} , χ_p , $\theta_{1,2}$, a_1 , a_2 . To examine the 4D parameter space of component spin magnitudes and tilts a 'spin disk' plot, (e.g. Fig. 12), can be useful.

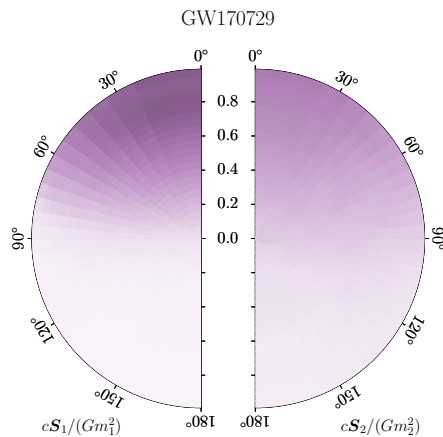


Fig. 12: An example ‘spin disk’ plot for GW170729, reproduced from [35]. The plot shows the posterior on the spin vectors’ magnitudes and tilts, marginalised over the spin azimuthal angles. Bin sizes are adjusted to contain equal prior probability, and the colour density represents the posterior probability in each bin. Left and right panels show the primary and secondary spin, respectively.

5.6 Optimization

Parameter estimation usually involves millions of likelihood evaluations, dominating the total computational cost. Numerous schemes have therefore been developed to reduce the cost of a likelihood evaluation. One can reduce the number of summation elements in the likelihood sum from Eq. (128) with various techniques. Multi-banding [176, 703, 329, 511] involves downsampling the data at different sampling rates depending on the signal’s frequency content. As CBCs increase in frequency as a function of time, one can compute the overlap for earlier parts of the signal with a much lower sampling rate than later parts of the signal, without loss of accuracy.

Another technique that can reduce the signal bandwidth to even greater extremes involves computing the waveform relative to a reference signal. The resulting likelihood can be written in terms of the difference between the signals, which occupies a much smaller bandwidth than the full signal, provided they are sufficiently similar. This technique is employed in various forms as the heterodyned likelihood [204], or relative binning [734] methods. It can result in a speed-up of up to four orders of magnitude in the likelihood computation [205]. This technique has also been shown to apply to signals containing multiple modes, which can otherwise prove a challenge to acceleration schemes [452] since the modes interfere with each other, and the signal cannot be described as having an instantaneous frequency.

Furthermore, using the reduced order basis approach described in section 2.7, it is possible to precompute a reduced set of quadrature weights that

accurately approximate the waveform likelihood integrals, called a Reduced Order Quadrature (ROQ) rule [90, 172, 171, 646, 512, 577, 513, 514]. Instead of evaluating the likelihood integral at each frequency sample, ROQ exploits the precomputed quadrature weights to efficiently compute the likelihood by taking a linear combination of the reduced basis waveforms. As show in section 5.5, one can expand the log-likelihood of Eq. (81) into a linear $\langle \mathbf{d} | \mathbf{h} \rangle$ and a quadratic $\langle \mathbf{h} | \mathbf{h} \rangle$ term, and a constant. The quadratic term is the same for all waveforms, and can be precomputed. The linear term can be written as a sum over the quadrature weights w_i and the inner product of the reduced basis waveforms \mathbf{h}_i with the data \mathbf{d} , $\langle \mathbf{d} | \mathbf{h} \rangle = \sum_i w_i \langle \mathbf{d} | \mathbf{h}_i \rangle$. The inner product of the data with the reduced basis waveforms can be precomputed and stored in a matrix \mathbf{R} , so that the likelihood can be written as $\log L = -\frac{1}{2} \langle \mathbf{d} | \mathbf{d} \rangle + \mathbf{w}^T \mathbf{R} \mathbf{d} + \text{const.}$, where \mathbf{w} is the vector of quadrature weights. The ROQ rule is then the set of quadrature weights \mathbf{w} that minimise the error in the likelihood integral. This can be computed by solving the linear system $\mathbf{R} \mathbf{w} = \mathbf{1}$, where $\mathbf{1}$ is a vector of ones. The ROQ rule can be used to compute the likelihood for any waveform in the reduced basis, and so can be used to compute the likelihood for any signal in the parameter space. This approach significantly reduces the computational burden, as the number of reduced order bases is typically much smaller than the number of frequency points in the likelihood integral. Integrals over more points, typically those for longer, lower-mass signals, will see a greater speed-up.

An effective optimization strategy is to marginalise (either analytically or numerically) over as many parameters as possible when evaluating the likelihood. While this usually makes each likelihood evaluation more computationally expensive, the reduced dimensionality almost always yields an overall speed-up. Marginalization has been applied to the orbital phase, coalescence time and distance parameters [700, 236, 99]. It is possible to recover the probability density function of the marginalised parameters in post-processing, at the cost of evaluating more likelihood values; however, as this post-processing step is done only on samples after thinning, the extra cost is small.

6 Combining Information

6.1 From one to many: Hierarchical inference

Section 5 discussed the inference of the parameters $\boldsymbol{\theta}$ describing an individual source. The posterior PDF $p(\boldsymbol{\theta}|d)$ with given data d depends on a choice of prior $p(\boldsymbol{\theta}|H_S)$. Section 5 also explained how to select between two models H_1 and H_2 , each with its corresponding prior distribution, using Bayes factors and posterior odds. The goal of hierarchical inference, discussed in this section, is to find the “best” prior, or equivalently population model that is common to all events. This can be thought of as an extension of the model selection presented in Sec. 5.

In general we consider a family of models for the prior PDF parametrized by \mathbf{A} , a vector of population hyper-parameters, writing the source prior as $p(\boldsymbol{\theta}|\mathbf{A})$. A hierarchical inference aims to use the data from all events $\{d_i\}_{i=1}^N$ to infer the hyper-parameters \mathbf{A} , in addition to the source parameters $\{\boldsymbol{\theta}_i\}_{i=1}^N$ for every event i . Such an analysis stacks information across events by jointly inferring parameters specific to each event as well as (hyper-)parameters common to all events. Thus, when additional events are observed, we update not only the population from which they are drawn, but also the parameters of previously seen events.

We can use Bayes’ theorem to write the joint posterior PDF over the source parameters and population hyper-parameters as [466, 478, 485]:

$$p(\{\boldsymbol{\theta}_i\}_{i=1}^N, \mathbf{A} | \{d_i\}_{i=1}^N, H_S) = \frac{p(\{\boldsymbol{\theta}_i\}_{i=1}^N | \mathbf{A}) p(\{d_i\}_{i=1}^N | \{\boldsymbol{\theta}_i\}_{i=1}^N, H_S) p(\mathbf{A})}{p(\{d_i\}_{i=1}^N | H_S)}, \quad (140)$$

where $p(\mathbf{A})$ is a prior distribution of hyper-parameters (or hyper-prior); note that this is a simplified expression that neglects observational selection effects, which are treated in the following Section 6.2. Assuming that each observation i is independent, we have

$$p(\{\boldsymbol{\theta}_i\}_{i=1}^N, \mathbf{A} | \{d_i\}_{i=1}^N, H_S) = \frac{p(\mathbf{A}) \prod_{i=1}^N p(d_i | \boldsymbol{\theta}_i, H_S) p(\boldsymbol{\theta}_i | \mathbf{A})}{p(\{d_i\}_{i=1}^N | H_S)}. \quad (141)$$

In many situations, we are only interested in inferring the population hyper-parameters \mathbf{A} , so we can marginalize over the single-event parameters $\{\boldsymbol{\theta}_i\}_{i=1}^N$:

$$p(\mathbf{A} | \{d_i\}_{i=1}^N, H_S) = \frac{p(\mathbf{A}) \prod_{i=1}^N \int p(d_i | \boldsymbol{\theta}_i, H_S) p(\boldsymbol{\theta}_i | \mathbf{A}) d\boldsymbol{\theta}_i}{p(\{d_i\}_{i=1}^N | H_S)}. \quad (142)$$

The numerator of Eq. (142) is the hyper-prior multiplied by the “single-event evidences” $\int p(d_i | \boldsymbol{\theta}_i, H_S) p(\boldsymbol{\theta}_i | \mathbf{A}) d\boldsymbol{\theta}_i$. This makes intuitive sense because the “best” (maximum-likelihood) \mathbf{A} corresponds to the choice of prior on $\boldsymbol{\theta}$ that maximizes the product of single-event evidences.

Single-event evidences may be evaluated by various methods. Assuming that parameter estimation has already been performed on each event using

some ‘‘interim prior’’ $\pi_{\text{PE}}(\boldsymbol{\theta})$, resulting in J PE samples $\boldsymbol{\theta}_i^j$ for each event i , importance sampling is often convenient to apply. The PE samples are drawn from a posterior PDF given by the likelihood $p(d_i|\boldsymbol{\theta}_i)$ with the ‘‘PE’’ prior,

$$\boldsymbol{\theta}_i^j \sim p(d_i|\boldsymbol{\theta}_i)\pi_{\text{PE}}(\boldsymbol{\theta}). \quad (143)$$

The single-event evidence can then be estimated as the following importance sampling, or Monte Carlo, approximation (in what follows we will drop the explicit dependence on the signal hypothesis H_S):

$$\int p(d_i|\boldsymbol{\theta}_i)p(\boldsymbol{\theta}_i|\mathbf{A})d\boldsymbol{\theta} \approx \frac{1}{J} \sum_{j=1}^J \frac{p(\boldsymbol{\theta}_i^j|\mathbf{A})}{\pi_{\text{PE}}(\boldsymbol{\theta}_i^j)}. \quad (144)$$

The error in this Monte Carlo approximation is small when the number of PE samples is large and the interim prior is not too different from the population model $p(\boldsymbol{\theta}|\mathbf{A})$. For this error to be small compared to the uncertainty in the population posterior, the effective number of PE, which depends on the chosen population model(s) $p(\boldsymbol{\theta}|\mathbf{A})$ for all choices of \mathbf{A} in the hyper-prior, must be large enough [259]. Certain population models, especially those that allow for rapid variation of the population PDF $p(\boldsymbol{\theta}|\mathbf{A})$ over parameter space, may require an especially large number of PE samples for each event, with a possibly prohibitive computational cost.

Instead of estimating the single-event evidences via importance sampling, one could first obtain a continuous functional approximation to the single-event likelihood $p(d_i|\boldsymbol{\theta}_i)$ using techniques such as kernel density estimates, Gaussian mixture models or Gaussian processes, based on the PE samples [443, 727, 231, 346, 230]. Equipped with an estimate for $p(d_i|\boldsymbol{\theta}_i)$, it is straightforward to evaluate the joint posterior over the single-event parameters and population hyper-parameters from Eq. (141). The density estimate still carries an uncertainty that scales inversely with the number of PE samples. Nevertheless, this approach can be better-behaved than importance sampling, for instance it correctly assigns regions of $\boldsymbol{\theta}_i$ parameter space without discrete samples a nonzero (but small) likelihood.

The hierarchical Bayesian likelihood may also be evaluated without the use of PE samples by directly sampling source parameters ($\boldsymbol{\theta}_i$) and population hyper-parameters (\mathbf{A}) from the joint likelihood (Eq. (141)). Thus, rather than sampling from the PE posterior for each event separately with a fixed ‘interim’ prior, PE samples are drawn jointly with the population hyper-parameters across all events simultaneously. This may be desirable when we are interested in the population-informed parameters for individual events. However, directly evaluating the joint likelihood may require many more evaluations of the PE likelihood $p(d_i|\boldsymbol{\theta}_i)$ in total, in part due to the much higher dimensionality of the joint parameter space, requiring in turn many more waveform evaluations and higher computational cost. Therefore, in order to update our inference of individual events’ parameters with our knowledge of the population, we can reweight pre-existing PE samples (drawn with an interim prior) in post-processing, once we have sampled from the marginalized likelihood of

Eq. (142) [299, 326, 506, 261, 510, 516]. This remains true when including selection effects (discussed in the following section).

6.1.1 Astrophysical events as a Poisson process

So far we have written the source prior, or “population model”, as a probability density $p(\boldsymbol{\theta}|\mathbf{A})$. For any fixed \mathbf{A} , such a PDF, integrating to unity across the $\boldsymbol{\theta}$ parameter space, describes the *relative* proportion of systems with different source properties. However, if considering *absolute* numbers of systems, for instance the astrophysical rate of binary mergers within some volume of space, we prefer to consider number densities $dN/d\boldsymbol{\theta}$ instead of PDFs $p(\boldsymbol{\theta})$, the difference being that $dN/d\boldsymbol{\theta}$ integrates to the total expected number of systems \mathcal{N} within the considered range of $\boldsymbol{\theta}$,

$$\frac{dN}{d\boldsymbol{\theta}}(\boldsymbol{\theta}|\mathbf{A}) = \mathcal{N}p(\boldsymbol{\theta}|\mathbf{A}). \quad (145)$$

We often consider $dN/d\boldsymbol{\theta}$ as the intensity function of an inhomogeneous Poisson process – “inhomogeneous” because the intensity is not constant across the space of $\boldsymbol{\theta}$. The corresponding likelihood is given by

$$p(\{\boldsymbol{\theta}_i\}, \{d_i\} | \mathbf{A}, \mathcal{N}) \propto \mathcal{N}^{\mathcal{N}} e^{-\mathcal{N}} \prod_{i=1}^{\mathcal{N}} p(d_i|\boldsymbol{\theta}_i)p(\boldsymbol{\theta}_i|\mathbf{A}) \quad (146)$$

where $\{\dots\}$ denotes the set over N events. Using this likelihood, we can then write the posterior over the source parameters and population hyperparameters (which now include the total number of systems \mathcal{N}):

$$p(\{\boldsymbol{\theta}_i\}, \mathbf{A}, \mathcal{N} | \{d_i\}) \propto p(\mathbf{A}, \mathcal{N}) \mathcal{N}^{\mathcal{N}} e^{-\mathcal{N}} \prod_{i=1}^{\mathcal{N}} p(d_i|\boldsymbol{\theta}_i)p(\boldsymbol{\theta}_i|\mathbf{A}). \quad (147)$$

We have hidden the $p(\{d_i\})$ factors in the proportionality because they are independent of \mathbf{A} and \mathcal{N} . We discuss the relation between Eq. (147) and Eq. (141) in the following subsection. Again, these expressions only hold in the absence of observational selection effects, where the expected number of *observed* events \mathcal{N} is the same as the number of events occurring in the astrophysical population.

6.2 Accounting for selection biases

GW observations, like most astrophysical observations, are subject to selection effects: most CBCs that occur in the Universe produce GWs that are too quiet to be confidently distinguished from noise in current detectors, thus only a small subset of mergers on our past light-cone make it into detection catalogs. Nearby, face-on binaries with high masses and large spins aligned with the orbital angular momentum are over-represented among GW detections,

because they emit louder signals. To learn about the underlying astrophysical population of CBCs, we must account for such observational selection effects in the hierarchical Bayesian inference.

Each CBC, with source properties θ , produces a signal lying within data d and is either detected, meaning that its estimated statistical significance, in terms of false alarm rate or probability of astrophysical origin, satisfies some numerical threshold, in which case we label it “det” and record its corresponding data d_i ; or non-detected, in which case we do not record it. Detection is therefore a binary property of the data resulting from a CBC signal within the detector noise at a particular time. We can write the probability that some hypothetical data is detected as $P(\text{det}|d)$. Typically, $P(\text{det}|d)$ is deterministically 0 or 1 for any piece of data d , based on whether the data passes some threshold in, for example, FAR or SNR [483], but this need not be the case [288].

In order to correct for selection effects, we must account for the fact that our analysis only includes data from detected sources. Given N detections, we explicitly include the label $\{\text{det}_i\}_{i=1}^N$ among $\{d_i\}_{i=1}^N$, $\{\theta_i\}_{i=1}^N$ and \mathbf{A} when describing joint probabilities:

$$p(\text{det}, d, \boldsymbol{\theta}, \mathbf{A}) = P(\text{det}|d)p(d|\boldsymbol{\theta})p(\boldsymbol{\theta}|\mathbf{A})p(\mathbf{A}). \quad (148)$$

Note the conditional structure implied by the above equation: given data d , detectability det is conditionally independent of the source properties $\boldsymbol{\theta}$ [466, 483, 262]. Marginalizing the above expression over data realizations d and then over the source parameters $\boldsymbol{\theta}$, we obtain $P(\text{det}|\mathbf{A})$, which also appears in the GW literature with the notation $\beta(\mathbf{A})$ [15] or $\alpha(\mathbf{A})$ [483]. This is the fraction of sources that are detected (out of the total number \mathcal{N} of astrophysical sources) for a hypothetical CBC population described by hyper-parameters \mathbf{A} :

$$P(\text{det}|\mathbf{A}) \equiv \iint P(\text{det}|d)p(d|\boldsymbol{\theta})p(\boldsymbol{\theta}|\mathbf{A}) dd d\boldsymbol{\theta}. \quad (149)$$

The inhomogeneous Poisson process likelihood of Eq. (146) is then modified as follows. The expected number of observed events in the exponent term is now $\mu(\mathbf{A}) \equiv \mathcal{N}P(\text{det}|\mathbf{A})$, while each factor i in the product over events is multiplied by $P(\text{det}_i|d_i)$ [466, 483, 680, 705, 262]:

$$\begin{aligned} p(\{\theta_i\}, \{d_i\}, \{\text{det}_i\} | \mathbf{A}, \mathcal{N}) \\ \propto \mathcal{N}^N e^{-\mu(\mathbf{A})} \prod_{i=1}^N P(\text{det}_i|d_i)p(d_i|\theta_i)p(\theta_i|\mathbf{A}) \\ \propto \frac{\mu(\mathbf{A})^N e^{-\mu(\mathbf{A})}}{P(\text{det}|\mathbf{A})^N} \prod_{i=1}^N p(d_i|\theta_i)p(\theta_i|\mathbf{A}). \quad (150) \end{aligned}$$

In the last line, we substitute for \mathcal{N} and hide the $P(\text{det}_i|d_i)$ terms in the proportionality because they are independent of the population hyperparameters \mathbf{A} and \mathcal{N} [262].

Now we can write the joint posterior over $\{\boldsymbol{\theta}_i\}$, \mathbf{A} , and μ (or alternatively \mathcal{N}) as

$$p(\{\boldsymbol{\theta}_i\}, \mathbf{A}, \mu | \{d_i\}, \{\text{det}_i\}) \propto p(\mathbf{A}, \mu) \frac{\mu^N e^{-\mu}}{P(\text{det}|\mathbf{A})^N} \prod_{i=1}^N p(d_i|\boldsymbol{\theta}_i) p(\boldsymbol{\theta}_i|\mathbf{A}). \quad (151)$$

If we are only interested in inferring the shape of the population rather than the number of sources, we can marginalize Eq. (151) over μ . If we adopt a separable prior on μ and \mathbf{A} , we recover the following posterior PDF for $\{\boldsymbol{\theta}_i\}$ and \mathbf{A} :

$$p(\{\boldsymbol{\theta}_i\}, \mathbf{A} | \{d_i\}, \{\text{det}_i\}) \propto \frac{p(\mathbf{A})}{P(\text{det}|\mathbf{A})^N} \prod_{i=1}^N p(d_i|\boldsymbol{\theta}_i) p(\boldsymbol{\theta}_i|\mathbf{A}), \quad (152)$$

which reduces to Eq. (141) if $P(\text{det}|\mathbf{A}) = 1$, implying there are no selection effects.

If we choose to work with the parameter \mathcal{N} rather than μ , an arbitrary prior on \mathcal{N} may not generally lead to a separable induced prior on μ and \mathbf{A} . However, the choice of a uniform prior over $\ln \mathcal{N}$ will always induce a uniform prior on $\ln \mu$, independently of \mathbf{A} : with this choice, marginalization over \mathcal{N} recovers Eq. (152). This allows us to sample from the joint posterior over the shape of the population \mathbf{A} and its amplitude \mathcal{N} or μ in two steps. First we can sample \mathbf{A} from the marginalized posterior of Eq. (152). Then we can draw μ samples from the distribution $p(\mu|N) \propto p(N|\mu)p(\mu)$, where the observed number of events follows a Poisson distribution, $p(N|\mu) \propto \mu^N e^{-\mu}$, and $p(\mu)$ is the prior on μ .

We now discuss how to evaluate the detection fraction $P(\text{det}|\mathbf{A})$. In Eq. (149), it is defined as a double integral over data and single-event parameters: this may be estimated by Monte Carlo sampling. We draw $\boldsymbol{\theta}_j$ samples from $p(\boldsymbol{\theta}|\mathbf{A})$, simulate the GW signal for each sample, add it to a realization of the noise distribution to get the corresponding mock detector data d_j , and evaluate $P(\text{det}|d_j)$ by processing the mock data with search pipelines. The integral $P(\text{det}|\mathbf{A})$ can then be approximated as the average over samples j :

$$P(\text{det}|\mathbf{A}) \approx \langle P(\text{det}|d_j) \rangle. \quad (153)$$

If $P(\text{det}|d_j)$ is deterministic (either 0 or 1 for each simulated data d_j), this is simply the fraction of simulated signals that pass the detection threshold. As discussed in 4.8.2, we refer to these simulated signals as ‘‘injections,’’ and the injections that pass the detection threshold are known as ‘‘found injections.’’

To save computational cost, we often evaluate $P(\text{det}|d_j)$ for just one set of $\boldsymbol{\theta}_j$ samples, drawn from some reference PDF $p_{\text{draw}}(\boldsymbol{\theta})$ (see the discussion in 4.8.2). We then estimate $P(\text{det}|\mathbf{A})$ by reweighting these injections:

$$P(\text{det}|\mathbf{A}) = \left\langle \frac{P(\text{det}|d_j) p(\boldsymbol{\theta}_j|\mathbf{A})}{p_{\text{draw}}(\boldsymbol{\theta}_j)} \right\rangle. \quad (154)$$

The use of importance sampling here is analogous to estimating single-event evidences using PE samples drawn under a reference prior distribution, Eq. (144); in both cases, the uncertainty in the Monte Carlo integral must be under control in order to obtain valid inferences [259].²⁶

For estimating $\beta(\mathbf{A})$, the effective number of injections required to avoid biasing the likelihood increases in proportion to the number of detected events. In principle, the injected distribution $p_{\text{draw}}(\boldsymbol{\theta})$ may be adjusted to better match the inferred astrophysical distribution $p(\boldsymbol{\theta}|\mathbf{A})$, so that fewer injections are required; however this requires *a priori* knowledge of the true population, which is necessarily incomplete if derived from previous observations. As an alternative to importance sampling, we can compute the integral $P(\text{det} | \mathbf{A})$ by first estimating a smooth approximation to $P(\text{det} | d)$ [725, 338, 664]. This is analogous to calculating the single-event evidence terms with a smooth approximation to the PE likelihood instead of averaging over PE samples.

6.3 Inference on astrophysical populations

A major goal of GW astrophysics is to understand the origin of merging binary compact objects. The formation and evolutionary histories of neutron stars and black holes in merging binaries is an open problem involving many astrophysical processes that are currently poorly understood. Many such processes also play a fundamental role in a variety of astrophysical contexts outside the production of CBC sources, including stellar evolution, galaxy assembly, and the production of heavy elements. The population of CBC sources also has implications for cosmology, as GWs from cosmological distances encode information about the cosmic expansion history of the Universe.

Binary compact object mergers likely represent extremely rare outcomes of massive stellar evolution. Stars more massive than $\sim 8 M_{\odot}$ end their lives as NSs or BHs [382]; in rare circumstances, such a NS or BH will be close enough to another compact object that they eventually merge within the age of the Universe. There are, broadly, two distinct channels to achieve this: either the two objects started off in a binary star system that remained gravitationally bound throughout its evolution [116, 113, 415], or they started off in a dense star cluster, interacting dynamically with other objects before assembling a tight binary [438, 640]; see Refs. [486, 481] for recent reviews. In either case, the two compact objects must reach a sufficiently tight orbit that will shrink through gravitational radiation to the point of merger. Alternatively, it has been proposed that primordial BHs produced shortly after the Big Bang could contribute to the CBC population [119]. The existence of a subpopulation of primordial origin, if discovered (for example, by finding BHs at subsolar masses or at redshifts higher than the first star formation), would have dramatic implications for early Universe cosmology and the composition of dark matter [182].

²⁶ [284] gives a simple initial treatment for the selection function case.

The hierarchical Bayesian approach discussed in the previous subsections allows us to infer properties of the compact binary population, such as their merger rate and how BHs and NSs are distributed in mass, spin and merger redshifts. These population distributions depend on the evolutionary pathways of BHs and NSs in merging binaries. By measuring the population properties of GW sources, we ultimately hope to reverse engineer the histories of CBC progenitors. The population of CBCs also depends on the cosmological parameters, particularly the relation between luminosity distance, which controls the GW signal amplitude, and redshift, which affects the signal frequency in the same way as a change in component masses (see Sec. 2.2.3). Any inference on the (source-frame) mass distribution thus depends on the events' redshifts, derived from their luminosity distances via a cosmological model. The cosmological redshift–distance relation may also be simultaneously inferred together with the astrophysical population parameters [634, 670, 285, 489, 272].

In general, a BBH population model describes the distribution over source-frame primary and secondary masses (or alternatively primary mass and mass ratio), component spin magnitudes and orientations (or alternatively, “effective” spins like χ_{eff} and χ_p ; see Section 2.3.1), merger redshift (plus background cosmology relating luminosity distance to redshift), and the binary position and orientation. Populations with NS components also have hyperparameters describing their tidal deformabilities, which are discussed in the following subsection.

Several different strategies for population modeling have then been followed. The first approach aims to infer physical parameters by directly comparing observations to simulations. The formation of CBCs is subject to several uncertainties, ranging from unknown initial conditions (for example, the initial mass distribution of stars) to uncertain physical quantities (for example, nuclear reaction rates in stellar cores), to evolutionary stages where direct modelling is too computationally difficult and we instead use approximate prescriptions (for example, the common envelope in binary stellar evolution). These uncertain elements may all leave some imprint on the CBC population, so one could in principle model the CBC population in terms of the corresponding physical parameters, and directly infer their values via hierarchical Bayesian analysis. We refer to such population models as *physics-driven models*.

At the opposite pole of methodology, *data-driven models*, also known as non-parametric models, aim to be flexible enough to recover an arbitrary CBC population distribution. For example, the “parameters” of these population models might simply be the merger rate density at each point in θ -space, and the number of parameters approaches infinity as one considers arbitrarily high resolution in θ space (e.g. a histogram in the limit of infinitely many, closely-spaced bins). In practice, the range of distributions covered is limited both by computational and statistical considerations, particularly in the limit of densities which vary rapidly over a small range of parameter space. Data-driven models give the most reliable description of the population in that they are unbiased by the systematic uncertainties that can plague (incomplete) physics-

driven models. However, for the same number of observations, the statistical uncertainties in the inferred population tend to be larger because of the high model flexibility. Furthermore, unlike physics-driven models, the parameter inferences often cannot be immediately read off as physical or astrophysical implications, usually requiring further interpretation.

Falling in between physics-driven and data-driven models, *parametric phenomenological models* are designed to consist of relatively simple functional forms, such as Gaussians or (truncated) power laws, but contain features that are motivated by astrophysical theory: e.g. a gap in the BH mass spectrum or a local excess of density for BH spin magnitudes close to zero. The main advantage of parametric phenomenological models is simplicity in writing them down and drawing initial astrophysical conclusions. Oftentimes, these models are also cheaper to fit to data than data-driven or physics-driven models, although this stops being the case if the parametric model is over-prescriptive and struggles to fit the data.

In the simplest parametric and data-driven population models, the probability distribution over source parameters is assumed to be separable, and thus can be written as a product,

$$p(\boldsymbol{\theta}|\boldsymbol{\Lambda}) = p_m(m_1, m_2|\boldsymbol{\Lambda}_m)p_\chi(\chi_1, \chi_2|\boldsymbol{\Lambda}_\chi)p_z(z|\boldsymbol{\Lambda}_z)p_\Omega(\boldsymbol{\Omega}|\boldsymbol{\Lambda}_\Omega)p_i(\boldsymbol{\iota}|\boldsymbol{\Lambda}_i). \quad (155)$$

Here $\boldsymbol{\Omega}$ and $\boldsymbol{\iota}$ are the angular parameters describing the position on the sky and the binary orientation, respectively; the corresponding distributions are usually assumed to be isotropic, but see for instance [260, 401, 704] for counter-examples.

In general, model parameters include cosmological parameters that set the redshift–distance relation and also the distribution p_z , which may be written

$$p_z(z) \propto \frac{1}{1+z} \frac{dV_c}{dz} f(z), \quad (156)$$

with V_c the comoving volume, such that the merger rate density per comoving volume per source-frame time evolves with redshift as

$$\frac{dN}{dV_c dt} \propto f(z), \quad (157)$$

and dV_c/dz also depends on the cosmological parameters. Common phenomenological models for $f(z)$ include a power law in $(1+z)$ or functional forms inspired by the star formation rate [303, 164].

The two-dimensional mass distribution is often factorized as [15, 301, 435]:

$$p_m(m_1, m_2) = p_1(m_1)p_2(m_2|m_1), \quad (158)$$

or similarly using the mass ratio $q = m_2/m_1$ in place of m_2 . Alternative factorizations may, though, be more natural in some contexts; for example, if we believe that both component BH masses are drawn from the same distribution, such that they both share features like local overdensities in the same locations, we may consider a “pairing function” parametrization [302, 280]:

$$p_m(m_1, m_2) \propto p(m_1)p(m_2)f(q, M_{\text{tot}}), \quad (159)$$

where p is the component mass distribution and f is a pairing function that depends on the mass ratio and/or total mass; two BH masses are randomly paired in a binary if $f \equiv 1$.

Typical phenomenological parametric models for the primary mass distribution $p_1(m_1)$ or the component mass distribution $p(m)$ include mixtures of (broken) power laws and Gaussians, with some smoothing applied at the minimum and maximum mass ends to avoid sharp cutoffs, and possible notch filters to represent dips or gaps [301, 435, 662, 726, 298, 253, 40]. The conditional secondary mass distribution, conditional mass ratio distribution, or pairing function is most commonly taken as a power law in mass ratio [301, 435]. However, there are already indications of additional structure in the mass ratio distribution; for example there are hints that at higher masses, the mass ratio distribution more strongly prefers symmetric ($q \approx 1$) systems compared to low masses [458, 277, 615].

The spin distribution can be parameterized in terms of “effective” spin parameters χ_{eff} and χ_p . Past work has modeled these distributions as truncated Gaussians [608, 506] or histograms with 3-5 bins [289, 281]. Alternatively, one can consider all six spin degrees of freedom; in spherical coordinates, the dimensionless spin magnitude and spin tilt angle and azimuthal angle of each component.²⁷ A common parameterization for the spin magnitude distribution is a beta distribution, because it is naturally truncated over the physical range between 0 and 1 [726]. To avoid statistical sampling issues, the prior is typically restricted to non-singular beta distributions; however, this choice excludes spin magnitude distributions that peak sharply at zero, which can be undesirable if we wish to measure a possible excess of nonspinning BHs, as some theories suggest [318, 604, 325, 168]. The cosine of the spin tilt distribution is often modeled as a truncated Gaussian; Ref. [661] introduced a mixture model between such a truncated Gaussian centered at zero (aligned spin) and a flat distribution in cosine tilt (isotropic spins); motivated by expectations from a mixture between isolated binary evolution formation channels, which are thought to produce binaries with nearly-aligned spins ([414] (although the double pulsar system may provide a counterexample [287])) and dynamical assembly, which, at least in gas-free environments like globular clusters, is thought to produce binaries with isotropic spins [566, 600]. The distributions of azimuthal spin angles are typically fixed as uniform, but theoretical predictions for spin-orbit resonances may also motivate explicit inference over these parameters [337, 698, 694]. The simplest models assume that the two compact object spins in a binary are independently drawn from the same distribution, but this contradicts some predictions in which, for example, first-born and second-born BHs preferentially follow different spin distributions [736, 110]. Recent work has thus relaxed this assumption, allowing primary and secondary BH spins to be drawn (independently or not) from different distributions [304, 62].

²⁷ Because these spin parameters evolve during the binary inspiral, a reference frequency must also be specified [698, 515].

Each phenomenological parametrization of the mass, spin or merger redshift distributions can be replaced by a data-driven or non-parametric model. Data-driven models commonly used in the GW literature include Gaussian mixture models [682, 684], splines [254, 255, 348], Gaussian processes (e.g. [278], including Gaussian-process regularized histograms [482, 456, 587] and autoregressive processes [165]), Dirichlet processes [596], and optimized kernel density estimates [616, 615]. Many such methods achieve flexibility by setting up an underlying parametric model, such as a power law, and allowing more or less general forms of deviation from it. Data-driven models typically impose some structure on the correlations between neighboring points in θ -space [384], in order to control the (lack of) smoothness of the population PDF, and thus limit the effective number of independent degrees of freedom to be fit. Such strategies to regularize data-driven models will become less necessary in the limit of large catalogs.

Once data-driven models are fit to the data, there is usually a second “feature extraction” step, where interesting features, such as local maxima, minima or trends, are identified. Although the model is not parameterized in terms of such features, posteriors on, e.g., the location of local maxima in the mass distribution may be calculated in post-processing [279, 165]. The significance of any features can also be evaluated by comparing the posterior against the prior of the data-driven model, noting that although such models are designed to be flexible they can induce nontrivial priors on the population distribution.

In both the parametric and data-driven models, the next level of complexity in modeling the CBC population is to allow parameter correlations rather than assuming that masses, redshifts and spins are independent. Two-parameter correlations investigated up to now include evolution of the mass or spin distribution with redshift [617, 297, 120, 109, 120], or the spin or mass ratio distributions varying over primary mass [618, 660, 314, 305, 712]. Empirically, a statistically significant correlation between the effective inspiral spin and the mass ratio has been identified [166], which may indicate that primary and secondary BH spins are drawn from different distributions, as discussed above.

The simplest such model allows for only a linear correlation, although quadratic and higher order polynomial terms may straightforwardly be included. For instance one can allow the location of a Gaussian peak μ in the primary mass distribution to vary linearly with redshift, $\mu(z) = \mu_0 + z \cdot d\mu/dz|_{z=0}$, with parameters μ_0 and $d\mu/dz|_{z=0}$. Another simple parametric model for two-parameter correlations is a switch point analysis: in such a model the parameters describing the distribution in one variable (e.g. mass) are allowed to take on different values depending if the second variable is above or below the switch point (e.g. at low versus high redshifts). Although a discontinuous jump in the distribution may not be physically well-motivated, switch point analysis can be a quick way to check if the data prefer correlations between two variables [297]. Correlations can also be encoded via mixture models, in which the population consists of different components (subpopulations) with

different properties; for example, allowing distinct parameterized power law or Gaussian peak components in the mass distribution to take on different spin distributions [712, 343, 457]. Copulas also naturally allow the analyst to fix the form of the one-dimensional marginal distributions, while exploring different two-dimensional correlations specified by a copula density function [63]. Data-driven models can also be extended to include correlations between variables, either by directly modeling multiple dimensions non-parametrically (e.g., a multi-dimensional Gaussian mixture [682, 683], a multi-dimensional Gaussian-process regulated histogram [587, 586] or a kernel density estimate [615]); or combining one-dimensional parametric models with flexible functions that describe correlations, for instance using a spline (rather than a linear function) to model evolution of a mass feature with redshift [383].

Fitting physics-driven models to GW catalogs requires a different strategy, based on population synthesis simulations. The model may be described in terms of a mixture of formation channels, such as isolated binary evolution with common envelope, isolated binary evolution with stable mass transfer, chemically homogeneous evolution, triple star evolution, stellar evolution in young star clusters, dynamical assembly in globular clusters, dynamical assembly in the disks of active galactic nuclei, primordial black holes, and so on. The relative mixture weights (also known as branching ratios) of different channels may be considered as free parameters, together with some of the uncertain astrophysical parameters within each channel [656, 738, 737, 140]. Such parameters may include the mass accretion efficiency, common envelope description, black hole natal spins and natal kicks, the metallicity-specific star formation rate, and the mass and radius distribution of globular clusters [539, 141, 655, 593, 300, 196]. For physics-driven models, it is computationally challenging to simulate enough populations that cover the resulting high-dimensional parameter space. Strategies to alleviate this issue such as interpolating between simulations and identifying where to run new simulations (e.g. using Gaussian processes) have been proposed [671, 147]. Simulation-based inference may also be a promising technique for comparing physics-driven models to GW data [211, 453]. An even bigger challenge, however, is that many of the uncertainties in physics-driven models are systematic, stemming from the lack of an adequate model, and therefore defy parameterization [146, 114]. This limitation might be tackled by combining physics-driven models with phenomenological or data-driven models: incorporating specific predictions from population synthesis simulations, such as the remnant mass function or the distribution of delay times between star formation and merger, into a phenomenological population model [111, 306, 345]. This hybrid approach can be used to test one aspect of the population synthesis model at a time against the data; for example, checking whether the predicted delay time distribution is consistent with the inferred merger rate and the assumed star formation rate.

As a technical aside, especially for data-driven or physics-driven CBC population models, it can be tempting to fit the “detected distribution” (i.e., the distribution of GW sources conditioned on detection), rather than the underlying, astrophysical distribution. However, one has to be careful that doing so

does not violate the conditional structure of the data-generating process [262] to obtain a correct hierarchical Bayesian likelihood.

6.3.1 Population model comparisons and checking

With so many population modeling choices, the question naturally arises of which model best describes the data. One answer is to compare models using their Bayes factors (the ratio of their evidences) or their posterior odds (see Section 5.1). Often, the population models we consider are nested, which means that we can easily compute a Bayes factor between two models with a Savage-Dickey density ratio [239] rather than directly computing their evidences. A simple application is to mixture models: either a mixture between two formation channels in physics-driven models, or a mixture between (e.g.) power laws and Gaussians as in commonly-used phenomenological parametric models. Given the posterior on the branching ratio f between two components, we can compute the posterior probability density at $f = 0$ compared to the prior probability density: this density ratio gives us the Bayes factor between the simpler one-component model and the two-component mixture model.

However, in practice the Bayes factor or evidence ratio has various drawbacks. In the mixture model example, if the data poorly constrain f , the posterior will closely resemble the prior, and the Bayes factor between the two models will be unity: the naive expectation that Bayesian model selection will penalize the more complex model fails when the additional parameters are not well-constrained by the data. More generally, the choice of hyper-prior can significantly affect the Bayes factor: this is easy to see in the mixture model example. Such dependence on the hyper-priors can be problematic for interpreting population results: particularly for phenomenological models, there may not be a single well-motivated choice of hyper-prior. For instance, two possible prior choices for the power-law slope of the BBH primary mass distribution would be a uniform distribution between limits -10 and 10 , or uniform between -5 and 5 ; no more fundamental principle enables us to prefer one of these priors to the other. Nevertheless, over a higher-dimensional space of hyper-parameters, different prior choices can yield evidences differing by orders of magnitude for otherwise identical models.

An alternative to comparing two models is to merely check whether a model adequately fits the data, with a goodness-of-fit test. In the Bayesian context, such tests are often provided by posterior predictive checks [299, 40, 602, 507]. After fitting a given population model to the data, one can generate mock observations from that population, which represent draws from the posterior predictive distribution. Ideally, the mock observations include both measurement uncertainty and selection effects, such that the posterior predictive distribution is a distribution over data-space d ; a less powerful posterior predictive check can be carried out at the level of true source parameters θ if one includes selection effects but not measurement uncertainty in generating mock observations. The predicted mock observations can then be checked for consistency with the actual observations: in one dimension, this can be done

by comparing the cumulative distribution function (CDF) of the predicted versus observed source parameters, e.g. via a Kolmogorov-Smirnov (K-S) or Anderson-Darling test. In higher dimensions, one can compare the predicted versus observed number of detections inside one or more regions of interest within source parameter space, e.g. [297]. For a choice of test statistic – in the K-S test case the maximum distance between two CDFs, or the number of detections in a region of parameter space – the tension between the population model and the data can be quantified by first constructing a null distribution of the test statistic by drawing many mock catalog realizations from the posterior predictive distribution. Then the “posterior predictive p-value” is calculated as the fraction of mock catalogs that are more extreme than the observed catalog with respect to the test statistic, quantifying where the observed value falls in the null distribution [299]. In addition to goodness-of-fit tests, posterior predictive checks have been used to classify population outliers in the GW literature [299, 41, 40, 258].

In general, posterior predictive p-values are also sensitive to the choice of model prior, insofar as this choice affects the posterior PDF, and consequently also the posterior predictive distribution. However, they are less sensitive than Bayes factors, which are affected by changes only in the prior (e.g. changes in prior boundaries) even in the case where the posterior is unaffected.

6.4 Matter effects and equation of state of dense matter

During the late stages of a binary coalescence that involves at least one neutron star, finite-size effects modify the expected binary evolution [188, 242]. The two lowest-order effects in the PN phase expansion are that of the spin-induced quadrupole moment at 2PN [562] and tidal interactions at 5PN [307]. Despite the higher PN order, the tidal interactions are more prominent in the signal due to the larger numerical prefactor [387], as well as the fact that the former effect depends on the neutron star spin quadratically [370]. Tidal interactions originate from the fact that NSs have a finite size, and are therefore distorted by the gravitational field of their companion, with two effects on the binary orbit: (i) the tidal deformation drains orbital energy from the system, and (ii) the tidally-induced quadrupole moment acts as another source of gravitational radiation. Black holes do not exhibit such tidal interactions [118, 197].

The degree of tidal deformation depends on the internal composition of the NS and the (unknown) equation of state of dense nuclear matter in beta equilibrium. For stable, cold neutron stars the equation of state is a relation between the pressure p and the energy density ϵ which is expected to be common among all NSs [448, 535, 112]. In general, softer equations of state predict lower internal pressures and smaller NSs that are less deformable, while stiffer equations of state predict higher pressures, larger NSs, and stronger tidal interactions. Further nuclear phenomena such as the emergence of strange degrees of freedom or deconfined quarks and phase transitions [362] might

complicate this picture or even predict the existence of “twin stars”, i.e., NSs with the same mass but different radii.

Inference for the common $p(\epsilon)$ equation of state is a sub-case of the hierarchical inference described above. Specifically, the generic hierarchical posterior from Eq. (142) now becomes [444,188]

$$p\left(\{\mathcal{E}, \mathbf{A}\}|\{d_i\}_{i=1}^N\right) = \frac{p(\{\mathcal{E}, \mathbf{A}\}) \prod_{i=1}^N \int p(d_i|\boldsymbol{\theta}_i) p(\boldsymbol{\theta}_i|\{\mathcal{E}, \mathbf{A}\}) d\boldsymbol{\theta}_i}{p(\{d_i\}_{i=1}^N)}, \quad (160)$$

where we have separated the equation of state $\mathcal{E} \equiv p(\epsilon)$ from the remaining population hyperparameters \mathbf{A} . The latter could now represent the mass or spin distribution of NSs [544]; this distribution must be inferred simultaneously with \mathcal{E} , as their uncertainties can be correlated [728,347]. Restricting \mathbf{A} to the NS mass distribution, the relevant event-level parameters are the binary masses and tidal deformabilities $\boldsymbol{\theta}_i = \{m_i, \Lambda_i\}$ and the population model (or source prior) is now

$$\begin{aligned} p(m_i, \Lambda_i|\{\mathcal{E}, \mathbf{A}\}) &= p(\Lambda_i|m_i, \{\mathcal{E}, \mathbf{A}\}) p(m_i|\{\mathcal{E}, \mathbf{A}\}) \\ &= \delta(\Lambda_i - \mathcal{E}(m_i)) p(m_i|\{\mathcal{E}, \mathbf{A}\}), \end{aligned} \quad (161)$$

where $\delta(x)$ is the Dirac delta function. The equation of state term $\delta(\Lambda_i - \mathcal{E}(m_i))$ represents the fact that the tidal deformability is unambiguously defined given an equation of state and a NS mass. The $p(m_i|\{\mathcal{E}, \mathbf{A}\})$ term couples the mass distribution parametrized by \mathbf{A} and the equation of state encoded in \mathcal{E} , and in general reflects assumptions about NS astrophysics. For example, a simple uniform mass distribution between limits M_l and M_h ,

$$p(m_i|\{\mathcal{E}, \mathbf{A}\}) = \frac{\Theta(M_l \leq m_i)\Theta(m_i \leq M_h)}{M_h - M_l}, \quad (162)$$

could contain an implicit dependence on the equation of state, $M_h = M_{\max}(\mathcal{E})$, if we assume that the maximum NS mass realized in the Universe is determined by nuclear physics, $M_{\max}(\mathcal{E})$ being the maximum mass of nonrotating NSs predicted by \mathcal{E} . If we instead assume that the astrophysical conditions dictating the formation of neutron stars limit neutron star masses to be below $M_{\max}(\mathcal{E})$, M_h would be independent of \mathcal{E} ; the effects of such assumptions are explored further in [450].

Equation (161) requires some functional form for \mathcal{E} . This may be achieved via parametric or nonparametric priors that prescribe candidate $p(\epsilon)$ curves (or equivalent functions). For example, the *piecewise-polytropic* parametrization expresses the pressure as a piecewise function of the baryon density ρ [589, 534], expressed in its simplest form, as

$$p(\rho; p_1 = p(\rho_1), \Gamma_1, \Gamma_2, \Gamma_3) = \begin{cases} K_1 \rho^{\Gamma_1} & : \rho < \rho_1 \\ K_2 \rho^{\Gamma_2} & : \rho_1 < \rho < \rho_2 \\ K_3 \rho^{\Gamma_3} & : \rho_2 < \rho, \end{cases} \quad (163)$$

where ρ_1 and ρ_2 are fixed by optimization against nuclear models [589], while K_1 and K_2 are fixed by continuity. A closely related form is the *spectral* parametrization that instead expands the polytropic index in a polynomial of the pressure [461,462]

$$p(\rho; \gamma_i) = \rho^{\Gamma(x)}, \quad \Gamma(x) = \sum_{i=0}^3 \gamma_i \log(x)^i, \quad (164)$$

where $x \equiv p/p_0$ and p_0 is the pressure where the equation of state transitions to a fixed crust model. An alternative approach instead parameterizes the dependence of the speed of sound [672,355]. Broad and uninformative priors are typically chosen for the parameters in each case, cf. [181,728].

A parallel method expresses the equation of state in a nonparametric way, a term used to refer to methods such as Gaussian processes [443,264,505,353] that parametrize the correlations between the values of a function at different points rather than the function itself. This approach offers the flexibility of directly selecting whether the equation of state prior includes strong or weak correlations [451] across different density scales while simultaneously imposing physical constraints such as thermodynamic stability and causality through the formulation of the Gaussian process.

Both of the above phenomenological approaches can be augmented to include information from nuclear theory, and the associated uncertainties. Specific examples include the use of chiral effective field theory [464,673,672,246,247] results at lower densities and perturbative quantum chromodynamics [353,648,433] results at high densities.

The improving understanding about NSs properties in the recent years is the outcome of combining GW data [29,33,36,39] with other probes: radio [92,212,310] and X-ray [504,594,505,595] observations of galactic neutron stars, observations of the electromagnetic counterpart of GW170817 [210,209,582,487], nuclear experiments [267,598,66,590,265], and nuclear theory [469,672,247,246]. Discussion of the intricacies involved in using such diverse data sets is beyond the scope of this review, however the emerging picture suggests that typical $1.4 M_\odot$ NSs have radii around 12 – 12.5 km (with uncertainties of a few kilometers) and maximum masses above $2 M_\odot$ [504,505,579,578,580,444,450,241,550,123,266]. Many questions remain about the maximum mass, the possibility of phase transitions, the effect of NSs rotation, as well as the nature of the 2–3 M_\odot objects observed with gravitational waves [42,263,290,674,234,124] that upcoming GW observations have the potential to offer information about.

6.5 Tests of General Relativity with multiple sources

The binary dynamics described in Sec. 2.1 are derived assuming General Relativity (GR): modified gravity theories can introduce both qualitative and quantitative changes in observable binary coalescence signals. GR is commonly

expected to be the low-energy limit of an as yet unknown full quantum theory of gravity, implying modifications at some, also unknown, energy or length scale [732]. An additional motivation for testing the theory is the fact that exploration of beyond-GR phenomena and dynamics can illuminate the properties of the theory itself. GW data offer the only probe of the theory in the strongly nonlinear and dynamical regime of compact binary mergers [23, 733, 37, 48, 49].

Efforts to test GR are hampered by the fact that no self-consistent alternative theory has been studied in comparable depth or thoroughness. Therefore, most tests are characterized as “phenomenological” or “model-dependent”, meaning that though they might be motivated by specific beyond-GR phenomena, they are not tuned to any specific high-energy completion of gravity. Tests of GR may be classified according to various criteria. The first criterion distinguishes between “generation” *vs.* “propagation” phenomena: those relating to how waves are generated at the source, or how they propagate to the detectors respectively. An alternative classification splits tests into those that target the fundamental or universal properties of the theory and of wave solutions (e.g., speed of propagation or existence of two transverse polarization modes), *vs.* “quantitative” results (e.g., measuring the phase evolution of binary emission at some PN order). Beyond these model-independent tests, theory-specific tests have also been pursued in certain cases, e.g. [554, 523].

Combining information about tests of GR with multiple sources proceeds again under the same hierarchical framework, with the likelihood given in Eq. (142) where \mathbf{A} are now the hyperparameters that describe the population distribution of the beyond-GR effect(s). The population model, $p(\boldsymbol{\theta}_i|\mathbf{A})$ depends on the test under consideration, with two limiting cases commonly employed. The first corresponds to tests that introduce event-level parameters that are common to all events: it is equivalent to the traditional practice of “multiplying the likelihoods of individual events” [741]. Examples here would be a massive graviton and other propagation effects, or a theory-specific test that is formulated directly in terms of the theory coupling constant(s). The population model now simplifies to a Dirac delta function

$$p(\boldsymbol{\theta}_i|\mathbf{A}_0) = \delta(\mathbf{A}_0 - \boldsymbol{\theta}_i), \quad (165)$$

where \mathbf{A}_0 is a common parameter that is shared by all events. The second approach instead corresponds to tests that introduce a *new* event-level parameter *for each new event*, and it is equivalent to the other traditional practice of “multiplying the Bayes factors of individual events” [741]. The Bayes Factors here compare the GR and beyond-GR hypothesis and are obtained by marginalizing over each event’s astrophysical parameters (such as masses and spins) and (in the case of parametrized GR tests) the beyond-GR parameters themselves. In this case the population model has no hyperparameters and corresponds to the fixed prior used when computing the Bayes Factor

$$p(\boldsymbol{\theta}_i|\mathbf{A}_0) = p(\boldsymbol{\theta}_i). \quad (166)$$

The assumption of completely independent event-level parameters corresponds to gravity theories that introduce a new coupling constant for each event, akin to a charge. This is a fairly strong assumption, as it prevents the analysis from “inferring” the population prior and assumes it is fixed to what was selected during PE inference, as described in Sec. 5. If this assumption is violated, the analysis could result in incorrect physical conclusions [399].

Between those two limiting cases lies the situation where the beyond-GR parameter values are not common among events, but come from a common, unknown underlying population distribution: a non-trivial population model $p(\boldsymbol{\theta}_i|\mathbf{A})$ is thus required. This is the most common situation, encompassing cases such as the parametrized post-Einsteinian inspiral test [731, 194, 455, 68, 494, 203, 622, 623], the inspiral-merger-ringdown consistency test [341, 340, 160, 400], parametrized ringdowns [184, 402, 398, 294], and even the generic residual test [339]. Since these tests introduce phenomenological deviations to the GW signals predicted by GR [410], defining a first-principles population model is impossible. To first order, then, analyses attempt to extract the mean and the standard deviation of the population model, with GR predicting a zero value for both.

Then without loss of generality, the population model can be taken as a Gaussian distribution for the beyond-GR parameters [397], motivated from the fact that the Gaussian distribution maximizes the entropy (i.e., minimizes the information) for a fixed mean and standard deviation. Moreover, it is desirable to consider the population distribution of beyond-GR and ‘within-GR’ parameters (for example, component masses and spins) simultaneously as their measurement uncertainties are typically correlated [553], similar to the discussion of Sec. 6.3. Results from both beyond-GR-only and joint analyses find no evidence for a nonzero mean or standard deviation [397, 48, 49], though the latter are in general more constraining as they incorporate more information about the astrophysical properties of the detected binaries [553]. A generalization of the Gaussian population model also considers the possibility that the population consists of a mixture of two types of binary: those described within, and those beyond GR [619]. In this case the population model is a mixture of a delta function at zero, for binaries that obey GR, and a Gaussian, for binaries that violate it.

Finally, population constraints on beyond-GR effects are subject to selection effects, that can be quantified and included in the analysis following the steps discussed in Sec. 6.2 by simulating beyond-GR waveforms and analyzing them with existing detection pipelines. In the context of parametrized tests of binary GW phase evolution, Ref. [472] showed that current constraints after ~ 100 detections are sufficiently constraining that the impact of selection effects is subdominant. However, this does not rule out the possibility of a “hidden” subpopulation of binaries with large deviations from GR, as population constraints derived from the detected events would not be applicable if binaries originate from multiple populations. Unmodeled burst searches [43] that do not make use of GR compact binary models could alleviate the concern that binaries exhibiting strong deviations from GR would not be detectable in

the first place. Efforts to quantify these effects for specific beyond-GR models, and to extend existing search methods, are underway, e.g., [198, 202, 525].

7 Outlook

7.1 Current and upcoming generations of compact binary observations

The ~ 100 transient GW signals detected during the first three LIGO-Virgo observing runs are all consistent with a compact binary origin: the coalescence of two black holes, two neutron stars, or a neutron star and a black hole. Figure 13 summarizes some key properties of these events: their source-frame chirp mass, motivated and defined in Sec. 2, and their distance from Earth. This catalog arose from an ever-expanding network of kilometre-scale advanced ground-based detectors operating in the $\sim 10 - 1000$ Hz regime which now includes, besides the twin LIGO [6] detectors, the European Virgo [57] and the Japanese cryogenic KAGRA [77] detector.

As interferometric detectors sense GW amplitude, rather than energy, a two-fold increase in sensitivity leads approximately to an eight-fold (volumetric) increase in the detection rate. During the first and second observing runs (O1 and O2) approximately 1 compact binary coalescence was detected per month, while the third observing run (O3) brought approximately 1.5 events per week [44], see Fig. 13. Future estimates depend on the exact sensitivity

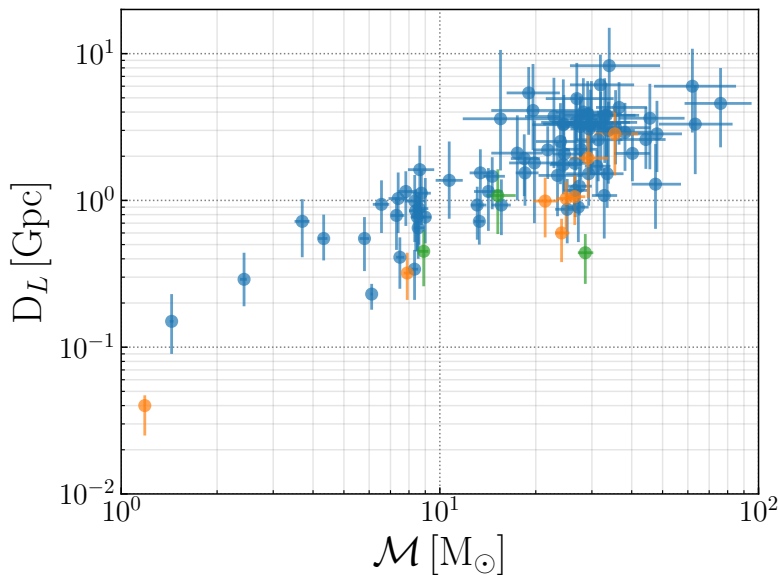


Fig. 13: Source-frame chirp mass and luminosity distances of detected compact binaries during O3 (blue), O2 (orange), O1 (green). The selection effect due to the amplitude scaling of CBC signals for a given detector network is apparent in the “exclusion region” at low masses and high distances. Increasing detector sensitivity allows for detection of more distant (and potentially rare) events.

achieved, but the fourth observing run (O4) that started on May 24, 2023, scheduled to last for 20 months, is yielding 1 event per few days, which will eventually yield a catalog of hundreds. The next steps for the current detector network include a fifth observing run starting around 2027 [34,60], the addition of the LIGO-Aundha detector in India [620], and proposals for further LIGO improvements toward the A# and/or Voyager [67] configurations. The ultimate sensitivity of the detector network is subject to upgrade plans, but it is reasonably expected to raise the total number of detections to the thousands by the end of its lifetime.

7.2 Next generation challenges

The next generation of ground-based gravitational wave observatories, planned for operation in the 2030s and beyond, are expected to have a ten-fold improvement in sensitivity compared to the design sensitivity of the current generation [572,27]: this translates naively to a thousand-fold increase in the detection rate – with, though, significant corrections for cosmological evolution [195]. Such a network would be capable of detecting nearly *all* binary black hole mergers, and roughly half of binary neutron star mergers in the observable universe (see e.g. [612,137]). In addition to the sheer number of detections, the reduction in noise level, while undoubtedly a boon for GW astronomy, will present novel data analysis challenges for future compact binary work. The greatly increased SNR of the loudest signals means that improvements will be needed both in waveform modelling, and in noise modelling, to fully exploit future observatories.

The Einstein Telescope [572] and Cosmic Explorer [271] detector designs anticipate a greatly reduced low frequency noise ‘wall’, allowing the early inspiral at frequencies of a few Hz to be observable in the data; thus, the lightest BNS signals will be visible for many hours and millions of signal cycles. With a possible detection rate of 10^3 events per day, signals will inevitably overlap in the sensitive band of the detectors, violating the usual model of a single signal buried in detector noise. Fortunately, unlike in the case of overlapping white dwarf binaries in LISA, the rapidly evolving CBC signal will not result in true confusion noise [409], but parameter inference can be affected when the coalescence times of two signals are within ~ 0.1 s of each other [621,560,592,409]. The residual power in overlapping signals may produce weak systematic biases in parameter estimation that could affect constraints on environmental and non-GR effects [91,391], and, unless overlapping signals are subtracted, can also impact detection efficiency [724].

The greatly increased population of detections, and therefore the amount of available data, will inflate the computational cost of inference for hierarchical models which marginalise over individual event uncertainties, as explained in 6.1. More complicated population models will probably also be required to explain, or even just accurately represent, as-yet-unknown structures in the astrophysical distribution of sources. Non-parametric methods, discussed in

Sec. 6.3, then offer a potentially useful means of modelling structure without specific assumptions for the functional form of distributions, as do classical statistical methods valid in the limit of high event count, e.g. density estimation [615].

For high-SNR signals, systematic errors in the waveform models themselves will become even more important [576]: this motivates the further improvement of such models, informed both by NR simulations and advances in analytic methods, as well as methods to mitigate remaining waveform errors and uncertainties within the analysis stage [508,718]. The future development of modelling and analysis tools to address these challenges will uncover a range of possible new observables, including deviations from general relativity [549,509], and effects of the source’s environment on the signal – for instance, the presence of a third body in a coalescing system may produce an observable net acceleration along the line of sight (e.g. [395]). Louder signals will also require yet more accurate modeling of subdominant waveform effects, such as higher mode content, orbital precession, and orbital eccentricity, e.g. [584,519]. The greater distance reach of future networks will reveal sources at higher redshifts (up to $z \sim 10$), which, along with improved low-frequency sensitivity, will result in detection of many more signals with chirp masses $\gtrsim \mathcal{O}(100) M_{\odot}$, whether from intermediate mass or redshifted stellar-mass black hole binaries. Such massive mergers will enable detailed investigation of the merger and ringdown portions of the signal [115,398].

The greatly increased length of low-mass signals will expand the quantity of data covered by both search and parameter estimation analyses. Thanks to the chirping nature of the CBC signal, information does not arrive uniformly throughout the signal: to limit computing cost, one may thus use a reduced data rate in the early inspiral for a multi-band analysis [511], or use a reference template to perform heterodyning of the data, reducing its effective bandwidth [205,734]. Long signal durations also offer the ability to provide early warning detection and pre-merger localisation of the source, to enable electromagnetic observations from the moment of coalescence onward (see [474,533] and discussion in Sec. 4.4); realization of this goal requires sufficiently rapid localization, and an associated low latency infrastructure to distribute pre-merger alerts [392].

Machine learning methods offer an avenue for performing extremely rapid inference which has been successfully demonstrated for signal durations of a few seconds, typical of BBH observations in the current detector network (see Sec. 5.4.4). These methods typically use the data stream as conditioning information for a neural network; however, as the data volume increases, the amount of information per datapoint will be reduced, motivating the development of compressed representations of the data that can efficiently encode the signal information. Large-scale use of advanced machine learning inference in production will also require more standardized and dedicated platforms to make efficient use of available processors, while retaining sufficient reliability and flexibility/scalability (e.g. Inference-as-a-Service [357]).

As a fundamental consideration, any method of identifying a modelled source, whether based on ML or a classical template bank to cover the signal space, must contend with the fact that the number of independent templates will explode with longer signal durations, as seen from the fact that the fractional precision of chirp mass measurement scales inversely with the number of observed signal cycles. The presence of higher modes, precession and eccentricity also increase the number of independent templates that must be considered by an analysis. This overall increase in our ability to resolve, and extract astrophysical information from, the complexity of CBC signals, implies that analysis methods are sure to continue development over the coming years.

It is not only CBC signals that will pose increasing challenges in a next-generation network: the characterization of detector noise will likely require more complex and sophisticated methods. We cannot predict what types of non-ideal behaviour will occur in detectors whose locations are not yet decided, but with their broad-band sensitivity pushing the limits from many disparate types of noise in different frequency ranges, there are more possible sources of glitches or non-stationary disturbance. Although such effects, for instance Newtonian noise (reviewed in [368,686]), are not limiting on our current observations, with increased sensitivity weaker glitches may become visible above the stationary noise floor. Also in general, the longer signal durations implied by larger bandwidths imply a higher probability that a glitch will intersect with any given signal, placing an increasing emphasis on modelling and subtraction of artefacts. Finally, the persistent presence of signals in the data stream suggests that the detector noise properties will need to be estimated concurrently with the astrophysical signals [561], as no “offsource” data might exist. Such considerations will become yet more pertinent with the advent of GW observatories in space, and the prospect of joint observations between Earth- and space-based interferometers [86,638,335,428] – pointing to a yet broader potential science scope, which will go hand in hand with these increased technical challenges.

7.3 Conclusion

The field of gravitational wave astronomy as an observational science has exploded in recent years, with compact binaries now being observed on a daily basis. Detecting and analysing CBC signals is the foundation of performing astrophysics with this wealth of new observations, and CBCs will continue to dominate the sources observed in future detectors.

Adjacent areas such as detector development [559,317,34], binary astrophysics [273,480], theoretical understanding of CBC sources [319,131,180,122,625], and their potential electromagnetic counterparts [501,441], strongly interact with the observation and analysis of CBCs, and deserve their own reviews. However, in this article we have aimed to describe the foundations of practical CBC analysis, from the modelling of the signals, through detection and parameter estimation, to performing population inference with a large

number of signals. We hope the reader finds this comprehensive review useful as an entry point into the field, or as a reference for advanced research addressing the challenges that the future will hold.

Acknowledgements The authors acknowledge many helpful and enlightening interactions with members of the LSC, Virgo and KAGRA Compact Binary Coalescence working group on the topics of this work, as well as with the wider community; we thank Jolien Creighton, Frédérique Marion, and Ben Farr for comments on a previous version of the manuscript. K.C. was supported by NSF Grant PHY-2110111 and the Department of Energy under award number DE-SC0023101. This work has received financial support from the Xunta de Galicia (CIGUS Network of research centers), the European Union, and the “María de Maeztu” Units of Excellence program CEX2020-001035-M. TD is supported by research grant PID2020-118635GB-I00 from the Spanish Ministerio de Ciencia e Innovación. MF acknowledges support from the Natural Sciences and Engineering Research Council of Canada (NSERC) RGPIN-2023-05511. VR was supported by the UK Science and Technology Facilities Council grant ST/V005618/1. JV was supported by the UK Science and Technology Facilities Council grant ST/V005634/1.

This research has made use of data or software obtained from the Gravitational Wave Open Science Center (gwosc.org), a service of the LIGO Scientific Collaboration, the Virgo Collaboration, and KAGRA. This material is based upon work supported by NSF’s LIGO Laboratory which is a major facility fully funded by the National Science Foundation, as well as the Science and Technology Facilities Council (STFC) of the United Kingdom, the Max-Planck-Society (MPS), and the State of Niedersachsen/Germany for support of the construction of Advanced LIGO and construction and operation of the GEO600 detector. Additional support for Advanced LIGO was provided by the Australian Research Council. Virgo is funded, through the European Gravitational Observatory (EGO), by the French Centre National de Recherche Scientifique (CNRS), the Italian Istituto Nazionale di Fisica Nucleare (INFN) and the Dutch Nikhef, with contributions by institutions from Belgium, Germany, Greece, Hungary, Ireland, Japan, Monaco, Poland, Portugal, Spain. KAGRA is supported by Ministry of Education, Culture, Sports, Science and Technology (MEXT), Japan Society for the Promotion of Science (JSPS) in Japan; National Research Foundation (NRF) and Ministry of Science and ICT (MSIT) in Korea; Academia Sinica (AS) and National Science and Technology Council (NSTC) in Taiwan.

References

1. <http://www.black-holes.org/waveforms>
2. <https://ccrgpages.rit.edu/~RITCatalog/>
3. <https://einstein.gatech.edu/catalog/>
4. <http://data.cardiffgravity.org/bam-catalogue/>
5. Aasi, J., et al.: Search for gravitational waves from binary black hole inspiral, merger, and ringdown in LIGO-Virgo data from 2009-2010. *Phys. Rev. D* **87**(2), 022002 (2013). DOI 10.1103/PhysRevD.87.022002
6. Aasi, J., et al.: Advanced LIGO. *Class. Quant. Grav.* **32**, 074001 (2015). DOI 10.1088/0264-9381/32/7/074001
7. Abadie, J., et al.: Predictions for the Rates of Compact Binary Coalescences Observable by Ground-based Gravitational-wave Detectors. *Class. Quant. Grav.* **27**, 173001 (2010). DOI 10.1088/0264-9381/27/17/173001
8. Abadie, J., et al.: Search for gravitational-wave inspiral signals associated with short Gamma-Ray Bursts during LIGO's fifth and Virgo's first science run. *Astrophys. J.* **715**, 1453–1461 (2010). DOI 10.1088/0004-637X/715/2/1453
9. Abadie, J., et al.: Search for gravitational waves from binary black hole inspiral, merger and ringdown. *Phys. Rev. D* **83**, 122005 (2011). DOI 10.1103/PhysRevD.83.122005. [Erratum: *Phys.Rev.D* 86, 069903 (2012)]
10. Abadie, J., et al.: Search for gravitational waves associated with gamma-ray bursts during LIGO science run 6 and Virgo science runs 2 and 3. *Astrophys. J.* **760**, 12 (2012). DOI 10.1088/0004-637X/760/1/12
11. Abadie, J., et al.: Search for Gravitational Waves from Low Mass Compact Binary Coalescence in LIGO's Sixth Science Run and Virgo's Science Runs 2 and 3. *Phys. Rev. D* **85**, 082002 (2012). DOI 10.1103/PhysRevD.85.082002
12. Abbott, B., et al.: Analysis of LIGO data for gravitational waves from binary neutron stars. *Phys. Rev. D* **69**, 122001 (2004). DOI 10.1103/PhysRevD.69.122001
13. Abbott, B.P., et al.: LIGO: The Laser interferometer gravitational-wave observatory. *Rept. Prog. Phys.* **72**, 076901 (2009). DOI 10.1088/0034-4885/72/7/076901
14. Abbott, B.P., et al.: Astrophysical Implications of the Binary Black-Hole Merger GW150914. *Astrophys. J. Lett.* **818**(2), L22 (2016). DOI 10.3847/2041-8205/818/2/L22
15. Abbott, B.P., et al.: Binary Black Hole Mergers in the first Advanced LIGO Observing Run. *Phys. Rev. X* **6**(4), 041015 (2016). DOI 10.1103/PhysRevX.6.041015. [Erratum: *Phys.Rev.X* 8, 039903 (2018)]
16. Abbott, B.P., et al.: Characterization of transient noise in Advanced LIGO relevant to gravitational wave signal GW150914. *Class. Quant. Grav.* **33**(13), 134001 (2016). DOI 10.1088/0264-9381/33/13/134001
17. Abbott, B.P., et al.: Directly comparing GW150914 with numerical solutions of Einstein's equations for binary black hole coalescence. *Phys. Rev. D* **94**(6), 064035 (2016). DOI 10.1103/PhysRevD.94.064035
18. Abbott, B.P., et al.: GW150914: First results from the search for binary black hole coalescence with Advanced LIGO. *Phys. Rev. D* **93**(12), 122003 (2016). DOI 10.1103/PhysRevD.93.122003
19. Abbott, B.P., et al.: Observation of Gravitational Waves from a Binary Black Hole Merger. *Phys. Rev. Lett.* **116**(6), 061102 (2016). DOI 10.1103/PhysRevLett.116.061102
20. Abbott, B.P., et al.: Observing gravitational-wave transient GW150914 with minimal assumptions. *Phys. Rev. D* **93**(12), 122004 (2016). DOI 10.1103/PhysRevD.93.122004. [Addendum: *Phys.Rev.D* 94, 069903 (2016)]
21. Abbott, B.P., et al.: Sensitivity of the Advanced LIGO detectors at the beginning of gravitational wave astronomy. *Phys. Rev. D* **93**(11), 112004 (2016). DOI 10.1103/PhysRevD.93.112004. [Erratum: *Phys.Rev.D* 97, 059901 (2018)]
22. Abbott, B.P., et al.: Supplement: The Rate of Binary Black Hole Mergers Inferred from Advanced LIGO Observations Surrounding GW150914. *Astrophys. J. Suppl.* **227**(2), 14 (2016). DOI 10.3847/0067-0049/227/2/14

23. Abbott, B.P., et al.: Tests of general relativity with GW150914. *Phys. Rev. Lett.* **116**(22), 221101 (2016). DOI 10.1103/PhysRevLett.116.221101. [Erratum: *Phys.Rev.Lett.* 121, 129902 (2018)]
24. Abbott, B.P., et al.: The Rate of Binary Black Hole Mergers Inferred from Advanced LIGO Observations Surrounding GW150914. *Astrophys. J. Lett.* **833**(1), L1 (2016). DOI 10.3847/2041-8205/833/1/L1
25. Abbott, B.P., et al.: A gravitational-wave standard siren measurement of the Hubble constant. *Nature* **551**(7678), 85–88 (2017). DOI 10.1038/nature24471
26. Abbott, B.P., et al.: Calibration of the Advanced LIGO detectors for the discovery of the binary black-hole merger GW150914. *Phys. Rev. D* **95**(6), 062003 (2017). DOI 10.1103/PhysRevD.95.062003
27. Abbott, B.P., et al.: Exploring the Sensitivity of Next Generation Gravitational Wave Detectors. *Class. Quant. Grav.* **34**(4), 044001 (2017). DOI 10.1088/1361-6382/aa51f4
28. Abbott, B.P., et al.: Gravitational Waves and Gamma-rays from a Binary Neutron Star Merger: GW170817 and GRB 170817A. *Astrophys. J. Lett.* **848**(2), L13 (2017). DOI 10.3847/2041-8213/aa920c
29. Abbott, B.P., et al.: GW170817: Observation of Gravitational Waves from a Binary Neutron Star Inspiral. *Phys. Rev. Lett.* **119**(16), 161101 (2017). DOI 10.1103/PhysRevLett.119.161101
30. Abbott, B.P., et al.: Multi-messenger Observations of a Binary Neutron Star Merger. *Astrophys. J. Lett.* **848**(2), L12 (2017). DOI 10.3847/2041-8213/aa91c9
31. Abbott, B.P., et al.: The basic physics of the binary black hole merger GW150914. *Annalen Phys.* **529**(1-2), 1600209 (2017). DOI 10.1002/andp.201600209
32. Abbott, B.P., et al.: GW170817: Implications for the Stochastic Gravitational-Wave Background from Compact Binary Coalescences. *Phys. Rev. Lett.* **120**(9), 091101 (2018). DOI 10.1103/PhysRevLett.120.091101
33. Abbott, B.P., et al.: GW170817: Measurements of neutron star radii and equation of state. *Phys. Rev. Lett.* **121**(16), 161101 (2018). DOI 10.1103/PhysRevLett.121.161101
34. Abbott, B.P., et al.: Prospects for observing and localizing gravitational-wave transients with Advanced LIGO, Advanced Virgo and KAGRA. *Living Rev. Rel.* **21**(1), 3 (2018). DOI 10.1007/s41114-020-00026-9
35. Abbott, B.P., et al.: GWTC-1: A Gravitational-Wave Transient Catalog of Compact Binary Mergers Observed by LIGO and Virgo during the First and Second Observing Runs. *Phys. Rev. X* **9**(3), 031040 (2019). DOI 10.1103/PhysRevX.9.031040
36. Abbott, B.P., et al.: Properties of the binary neutron star merger GW170817. *Phys. Rev. X* **9**(1), 011001 (2019). DOI 10.1103/PhysRevX.9.011001
37. Abbott, B.P., et al.: Tests of General Relativity with the Binary Black Hole Signals from the LIGO-Virgo Catalog GWTC-1. *Phys. Rev. D* **100**(10), 104036 (2019). DOI 10.1103/PhysRevD.100.104036
38. Abbott, B.P., et al.: A guide to LIGO-Virgo detector noise and extraction of transient gravitational-wave signals. *Class. Quant. Grav.* **37**(5), 055002 (2020). DOI 10.1088/1361-6382/ab685e
39. Abbott, B.P., et al.: GW190425: Observation of a Compact Binary Coalescence with Total Mass $\sim 3.4M_{\odot}$. *Astrophys. J. Lett.* **892**(1), L3 (2020). DOI 10.3847/2041-8213/ab75f5
40. Abbott, R., Abbott, T.D., Abraham, S., Acernese, F., Ackley, K., Adams, A., Adams, C., Adhikari, R.X., Adya, V.B., Affeldt, C., et al.: Population Properties of Compact Objects from the Second LIGO-Virgo Gravitational-Wave Transient Catalog. *ApJ* **913**(1), L7 (2021). DOI 10.3847/2041-8213/abe949
41. Abbott, R., Abbott, T.D., Abraham, S., Acernese, F., Ackley, K., Adams, C., Adhikari, R.X., Adya, V.B., Affeldt, C., Agathos, M., et al.: GW190412: Observation of a binary-black-hole coalescence with asymmetric masses. *Phys. Rev. D* **102**(4), 043015 (2020). DOI 10.1103/PhysRevD.102.043015
42. Abbott, R., et al.: GW190814: Gravitational Waves from the Coalescence of a 23 Solar Mass Black Hole with a 2.6 Solar Mass Compact Object. *Astrophys. J. Lett.* **896**(2), L44 (2020). DOI 10.3847/2041-8213/ab960f
43. Abbott, R., et al.: All-sky search for short gravitational-wave bursts in the third Advanced LIGO and Advanced Virgo run. *Phys. Rev. D* **104**(12), 122004 (2021). DOI 10.1103/PhysRevD.104.122004

44. Abbott, R., et al.: GWTC-2: Compact Binary Coalescences Observed by LIGO and Virgo During the First Half of the Third Observing Run. *Phys. Rev. X* **11**, 021053 (2021). DOI 10.1103/PhysRevX.11.021053
45. Abbott, R., et al.: GWTC-3: Compact Binary Coalescences Observed by LIGO and Virgo During the Second Part of the Third Observing Run (2021)
46. Abbott, R., et al.: Observation of Gravitational Waves from Two Neutron Star-Black Hole Coalescences. *Astrophys. J. Lett.* **915**(1), L5 (2021). DOI 10.3847/2041-8213/ac082e
47. Abbott, R., et al.: Search for Lensing Signatures in the Gravitational-Wave Observations from the First Half of LIGO–Virgo’s Third Observing Run. *Astrophys. J.* **923**(1), 14 (2021). DOI 10.3847/1538-4357/ac23db
48. Abbott, R., et al.: Tests of general relativity with binary black holes from the second LIGO–Virgo gravitational-wave transient catalog. *Phys. Rev. D* **103**(12), 122002 (2021). DOI 10.1103/PhysRevD.103.122002
49. Abbott, R., et al.: Tests of General Relativity with GWTC-3 (2021)
50. Abbott, R., et al.: Search for Gravitational Waves Associated with Fast Radio Bursts Detected by CHIME/FRB During the LIGO–Virgo Observing Run O3a (2022)
51. Abbott, R., et al.: Search for Gravitational Waves Associated with Gamma-Ray Bursts Detected by Fermi and Swift during the LIGO–Virgo Run O3b. *Astrophys. J.* **928**(2), 186 (2022). DOI 10.3847/1538-4357/ac532b
52. Abbott, R., et al.: Population of Merging Compact Binaries Inferred Using Gravitational Waves through GWTC-3. *Phys. Rev. X* **13**(1), 011048 (2023). DOI 10.1103/PhysRevX.13.011048
53. Abbott, R., et al.: Search for Gravitational-lensing Signatures in the Full Third Observing Run of the LIGO–Virgo Network. *Astrophys. J.* **970**(2), 191 (2024). DOI 10.3847/1538-4357/ad3e83
54. Abramovici, A., et al.: LIGO: The Laser interferometer gravitational wave observatory. *Science* **256**, 325–333 (1992). DOI 10.1126/science.256.5055.325
55. Accadia, T., et al.: Noise from scattered light in Virgo’s second science run data. *Class. Quant. Grav.* **27**, 194011 (2010). DOI 10.1088/0264-9381/27/19/194011
56. Accadia, T., et al.: Virgo: a laser interferometer to detect gravitational waves. *JINST* **7**, P03012 (2012). DOI 10.1088/1748-0221/7/03/P03012
57. Acernese, F., et al.: Advanced Virgo: a second-generation interferometric gravitational wave detector. *Class. Quant. Grav.* **32**(2), 024001 (2015). DOI 10.1088/0264-9381/32/2/024001
58. Acernese, F., et al.: Calibration of Advanced Virgo and Reconstruction of the Gravitational Wave Signal $h(t)$ during the Observing Run O2. *Class. Quant. Grav.* **35**(20), 205004 (2018). DOI 10.1088/1361-6382/aadf1a
59. Acernese, F., et al.: Calibration of advanced Virgo and reconstruction of the detector strain $h(t)$ during the observing run O3. *Class. Quant. Grav.* **39**(4), 045006 (2022). DOI 10.1088/1361-6382/ac3c8e
60. Acernese, F., et al.: Advanced Virgo Plus: Future Perspectives. *J. Phys. Conf. Ser.* **2429**(1), 012040 (2023). DOI 10.1088/1742-6596/2429/1/012040
61. Acernese, F., et al.: Virgo detector characterization and data quality: results from the O3 run. *Class. Quant. Grav.* **40**(18), 185006 (2023). DOI 10.1088/1361-6382/acd92d
62. Adamcewicz, C., Galaudage, S., Lasky, P.D., Thrane, E.: Which black hole is spinning? Probing the origin of black-hole spin with gravitational waves. *arXiv e-prints arXiv:2311.05182* (2023). DOI 10.48550/arXiv.2311.05182
63. Adamcewicz, C., Thrane, E.: Do unequal-mass binary black hole systems have larger χ_{eff} ? Probing correlations with copulas in gravitational-wave astronomy. *MNRAS* **517**(3), 3928–3937 (2022). DOI 10.1093/mnras/stac2961
64. Adams, T., Buskulic, D., Germain, V., Guidi, G.M., Marion, F., Montani, M., Mours, B., Piergiovanni, F., Wang, G.: Low-latency analysis pipeline for compact binary coalescences in the advanced gravitational wave detector era. *Class. Quant. Grav.* **33**(17), 175012 (2016). DOI 10.1088/0264-9381/33/17/175012
65. Adams, W.S.: An a-type star of very low luminosity. *Publications of the Astronomical Society of the Pacific* **26**(155), 198 (1914). DOI 10.1086/122337. URL <https://dx.doi.org/10.1086/122337>

66. Adhikari, D., et al.: Accurate Determination of the Neutron Skin Thickness of ^{208}Pb through Parity-Violation in Electron Scattering. *Phys. Rev. Lett.* **126**(17), 172502 (2021). DOI 10.1103/PhysRevLett.126.172502
67. Adhikari, R.X., et al.: A cryogenic silicon interferometer for gravitational-wave detection. *Class. Quant. Grav.* **37**(16), 165003 (2020). DOI 10.1088/1361-6382/ab9143
68. Agathos, M., Del Pozzo, W., Li, T.G.F., Van Den Broeck, C., Veitch, J., Vitale, S.: TIGER: A data analysis pipeline for testing the strong-field dynamics of general relativity with gravitational wave signals from coalescing compact binaries. *Phys. Rev. D* **89**(8), 082001 (2014). DOI 10.1103/PhysRevD.89.082001
69. Aguiar, O.D.: The Past, Present and Future of the Resonant-Mass Gravitational Wave Detectors. *Res. Astron. Astrophys.* **11**, 1–42 (2011). DOI 10.1088/1674-4527/11/1/001
70. Ajith, P.: Addressing the spin question in gravitational-wave searches: Waveform templates for inspiralling compact binaries with nonprecessing spins. *Phys. Rev. D* **84**, 084037 (2011). DOI 10.1103/PhysRevD.84.084037
71. Ajith, P., Fotopoulos, N., Privitera, S., Neunzert, A., Weinstein, A.J.: Effectual template bank for the detection of gravitational waves from inspiralling compact binaries with generic spins. *Phys. Rev. D* **89**(8), 084041 (2014). DOI 10.1103/PhysRevD.89.084041
72. Ajith, P., Hewitson, M., Heng, I.S.: Null-stream veto for two co-located detectors: Implementation issues. *Class. Quant. Grav.* **23**, S741–S749 (2006). DOI 10.1088/0264-9381/23/19/S13
73. Ajith, P., et al.: A Template bank for gravitational waveforms from coalescing binary black holes. I. Non-spinning binaries. *Phys. Rev. D* **77**, 104017 (2008). DOI 10.1103/PhysRevD.77.104017. [Erratum: *Phys. Rev. D* 79, 129901 (2009)]
74. Ajith, P., et al.: Inspiral-merger-ringdown waveforms for black-hole binaries with nonprecessing spins. *Phys. Rev. Lett.* **106**, 241101 (2011). DOI 10.1103/PhysRevLett.106.241101
75. Akcay, S., Bernuzzi, S., Messina, F., Nagar, A., Ortiz, N., Rettegno, P.: Effective-one-body multipolar waveform for tidally interacting binary neutron stars up to merger. *Phys. Rev. D* **99**(4), 044051 (2019). DOI 10.1103/PhysRevD.99.044051
76. Akcay, S., Gamba, R., Bernuzzi, S.: Hybrid post-Newtonian effective-one-body scheme for spin-precessing compact-binary waveforms up to merger. *Phys. Rev. D* **103**(2), 024014 (2021). DOI 10.1103/PhysRevD.103.024014
77. Akutsu, T., et al.: Overview of KAGRA: Calibration, detector characterization, physical environmental monitors, and the geophysics interferometer. *Progress of Theoretical and Experimental Physics* **2021**(5) (2021). DOI 10.1093/ptep/ptab018
78. Alcubierre, M.: *Introduction to 3+1 Numerical Relativity*. Oxford University Press (2008). DOI 10.1093/acprof:oso/9780199205677.001.0001. URL <https://doi.org/10.1093/acprof:oso/9780199205677.001.0001>
79. Allen, B.: LIGO calibration accuracy. <https://dcc.ligo.org/LIGO-T960189/public> (1996)
80. Allen, B.: χ^2 time-frequency discriminator for gravitational wave detection. *Phys. Rev. D* **71**, 062001 (2005). DOI 10.1103/PhysRevD.71.062001
81. Allen, B.: Optimal template banks. *Phys. Rev. D* **104**(4), 042005 (2021). DOI 10.1103/PhysRevD.104.042005
82. Allen, B., Anderson, W.G., Brady, P.R., Brown, D.A., Creighton, J.D.E.: FINDCHIRP: An Algorithm for detection of gravitational waves from inspiraling compact binaries. *Phys. Rev. D* **85**, 122006 (2012). DOI 10.1103/PhysRevD.85.122006
83. Álvares, J.D., Font, J.A., Freitas, F.F., Freitas, O.G., Morais, A.P., Nunes, S., Onofre, A., Torres-Forné, A.: Gravitational-wave parameter inference using Deep Learning (2020). DOI 10.1109/CBMT50038.2021.9461893
84. Amari, S., Nagaoka, H.: *Methods of Information Geometry* (2000). DOI 10.1090/mmono/191
85. Amaro-Seoane, P., et al.: eLISA/NGO: Astrophysics and cosmology in the gravitational-wave millihertz regime. *GW Notes* **6**, 4–110 (2013)
86. Amaro-Seoane, P., et al.: *Laser Interferometer Space Antenna* (2017)

87. Andres, N., et al.: Assessing the compact-binary merger candidates reported by the MBTA pipeline in the LIGO-Virgo O3 run: probability of astrophysical origin, classification, and associated uncertainties. *Class. Quant. Grav.* **39**(5), 055002 (2022). DOI 10.1088/1361-6382/ac482a
88. Andrieu, C., Thoms, J.: A tutorial on adaptive mcmc. *Statistics and Computing* **18**(4), 343–373 (2008). DOI 10.1007/s11222-008-9110-y. URL <https://doi.org/10.1007/s11222-008-9110-y>
89. Antil, H., Field, S.E., Herrmann, F., Nochetto, R.H., Tiglio, M.: Two-step greedy algorithm for reduced order quadratures. *Journal of Scientific Computing* **57**, 604–637 (2013)
90. Antil, H., Field, S.E., Herrmann, F., Nochetto, R.H., Tiglio, M.: Two-step greedy algorithm for reduced order quadratures. *J. Sci. Comput.* **57**, 604–637 (2013). DOI 10.1007/s10915-013-9722-z
91. Antonelli, A., Burke, O., Gair, J.R.: Noisy neighbours: inference biases from overlapping gravitational-wave signals. *Mon. Not. Roy. Astron. Soc.* **507**(4), 5069–5086 (2021). DOI 10.1093/mnras/stab2358
92. Antoniadis, J., et al.: A Massive Pulsar in a Compact Relativistic Binary. *Science* **340**, 6131 (2013). DOI 10.1126/science.1233232
93. Apostolatos, T.A.: Search templates for gravitational waves from precessing, inspiraling binaries. *Phys. Rev. D* **52**, 605–620 (1995). DOI 10.1103/PhysRevD.52.605
94. Apostolatos, T.A., Cutler, C., Sussman, G.J., Thorne, K.S.: Spin induced orbital precession and its modulation of the gravitational wave forms from merging binaries. *Phys. Rev. D* **49**, 6274–6297 (1994). DOI 10.1103/PhysRevD.49.6274
95. Arun, K.G., Buonanno, A., Faye, G., Ochsner, E.: Higher-order spin effects in the amplitude and phase of gravitational waveforms emitted by inspiraling compact binaries: Ready-to-use gravitational waveforms. *Phys. Rev. D* **79**, 104023 (2009). DOI 10.1103/PhysRevD.79.104023. [Erratum: *Phys.Rev.D* 84, 049901 (2011)]
96. Arun, K.G., Iyer, B.R., Sathyaprakash, B.S., Sundararajan, P.A.: Parameter estimation of inspiralling compact binaries using 3.5 post-Newtonian gravitational wave phasing: The Non-spinning case. *Phys. Rev. D* **71**, 084008 (2005). DOI 10.1103/PhysRevD.71.084008. [Erratum: *Phys.Rev.D* 72, 069903 (2005)]
97. Ashton, G.: Gaussian processes for glitch-robust gravitational-wave astronomy. *Mon. Not. Roy. Astron. Soc.* **520**(2), 2983–2994 (2023). DOI 10.1093/mnras/stad341
98. Ashton, G., Talbot, C.: Bilby-MCMC: an MCMC sampler for gravitational-wave inference. *Mon. Not. Roy. Astron. Soc.* **507**(2), 2037–2051 (2021). DOI 10.1093/mnras/stab2236
99. Ashton, G., et al.: BILBY: A user-friendly Bayesian inference library for gravitational-wave astronomy. *Astrophys. J. Suppl.* **241**(2), 27 (2019). DOI 10.3847/1538-4365/ab06fc
100. Aubin, F., et al.: The MBTA pipeline for detecting compact binary coalescences in the third LIGO-Virgo observing run. *Class. Quant. Grav.* **38**(9), 095004 (2021). DOI 10.1088/1361-6382/abe913
101. Baade, W., Zwicky, F.: Remarks on Super-Novae and Cosmic Rays. *Phys. Rev.* **46**(1), 76 (1934). DOI 10.1103/PhysRev.46.76.2
102. Babak, S.: Building a stochastic template bank for detecting massive black hole binaries. *Class. Quant. Grav.* **25**, 195011 (2008). DOI 10.1088/0264-9381/25/19/195011
103. Babak, S., Taracchini, A., Buonanno, A.: Validating the effective-one-body model of spinning, precessing binary black holes against numerical relativity. *Phys. Rev. D* **95**(2), 024010 (2017). DOI 10.1103/PhysRevD.95.024010
104. Babak, S., et al.: Searching for gravitational waves from binary coalescence. *Phys. Rev. D* **87**(2), 024033 (2013). DOI 10.1103/PhysRevD.87.024033
105. Baird, E., Fairhurst, S., Hannam, M., Murphy, P.: Degeneracy between mass and spin in black-hole-binary waveforms. *Phys. Rev. D* **87**(2), 024035 (2013). DOI 10.1103/PhysRevD.87.024035
106. Baker, J.G., Centrella, J., Choi, D.I., Koppitz, M., van Meter, J.: Gravitational wave extraction from an inspiraling configuration of merging black holes. *Phys. Rev. Lett.* **96**, 111102 (2006). DOI 10.1103/PhysRevLett.96.111102

107. Baker, P.T., Caudill, S., Hodge, K.A., Talukder, D., Capano, C., Cornish, N.J.: Multivariate Classification with Random Forests for Gravitational Wave Searches of Black Hole Binary Coalescence. *Phys. Rev. D* **91**(6), 062004 (2015). DOI 10.1103/PhysRevD.91.062004
108. Baumgarte, T.W., Shapiro, S.L.: *Numerical Relativity: Solving Einstein's Equations on the Computer*. Cambridge University Press (2010). DOI 10.1017/CBO9781139193344
109. Bavera, S.S., Fishbach, M., Zevin, M., Zapartas, E., Fragos, T.: The $\chi_{\text{eff}} - z$ correlation of field binary black hole mergers and how 3G gravitational-wave detectors can constrain it. *A&A* **665**, A59 (2022). DOI 10.1051/0004-6361/202243724
110. Bavera, S.S., Fragos, T., Qin, Y., Zapartas, E., Neijssel, C.J., Mandel, I., Batta, A., Gaebel, S.M., Kimball, C., Stevenson, S.: The origin of spin in binary black holes. Predicting the distributions of the main observables of Advanced LIGO. *A&A* **635**, A97 (2020). DOI 10.1051/0004-6361/201936204
111. Baxter, E.J., Croon, D., McDermott, S.D., Sakstein, J.: Find the Gap: Black Hole Population Analysis with an Astrophysically Motivated Mass Function. *ApJ* **916**(2), L16 (2021). DOI 10.3847/2041-8213/ac11fc
112. Baym, G., Hatsuda, T., Kojo, T., Powell, P.D., Song, Y., Takatsuka, T.: From hadrons to quarks in neutron stars: a review. *Rept. Prog. Phys.* **81**(5), 056902 (2018). DOI 10.1088/1361-6633/aaae14
113. Belczynski, K., Kalogera, V., Bulik, T.: A Comprehensive Study of Binary Compact Objects as Gravitational Wave Sources: Evolutionary Channels, Rates, and Physical Properties. *ApJ* **572**(1), 407–431 (2002). DOI 10.1086/340304
114. Belczynski, K., Romagnolo, A., Olejak, A., Klencki, J., Chattopadhyay, D., Stevenson, S., Coleman Miller, M., Lasota, J.P., Crowther, P.A.: The Uncertain Future of Massive Binaries Obscures the Origin of LIGO/Virgo Sources. *ApJ* **925**(1), 69 (2022). DOI 10.3847/1538-4357/ac375a
115. Berti, E., Cardoso, V., Will, C.M.: On gravitational-wave spectroscopy of massive black holes with the space interferometer LISA. *Phys. Rev. D* **73**, 064030 (2006). DOI 10.1103/PhysRevD.73.064030
116. Bethe, H.A., Brown, G.E.: Evolution of Binary Compact Objects That Merge. *ApJ* **506**(2), 780–789 (1998). DOI 10.1086/306265
117. Bhardwaj, U., Alvey, J., Miller, B.K., Nissanke, S., Weniger, C.: Sequential simulation-based inference for gravitational wave signals. *Phys. Rev. D* **108**(4), 042004 (2023). DOI 10.1103/PhysRevD.108.042004
118. Binnington, T., Poisson, E.: Relativistic theory of tidal Love numbers. *Phys. Rev. D* **80**, 084018 (2009). DOI 10.1103/PhysRevD.80.084018
119. Bird, S., Cholis, I., Muñoz, J.B., Ali-Haïmoud, Y., Kamionkowski, M., Kovetz, E.D., Raccanelli, A., Riess, A.G.: Did LIGO Detect Dark Matter? *Phys. Rev. Lett.* **116**(20), 201301 (2016). DOI 10.1103/PhysRevLett.116.201301
120. Biscoveanu, S., Callister, T.A., Haster, C.J., Ng, K.K.Y., Vitale, S., Farr, W.M.: The Binary Black Hole Spin Distribution Likely Broadens with Redshift. *ApJ* **932**(2), L19 (2022). DOI 10.3847/2041-8213/ac71a8
121. Biscoveanu, S., Haster, C.J., Vitale, S., Davies, J.: Quantifying the Effect of Power Spectral Density Uncertainty on Gravitational-Wave Parameter Estimation for Compact Binary Sources. *Phys. Rev. D* **102**(2), 023008 (2020). DOI 10.1103/PhysRevD.102.023008
122. Bishop, N.T., Rezzolla, L.: *Extraction of Gravitational Waves in Numerical Relativity*. *Living Rev. Rel.* **19**, 2 (2016). DOI 10.1007/s41114-016-0001-9
123. Biswas, B.: Impact of PREX-II, the revised mass measurement of PSRJ0740+6620, and possible NICER observation on the dense matter equation of state (2021)
124. Biswas, B., Nandi, R., Char, P., Bose, S., Stergioulas, N.: GW190814: on the properties of the secondary component of the binary. *Mon. Not. Roy. Astron. Soc.* **505**(2), 1600–1606 (2021). DOI 10.1093/mnras/stab1383
125. Biswas, R., Brady, P.R., Creighton, J.D.E., Fairhurst, S.: The Loudest event statistic: General formulation, properties and applications. *Class. Quant. Grav.* **26**, 175009 (2009). DOI 10.1088/0264-9381/26/17/175009. [Erratum: *Class. Quant. Grav.* **30**, 079502 (2013)]

126. Biswas, R., et al.: Likelihood-ratio ranking of gravitational-wave candidates in a non-Gaussian background. *Phys. Rev. D* **85**, 122008 (2012). DOI 10.1103/PhysRevD.85.122008
127. Biwer, C.M., Capano, C.D., De, S., Cabero, M., Brown, D.A., Nitz, A.H., Raymond, V.: PyCBC Inference: A Python-based parameter estimation toolkit for compact binary coalescence signals. *Publ. Astron. Soc. Pac.* **131**(996), 024503 (2019). DOI 10.1088/1538-3873/aaef0b
128. Blackman, J., Field, S.E., Scheel, M.A., Galley, C.R., Hemberger, D.A., Schmidt, P., Smith, R.: A Surrogate Model of Gravitational Waveforms from Numerical Relativity Simulations of Precessing Binary Black Hole Mergers. *Phys. Rev. D* **95**(10), 104023 (2017). DOI 10.1103/PhysRevD.95.104023
129. Blackman, J., Field, S.E., Scheel, M.A., Galley, C.R., Ott, C.D., Boyle, M., Kidder, L.E., Pfeiffer, H.P., Szilágyi, B.: Numerical relativity waveform surrogate model for generically precessing binary black hole mergers. *Phys. Rev. D* **96**(2), 024058 (2017). DOI 10.1103/PhysRevD.96.024058
130. Blanchet, L.: Second postNewtonian generation of gravitational radiation. *Phys. Rev. D* **51**, 2559–2583 (1995). DOI 10.1103/PhysRevD.51.2559
131. Blanchet, L.: Gravitational Radiation from Post-Newtonian Sources and Inspiralling Compact Binaries. *Living Rev. Rel.* **17**, 2 (2014). DOI 10.12942/lrr-2014-2
132. Blanchet, L.: Analyzing Gravitational Waves with General Relativity. *Comptes Rendus Physique* **20**, 507–520 (2019). DOI 10.1016/j.crhy.2019.02.004
133. Blanchet, L., Damour, T., Iyer, B.R.: Gravitational waves from inspiralling compact binaries: Energy loss and wave form to second postNewtonian order. *Phys. Rev. D* **51**, 5360 (1995). DOI 10.1103/PhysRevD.51.5360, 10.1103/PhysRevD.54.1860. [Erratum: *Phys. Rev. D* 54, 1860 (1996)]
134. Blanchet, L., Damour, T., Iyer, B.R., Will, C.M., Wiseman, A.: Gravitational radiation damping of compact binary systems to second postNewtonian order. *Phys. Rev. Lett.* **74**, 3515–3518 (1995). DOI 10.1103/PhysRevLett.74.3515
135. Bohé, A., et al.: Improved effective-one-body model of spinning, nonprecessing binary black holes for the era of gravitational-wave astrophysics with advanced detectors. *Phys. Rev. D* **95**(4), 044028 (2017). DOI 10.1103/PhysRevD.95.044028
136. de Boor, C.: *A Practical Guide to Splines*. Springer (2001)
137. Borhanian, S., Sathyaprakash, B.S.: *Listening to the Universe with Next Generation Ground-Based Gravitational-Wave Detectors* (2022)
138. Bose, S., Dayanga, T., Ghosh, S., Talukder, D.: A blind hierarchical coherent search for gravitational-wave signals from coalescing compact binaries in a network of interferometric detectors. *Class. Quant. Grav.* **28**, 134009 (2011). DOI 10.1088/0264-9381/28/13/134009
139. Bose, S., Dhurandhar, S.V., Pai, A.: Detection of gravitational waves using a network of detectors. *Pramana* **53**, 1125–1136 (1999). DOI 10.1007/s12043-999-0072-1
140. Bouffanais, Y., Mapelli, M., Santoliquido, F., Giacobbo, N., Di Carlo, U.N., Rastello, S., Artale, M.C., Iorio, G.: New insights on binary black hole formation channels after GWTC-2: young star clusters versus isolated binaries. *MNRAS* **507**(4), 5224–5235 (2021). DOI 10.1093/mnras/stab2438
141. Bouffanais, Y., Mapelli, M., Santoliquido, F., Giacobbo, N., Iorio, G., Costa, G.: Constraining accretion efficiency in massive binary stars with LIGO -Virgo black holes. *MNRAS* **505**(3), 3873–3882 (2021). DOI 10.1093/mnras/stab1589
142. Boyle, M.: Angular velocity of gravitational radiation from precessing binaries and the corotating frame. *Phys. Rev. D* **87**(10), 104006 (2013). DOI 10.1103/PhysRevD.87.104006
143. Boyle, M., Kidder, L.E., Ossokine, S., Pfeiffer, H.P.: Gravitational-wave modes from precessing black-hole binaries (2014)
144. Boyle, M., Owen, R., Pfeiffer, H.P.: A geometric approach to the precession of compact binaries. *Phys. Rev. D* **84**, 124011 (2011). DOI 10.1103/PhysRevD.84.124011
145. Boyle, M., et al.: The SXS Collaboration catalog of binary black hole simulations. *Class. Quant. Grav.* **36**(19), 195006 (2019). DOI 10.1088/1361-6382/ab34e2
146. Broekgaarden, F.S., Berger, E., Neijssel, C.J., Vigna-Gómez, A., Chattopadhyay, D., Stevenson, S., Chruslinska, M., Justham, S., de Mink, S.E., Mandel, I.: Impact of

- massive binary star and cosmic evolution on gravitational wave observations I: black hole-neutron star mergers. *MNRAS***508**(4), 5028–5063 (2021). DOI 10.1093/mnras/stab2716
147. Broekgaarden, F.S., Justham, S., de Mink, S.E., Gair, J., Mandel, I., Stevenson, S., Barrett, J.W., Vigna-Gómez, A., Neijssel, C.J.: STROOPWAFEL: simulating rare outcomes from astrophysical populations, with application to gravitational-wave sources. *MNRAS***490**(4), 5228–5248 (2019). DOI 10.1093/mnras/stz2558
 148. Brown, D.A.: Searching for gravitational radiation from binary black hole MACHOs in the galactic halo. Ph.D. thesis, University of Wisconsin Milwaukee (2004)
 149. Brown, D.A., Harry, I., Lundgren, A., Nitz, A.H.: Detecting binary neutron star systems with spin in advanced gravitational-wave detectors. *Phys. Rev. D* **86**, 084017 (2012). DOI 10.1103/PhysRevD.86.084017
 150. Brown, D.A., Zimmerman, P.J.: The Effect of Eccentricity on Searches for Gravitational-Waves from Coalescing Compact Binaries in Ground-based Detectors. *Phys. Rev. D* **81**, 024007 (2010). DOI 10.1103/PhysRevD.81.024007
 151. Buikema, A., et al.: Sensitivity and performance of the Advanced LIGO detectors in the third observing run. *Phys. Rev. D* **102**(6), 062003 (2020). DOI 10.1103/PhysRevD.102.062003
 152. Buonanno, A.: Gravitational waves. In: *Les Houches Summer School - Session 86: Particle Physics and Cosmology: The Fabric of Spacetime* (2007)
 153. Buonanno, A., Chen, Y.b., Pan, Y., Vallisneri, M.: A Quasi-physical family of gravity-wave templates for precessing binaries of spinning compact objects. 2. Application to double-spin precessing binaries. *Phys. Rev. D* **70**, 104003 (2004). DOI 10.1103/PhysRevD.70.104003. [Erratum: *Phys. Rev. D* 74, 029902 (2006)]
 154. Buonanno, A., Chen, Y.b., Vallisneri, M.: Detecting gravitational waves from precessing binaries of spinning compact objects: Adiabatic limit. *Phys. Rev. D* **67**, 104025 (2003). DOI 10.1103/PhysRevD.67.104025. [Erratum: *Phys. Rev. D* 74, 029904 (2006)]
 155. Buonanno, A., Damour, T.: Effective one-body approach to general relativistic two-body dynamics. *Phys. Rev. D* **59**, 084006 (1999). DOI 10.1103/PhysRevD.59.084006
 156. Buonanno, A., Damour, T.: Transition from inspiral to plunge in binary black hole coalescences. *Phys. Rev. D* **62**, 064015 (2000). DOI 10.1103/PhysRevD.62.064015
 157. Buonanno, A., Iyer, B., Ochsner, E., Pan, Y., Sathyaprakash, B.S.: Comparison of post-Newtonian templates for compact binary inspiral signals in gravitational-wave detectors. *Phys. Rev. D* **80**, 084043 (2009). DOI 10.1103/PhysRevD.80.084043
 158. Buskulic, D.: Very low latency search pipeline for low mass compact binary coalescences in the LIGO S6 and Virgo VSR2 data. *Class. Quant. Grav.* **27**(19), 194013 (2010). DOI 10.1088/0264-9381/27/19/194013
 159. Buskulic, D., Flaminio, R., Marion, F., Massonnet, L., Morand, R., Mours, B., Verkindt, D., Yvert, M.: Estimation of the needed accuracy for the calibration of the VIRGO interferometer in relation to the detection of coalescing binaries. *Astropart. Phys.* **15**(4), 383–389 (2001). DOI 10.1016/S0927-6505(00)00168-7
 160. Cabero, M., Capano, C.D., Fischer-Birnholtz, O., Krishnan, B., Nielsen, A.B., Nitz, A.H., Biwer, C.M.: Observational tests of the black hole area increase law. *Phys. Rev. D* **97**(12), 124069 (2018). DOI 10.1103/PhysRevD.97.124069
 161. Cabero, M., et al.: Blip glitches in Advanced LIGO data. *Class. Quant. Grav.* **36**(15), 15 (2019). DOI 10.1088/1361-6382/ab2e14
 162. Calderón Bustillo, J., Husa, S., Sintés, A.M., Pürrer, M.: Impact of gravitational radiation higher order modes on single aligned-spin gravitational wave searches for binary black holes. *Phys. Rev. D* **93**(8), 084019 (2016). DOI 10.1103/PhysRevD.93.084019
 163. Callister, T.: A Thesaurus for Common Priors in Gravitational-Wave Astronomy (2021)
 164. Callister, T., Fishbach, M., Holz, D.E., Farr, W.M.: Shouts and Murmurs: Combining Individual Gravitational-wave Sources with the Stochastic Background to Measure the History of Binary Black Hole Mergers. *ApJ***896**(2), L32 (2020). DOI 10.3847/2041-8213/ab9743
 165. Callister, T.A., Farr, W.M.: A Parameter-Free Tour of the Binary Black Hole Population. *arXiv e-prints arXiv:2302.07289* (2023). DOI 10.48550/arXiv.2302.07289

166. Callister, T.A., Haster, C.J., Ng, K.K.Y., Vitale, S., Farr, W.M.: Who Ordered That? Unequal-mass Binary Black Hole Mergers Have Larger Effective Spins. *ApJ***922**(1), L5 (2021). DOI 10.3847/2041-8213/ac2ccc
167. Callister, T.A., Kanner, J.B., Massinger, T.J., Dhurandhar, S., Weinstein, A.J.: Observing Gravitational Waves with a Single Detector. *Class. Quant. Grav.* **34**(15), 155007 (2017). DOI 10.1088/1361-6382/aa7a76
168. Callister, T.A., Miller, S.J., Chatziioannou, K., Farr, W.M.: No Evidence that the Majority of Black Holes in Binaries Have Zero Spin. *ApJ***937**(1), L13 (2022). DOI 10.3847/2041-8213/ac847e
169. Campanelli, M., Lousto, C.O., Marronetti, P., Zlochower, Y.: Accurate evolutions of orbiting black-hole binaries without excision. *Phys. Rev. Lett.* **96**, 111101 (2006). DOI 10.1103/PhysRevLett.96.111101
170. Campanelli, M., Lousto, C.O., Zlochower, Y.: Spinning-black-hole binaries: The orbital hang up. *Phys. Rev. D* **74**, 041501 (2006). DOI 10.1103/PhysRevD.74.041501
171. Canizares, P., Field, S.E., Gair, J., Raymond, V., Smith, R., Tiglio, M.: Accelerated gravitational-wave parameter estimation with reduced order modeling. *Phys. Rev. Lett.* **114**(7), 071104 (2015). DOI 10.1103/PhysRevLett.114.071104
172. Canizares, P., Field, S.E., Gair, J.R., Tiglio, M.: Gravitational wave parameter estimation with compressed likelihood evaluations. *Phys. Rev. D* **87**(12), 124005 (2013). DOI 10.1103/PhysRevD.87.124005
173. Cannon, K., Chapman, A., Hanna, C., Keppel, D., Searle, A.C., Weinstein, A.J.: Singular value decomposition applied to compact binary coalescence gravitational-wave signals. *Phys. Rev. D* **82**, 044025 (2010). DOI 10.1103/PhysRevD.82.044025
174. Cannon, K., Hanna, C., Keppel, D.: Method to estimate the significance of coincident gravitational-wave observations from compact binary coalescence. *Phys. Rev. D* **88**(2), 024025 (2013). DOI 10.1103/PhysRevD.88.024025
175. Cannon, K., Hanna, C., Peoples, J.: Likelihood-Ratio Ranking Statistic for Compact Binary Coalescence Candidates with Rate Estimation (2015)
176. Cannon, K., et al.: Toward Early-Warning Detection of Gravitational Waves from Compact Binary Coalescence. *Astrophys. J.* **748**, 136 (2012). DOI 10.1088/0004-637X/748/2/136
177. Capano, C., Dent, T., Hanna, C., Hendry, M., Hu, Y.M., Messenger, C., Veitch, J.: Systematic errors in estimation of gravitational-wave candidate significance. *Phys. Rev. D* **96**(8), 082002 (2017). DOI 10.1103/PhysRevD.96.082002
178. Capano, C., Harry, I., Privitera, S., Buonanno, A.: Implementing a search for gravitational waves from binary black holes with nonprecessing spin. *Phys. Rev. D* **93**(12), 124007 (2016). DOI 10.1103/PhysRevD.93.124007
179. Capano, C., Pan, Y., Buonanno, A.: Impact of higher harmonics in searching for gravitational waves from nonspinning binary black holes. *Phys. Rev. D* **89**(10), 102003 (2014). DOI 10.1103/PhysRevD.89.102003
180. Cardoso, V., Gualtieri, L., Herdeiro, C., Sperhake, U.: Exploring New Physics Frontiers Through Numerical Relativity. *Living Rev. Relativity* **18**, 1 (2015). DOI 10.1007/lrr-2015-1
181. Carney, M.F., Wade, L.E., Irwin, B.S.: Comparing two models for measuring the neutron star equation of state from gravitational-wave signals. *Phys. Rev. D* **98**(6), 063004 (2018). DOI 10.1103/PhysRevD.98.063004
182. Carr, B., Kühnel, F.: Primordial Black Holes as Dark Matter: Recent Developments. *Annual Review of Nuclear and Particle Science* **70**, 355–394 (2020). DOI 10.1146/annurev-nucl-050520-125911
183. Carroll, S.: *Spacetime and Geometry*. Cambridge University Press (2019)
184. Carullo, G., Del Pozzo, W., Veitch, J.: Observational Black Hole Spectroscopy: A time-domain multimode analysis of GW150914. *Phys. Rev. D* **99**(12), 123029 (2019). DOI 10.1103/PhysRevD.99.123029. [Erratum: *Phys. Rev. D* **100**, 089903 (2019)]
185. Chandra, K., Calderón Bustillo, J., Pai, A., Harry, I.: First gravitational-wave search for intermediate-mass black hole mergers with higher order harmonics (2022)
186. Chandra, K., Villa-Ortega, V., Dent, T., McIsaac, C., Pai, A., Harry, I.W., Davies, G.S.C., Soni, K.: An optimized PyCBC search for gravitational waves from intermediate-mass black hole mergers. *Phys. Rev. D* **104**, 042004 (2021). DOI 10.1103/PhysRevD.104.042004

187. Chaturantabut, S., Sorensen, D.C.: Nonlinear model reduction via discrete empirical interpolation. *SIAM Journal on Scientific Computing* **32**(5), 2737–2764 (2010)
188. Chatziioannou, K.: Neutron star tidal deformability and equation of state constraints. *Gen. Rel. Grav.* **52**(11), 109 (2020). DOI 10.1007/s10714-020-02754-3
189. Chatziioannou, K., Cornish, N., Wijngaarden, M., Littenberg, T.B.: Modeling compact binary signals and instrumental glitches in gravitational wave data. *Phys. Rev. D* **103**(4), 044013 (2021). DOI 10.1103/PhysRevD.103.044013
190. Chatziioannou, K., Haster, C.J., Littenberg, T.B., Farr, W.M., Ghonge, S., Millhouse, M., Clark, J.A., Cornish, N.: Noise spectral estimation methods and their impact on gravitational wave measurement of compact binary mergers. *Phys. Rev. D* **100**(10), 104004 (2019). DOI 10.1103/PhysRevD.100.104004
191. Chatziioannou, K., Klein, A., Cornish, N., Yunes, N.: Analytic Gravitational Waveforms for Generic Precessing Binary Inspirals. *Phys. Rev. Lett.* **118**(5), 051101 (2017). DOI 10.1103/PhysRevLett.118.051101
192. Chatziioannou, K., Klein, A., Yunes, N., Cornish, N.: Constructing Gravitational Waves from Generic Spin-Precessing Compact Binary Inspirals. *Phys. Rev. D* **95**(10), 104004 (2017). DOI 10.1103/PhysRevD.95.104004
193. Chatziioannou, K., Lovelace, G., Boyle, M., Giesler, M., Hemberger, D.A., Katebi, R., Kidder, L.E., Pfeiffer, H.P., Scheel, M.A., Szilágyi, B.: Measuring the properties of nearly extremal black holes with gravitational waves. *Phys. Rev. D* **98**(4), 044028 (2018). DOI 10.1103/PhysRevD.98.044028
194. Chatziioannou, K., Yunes, N., Cornish, N.: Model-Independent Test of General Relativity: An Extended post-Einsteinian Framework with Complete Polarization Content. *Phys. Rev. D* **86**, 022004 (2012). DOI 10.1103/PhysRevD.86.022004. [Erratum: *Phys.Rev.D* 95, 129901 (2017)]
195. Chen, H.Y., Holz, D.E., Miller, J., Evans, M., Vitale, S., Creighton, J.: Distance measures in gravitational-wave astrophysics and cosmology. *Class. Quant. Grav.* **38**(5), 055010 (2021). DOI 10.1088/1361-6382/abd594
196. Cheng, A.Q., Zevin, M., Vitale, S.: What You Don't Know Can Hurt You: Use and Abuse of Astrophysical Models in Gravitational-wave Population Analyses. *ApJ* **955**(2), 127 (2023). DOI 10.3847/1538-4357/aced98
197. Chia, H.S.: Tidal deformation and dissipation of rotating black holes. *Phys. Rev. D* **104**(2), 024013 (2021). DOI 10.1103/PhysRevD.104.024013
198. Chia, H.S., Edwards, T.D.P.: Searching for General Binary Inspirals with Gravitational Waves. *JCAP* **11**, 033 (2020). DOI 10.1088/1475-7516/2020/11/033
199. Chu, Q., et al.: SPIIR online coherent pipeline to search for gravitational waves from compact binary coalescences. *Phys. Rev. D* **105**(2), 024023 (2022). DOI 10.1103/PhysRevD.105.024023
200. Cokelaer, T.: Gravitational waves from inspiralling compact binaries: Hexagonal template placement and its efficiency in detecting physical signals. *Phys. Rev. D* **76**, 102004 (2007). DOI 10.1103/PhysRevD.76.102004
201. Congedo, G., Taylor, A.: Joint cosmological inference of standard sirens and gravitational wave weak lensing. *Phys. Rev. D* **99**(8), 083526 (2019). DOI 10.1103/PhysRevD.99.083526
202. Coogan, A., Edwards, T.D.P., Chia, H.S., George, R.N., Freese, K., Messick, C., Setzer, C.N., Weniger, C., Zimmerman, A.: Efficient gravitational wave template bank generation with differentiable waveforms. *Phys. Rev. D* **106**(12), 122001 (2022). DOI 10.1103/PhysRevD.106.122001
203. Cornish, N., Sampson, L., Yunes, N., Pretorius, F.: Gravitational Wave Tests of General Relativity with the Parameterized Post-Einsteinian Framework. *Phys. Rev. D* **84**, 062003 (2011). DOI 10.1103/PhysRevD.84.062003
204. Cornish, N.J.: Fast Fisher Matrices and Lazy Likelihoods (2010)
205. Cornish, N.J.: Heterodyned likelihood for rapid gravitational wave parameter inference. *Phys. Rev. D* **104**(10), 104054 (2021). DOI 10.1103/PhysRevD.104.104054
206. Cornish, N.J., Littenberg, T.B.: BayesWave: Bayesian Inference for Gravitational Wave Bursts and Instrument Glitches. *Class. Quant. Grav.* **32**(13), 135012 (2015). DOI 10.1088/0264-9381/32/13/135012

207. Cotesta, R., Buonanno, A., Bohé, A., Taracchini, A., Hinder, I., Ossokine, S.: Enriching the Symphony of Gravitational Waves from Binary Black Holes by Tuning Higher Harmonics. *Phys. Rev. D* **98**(8), 084028 (2018). DOI 10.1103/PhysRevD.98.084028
208. Cotesta, R., Marsat, S., Pürrer, M.: Frequency domain reduced order model of aligned-spin effective-one-body waveforms with higher-order modes. *Phys. Rev. D* **101**(12), 124040 (2020). DOI 10.1103/PhysRevD.101.124040
209. Coughlin, M.W., Dietrich, T., Margalit, B., Metzger, B.D.: Multimessenger Bayesian parameter inference of a binary neutron star merger. *Mon. Not. Roy. Astron. Soc.* **489**(1), L91–L96 (2019). DOI 10.1093/mnras/slz133
210. Coughlin, M.W., et al.: Constraints on the neutron star equation of state from AT2017gfo using radiative transfer simulations. *Mon. Not. Roy. Astron. Soc.* **480**(3), 3871–3878 (2018). DOI 10.1093/mnras/sty2174
211. Cranmer, K., Brehmer, J., Louppe, G.: The frontier of simulation-based inference. *Proceedings of the National Academy of Science* **117**(48), 30055–30062 (2020). DOI 10.1073/pnas.1912789117
212. Cromartie, H.T., et al.: Relativistic Shapiro delay measurements of an extremely massive millisecond pulsar. *Nature Astron.* **4**(1), 72–76 (2019). DOI 10.1038/s41550-019-0880-2
213. Cuoco, E., et al.: Enhancing Gravitational-Wave Science with Machine Learning. *Mach. Learn. Sci. Tech.* **2**(1), 011002 (2021). DOI 10.1088/2632-2153/abb93a
214. Cutler, C., Flanagan, E.E.: Gravitational waves from merging compact binaries: How accurately can one extract the binary’s parameters from the inspiral wave form? *Phys. Rev. D* **49**, 2658–2697 (1994). DOI 10.1103/PhysRevD.49.2658
215. Cutler, C., Schutz, B.F.: The Generalized F-statistic: Multiple detectors and multiple GW pulsars. *Phys. Rev. D* **72**, 063006 (2005). DOI 10.1103/PhysRevD.72.063006
216. Cutler, C., et al.: The Last three minutes: issues in gravitational wave measurements of coalescing compact binaries. *Phys. Rev. Lett.* **70**, 2984–2987 (1993). DOI 10.1103/PhysRevLett.70.2984
217. Dal Canton, T.: Efficient searches for spinning compact binaries with advanced gravitational-wave observatories. Ph.D. thesis, Leibniz U., Hannover (2015). DOI 10.15488/8427
218. Dal Canton, T., Harry, I.W.: Designing a template bank to observe compact binary coalescences in Advanced LIGO’s second observing run (2017)
219. Dal Canton, T., Nitz, A.H., Gadre, B., Cabourn Davies, G.S., Villa-Ortega, V., Dent, T., Harry, I., Xiao, L.: Real-time Search for Compact Binary Mergers in Advanced LIGO and Virgo’s Third Observing Run Using PyCBC Live. *Astrophys. J.* **923**(2), 254 (2021). DOI 10.3847/1538-4357/ac2f9a
220. Dal Canton, T., et al.: Implementing a search for aligned-spin neutron star-black hole systems with advanced ground based gravitational wave detectors. *Phys. Rev. D* **90**(8), 082004 (2014). DOI 10.1103/PhysRevD.90.082004
221. Damlen, P., Wakefield, J., Walker, S.: Gibbs Sampling for Bayesian Non-Conjugate and Hierarchical Models by Using Auxiliary Variables. *Journal of the Royal Statistical Society Series B: Statistical Methodology* **61**(2), 331–344 (2002). DOI 10.1111/1467-9868.00179. URL <https://doi.org/10.1111/1467-9868.00179>
222. Damour, T., Deruelle, N.: Radiation Reaction and Angular Momentum Loss in Small Angle Gravitational Scattering. *Phys. Lett.* **A87**, 81 (1981). DOI 10.1016/0375-9601(81)90567-3
223. Damour, T., Iyer, B.R., Sathyaprakash, B.S.: A Comparison of search templates for gravitational waves from binary inspiral. *Phys. Rev. D* **63**, 044023 (2001). DOI 10.1103/PhysRevD.63.044023. [Erratum: *Phys. Rev. D* **72**, 029902 (2005)]
224. Damour, T., Iyer, B.R., Sathyaprakash, B.S.: A Comparison of search templates for gravitational waves from binary inspiral - 3.5PN update. *Phys. Rev. D* **66**, 027502 (2002). DOI 10.1103/PhysRevD.66.027502
225. Damour, T., Nagar, A., Villain, L.: Measurability of the tidal polarizability of neutron stars in late-inspiral gravitational-wave signals. *Phys. Rev. D* **85**, 123007 (2012). DOI 10.1103/PhysRevD.85.123007
226. Davies, G.S.C., Harry, I.W.: Establishing significance of gravitational-wave signals from a single observatory in the PyCBC offline search. *Class. Quant. Grav.* **39**(21), 215012 (2022). DOI 10.1088/1361-6382/ac8862

227. Davis, D., Littenberg, T.B., Romero-Shaw, I.M., Millhouse, M., McIver, J., Di Renzo, F., Ashton, G.: Subtracting glitches from gravitational-wave detector data during the third LIGO-Virgo observing run. *Class. Quant. Grav.* **39**(24), 245013 (2022). DOI 10.1088/1361-6382/aca238
228. Davis, D., et al.: LIGO detector characterization in the second and third observing runs. *Class. Quant. Grav.* **38**(13), 135014 (2021). DOI 10.1088/1361-6382/abfd85
229. Dax, M., Green, S.R., Gair, J., Macke, J.H., Buonanno, A., Schölkopf, B.: Real-Time Gravitational Wave Science with Neural Posterior Estimation. *Phys. Rev. Lett.* **127**(24), 241103 (2021). DOI 10.1103/PhysRevLett.127.241103
230. Delfavero, V., O’Shaughnessy, R., Wysocki, D., Yelikar, A.: Compressed Parametric and Non-Parametric Approximations to the Gravitational Wave Likelihood. arXiv e-prints arXiv:2205.14154 (2022). DOI 10.48550/arXiv.2205.14154
231. D’Emilio, V., Green, R., Raymond, V.: Density estimation with Gaussian processes for gravitational wave posteriors. *MNRAS* **508**(2), 2090–2097 (2021). DOI 10.1093/mnras/stab2623
232. Dent, T., Veitch, J.: Optimizing gravitational-wave searches for a population of coalescing binaries: Intrinsic parameters. *Phys. Rev. D* **89**(6), 062002 (2014). DOI 10.1103/PhysRevD.89.062002
233. Devine, C., Etienne, Z.B., McWilliams, S.T.: Optimizing spinning time-domain gravitational waveforms for Advanced LIGO data analysis. *Class. Quant. Grav.* **33**(12), 125025 (2016). DOI 10.1088/0264-9381/33/12/125025
234. Dexheimer, V., Gomes, R.O., Klähn, T., Han, S., Salinas, M.: GW190814 as a massive rapidly rotating neutron star with exotic degrees of freedom. *Phys. Rev. C* **103**(2), 025808 (2021). DOI 10.1103/PhysRevC.103.025808
235. Dhurandhar, S., Gupta, A., Gadre, B., Bose, S.: A unified approach to χ^2 discriminators for searches of gravitational waves from compact binary coalescences. *Phys. Rev. D* **96**(10), 103018 (2017). DOI 10.1103/PhysRevD.96.103018
236. Dhurandhar, S., Krishnan, B., Willis, J.L.: Marginalizing the likelihood function for modeled gravitational wave searches (2017)
237. Dhurkunde, R., Fehrmann, H., Nitz, A.H.: Hierarchical approach to matched filtering using a reduced basis. *Phys. Rev. D* **105**(10), 103001 (2022). DOI 10.1103/PhysRevD.105.103001
238. Dhurkunde, R., Nitz, A.H.: Search for eccentric NSBH and BNS mergers in the third observing run of Advanced LIGO and Virgo (2023)
239. Dickey, J.M., Lientz, B.P.: The Weighted Likelihood Ratio, Sharp Hypotheses about Chances, the Order of a Markov Chain. *The Annals of Mathematical Statistics* **41**(1), 214 – 226 (1970). DOI 10.1214/aoms/1177697203. URL <https://doi.org/10.1214/aoms/1177697203>
240. Dietrich, T., Bernuzzi, S., Tichy, W.: Closed-form tidal approximants for binary neutron star gravitational waveforms constructed from high-resolution numerical relativity simulations. *Phys. Rev. D* **96**(12), 121501 (2017). DOI 10.1103/PhysRevD.96.121501
241. Dietrich, T., Coughlin, M.W., Pang, P.T.H., Bulla, M., Heinzl, J., Issa, L., Tews, I., Antier, S.: Multimessenger constraints on the neutron-star equation of state and the Hubble constant. *Science* **370**(6523), 1450–1453 (2020). DOI 10.1126/science.abb4317
242. Dietrich, T., Hinderer, T., Samajdar, A.: Interpreting Binary Neutron Star Mergers: Describing the Binary Neutron Star Dynamics, Modelling Gravitational Waveforms, and Analyzing Detections. *Gen. Rel. Grav.* **53**(3), 27 (2021). DOI 10.1007/s10714-020-02751-6
243. Dietrich, T., Samajdar, A., Khan, S., Johnson-McDaniel, N.K., Dudi, R., Tichy, W.: Improving the NRTidal model for binary neutron star systems. *Phys. Rev. D* **100**(4), 044003 (2019). DOI 10.1103/PhysRevD.100.044003
244. Divyajyoti, Kumar, S., Tibrewal, S., Romero-Shaw, I.M., Mishra, C.K.: Blind spots and biases: The dangers of ignoring eccentricity in gravitational-wave signals from binary black holes. *Phys. Rev. D* **109**(4), 043037 (2024). DOI 10.1103/PhysRevD.109.043037
245. Doctor, Z., Farr, B., Holz, D.E., Pürrer, M.: Statistical Gravitational Waveform Models: What to Simulate Next? *Phys. Rev. D* **96**(12), 123011 (2017). DOI 10.1103/PhysRevD.96.123011

246. Drischler, C., Furnstahl, R.J., Melendez, J.A., Phillips, D.R.: How Well Do We Know the Neutron-Matter Equation of State at the Densities Inside Neutron Stars? A Bayesian Approach with Correlated Uncertainties. *Phys. Rev. Lett.* **125**(20), 202702 (2020). DOI 10.1103/PhysRevLett.125.202702
247. Drischler, C., Melendez, J.A., Furnstahl, R.J., Phillips, D.R.: Quantifying uncertainties and correlations in the nuclear-matter equation of state. *Phys. Rev. C* **102**(5), 054315 (2020). DOI 10.1103/PhysRevC.102.054315
248. Droz, S., Knapp, D.J., Poisson, E., Owen, B.J.: Gravitational waves from inspiraling compact binaries: Validity of the stationary phase approximation to the Fourier transform. *Phys. Rev. D* **59**, 124016 (1999). DOI 10.1103/PhysRevD.59.124016
249. Duane, S., Kennedy, A.D., Pendleton, B.J., Roweth, D.: Hybrid Monte Carlo. *Physics Letters B* **195**(2), 216–222 (1987). DOI 10.1016/0370-2693(87)91197-X
250. Dyson, F.J.: Gravitational machines. <https://www.gravityresearchfoundation.org/name#D> (1962). Reprinted in “Interstellar Communication” ed. A.G.W. Cameron, (New York: Benjamin)
251. Earl, D.J., Deem, M.W.: Parallel tempering: Theory, applications, and new perspectives. *Phys. Chem. Chem. Phys.* **7**, 3910–3916 (2005). DOI 10.1039/B509983H. URL <http://dx.doi.org/10.1039/B509983H>
252. Eddington, A.S.: The propagation of gravitational waves. *Proc. Roy. Soc. Lond. A* **102**, 268–282 (1922). DOI 10.1098/rspa.1922.0085
253. Edelman, B., Doctor, Z., Farr, B.: Poking Holes: Looking for Gaps in LIGO/Virgo’s Black Hole Population. *ApJ***913**(2), L23 (2021). DOI 10.3847/2041-8213/abfdb3
254. Edelman, B., Doctor, Z., Godfrey, J., Farr, B.: Ain’t No Mountain High Enough: Semiparametric Modeling of LIGO-Virgo’s Binary Black Hole Mass Distribution. *ApJ***924**(2), 101 (2022). DOI 10.3847/1538-4357/ac3667
255. Edelman, B., Farr, B., Doctor, Z.: Cover Your Basis: Comprehensive Data-driven Characterization of the Binary Black Hole Population. *ApJ***946**(1), 16 (2023). DOI 10.3847/1538-4357/acb5ed
256. Einstein, A.: Über Gravitationswellen. *Sitzungsber. Preuss. Akad. Wiss. Berlin (Math. Phys.)* **1918**, 154–167 (1918)
257. Einstein, A., Infeld, L., Hoffmann, B.: The Gravitational equations and the problem of motion. *Annals Math.* **39**, 65–100 (1938). DOI 10.2307/1968714
258. Essick, R., Farah, A., Galadage, S., Talbot, C., Fishbach, M., Thrane, E., Holz, D.E.: Probing Extremal Gravitational-wave Events with Coarse-grained Likelihoods. *ApJ***926**(1), 34 (2022). DOI 10.3847/1538-4357/ac3978
259. Essick, R., Farr, W.: Precision Requirements for Monte Carlo Sums within Hierarchical Bayesian Inference. *arXiv e-prints arXiv:2204.00461* (2022). DOI 10.48550/arXiv.2204.00461
260. Essick, R., Farr, W.M., Fishbach, M., Holz, D.E., Katsavounidis, E.: (An)isotropy measurement with gravitational wave observations. *Phys. Rev. D***107**(4), 043016 (2023). DOI 10.1103/PhysRevD.107.043016
261. Essick, R., Fishbach, M.: On reweighing single-event posteriors with population priors. <https://dcc.ligo.org/LIGO-T1900895/public> (2021)
262. Essick, R., Fishbach, M.: DAGnabbit! Ensuring Consistency between Noise and Detection in Hierarchical Bayesian Inference. *arXiv e-prints arXiv:2310.02017* (2023). DOI 10.48550/arXiv.2310.02017
263. Essick, R., Landry, P.: Discriminating between Neutron Stars and Black Holes with Imperfect Knowledge of the Maximum Neutron Star Mass. *Astrophys. J.* **904**(1), 80 (2020). DOI 10.3847/1538-4357/abbd3b
264. Essick, R., Landry, P., Holz, D.E.: Nonparametric inference of neutron star composition, equation of state, and maximum mass with GW170817. *Phys. Rev. D* **101**(6), 063007 (2020). DOI 10.1103/PhysRevD.101.063007
265. Essick, R., Landry, P., Schwenk, A., Tews, I.: A Detailed Examination of Astrophysical Constraints on the Symmetry Energy and the Neutron Skin of ^{208}Pb with Minimal Modeling Assumptions (2021)
266. Essick, R., Legred, I., Chatziioannou, K., Han, S., Landry, P.: Phase Transition Phenomenology with Nonparametric Representations of the Neutron Star Equation of State (2023)

267. Essick, R., Tews, I., Landry, P., Reddy, S., Holz, D.E.: Direct Astrophysical Tests of Chiral Effective Field Theory at Supranuclear Densities. *Phys. Rev. C* **102**(5), 055803 (2020). DOI 10.1103/PhysRevC.102.055803
268. Estellés, H., Colleoni, M., García-Quirós, C., Husa, S., Keitel, D., Mateu-Lucena, M., Planas, M.d.L., Ramos-Buades, A.: New twists in compact binary waveform modeling: A fast time-domain model for precession. *Phys. Rev. D* **105**(8), 084040 (2022). DOI 10.1103/PhysRevD.105.084040
269. Estellés, H., Husa, S., Colleoni, M., Keitel, D., Mateu-Lucena, M., García-Quirós, C., Ramos-Buades, A., Borchers, A.: Time-domain phenomenological model of gravitational-wave subdominant harmonics for quasicircular nonprecessing binary black hole coalescences. *Phys. Rev. D* **105**(8), 084039 (2022). DOI 10.1103/PhysRevD.105.084039
270. Estellés, H., Ramos-Buades, A., Husa, S., García-Quirós, C., Colleoni, M., Haegel, L., Jaume, R.: Phenomenological time domain model for dominant quadrupole gravitational wave signal of coalescing binary black holes. *Phys. Rev. D* **103**(12), 124060 (2021). DOI 10.1103/PhysRevD.103.124060
271. Evans, M., Corsi, A., Afle, C., et al.: Cosmic explorer: A submission to the nsf mpsac nggw subcommittee (2023)
272. Ezquiaga, J.M., Holz, D.E.: Spectral Sirens: Cosmology from the Full Mass Distribution of Compact Binaries. *Phys. Rev. Lett.* **129**(6), 061102 (2022). DOI 10.1103/PhysRevLett.129.061102
273. Faber, J.A., Rasio, F.A.: Binary Neutron Star Mergers. *Living Rev. Rel.* **15**, 8 (2012). DOI 10.12942/lrr-2012-8
274. Fairhurst, S.: Source localization with an advanced gravitational wave detector network. *Class. Quant. Grav.* **28**, 105021 (2011). DOI 10.1088/0264-9381/28/10/105021
275. Fairhurst, S., Brady, P.: Interpreting the results of searches for gravitational waves from coalescing binaries. *Class. Quant. Grav.* **25**, 105002 (2008). DOI 10.1088/0264-9381/25/10/105002
276. Fairhurst, S., Green, R., Hoy, C., Hannam, M., Muir, A.: Two-harmonic approximation for gravitational waveforms from precessing binaries. *Phys. Rev. D* **102**(2), 024055 (2020). DOI 10.1103/PhysRevD.102.024055
277. Farah, A., Fishbach, M., Essick, R., Holz, D.E., Galaudage, S.: Bridging the Gap: Categorizing Gravitational-wave Events at the Transition between Neutron Stars and Black Holes. *ApJ* **931**(2), 108 (2022). DOI 10.3847/1538-4357/ac5f03
278. Farah, A.M., Callister, T.A., María Ezquiaga, J., Zevin, M., Holz, D.E.: No need to know: astrophysics-free gravitational-wave cosmology. *arXiv e-prints arXiv:2404.02210* (2024). DOI 10.48550/arXiv.2404.02210
279. Farah, A.M., Edelman, B., Zevin, M., Fishbach, M., María Ezquiaga, J., Farr, B., Holz, D.E.: Things That Might Go Bump in the Night: Assessing Structure in the Binary Black Hole Mass Spectrum. *ApJ* **955**(2), 107 (2023). DOI 10.3847/1538-4357/aced02
280. Farah, A.M., Fishbach, M., Holz, D.E.: Two of a Kind: Comparing big and small black holes in binaries with gravitational waves. *arXiv e-prints arXiv:2308.05102* (2023). DOI 10.48550/arXiv.2308.05102
281. Farr, B., Holz, D.E., Farr, W.M.: Using Spin to Understand the Formation of LIGO and Virgo's Black Holes. *ApJ* **854**(1), L9 (2018). DOI 10.3847/2041-8213/aaa64
282. Farr, B., Kalogera, V., Lijten, E.: A more efficient approach to parallel-tempered markov-chain monte carlo for the highly structured posteriors of gravitational-wave signals. *Phys. Rev. D* **90**, 024014 (2014). DOI 10.1103/PhysRevD.90.024014. URL <https://link.aps.org/doi/10.1103/PhysRevD.90.024014>
283. Farr, B., Ochsner, E., Farr, W.M., O'Shaughnessy, R.: A more effective coordinate system for parameter estimation of precessing compact binaries from gravitational waves. *Phys. Rev. D* **90**(2), 024018 (2014). DOI 10.1103/PhysRevD.90.024018
284. Farr, W.M.: Accuracy Requirements for Empirically-Measured Selection Functions. *Research Notes of the AAS* **3**(5), 66 (2019). DOI 10.3847/2515-5172/ab1d5f
285. Farr, W.M., Fishbach, M., Ye, J., Holz, D.E.: A Future Percent-level Measurement of the Hubble Expansion at Redshift 0.8 with Advanced LIGO. *ApJ* **883**(2), L42 (2019). DOI 10.3847/2041-8213/ab4284

286. Farr, W.M., Gair, J.R., Mandel, I., Cutler, C.: Counting And Confusion: Bayesian Rate Estimation With Multiple Populations. *Phys. Rev. D* **91**(2), 023005 (2015). DOI 10.1103/PhysRevD.91.023005
287. Farr, W.M., Kremer, K., Lyutikov, M., Kalogera, V.: Spin Tilts in the Double Pulsar Reveal Supernova Spin Angular-momentum Production. *ApJ***742**(2), 81 (2011). DOI 10.1088/0004-637X/742/2/81
288. Farr, W.M., Mandel, I., Aldridge, C., Stroud, K.: The Occurrence of Earth-Like Planets Around Other Stars. arXiv e-prints arXiv:1412.4849 (2014). DOI 10.48550/arXiv.1412.4849
289. Farr, W.M., Stevenson, S., Miller, M.C., Mandel, I., Farr, B., Vecchio, A.: Distinguishing spin-aligned and isotropic black hole populations with gravitational waves. *Nature***548**(7667), 426–429 (2017). DOI 10.1038/nature23453
290. Fattoyev, F.J., Horowitz, C.J., Piekarewicz, J., Reed, B.: GW190814: Impact of a 2.6 solar mass neutron star on the nucleonic equations of state. *Phys. Rev. C* **102**(6), 065805 (2020). DOI 10.1103/PhysRevC.102.065805
291. Favata, M.: Systematic parameter errors in inspiraling neutron star binaries. *Phys. Rev. Lett.* **112**, 101101 (2014). DOI 10.1103/PhysRevLett.112.101101
292. Feroz, F., Hobson, M.P., Bridges, M.: MultiNest: an efficient and robust Bayesian inference tool for cosmology and particle physics. *Mon. Not. Roy. Astron. Soc.* **398**, 1601–1614 (2009). DOI 10.1111/j.1365-2966.2009.14548.x
293. Field, S.E., Galley, C.R., Hesthaven, J.S., Kaye, J., Tiglio, M.: Fast prediction and evaluation of gravitational waveforms using surrogate models. *Phys. Rev. X* **4**(3), 031006 (2014). DOI 10.1103/PhysRevX.4.031006
294. Finch, E., Moore, C.J.: Frequency-domain analysis of black-hole ringdowns. *Phys. Rev. D* **104**(12), 123034 (2021). DOI 10.1103/PhysRevD.104.123034
295. Finn, L.S.: Detection, measurement and gravitational radiation. *Phys. Rev. D* **46**, 5236–5249 (1992). DOI 10.1103/PhysRevD.46.5236
296. Finn, L.S., Chernoff, D.F.: Observing binary inspiral in gravitational radiation: One interferometer. *Phys. Rev. D* **47**, 2198–2219 (1993). DOI 10.1103/PhysRevD.47.2198
297. Fishbach, M., Doctor, Z., Callister, T., Edelman, B., Ye, J., Essick, R., Farr, W.M., Farr, B., Holz, D.E.: When Are LIGO/Virgo’s Big Black Hole Mergers? *ApJ***912**(2), 98 (2021). DOI 10.3847/1538-4357/abee11
298. Fishbach, M., Essick, R., Holz, D.E.: Does Matter Matter? Using the Mass Distribution to Distinguish Neutron Stars and Black Holes. *ApJ***899**(1), L8 (2020). DOI 10.3847/2041-8213/aba7b6
299. Fishbach, M., Farr, W.M., Holz, D.E.: The Most Massive Binary Black Hole Detections and the Identification of Population Outliers. *ApJ***891**(2), L31 (2020). DOI 10.3847/2041-8213/ab77c9
300. Fishbach, M., Fragione, G.: Globular cluster formation histories, masses, and radii inferred from gravitational waves. *MNRAS***522**(4), 5546–5557 (2023). DOI 10.1093/mnras/stad1364
301. Fishbach, M., Holz, D.E.: Where Are LIGO’s Big Black Holes? *ApJ***851**(2), L25 (2017). DOI 10.3847/2041-8213/aa9bf6
302. Fishbach, M., Holz, D.E.: Picky Partners: The Pairing of Component Masses in Binary Black Hole Mergers. *ApJ***891**(1), L27 (2020). DOI 10.3847/2041-8213/ab7247
303. Fishbach, M., Holz, D.E., Farr, W.M.: Does the Black Hole Merger Rate Evolve with Redshift? *Astrophys. J. Lett.* **863**(2), L41 (2018). DOI 10.3847/2041-8213/aad800
304. Fishbach, M., Kalogera, V.: Apples and Oranges: Comparing Black Holes in X-Ray Binaries and Gravitational-wave Sources. *ApJ***929**(2), L26 (2022). DOI 10.3847/2041-8213/ac64a5
305. Fishbach, M., Kimball, C., Kalogera, V.: Limits on Hierarchical Black Hole Mergers from the Most Negative χ_{eff} Systems. *ApJ***935**(2), L26 (2022). DOI 10.3847/2041-8213/ac86c4
306. Fishbach, M., van Son, L.: LIGO-Virgo-KAGRA’s Oldest Black Holes: Probing Star Formation at Cosmic Noon With GWTC-3. *ApJ***957**(2), L31 (2023). DOI 10.3847/2041-8213/ad0560
307. Flanagan, E.E., Hinderer, T.: Constraining neutron star tidal Love numbers with gravitational wave detectors. *Phys. Rev. D* **77**, 021502 (2008). DOI 10.1103/PhysRevD.77.021502

308. Flanagan, E.E., Hughes, S.A.: Measuring gravitational waves from binary black hole coalescences: 1. Signal-to-noise for inspiral, merger, and ringdown. *Phys. Rev. D* **57**, 4535–4565 (1998). DOI 10.1103/PhysRevD.57.4535
309. Fong, H.K.Y.: From simulations to signals: Analyzing gravitational waves from compact binary coalescences. Ph.D. thesis, Toronto U. (2018)
310. Fonseca, E., et al.: Refined Mass and Geometric Measurements of the High-mass PSR J0740+6620. *Astrophys. J. Lett.* **915**(1), L12 (2021). DOI 10.3847/2041-8213/ac03b8
311. Foreman-Mackey, D., Hogg, D.W., Lang, D., Goodman, J.: emcee: the mcmc hammer. *Publications of the Astronomical Society of the Pacific* **125**(925), 306 (2013)
312. Forward, R.L., Berman, D.: Gravitational-radiation detection range for binary stellar systems. *Phys. Rev. Lett.* **18**, 1071–1074 (1967). DOI 10.1103/PhysRevLett.18.1071. URL <https://link.aps.org/doi/10.1103/PhysRevLett.18.1071>
313. Fotopoulos, N.V.: Searching for stochastic gravitational-wave background with the co-located LIGO interferometers. *J. Phys. Conf. Ser.* **122**, 012032 (2008). DOI 10.1088/1742-6596/122/1/012032
314. Franciolini, G., Pani, P.: Searching for mass-spin correlations in the population of gravitational-wave events: The GWTC-3 case study. *Phys. Rev. D* **105**(12), 123024 (2022). DOI 10.1103/PhysRevD.105.123024
315. Freedman, G.E., Johnson, A.D., van Haasteren, R., Vigeland, S.J.: Efficient gravitational wave searches with pulsar timing arrays using hamiltonian monte carlo. *Phys. Rev. D* **107**, 043013 (2023). DOI 10.1103/PhysRevD.107.043013. URL <https://link.aps.org/doi/10.1103/PhysRevD.107.043013>
316. Freise, A., Chelkowski, S., Hild, S., Del Pozzo, W., Perreca, A., Vecchio, A.: Triple Michelson Interferometer for a Third-Generation Gravitational Wave Detector. *Class. Quant. Grav.* **26**, 085012 (2009). DOI 10.1088/0264-9381/26/8/085012
317. Freise, A., Strain, K.: Interferometer Techniques for Gravitational-Wave Detection. *Living Rev. Rel.* **13**, 1 (2010). DOI 10.12942/lrr-2010-1
318. Fuller, J., Ma, L.: Most Black Holes Are Born Very Slowly Rotating. *ApJ* **881**(1), L1 (2019). DOI 10.3847/2041-8213/ab339b
319. Futamase, T., Itoh, Y.: The post-Newtonian approximation for relativistic compact binaries. *Living Rev. Rel.* **10**, 2 (2007). DOI 10.12942/lrr-2007-2
320. Gabbard, H., Messenger, C., Heng, I.S., Tonolini, F., Murray-Smith, R.: Bayesian parameter estimation using conditional variational autoencoders for gravitational-wave astronomy. *Nature Phys.* **18**(1), 112–117 (2022). DOI 10.1038/s41567-021-01425-7
321. Gabbard, H., Williams, M., Hayes, F., Messenger, C.: Matching matched filtering with deep networks for gravitational-wave astronomy. *Phys. Rev. Lett.* **120**(14), 141103 (2018). DOI 10.1103/PhysRevLett.120.141103
322. Gadre, B., Mitra, S., Dhurandhar, S.: Hierarchical search strategy for the efficient detection of gravitational waves from nonprecessing coalescing compact binaries with aligned-spins. *Phys. Rev. D* **99**(12), 124035 (2019). DOI 10.1103/PhysRevD.99.124035
323. Gadre, B., Pürrer, M., Field, S.E., Ossokine, S., Varma, V.: A fully precessing higher-mode surrogate model of effective-one-body waveforms (2022)
324. Gadre, B., Soni, K., Tiwari, S., Ramos-Buades, A., Haney, M., Mitra, S.: Detectability of eccentric binary black holes with PyCBC and cWB pipelines during the third observing run of LIGO-Virgo-KAGRA (2024)
325. Galaudage, S., Talbot, C., Nagar, T., Jain, D., Thrane, E., Mandel, I.: Building Better Spin Models for Merging Binary Black Holes: Evidence for Nonspinning and Rapidly Spinning Nearly Aligned Subpopulations. *ApJ* **921**(1), L15 (2021). DOI 10.3847/2041-8213/ac2f3c
326. Galaudage, S., Talbot, C., Thrane, E.: Gravitational-wave inference in the catalog era: Evolving priors and marginal events. *Phys. Rev. D* **102**(8), 083026 (2020). DOI 10.1103/PhysRevD.102.083026
327. Gamba, R., Akçay, S., Bernuzzi, S., Williams, J.: Effective-one-body waveforms for precessing coalescing compact binaries with post-Newtonian twist. *Phys. Rev. D* **106**(2), 024020 (2022). DOI 10.1103/PhysRevD.106.024020
328. García-Quirós, C., Colleoni, M., Husa, S., Estellés, H., Pratten, G., Ramos-Buades, A., Mateu-Lucena, M., Jaume, R.: Multimode frequency-domain model for the gravitational wave signal from nonprecessing black-hole binaries. *Phys. Rev. D* **102**(6), 064002 (2020). DOI 10.1103/PhysRevD.102.064002

329. García-Quiros, C., Husa, S., Mateu-Lucena, M., Borchers, A.: Accelerating the evaluation of inspiral-merger-ringdown waveforms with adapted grids. *Class. Quant. Grav.* **38**(1), 015006 (2021). DOI 10.1088/1361-6382/abc36e
330. Gebhard, T.D., Kilbertus, N., Harry, I., Schölkopf, B.: Convolutional neural networks: a magic bullet for gravitational-wave detection? *Phys. Rev. D* **100**(6), 063015 (2019). DOI 10.1103/PhysRevD.100.063015
331. Gelfand, A.E., Smith, A.F.M.: Sampling-based approaches to calculating marginal densities. *Journal of the American Statistical Association* **85**(410), 398–409 (1990). DOI 10.1080/01621459.1990.10476213. URL <https://www.tandfonline.com/doi/abs/10.1080/01621459.1990.10476213>
332. Gelman, A., Carlin, J., Stern, H., Dunson, D., Vehtari, A., Rubin, D.: *Bayesian Data Analysis, Third Edition*. Chapman & Hall/CRC Texts in Statistical Science. Taylor & Francis (2013)
333. Geman, S., Geman, D.: Stochastic relaxation, gibbs distributions, and the bayesian restoration of images. *IEEE Transactions on Pattern Analysis and Machine Intelligence* **PAMI-6**(6), 721–741 (1984). DOI 10.1109/TPAMI.1984.4767596
334. George, D., Huerta, E.A.: Deep Neural Networks to Enable Real-time Multimessenger Astrophysics. *Phys. Rev. D* **97**(4), 044039 (2018). DOI 10.1103/PhysRevD.97.044039
335. Gerosa, D., Ma, S., Wong, K.W.K., Berti, E., O’Shaughnessy, R., Chen, Y., Belczynski, K.: Multiband gravitational-wave event rates and stellar physics. *Phys. Rev. D* **99**(10), 103004 (2019). DOI 10.1103/PhysRevD.99.103004
336. Gerosa, D., Mould, M., Gangardt, D., Schmidt, P., Pratten, G., Thomas, L.M.: A generalized precession parameter χ_p to interpret gravitational-wave data. *Phys. Rev. D* **103**(6), 064067 (2021). DOI 10.1103/PhysRevD.103.064067
337. Gerosa, D., O’Shaughnessy, R., Kesden, M., Berti, E., Sperhake, U.: Distinguishing black-hole spin-orbit resonances by their gravitational-wave signatures. *Phys. Rev. D* **89**(12), 124025 (2014). DOI 10.1103/PhysRevD.89.124025
338. Gerosa, D., Pratten, G., Vecchio, A.: Gravitational-wave selection effects using neural-network classifiers. *Phys. Rev. D* **102**(10), 103020 (2020). DOI 10.1103/PhysRevD.102.103020
339. Ghonge, S., Chatziioannou, K., Clark, J.A., Littenberg, T., Millhouse, M., Cadonati, L., Cornish, N.: Reconstructing gravitational wave signals from binary black hole mergers with minimal assumptions. *Phys. Rev. D* **102**(6), 064056 (2020). DOI 10.1103/PhysRevD.102.064056
340. Ghosh, A., Johnson-Mcdaniel, N.K., Ghosh, A., Mishra, C.K., Ajith, P., Del Pozzo, W., Berry, C.P.L., Nielsen, A.B., London, L.: Testing general relativity using gravitational wave signals from the inspiral, merger and ringdown of binary black holes. *Class. Quant. Grav.* **35**(1), 014002 (2018). DOI 10.1088/1361-6382/aa972e
341. Ghosh, A., et al.: Testing general relativity using golden black-hole binaries. *Phys. Rev. D* **94**(2), 021101 (2016). DOI 10.1103/PhysRevD.94.021101
342. Glanzer, J., et al.: Data quality up to the third observing run of advanced LIGO: Gravity Spy glitch classifications. *Class. Quant. Grav.* **40**(6), 065004 (2023). DOI 10.1088/1361-6382/acb633
343. Godfrey, J., Edelman, B., Farr, B.: Cosmic Cousins: Identification of a Subpopulation of Binary Black Holes Consistent with Isolated Binary Evolution. *arXiv e-prints* arXiv:2304.01288 (2023). DOI 10.48550/arXiv.2304.01288
344. Goldberg, J.N., MacFarlane, A.J., Newman, E.T., Rohrlich, F., Sudarshan, E.C.G.: Spin s spherical harmonics and edth. *J. Math. Phys.* **8**, 2155 (1967). DOI 10.1063/1.1705135
345. Golomb, J., Isi, M., Farr, W.: Physical Models for the Astrophysical Population of Black Holes: Application to the Bump in the Mass Distribution of Gravitational Wave Sources. *arXiv e-prints* arXiv:2312.03973 (2023). DOI 10.48550/arXiv.2312.03973
346. Golomb, J., Talbot, C.: Hierarchical Inference of Binary Neutron Star Mass Distribution and Equation of State with Gravitational Waves. *ApJ* **926**(1), 79 (2022). DOI 10.3847/1538-4357/ac43bc
347. Golomb, J., Talbot, C.: Hierarchical Inference of Binary Neutron Star Mass Distribution and Equation of State with Gravitational Waves. *Astrophys. J.* **926**(1), 79 (2022). DOI 10.3847/1538-4357/ac43bc

348. Golomb, J., Talbot, C.: Searching for structure in the binary black hole spin distribution. *Phys. Rev. D* **108**(10), 103009 (2023). DOI 10.1103/PhysRevD.108.103009
349. Golub, G.H., Loan, C.F.V.: *Matrix Computations* (3rd ed.). Johns Hopkins (1996)
350. Goncharov, B., Nitz, A.H., Harms, J.: Utilizing the null stream of the Einstein Telescope. *Phys. Rev. D* **105**(12), 122007 (2022). DOI 10.1103/PhysRevD.105.122007
351. Goodfellow, I., Bengio, Y., Courville, A.: *Deep Learning. Adaptive computation and machine learning*. MIT Press (2016)
352. Goodman, J., Weare, J.: Ensemble samplers with affine invariance. *Communications in Applied Mathematics and Computational Science* **5**(1), 65 – 80 (2010). DOI 10.2140/camcos.2010.5.65. URL <https://doi.org/10.2140/camcos.2010.5.65>
353. Gorda, T., Komoltsev, O., Kurkela, A.: Ab-initio QCD calculations impact the inference of the neutron-star-matter equation of state (2022)
354. Graff, P., Feroz, F., Hobson, M.P., Lasenby, A.: Bambi: blind accelerated multimodal bayesian inference. *Monthly Notices of the Royal Astronomical Society* **421**(1), 169–180 (2012)
355. Greif, S.K., Raaijmakers, G., Hebel, K., Schwenk, A., Watts, A.L.: Equation of state sensitivities when inferring neutron star and dense matter properties. *Mon. Not. Roy. Astron. Soc.* **485**(4), 5363–5376 (2019). DOI 10.1093/mnras/stz654
356. Grote, H.: The GEO 600 status. *Class. Quant. Grav.* **27**, 084003 (2010). DOI 10.1088/0264-9381/27/8/084003
357. Gunny, A., Rankin, D., Krupa, J., et al.: Hardware-accelerated inference for real-time gravitational-wave astronomy. *Nature Astronomy* **6**(5), 529–536 (2022). DOI 10.1038/s41550-022-01651-w. URL <https://doi.org/10.1038/s41550-022-01651-w>
358. Haario, H., Saksman, E., Tamminen, J.: An adaptive Metropolis algorithm. *Bernoulli* **7**(2), 223 – 242 (2001)
359. Hajian, A.: Efficient cosmological parameter estimation with hamiltonian monte carlo technique. *Phys. Rev. D* **75**, 083525 (2007). DOI 10.1103/PhysRevD.75.083525. URL <https://link.aps.org/doi/10.1103/PhysRevD.75.083525>
360. Hamilton, E., London, L., Thompson, J.E., Fauchon-Jones, E., Hannam, M., Kalaghatgi, C., Khan, S., Pannarale, F., Vano-Vinuales, A.: Model of gravitational waves from precessing black-hole binaries through merger and ringdown. *Phys. Rev. D* **104**(12), 124027 (2021). DOI 10.1103/PhysRevD.104.124027
361. Hamilton, E., et al.: A catalogue of precessing black-hole-binary numerical-relativity simulations (2023)
362. Han, S., Mamun, M.A.A., Lalit, S., Constantinou, C., Prakash, M.: Treating quarks within neutron stars. *Phys. Rev. D* **100**(10), 103022 (2019). DOI 10.1103/PhysRevD.100.103022
363. Hanna, C.: Searching for gravitational waves from binary systems in non-stationary data. Ph.D. thesis, Louisiana State University (2008)
364. Hanna, C., et al.: Fast evaluation of multidetector consistency for real-time gravitational wave searches. *Phys. Rev. D* **101**(2), 022003 (2020). DOI 10.1103/PhysRevD.101.022003
365. Hanna, C., et al.: Metric assisted stochastic sampling search for gravitational waves from binary black hole mergers. *Phys. Rev. D* **106**(8), 084033 (2022). DOI 10.1103/PhysRevD.106.084033
366. Hannam, M., Schmidt, P., Bohé, A., Haegel, L., Husa, S., Ohme, F., Pratten, G., Pürrer, M.: Simple Model of Complete Precessing Black-Hole-Binary Gravitational Waveforms. *Phys. Rev. Lett.* **113**(15), 151101 (2014). DOI 10.1103/PhysRevLett.113.151101
367. Hannuksela, O.A., Haris, K., Ng, K.K.Y., Kumar, S., Mehta, A.K., Keitel, D., Li, T.G.F., Ajith, P.: Search for gravitational lensing signatures in LIGO-Virgo binary black hole events. *Astrophys. J. Lett.* **874**(1), L2 (2019). DOI 10.3847/2041-8213/ab0c0f
368. Harms, J.: Terrestrial gravity fluctuations. *Living Rev. Rel.* **22**(1), 6 (2019). DOI 10.1007/s41114-019-0022-2
369. Harry, I., Calderón Bustillo, J., Nitz, A.: Searching for the full symphony of black hole binary mergers. *Phys. Rev. D* **97**(2), 023004 (2018). DOI 10.1103/PhysRevD.97.023004

370. Harry, I., Hinderer, T.: Observing and measuring the neutron-star equation-of-state in spinning binary neutron star systems. *Class. Quant. Grav.* **35**(14), 145010 (2018). DOI 10.1088/1361-6382/aac7e3
371. Harry, I., Lundgren, A.: Failure of the Fisher matrix when including tidal terms: Considering construction of template banks of tidally deformed binary neutron stars. *Phys. Rev. D* **104**(4), 043008 (2021). DOI 10.1103/PhysRevD.104.043008
372. Harry, I., Privitera, S., Bohé, A., Buonanno, A.: Searching for Gravitational Waves from Compact Binaries with Precessing Spins. *Phys. Rev. D* **94**(2), 024012 (2016). DOI 10.1103/PhysRevD.94.024012
373. Harry, I.W., Allen, B., Sathyaprakash, B.S.: A Stochastic template placement algorithm for gravitational wave data analysis. *Phys. Rev. D* **80**, 104014 (2009). DOI 10.1103/PhysRevD.80.104014
374. Harry, I.W., Fairhurst, S.: A targeted coherent search for gravitational waves from compact binary coalescences. *Phys. Rev. D* **83**, 084002 (2011). DOI 10.1103/PhysRevD.83.084002
375. Harry, I.W., Nitz, A.H., Brown, D.A., Lundgren, A.P., Ochsner, E., Keppel, D.: Investigating the effect of precession on searches for neutron-star-black-hole binaries with Advanced LIGO. *Phys. Rev. D* **89**(2), 024010 (2014). DOI 10.1103/PhysRevD.89.024010
376. Hartle, J.: *Gravity: An Introduction to Einstein's General Relativity*. Always Learning. Pearson Education, Limited (2013)
377. Hastings, W.K.: Monte Carlo sampling methods using Markov chains and their applications. *Biometrika* **57**(1), 97–109 (1970). DOI 10.1093/biomet/57.1.97. URL <https://doi.org/10.1093/biomet/57.1.97>
378. Healy, J., Lousto, C.O.: Third RIT binary black hole simulations catalog. *Phys. Rev. D* **102**(10), 104018 (2020). DOI 10.1103/PhysRevD.102.104018
379. Healy, J., Lousto, C.O.: Fourth RIT binary black hole simulations catalog: Extension to eccentric orbits. *Phys. Rev. D* **105**(12), 124010 (2022). DOI 10.1103/PhysRevD.105.124010
380. Healy, J., Lousto, C.O., Lange, J., O'Shaughnessy, R., Zlochower, Y., Campanelli, M.: Second RIT binary black hole simulations catalog and its application to gravitational waves parameter estimation. *Phys. Rev. D* **100**(2), 024021 (2019). DOI 10.1103/PhysRevD.100.024021
381. Healy, J., Lousto, C.O., Zlochower, Y., Campanelli, M.: The RIT binary black hole simulations catalog. *Class. Quant. Grav.* **34**(22), 224001 (2017). DOI 10.1088/1361-6382/aa91b1
382. Heger, A., Müller, B., Mandel, I.: Black holes as the end state of stellar evolution: Theory and simulations. *arXiv e-prints arXiv:2304.09350* (2023). DOI 10.48550/arXiv.2304.09350
383. Heinzl, J., Biscoveanu, S., Vitale, S.: Probing Correlations in the Binary Black Hole Population with Flexible Models. *arXiv e-prints arXiv:2312.00993* (2023). DOI 10.48550/arXiv.2312.00993
384. Heinzl, J., Mould, M., Álvarez-López, S., Vitale, S.: PixelPop: High Resolution Nonparametric Inference of Gravitational-Wave Populations in Multiple Dimensions (2024)
385. Hewish, A., Bell, S.J., Pilkington, J.D.H., Scott, P.F., Collins, R.A.: Observation of a rapidly pulsating radio source. *Nature* **217**, 709–713 (1968). DOI 10.1038/217709a0
386. Hilbert, S., Gair, J.R., King, L.J.: Reducing distance errors for standard candles and standard sirens with weak-lensing shear and flexion maps. *Mon. Not. Roy. Astron. Soc.* **412**, 1023–1037 (2011). DOI 10.1111/j.1365-2966.2010.17963.x
387. Hinderer, T., Lackey, B.D., Lang, R.N., Read, J.S.: Tidal deformability of neutron stars with realistic equations of state and their gravitational wave signatures in binary inspiral. *Phys. Rev. D* **81**, 123016 (2010). DOI 10.1103/PhysRevD.81.123016
388. Hogg, D.W.: *Distance measures in cosmology* (1999)
389. Hooper, S., Chung, S.K., Luan, J., Blair, D., Chen, Y., Wen, L.: Summed Parallel Infinite Impulse Response (SPIIR) Filters For Low-Latency Gravitational Wave Detection. *Phys. Rev. D* **86**, 024012 (2012). DOI 10.1103/PhysRevD.86.024012
390. Hourihane, S., Chatziioannou, K., Wijngaarden, M., Davis, D., Littenberg, T., Cornish, N.: Accurate modeling and mitigation of overlapping signals and glitches in gravitational-wave data. *Phys. Rev. D* **106**(4), 042006 (2022). DOI 10.1103/PhysRevD.106.042006

391. Hu, Q., Veitch, J.: Accumulating Errors in Tests of General Relativity with Gravitational Waves: Overlapping Signals and Inaccurate Waveforms. *Astrophys. J.* **945**(2), 103 (2023). DOI 10.3847/1538-4357/acbc18
392. Hu, Q., Veitch, J.: Rapid Premerger Localization of Binary Neutron Stars in Third-generation Gravitational-wave Detectors. *Astrophys. J. Lett.* **958**(2), L43 (2023). DOI 10.3847/2041-8213/ad0ed4
393. Huerta, E.A., et al.: Accelerated, scalable and reproducible AI-driven gravitational wave detection. *Nature Astron.* **5**(10), 1062–1068 (2021). DOI 10.1038/s41550-021-01405-0
394. Hulse, R.A., Taylor, J.H.: Discovery of a pulsar in a binary system. *Astrophys. J. Lett.* **195**, L51–L53 (1975). DOI 10.1086/181708
395. Inayoshi, K., Tamanini, N., Caprini, C., Haiman, Z.: Probing stellar binary black hole formation in galactic nuclei via the imprint of their center of mass acceleration on their gravitational wave signal. *Phys. Rev. D* **96**(6), 063014 (2017). DOI 10.1103/PhysRevD.96.063014
396. Indik, N., Haris, K., Dal Canton, T., Fehrmann, H., Krishnan, B., Lundgren, A., Nielsen, A.B., Pai, A.: Stochastic template bank for gravitational wave searches for precessing neutron-star–black-hole coalescence events. *Phys. Rev. D* **95**(6), 064056 (2017). DOI 10.1103/PhysRevD.95.064056
397. Isi, M., Chatziioannou, K., Farr, W.M.: Hierarchical test of general relativity with gravitational waves. *Phys. Rev. Lett.* **123**(12), 121101 (2019). DOI 10.1103/PhysRevLett.123.121101
398. Isi, M., Farr, W.M.: Analyzing black-hole ringdowns (2021)
399. Isi, M., Farr, W.M., Chatziioannou, K.: Comparing Bayes factors and hierarchical inference for testing general relativity with gravitational waves (2022)
400. Isi, M., Farr, W.M., Giesler, M., Scheel, M.A., Teukolsky, S.A.: Testing the Black-Hole Area Law with GW150914. *Phys. Rev. Lett.* **127**(1), 011103 (2021). DOI 10.1103/PhysRevLett.127.011103
401. Isi, M., Farr, W.M., Varma, V.: The directional isotropy of LIGO-Virgo binaries. *arXiv e-prints arXiv:2304.13254* (2023). DOI 10.48550/arXiv.2304.13254
402. Isi, M., Giesler, M., Farr, W.M., Scheel, M.A., Teukolsky, S.A.: Testing the no-hair theorem with GW150914. *Phys. Rev. Lett.* **123**(11), 111102 (2019). DOI 10.1103/PhysRevLett.123.111102
403. Isi, M., Smith, R., Vitale, S., Massinger, T.J., Kanner, J., Vajpeyi, A.: Enhancing confidence in the detection of gravitational waves from compact binaries using signal coherence. *Phys. Rev. D* **98**(4), 042007 (2018). DOI 10.1103/PhysRevD.98.042007
404. Islam, T., Varma, V., Lodman, J., Field, S.E., Khanna, G., Scheel, M.A., Pfeiffer, H.P., Gerosa, D., Kidder, L.E.: Eccentric binary black hole surrogate models for the gravitational waveform and remnant properties: comparable mass, nonspinning case. *Phys. Rev. D* **103**(6), 064022 (2021). DOI 10.1103/PhysRevD.103.064022
405. Jani, K., Healy, J., Clark, J.A., London, L., Laguna, P., Shoemaker, D.: Georgia Tech Catalog of Gravitational Waveforms. *Class. Quant. Grav.* **33**(20), 204001 (2016). DOI 10.1088/0264-9381/33/20/204001
406. Jaranowski, P., Krolak, A., Schutz, B.F.: Data analysis of gravitational - wave signals from spinning neutron stars. 1. The Signal and its detection. *Phys. Rev. D* **58**, 063001 (1998). DOI 10.1103/PhysRevD.58.063001
407. Jaynes, E.T.: *Probability Theory: The Logic of Science*. Cambridge University Press (2002)
408. Jeffreys, H.: *The Theory of Probability*. Clarendon Press (1939)
409. Johnson, A.D., Chatziioannou, K., Farr, W.M.: Source Confusion from Neutron Star Binaries in Ground-Based Gravitational Wave Detectors is Minimal (2024)
410. Johnson-McDaniel, N.K., Ghosh, A., Ghonge, S., Saleem, M., Krishnendu, N.V., Clark, J.A.: Investigating the relation between gravitational wave tests of general relativity. *Phys. Rev. D* **105**(4), 044020 (2022). DOI 10.1103/PhysRevD.105.044020
411. Joshi, P., Dhurkunde, R., Dhurandhar, S., Bose, S.: Optimal χ^2 discriminator against modeled noise transients in interferometric data in searches for binary black-hole mergers. *Phys. Rev. D* **103**(4), 044035 (2021). DOI 10.1103/PhysRevD.103.044035

412. Joshi, P., Tsukada, L., Hanna, C.: Method for removing signal contamination during significance estimation of a GstLAL analysis. *Phys. Rev. D* **108**(8), 084032 (2023). DOI 10.1103/PhysRevD.108.084032
413. Kalaghatgi, C., Ajith, P., Arun, K.G.: Template-space metric for searches for gravitational waves from the inspiral, merger and ringdown of binary black holes. *Phys. Rev. D* **91**(12), 124042 (2015). DOI 10.1103/PhysRevD.91.124042
414. Kalogera, V.: Spin-Orbit Misalignment in Close Binaries with Two Compact Objects. *ApJ* **541**(1), 319–328 (2000). DOI 10.1086/309400
415. Kalogera, V., Belczynski, K., Kim, C., O’Shaughnessy, R., Willems, B.: Formation of double compact objects. *Phys. Rep.* **442**(1-6), 75–108 (2007). DOI 10.1016/j.physrep.2007.02.008
416. Kalogera, V., Narayan, R., Spergel, D.N., Taylor, J.H.: The Coalescence rate of double neutron star systems. *Astrophys. J.* **556**, 340–356 (2001). DOI 10.1086/321583
417. Kapadia, S.J., Dent, T., Dal Canton, T.: Classifier for gravitational-wave inspiral signals in nonideal single-detector data. *Phys. Rev. D* **96**(10), 104015 (2017). DOI 10.1103/PhysRevD.96.104015
418. Kapadia, S.J., et al.: A self-consistent method to estimate the rate of compact binary coalescences with a Poisson mixture model. *Class. Quant. Grav.* **37**(4), 045007 (2020). DOI 10.1088/1361-6382/ab5f2d
419. Keppel, D.: Metrics for multi-detector template placement in searches for short-duration nonprecessing inspiral gravitational-wave signals (2013)
420. Keramidias, E., Kaufman, S.: Computing Science and Statistics: Proceedings of the 23rd Symposium on the Interface, Seattle, Washington, April 21-24, 1991. Interface Foundation of North America (1991). URL <https://books.google.co.uk/books?id=Bfc1NAAACAAJ>
421. Khan, S., Chatziioannou, K., Hannam, M., Ohme, F.: Phenomenological model for the gravitational-wave signal from precessing binary black holes with two-spin effects. *Phys. Rev. D* **100**(2), 024059 (2019). DOI 10.1103/PhysRevD.100.024059
422. Khan, S., Green, R.: Gravitational-wave surrogate models powered by artificial neural networks: The ANN-Sur for waveform generation (2020)
423. Khan, S., Husa, S., Hannam, M., Ohme, F., Pürrer, M., Jiménez Forteza, X., Bohé, A.: Frequency-domain gravitational waves from nonprecessing black-hole binaries. II. A phenomenological model for the advanced detector era. *Phys. Rev. D* **93**(4), 044007 (2016). DOI 10.1103/PhysRevD.93.044007
424. Kidder, L.E.: Coalescing binary systems of compact objects to postNewtonian 5/2 order. 5. Spin effects. *Phys. Rev.* **D52**, 821–847 (1995). DOI 10.1103/PhysRevD.52.821
425. Kidder, L.E., Will, C.M., Wiseman, A.G.: Spin effects in the inspiral of coalescing compact binaries. *Phys. Rev.* **D47**(10), R4183–R4187 (1993). DOI 10.1103/PhysRevD.47.R4183
426. Kim, K., Harry, I.W., Hodge, K.A., Kim, Y.M., Lee, C.H., Lee, H.K., Oh, J.J., Oh, S.H., Son, E.J.: Application of Artificial Neural Network to Search for Gravitational-Wave Signals Associated with Short Gamma-Ray Bursts. *Class. Quant. Grav.* **32**(24), 245002 (2015). DOI 10.1088/0264-9381/32/24/245002
427. Kim, K., Li, T.G.F., Lo, R.K.L., Sachdev, S., Yuen, R.S.H.: Ranking candidate signals with machine learning in low-latency searches for gravitational waves from compact binary mergers. *Phys. Rev. D* **101**(8), 083006 (2020). DOI 10.1103/PhysRevD.101.083006
428. Klein, A., et al.: The last three years: multiband gravitational-wave observations of stellar-mass binary black holes (2022)
429. Klimentenko, S., et al.: Method for detection and reconstruction of gravitational wave transients with networks of advanced detectors. *Phys. Rev. D* **93**(4), 042004 (2016). DOI 10.1103/PhysRevD.93.042004
430. Knowles, T.D., Devine, C., Buch, D.A., Bilgili, S.A., Adams, T.R., Etienne, Z.B., McWilliams, S.T.: Improving performance of SEOBNRv3 by $\sim 300\times$. *Class. Quant. Grav.* **35**(15), 155003 (2018). DOI 10.1088/1361-6382/aacb8c
431. Kobayev, I., Prince, S., Brubaker, M.A.: Normalizing flows: An introduction and review of current methods. *Ieee Transactions On Pattern Analysis And Machine Intelligence* (2020). DOI 10.1109/TPAMI.2020.2992934

432. Kolitsidou, P., Thompson, J.E., Hannam, M.: Impact of anti-symmetric contributions to signal multipoles in the measurement of black-hole spins (2024)
433. Komoltsev, O., Kurkela, A.: How perturbative QCD constrains the Equation of State at Neutron-Star densities (2021)
434. Kovalam, M., Patwary, M.A.K., Sreekumar, A.K., Wen, L., Panther, F.H., Chu, Q.: Early Warnings of Binary Neutron Star Coalescence Using the SPIIR Search. *Astrophys. J. Lett.* **927**(1), L9 (2022). DOI 10.3847/2041-8213/ac5687
435. Kovetz, E.D., Cholis, I., Breyse, P.C., Kamionkowski, M.: Black hole mass function from gravitational wave measurements. *Phys. Rev. D* **95**(10), 103010 (2017). DOI 10.1103/PhysRevD.95.103010
436. Krastev, P.G.: Real-Time Detection of Gravitational Waves from Binary Neutron Stars using Artificial Neural Networks. *Phys. Lett. B* **803**, 135330 (2020). DOI 10.1016/j.physletb.2020.135330
437. Krolak, A., Schutz, B.F.: Coalescing binaries — Probe of the universe. *Gen. Rel. Grav.* **19**, 1163–1171 (1987). DOI 10.1007/BF00759095
438. Kulkarni, S.R., Hut, P., McMillan, S.: Stellar black holes in globular clusters. *Nature* **364**(6436), 421–423 (1993). DOI 10.1038/364421a0
439. Kumar, P., Dent, T.: Optimized Search for a Binary Black Hole Merger Population in LIGO-Virgo O3 Data (2024)
440. Kumar, P., et al.: Template Banks for Binary black hole searches with Numerical Relativity waveforms. *Phys. Rev. D* **89**(4), 042002 (2014). DOI 10.1103/PhysRevD.89.042002
441. Kyutoku, K., Shibata, M., Taniguchi, K.: Coalescence of black hole-neutron star binaries. *Living Rev. Rel.* **24**(1), 5 (2021). DOI 10.1007/s41114-021-00033-4
442. Lackey, B.D., Pürrer, M., Taracchini, A., Marsat, S.: Surrogate model for an aligned-spin effective one body waveform model of binary neutron star inspirals using Gaussian process regression. *Phys. Rev. D* **100**(2), 024002 (2019). DOI 10.1103/PhysRevD.100.024002
443. Landry, P., Essick, R.: Nonparametric inference of the neutron star equation of state from gravitational wave observations. *Phys. Rev. D* **99**(8), 084049 (2019). DOI 10.1103/PhysRevD.99.084049
444. Landry, P., Essick, R., Chatziioannou, K.: Nonparametric constraints on neutron star matter with existing and upcoming gravitational wave and pulsar observations. *Phys. Rev. D* **101**(12), 123007 (2020). DOI 10.1103/PhysRevD.101.123007
445. Lange, J., O’Shaughnessy, R., Rizzo, M.: Rapid and accurate parameter inference for coalescing, precessing compact binaries (2018)
446. Lange, J., et al.: Parameter estimation method that directly compares gravitational wave observations to numerical relativity. *Phys. Rev. D* **96**(10), 104041 (2017). DOI 10.1103/PhysRevD.96.104041
447. Langendorff, J., Kolmus, A., Janquart, J., Van Den Broeck, C.: Normalizing flows as an avenue to study overlapping gravitational wave signals (2022)
448. Lattimer, J.M., Prakash, M.: The Equation of State of Hot, Dense Matter and Neutron Stars. *Phys. Rept.* **621**, 127–164 (2016). DOI 10.1016/j.physrep.2015.12.005
449. Lazzarini, A., Bose, S., Fritschel, P., McHugh, M., Regimbau, T., Reilly, K., Romano, J.D., Whelan, J.T., Whitcomb, S.E., Whiting, B.F.: Optimal combination of signals from co-located gravitational wave interferometers for use in searches for a stochastic background. *Phys. Rev. D* **70**, 062001 (2004). DOI 10.1103/PhysRevD.70.062001
450. Legred, I., Chatziioannou, K., Essick, R., Han, S., Landry, P.: Impact of the PSR J0740+6620 radius constraint on the properties of high-density matter. *Phys. Rev. D* **104**(6), 063003 (2021). DOI 10.1103/PhysRevD.104.063003
451. Legred, I., Chatziioannou, K., Essick, R., Landry, P.: Implicit correlations within phenomenological parametric models of the neutron star equation of state. *Phys. Rev. D* **105**(4), 043016 (2022). DOI 10.1103/PhysRevD.105.043016
452. Leslie, N., Dai, L., Pratten, G.: Mode-by-mode relative binning: Fast likelihood estimation for gravitational waveforms with spin-orbit precession and multiple harmonics. *Phys. Rev. D* **104**(12), 123030 (2021). DOI 10.1103/PhysRevD.104.123030
453. Leyde, K., Green, S.R., Toubiana, A., Gair, J.: Gravitational wave populations and cosmology with neural posterior estimation. *arXiv e-prints arXiv:2311.12093* (2023). DOI 10.48550/arXiv.2311.12093

454. Li, A.K.Y., Chan, J.C.L., Fong, H., Chong, A.H.Y., Weinstein, A.J., Ezquiaga, J.M.: TESLA-X: An effective method to search for sub-threshold lensed gravitational waves with a targeted population model (2023)
455. Li, T.G.F., Del Pozzo, W., Vitale, S., Van Den Broeck, C., Agathos, M., Veitch, J., Grover, K., Sidery, T., Sturani, R., Vecchio, A.: Towards a generic test of the strong field dynamics of general relativity using compact binary coalescence. *Phys. Rev. D* **85**, 082003 (2012). DOI 10.1103/PhysRevD.85.082003
456. Li, Y.J., Wang, Y.Z., Han, M.Z., Tang, S.P., Yuan, Q., Fan, Y.Z., Wei, D.M.: A Flexible Gaussian Process Reconstruction Method and the Mass Function of the Coalescing Binary Black Hole Systems. *Astrophys. J.* **917**(1), 33 (2021). DOI 10.3847/1538-4357/ac0971
457. Li, Y.J., Wang, Y.Z., Tang, S.P., Fan, Y.Z.: Resolving the stellar-collapse and hierarchical-merger origins of the coalescing black holes. arXiv e-prints arXiv:2303.02973 (2023). DOI 10.48550/arXiv.2303.02973
458. Li, Y.J., Wang, Y.Z., Tang, S.P., Yuan, Q., Fan, Y.Z., Wei, D.M.: Divergence in Mass Ratio Distributions between Low-mass and High-mass Coalescing Binary Black Holes. *ApJ* **933**(1), L14 (2022). DOI 10.3847/2041-8213/ac78dd
459. LIGO Scientific Collaboration: LALSimulation. https://lscsoft.docs.ligo.org/lalsuite/lalsimulation/group__lalsimulation__inspiral.html (2023)
460. LIGO Scientific Collaboration: LIGO Algorithm Library - LALSuite (2023). DOI 10.7935/GT1W-FZ16
461. Lindblom, L.: Spectral Representations of Neutron-Star Equations of State. *Phys. Rev. D* **82**, 103011 (2010). DOI 10.1103/PhysRevD.82.103011
462. Lindblom, L., Indik, N.M.: Spectral Approach to the Relativistic Inverse Stellar Structure Problem II. *Phys. Rev. D* **89**(6), 064003 (2014). DOI 10.1103/PhysRevD.89.064003. [Erratum: *Phys.Rev.D* 93, 129903 (2016)]
463. Littenberg, T.B., Cornish, N.J.: Bayesian inference for spectral estimation of gravitational wave detector noise. *Phys. Rev. D* **91**(8), 084034 (2015). DOI 10.1103/PhysRevD.91.084034
464. Lonardonì, D., Tews, I., Gandolfi, S., Carlson, J.: Nuclear and neutron-star matter from local chiral interactions. *Phys. Rev. Res.* **2**(2), 022033 (2020). DOI 10.1103/PhysRevResearch.2.022033
465. London, L., Khan, S., Fauchon-Jones, E., García, C., Hannam, M., Husa, S., Jiménez-Forsteza, X., Kalaghatgi, C., Ohme, F., Pannarale, F.: First higher-multipole model of gravitational waves from spinning and coalescing black-hole binaries. *Phys. Rev. Lett.* **120**(16), 161102 (2018). DOI 10.1103/PhysRevLett.120.161102
466. Loredo, T.J.: Accounting for Source Uncertainties in Analyses of Astronomical Survey Data. In: R. Fischer, R. Preuss, U.V. Toussaint (eds.) *Bayesian Inference and Maximum Entropy Methods in Science and Engineering: 24th International Workshop on Bayesian Inference and Maximum Entropy Methods in Science and Engineering, American Institute of Physics Conference Series*, vol. 735, pp. 195–206 (2004). DOI 10.1063/1.1835214
467. Lorentz, H.A., Droste, J.: *The Motion of a System of Bodies under the Influence of their Mutual Attraction, According to Einstein's Theory*, pp. 330–355. Springer Netherlands, Dordrecht (1937). DOI 10.1007/978-94-015-3445-1_11. URL https://doi.org/10.1007/978-94-015-3445-1_11
468. Luan, J., Hooper, S., Wen, L., Chen, Y.: Towards low-latency real-time detection of gravitational waves from compact binary coalescences in the era of advanced detectors. *Phys. Rev. D* **85**, 102002 (2012). DOI 10.1103/PhysRevD.85.102002
469. Machleidt, R., Entem, D.R.: Chiral effective field theory and nuclear forces. *Phys. Rept.* **503**, 1–75 (2011). DOI 10.1016/j.physrep.2011.02.001
470. Macleod, D., Harry, I.W., Fairhurst, S.: Fully-coherent all-sky search for gravitational-waves from compact binary coalescences. *Phys. Rev. D* **93**(6), 064004 (2016). DOI 10.1103/PhysRevD.93.064004
471. Maday, Y., Nguyen, N.C., Patera, A.T., Pau, G.S.: A general, multipurpose interpolation procedure: the magic points (2007)
472. Magee, R., Isi, M., Payne, E., Chatziioannou, K., Farr, W.M., Pratten, G., Vitale, S.: Impact of selection biases on tests of general relativity with gravitational-wave inspirals. *Phys. Rev. D* **109**(2), 023014 (2024). DOI 10.1103/PhysRevD.109.023014

473. Magee, R., et al.: Sub-threshold Binary Neutron Star Search in Advanced LIGO's First Observing Run. *Astrophys. J. Lett.* **878**(1), L17 (2019). DOI 10.3847/2041-8213/ab20cf
474. Magee, R., et al.: First demonstration of early warning gravitational wave alerts. *Astrophys. J. Lett.* **910**(2), L21 (2021). DOI 10.3847/2041-8213/abed54
475. Maggiore, M.: *Gravitational Waves. Vol. 1: Theory and Experiments.* Oxford Master Series in Physics. Oxford University Press (2007)
476. Maggiore, M.: *Gravitational Waves. Vol. 2: Astrophysics and Cosmology.* Oxford University Press (2018)
477. Manca, G.M., Vallisneri, M.: Cover art: Issues in the metric-guided and metric-less placement of random and stochastic template banks. *Phys. Rev. D* **81**, 024004 (2010). DOI 10.1103/PhysRevD.81.024004
478. Mandel, I.: Parameter estimation on gravitational waves from multiple coalescing binaries. *Phys. Rev. D* **81**(8), 084029 (2010). DOI 10.1103/PhysRevD.81.084029
479. Mandel, I., Berry, C.P.L., Ohme, F., Fairhurst, S., Farr, W.M.: Parameter estimation on compact binary coalescences with abruptly terminating gravitational waveforms. *Class. Quant. Grav.* **31**, 155005 (2014). DOI 10.1088/0264-9381/31/15/155005
480. Mandel, I., Broekgaarden, F.S.: Rates of compact object coalescences. *Living Rev. Rel.* **25**(1), 1 (2022). DOI 10.1007/s41114-021-00034-3
481. Mandel, I., Farmer, A.: Merging stellar-mass binary black holes. *Phys. Rep.* **955**, 1–24 (2022). DOI 10.1016/j.physrep.2022.01.003
482. Mandel, I., Farr, W.M., Colonna, A., Stevenson, S., Tiño, P., Veitch, J.: Model-independent inference on compact-binary observations. *MNRAS* **465**(3), 3254–3260 (2017). DOI 10.1093/mnras/stw2883
483. Mandel, I., Farr, W.M., Gair, J.R.: Extracting distribution parameters from multiple uncertain observations with selection biases. *MNRAS* **486**(1), 1086–1093 (2019). DOI 10.1093/mnras/stz896
484. Mandel, I., Fragos, T.: An alternative interpretation of GW190412 as a binary black hole merger with a rapidly spinning secondary. *Astrophys. J. Lett.* **895**(2), L28 (2020). DOI 10.3847/2041-8213/ab8e41
485. Mandel, K.S., Narayan, G., Kirshner, R.P.: Type Ia Supernova Light Curve Inference: Hierarchical Models in the Optical and Near-infrared. *ApJ* **731**(2), 120 (2011). DOI 10.1088/0004-637X/731/2/120
486. Mapelli, M.: Formation Channels of Single and Binary Stellar-Mass Black Holes. In: *Handbook of Gravitational Wave Astronomy*, p. 16 (2021). DOI 10.1007/978-981-15-4702-7_16-1
487. Margalit, B., Metzger, B.D.: The Multi-Messenger Matrix: the Future of Neutron Star Merger Constraints on the Nuclear Equation of State. *Astrophys. J.* **880**(1), L15 (2019). DOI 10.3847/2041-8213/ab2ae2
488. Marx, E., et al.: A machine-learning pipeline for real-time detection of gravitational waves from compact binary coalescences (2024)
489. Mastrogianni, S., Leyde, K., Karathanasis, C., Chassande-Mottin, E., Steer, D.A., Gair, J., Ghosh, A., Gray, R., Mukherjee, S., Rinaldi, S.: On the importance of source population models for gravitational-wave cosmology. *Phys. Rev. D* **104**(6), 062009 (2021). DOI 10.1103/PhysRevD.104.062009
490. Matas, A., et al.: Aligned-spin neutron-star–black-hole waveform model based on the effective-one-body approach and numerical-relativity simulations. *Phys. Rev. D* **102**(4), 043023 (2020). DOI 10.1103/PhysRevD.102.043023
491. Mathews, J.: Gravitational multipole radiation. *Journal of the Society for Industrial and Applied Mathematics* **10**(4), 768–780 (1962). URL <http://www.jstor.org/stable/2098922>
492. McIsaac, C., Hoy, C., Harry, I.: A search technique to observe precessing compact binary mergers in the advanced detector era (2023)
493. Meacher, D., Cannon, K., Hanna, C., Regimbau, T., Sathyaprakash, B.S.: Second Einstein Telescope Mock Data and Science Challenge: Low Frequency Binary Neutron Star Data Analysis. *Phys. Rev. D* **93**(2), 024018 (2016). DOI 10.1103/PhysRevD.93.024018
494. Meidam, J., et al.: Parametrized tests of the strong-field dynamics of general relativity using gravitational wave signals from coalescing binary black holes: Fast likelihood

- calculations and sensitivity of the method. *Phys. Rev. D* **97**(4), 044033 (2018). DOI 10.1103/PhysRevD.97.044033
495. Merritt, J., Farr, B., Hur, R., Edelman, B., Doctor, Z.: Transient glitch mitigation in Advanced LIGO data. *Phys. Rev. D* **104**(10), 102004 (2021). DOI 10.1103/PhysRevD.104.102004
496. Messenger, C., Read, J.: Measuring a cosmological distance-redshift relationship using only gravitational wave observations of binary neutron star coalescences. *Phys. Rev. Lett.* **108**, 091101 (2012). DOI 10.1103/PhysRevLett.108.091101
497. Messenger, C., Veitch, J.: Avoiding selection bias in gravitational wave astronomy. *New J. Phys.* **15**, 053027 (2013). DOI 10.1088/1367-2630/15/5/053027
498. Messick, C., et al.: Analysis Framework for the Prompt Discovery of Compact Binary Mergers in Gravitational-wave Data. *Phys. Rev. D* **95**(4), 042001 (2017). DOI 10.1103/PhysRevD.95.042001
499. Metropolis, N., Rosenbluth, A.W., Rosenbluth, M.N., Teller, A.H., Teller, E.: Equation of State Calculations by Fast Computing Machines. *The Journal of Chemical Physics* **21**(6), 1087–1092 (1953). DOI 10.1063/1.1699114. URL <https://doi.org/10.1063/1.1699114>
500. Metropolis, N., Rosenbluth, A.W., Rosenbluth, M.N., Teller, A.H., Teller, E.: Equation of state calculations by fast computing machines (1953). DOI 10.2172/4390578. URL <https://www.osti.gov/biblio/4390578>
501. Metzger, B.D.: Kilonovae. *Living Rev. Rel.* **23**(1), 1 (2020). DOI 10.1007/s41114-019-0024-0
502. Mihaylov, D.P., Ossokine, S., Buonanno, A., Ghosh, A.: Fast post-adiabatic waveforms in the time domain: Applications to compact binary coalescences in LIGO and Virgo. *Phys. Rev. D* **104**(12), 124087 (2021). DOI 10.1103/PhysRevD.104.124087
503. Miller, B.K., Cole, A., Weniger, C., Nattino, F., Ku, O., Grootes, M.W.: swyft: Truncated Marginal Neural Ratio Estimation in Python. *J. Open Source Softw.* **7**(75), 4205 (2022). DOI 10.21105/joss.04205
504. Miller, M.C., et al.: PSR J0030+0451 Mass and Radius from *NICER* Data and Implications for the Properties of Neutron Star Matter. *Astrophys. J. Lett.* **887**(1), L24 (2019). DOI 10.3847/2041-8213/ab50c5
505. Miller, M.C., et al.: The Radius of PSR J0740+6620 from *NICER* and *XMM-Newton* Data. *Astrophys. J. Lett.* **918**(2), L28 (2021). DOI 10.3847/2041-8213/ac089b
506. Miller, S., Callister, T.A., Farr, W.M.: The Low Effective Spin of Binary Black Holes and Implications for Individual Gravitational-wave Events. *ApJ* **895**(2), 128 (2020). DOI 10.3847/1538-4357/ab80c0
507. Miller, S.J., Ko, Z., Callister, T.A., Chatziioannou, K.: Gravitational waves carry information beyond effective spin parameters but it is hard to extract (2024)
508. Moore, C.J., Berry, C.P.L., Chua, A.J.K., Gair, J.R.: Improving gravitational-wave parameter estimation using Gaussian process regression. *Phys. Rev. D* **93**(6), 064001 (2016). DOI 10.1103/PhysRevD.93.064001
509. Moore, C.J., Finch, E., Buscicchio, R., Gerosa, D.: Testing general relativity with gravitational-wave catalogs: the insidious nature of waveform systematics. *iScience* **24**, 102577 (2021). DOI 10.1016/j.isci.2021.102577
510. Moore, C.J., Gerosa, D.: Population-informed priors in gravitational-wave astronomy. *Phys. Rev. D* **104**(8), 083008 (2021). DOI 10.1103/PhysRevD.104.083008
511. Morisaki, S.: Accelerating parameter estimation of gravitational waves from compact binary coalescence using adaptive frequency resolutions. *Phys. Rev. D* **104**(4), 044062 (2021). DOI 10.1103/PhysRevD.104.044062
512. Morisaki, S., Raymond, V.: Rapid Parameter Estimation of Gravitational Waves from Binary Neutron Star Coalescence using Focused Reduced Order Quadrature. *Phys. Rev. D* **102**(10), 104020 (2020). DOI 10.1103/PhysRevD.102.104020
513. Morisaki, S., Smith, R., Tsukada, L., Sachdev, S., Stevenson, S., Talbot, C., Zimmerman, A.: Rapid localization and inference on compact binary coalescences with the Advanced LIGO-Virgo-KAGRA gravitational-wave detector network. *Phys. Rev. D* **108**(12), 123040 (2023). DOI 10.1103/PhysRevD.108.123040
514. Morras, G., Siles, J.F.N., Garcia-Bellido, J.: Efficient reduced order quadrature construction algorithms for fast gravitational wave inference. *Phys. Rev. D* **108**(12), 123025 (2023). DOI 10.1103/PhysRevD.108.123025

515. Mould, M., Gerosa, D.: Gravitational-wave population inference at past time infinity. *Phys. Rev. D* **105**(2), 024076 (2022). DOI 10.1103/PhysRevD.105.024076
516. Mould, M., Gerosa, D., Dall’Amico, M., Mapelli, M.: One to many: comparing single gravitational-wave events to astrophysical populations. *MNRAS* **525**(3), 3986–3997 (2023). DOI 10.1093/mnras/stad2502
517. Mozzon, S., Nuttall, L.K., Lundgren, A., Dent, T., Kumar, S., Nitz, A.H.: Dynamic Normalization for Compact Binary Coalescence Searches in Non-Stationary Noise. *Class. Quant. Grav.* **37**(21), 215014 (2020). DOI 10.1088/1361-6382/abac6c
518. Mroue, A.H., et al.: Catalog of 174 Binary Black Hole Simulations for Gravitational Wave Astronomy. *Phys. Rev. Lett.* **111**(24), 241104 (2013). DOI 10.1103/PhysRevLett.111.241104
519. Nagar, A., Bonino, A., Rettengo, P.: Effective one-body multipolar waveform model for spin-aligned, quasicircular, eccentric, hyperbolic black hole binaries. *Phys. Rev. D* **103**(10), 104021 (2021). DOI 10.1103/PhysRevD.103.104021
520. Nagar, A., Messina, F., Rettengo, P., Bini, D., Damour, T., Geralico, A., Akcay, S., Bernuzzi, S.: Nonlinear-in-spin effects in effective-one-body waveform models of spin-aligned, inspiralling, neutron star binaries. *Phys. Rev. D* **99**(4), 044007 (2019). DOI 10.1103/PhysRevD.99.044007
521. Nagar, A., Rettengo, P.: Efficient effective one body time-domain gravitational waveforms. *Phys. Rev. D* **99**(2), 021501 (2019). DOI 10.1103/PhysRevD.99.021501
522. Nagar, A., et al.: Time-domain effective-one-body gravitational waveforms for coalescing compact binaries with nonprecessing spins, tides and self-spin effects. *Phys. Rev. D* **98**(10), 104052 (2018). DOI 10.1103/PhysRevD.98.104052
523. Nair, R., Perkins, S., Silva, H.O., Yunes, N.: Fundamental Physics Implications for Higher-Curvature Theories from Binary Black Hole Signals in the LIGO-Virgo Catalog GWTC-1. *Phys. Rev. Lett.* **123**(19), 191101 (2019). DOI 10.1103/PhysRevLett.123.191101
524. Nakamura, T.T.: Gravitational lensing of gravitational waves from inspiraling binaries by a point mass lens. *Phys. Rev. Lett.* **80**, 1138–1141 (1998). DOI 10.1103/PhysRevLett.80.1138
525. Narola, H., Roy, S., Sengupta, A.S.: Beyond general relativity: Designing a template-based search for exotic gravitational wave signals. *Phys. Rev. D* **107**(2), 024017 (2023). DOI 10.1103/PhysRevD.107.024017
526. Neal, R.M.: Slice sampling. *The Annals of Statistics* **31**(3), 705 – 767 (2003). DOI 10.1214/aos/1056562461. URL <https://doi.org/10.1214/aos/1056562461>
527. Ng, K.K.Y., Wong, K.W.K., Broadhurst, T., Li, T.G.F.: Precise LIGO Lensing Rate Predictions for Binary Black Holes. *Phys. Rev. D* **97**(2), 023012 (2018). DOI 10.1103/PhysRevD.97.023012
528. Nitz, A.H.: Distinguishing short duration noise transients in LIGO data to improve the PyCBC search for gravitational waves from high mass binary black hole mergers. *Class. Quant. Grav.* **35**(3), 035016 (2018). DOI 10.1088/1361-6382/aaa13d
529. Nitz, A.H., Dal Canton, T., Davis, D., Reyes, S.: Rapid detection of gravitational waves from compact binary mergers with PyCBC Live. *Phys. Rev. D* **98**(2), 024050 (2018). DOI 10.1103/PhysRevD.98.024050
530. Nitz, A.H., Dent, T., Dal Canton, T., Fairhurst, S., Brown, D.A.: Detecting binary compact-object mergers with gravitational waves: Understanding and Improving the sensitivity of the PyCBC search. *Astrophys. J.* **849**(2), 118 (2017). DOI 10.3847/1538-4357/aa8f50
531. Nitz, A.H., Dent, T., Davies, G.S., Harry, I.: A Search for Gravitational Waves from Binary Mergers with a Single Observatory. *Astrophys. J.* **897**(2), 169 (2020). DOI 10.3847/1538-4357/ab96c7
532. Nitz, A.H., Lenon, A., Brown, D.A.: Search for Eccentric Binary Neutron Star Mergers in the first and second observing runs of Advanced LIGO. *Astrophys. J.* **890**, 1 (2019). DOI 10.3847/1538-4357/ab6611
533. Nitz, A.H., Schäfer, M., Dal Canton, T.: Gravitational-wave Merger Forecasting: Scenarios for the Early Detection and Localization of Compact-binary Mergers with Ground-based Observatories. *Astrophys. J. Lett.* **902**, L29 (2020). DOI 10.3847/2041-8213/abbc10

534. O'Boyle, M.F., Markakis, C., Stergioulas, N., Read, J.S.: Parametrized equation of state for neutron star matter with continuous sound speed. *Phys. Rev. D* **102**(8), 083027 (2020). DOI 10.1103/PhysRevD.102.083027
535. Oertel, M., Hempel, M., Klöhn, T., Typel, S.: Equations of state for supernovae and compact stars. *Rev. Mod. Phys.* **89**(1), 015007 (2017). DOI 10.1103/RevModPhys.89.015007
536. Oguri, M.: Strong gravitational lensing of explosive transients. *Rept. Prog. Phys.* **82**(12), 126901 (2019). DOI 10.1088/1361-6633/ab4fc5
537. Ohme, F., Nielsen, A.B., Keppel, D., Lundgren, A.: Statistical and systematic errors for gravitational-wave inspiral signals: A principal component analysis. *Phys. Rev. D* **88**(4), 042002 (2013). DOI 10.1103/PhysRevD.88.042002
538. Olsen, S., Venumadhav, T., Mushkin, J., Roulet, J., Zackay, B., Zaldarriaga, M.: New binary black hole mergers in the LIGO-Virgo O3a data. *Phys. Rev. D* **106**(4), 043009 (2022). DOI 10.1103/PhysRevD.106.043009
539. O'Shaughnessy, R., Kim, C., Kalogera, V., Belczynski, K.: Constraining Population Synthesis Models via Empirical Binary Compact Object Merger and Supernova Rates. *ApJ* **672**(1), 479–488 (2008). DOI 10.1086/523620
540. O'Shaughnessy, R., Vaishnav, B., Healy, J., Meeks, Z., Shoemaker, D.: Efficient asymptotic frame selection for binary black hole spacetimes using asymptotic radiation. *Phys. Rev. D* **84**, 124002 (2011). DOI 10.1103/PhysRevD.84.124002
541. Ossokine, S., et al.: Multipolar Effective-One-Body Waveforms for Precessing Binary Black Holes: Construction and Validation. *Phys. Rev. D* **102**(4), 044055 (2020). DOI 10.1103/PhysRevD.102.044055
542. Owen, B.J.: Search templates for gravitational waves from inspiraling binaries: Choice of template spacing. *Phys. Rev. D* **53**, 6749–6761 (1996). DOI 10.1103/PhysRevD.53.6749
543. Owen, B.J., Sathyaprakash, B.S.: Matched filtering of gravitational waves from inspiraling compact binaries: Computational cost and template placement. *Phys. Rev. D* **60**, 022002 (1999). DOI 10.1103/PhysRevD.60.022002
544. Özel, F., Freire, P.: Masses, Radii, and the Equation of State of Neutron Stars. *Ann. Rev. Astron. Astrophys.* **54**, 401–440 (2016). DOI 10.1146/annurev-astro-081915-023322
545. Pai, A., Arun, K.G.: Singular value decomposition in parametrised tests of post-Newtonian theory. *Class. Quant. Grav.* **30**, 025011 (2013). DOI 10.1088/0264-9381/30/2/025011
546. Pal, S., Nayak, K.R.: Swarm-intelligent search for gravitational waves from eccentric binary mergers (2023)
547. Pan, Y., Buonanno, A., Chen, Y.b., Vallisneri, M.: A Physical template family for gravitational waves from precessing binaries of spinning compact objects: Application to single spin binaries. *Phys. Rev. D* **69**, 104017 (2004). DOI 10.1103/PhysRevD.69.104017. [Erratum: *Phys.Rev.D* 74, 029905 (2006)]
548. Pan, Y., Buonanno, A., Taracchini, A., Kidder, L.E., Mroué, A.H., Pfeiffer, H.P., Scheel, M.A., Szilágyi, B.: Inspiral-merger-ringdown waveforms of spinning, precessing black-hole binaries in the effective-one-body formalism. *Phys. Rev. D* **89**(8), 084006 (2014). DOI 10.1103/PhysRevD.89.084006
549. Pang, P.T.H., Calderón Bustillo, J., Wang, Y., Li, T.G.F.: Potential observations of false deviations from general relativity in gravitational wave signals from binary black holes. *Phys. Rev. D* **98**(2), 024019 (2018). DOI 10.1103/PhysRevD.98.024019
550. Pang, P.T.H., Tews, I., Coughlin, M.W., Bulla, M., Van Den Broeck, C., Dietrich, T.: Nuclear-Physics Multi-Messenger Astrophysics Constraints on the Neutron-Star Equation of State: Adding NICER's PSR J0740+6620 Measurement (2021)
551. Pankow, C., Brady, P., Ochsner, E., O'Shaughnessy, R.: Novel scheme for rapid parallel parameter estimation of gravitational waves from compact binary coalescences. *Phys. Rev. D* **92**(2), 023002 (2015). DOI 10.1103/PhysRevD.92.023002
552. Pathak, L., Reza, A., Sengupta, A.S.: Fast and faithful interpolation of numerical relativity surrogate waveforms using meshfree approximation (2024)
553. Payne, E., Isi, M., Chatziioannou, K., Farr, W.M.: Fortifying gravitational-wave tests of general relativity against astrophysical assumptions. *Phys. Rev. D* **108**(12), 124060 (2023). DOI 10.1103/PhysRevD.108.124060

554. Perkins, S.E., Nair, R., Silva, H.O., Yunes, N.: Improved gravitational-wave constraints on higher-order curvature theories of gravity. *Phys. Rev. D* **104**(2), 024060 (2021). DOI 10.1103/PhysRevD.104.024060
555. Peters, P.C.: Gravitational Radiation and the Motion of Two Point Masses. *Phys. Rev.* **136**, B1224–B1232 (1964). DOI 10.1103/PhysRev.136.B1224
556. Peters, P.C., Mathews, J.: Gravitational radiation from point masses in a Keplerian orbit. *Phys. Rev.* **131**, 435–439 (1963). DOI 10.1103/PhysRev.131.435
557. Phinney, E.S.: The Rate of neutron star binary mergers in the universe: Minimal predictions for gravity wave detector. *Astrophys. J. Lett.* **380**, L17–L21 (1991). DOI 10.1086/186163
558. Phukon, K.S., Baltus, G., Caudill, S., Clesse, S., Depasse, A., Fays, M., Fong, H., Kapadia, S.J., Magee, R., Tanasijczuk, A.J.: The hunt for sub-solar primordial black holes in low mass ratio binaries is open (2021)
559. Pitkin, M., Reid, S., Rowan, S., Hough, J.: Gravitational Wave Detection by Interferometry (Ground and Space). *Living Rev. Rel.* **14**, 5 (2011). DOI 10.12942/lrr-2011-5
560. Pizzati, E., Sachdev, S., Gupta, A., Sathyaprakash, B.: Toward inference of overlapping gravitational-wave signals. *Phys. Rev. D* **105**(10), 104016 (2022). DOI 10.1103/PhysRevD.105.104016
561. Plunkett, C., Hourihane, S., Chatziioannou, K.: Concurrent estimation of noise and compact-binary signal parameters in gravitational-wave data. *Phys. Rev. D* **106**(10), 104021 (2022). DOI 10.1103/PhysRevD.106.104021
562. Poisson, E.: Gravitational waves from inspiraling compact binaries: The Quadrupole moment term. *Phys. Rev. D* **57**, 5287–5290 (1998). DOI 10.1103/PhysRevD.57.5287
563. Poisson, E., Will, C.M.: Gravitational waves from inspiraling compact binaries: Parameter estimation using second postNewtonian wave forms. *Phys. Rev. D* **52**, 848–855 (1995). DOI 10.1103/PhysRevD.52.848
564. Poisson, E., Will, C.M.: *Gravity: Newtonian, Post-Newtonian, Relativistic*. Cambridge University Press (2014)
565. Pompili, L., et al.: Laying the foundation of the effective-one-body waveform models SEOBNRv5: improved accuracy and efficiency for spinning non-precessing binary black holes (2023)
566. Portegies Zwart, S.F., McMillan, S.L.W.: Black Hole Mergers in the Universe. *ApJ* **528**(1), L17–L20 (2000). DOI 10.1086/312422
567. Porter, E.K., Carré, J.: A hamiltonian monte-carlo method for bayesian inference of supermassive black hole binaries. *Classical and Quantum Gravity* **31**(14), 145004 (2014). DOI 10.1088/0264-9381/31/14/145004. URL <https://dx.doi.org/10.1088/0264-9381/31/14/145004>
568. Pratten, G., Husa, S., Garcia-Quiros, C., Colleoni, M., Ramos-Buades, A., Estelles, H., Jaume, R.: Setting the cornerstone for a family of models for gravitational waves from compact binaries: The dominant harmonic for nonprecessing quasicircular black holes. *Phys. Rev. D* **102**(6), 064001 (2020). DOI 10.1103/PhysRevD.102.064001
569. Pratten, G., et al.: Computationally efficient models for the dominant and subdominant harmonic modes of precessing binary black holes. *Phys. Rev. D* **103**(10), 104056 (2021). DOI 10.1103/PhysRevD.103.104056
570. Pretorius, F.: Evolution of binary black hole spacetimes. *Phys. Rev. Lett.* **95**, 121101 (2005). DOI 10.1103/PhysRevLett.95.121101
571. Privitera, S., Mohapatra, S.R.P., Ajith, P., Cannon, K., Fotopoulos, N., Frei, M.A., Hanna, C., Weinstein, A.J., Whelan, J.T.: Improving the sensitivity of a search for coalescing binary black holes with nonprecessing spins in gravitational wave data. *Phys. Rev. D* **89**(2), 024003 (2014). DOI 10.1103/PhysRevD.89.024003
572. Punturo, M., et al.: The Einstein Telescope: A third-generation gravitational wave observatory. *Class. Quant. Grav.* **27**, 194002 (2010). DOI 10.1088/0264-9381/27/19/194002
573. Pürrer, M.: Frequency domain reduced order models for gravitational waves from aligned-spin compact binaries. *Class. Quant. Grav.* **31**(19), 195010 (2014). DOI 10.1088/0264-9381/31/19/195010
574. Pürrer, M.: Frequency domain reduced order model of aligned-spin effective-one-body waveforms with generic mass-ratios and spins. *Phys. Rev. D* **93**(6), 064041 (2016). DOI 10.1103/PhysRevD.93.064041

575. Pürrer, M., Hannam, M., Ohme, F.: Can we measure individual black-hole spins from gravitational-wave observations? *Phys. Rev. D* **93**(8), 084042 (2016). DOI 10.1103/PhysRevD.93.084042
576. Pürrer, M., Haster, C.J.: Gravitational waveform accuracy requirements for future ground-based detectors. *Phys. Rev. Res.* **2**(2), 023151 (2020). DOI 10.1103/PhysRevResearch.2.023151
577. Qi, H., Raymond, V.: Python-based reduced order quadrature building code for fast gravitational wave inference. *Phys. Rev. D* **104**(6), 063031 (2021). DOI 10.1103/PhysRevD.104.063031
578. Raaijmakers, G., Greif, S.K., Hebeler, K., Hinderer, T., Nisanke, S., Schwenk, A., Riley, T.E., Watts, A.L., Lattimer, J.M., Ho, W.C.G.: Constraints on the dense matter equation of state and neutron star properties from NICER's mass-radius estimate of PSR J0740+6620 and multimessenger observations (2021)
579. Raaijmakers, G., et al.: A NICER view of PSR J0030+0451: Implications for the dense matter equation of state. *Astrophys. J. Lett.* **887**, L22 (2019). DOI 10.3847/2041-8213/ab451a
580. Raaijmakers, G., et al.: Constraining the dense matter equation of state with joint analysis of NICER and LIGO/Virgo measurements. *Astrophys. J. Lett.* **893**(1), L21 (2020). DOI 10.3847/2041-8213/ab822f
581. Racine, E.: Analysis of spin precession in binary black hole systems including quadrupole-monopole interaction. *Phys. Rev. D* **78**, 044021 (2008). DOI 10.1103/PhysRevD.78.044021
582. Radice, D., Dai, L.: Multimessenger Parameter Estimation of GW170817. *Eur. Phys. J. A* **55**(4), 50 (2019). DOI 10.1140/epja/i2019-12716-4
583. Ramos-Buades, A., Buonanno, A., Estellés, H., Khalil, M., Mihaylov, D.P., Ossokine, S., Pompili, L., Shiferaw, M.: SEOBNRv5PHM: Next generation of accurate and efficient multipolar precessing-spin effective-one-body waveforms for binary black holes (2023)
584. Ramos-Buades, A., Buonanno, A., Khalil, M., Ossokine, S.: Effective-one-body multipolar waveforms for eccentric binary black holes with nonprecessing spins. *Phys. Rev. D* **105**(4), 044035 (2022). DOI 10.1103/PhysRevD.105.044035
585. Rasmussen, C.E., Williams, C.K.I.: *Gaussian Processes for Machine Learning*. MIT Press (2006)
586. Ray, A., Magaña Hernandez, I., Breivik, K., Creighton, J.: Searching for binary black hole sub-populations in gravitational wave data using binned Gaussian processes (2024)
587. Ray, A., Hernandez, I.M., Mohite, S., Creighton, J., Kapadia, S.: Nonparametric Inference of the Population of Compact Binaries from Gravitational-wave Observations Using Binned Gaussian Processes. *ApJ* **957**(1), 37 (2023). DOI 10.3847/1538-4357/acf452
588. Raymond, V., Farr, W.M.: Physically motivated exploration of the extrinsic parameter space in ground-based gravitational-wave astronomy (2014)
589. Read, J.S., Lackey, B.D., Owen, B.J., Friedman, J.L.: Constraints on a phenomenologically parameterized neutron-star equation of state. *Phys. Rev. D* **79**, 124032 (2009). DOI 10.1103/PhysRevD.79.124032
590. Reed, B.T., Fattoyev, F.J., Horowitz, C.J., Piekarewicz, J.: Implications of PREX-2 on the Equation of State of Neutron-Rich Matter. *Phys. Rev. Lett.* **126**(17), 172503 (2021). DOI 10.1103/PhysRevLett.126.172503
591. Regimbau, T., et al.: A Mock Data Challenge for the Einstein Gravitational-Wave Telescope. *Phys. Rev. D* **86**, 122001 (2012). DOI 10.1103/PhysRevD.86.122001
592. Relton, P., Raymond, V.: Parameter estimation bias from overlapping binary black hole events in second generation interferometers. *Phys. Rev. D* **104**(8), 084039 (2021). DOI 10.1103/PhysRevD.104.084039
593. Riley, J., Mandel, I.: Surrogate Forward Models for Population Inference on Compact Binary Mergers. *ApJ* **950**(2), 80 (2023). DOI 10.3847/1538-4357/acf90
594. Riley, T.E., et al.: A *NICER* View of PSR J0030+0451: Millisecond Pulsar Parameter Estimation. *Astrophys. J. Lett.* **887**(1), L21 (2019). DOI 10.3847/2041-8213/ab481c
595. Riley, T.E., et al.: A *NICER* View of the Massive Pulsar PSR J0740+6620 Informed by Radio Timing and XMM-Newton Spectroscopy. *Astrophys. J. Lett.* **918**(2), L27 (2021). DOI 10.3847/2041-8213/ac0a81

596. Rinaldi, S., Del Pozzo, W.: (H)DPGMM: a hierarchy of Dirichlet process Gaussian mixture models for the inference of the black hole mass function. *MNRAS***509**(4), 5454–5466 (2022). DOI 10.1093/mnras/stab3224
597. Robinson, C.A.K., Sathyaprakash, B.S., Sengupta, A.S.: A Geometric algorithm for efficient coincident detection of gravitational waves. *Phys. Rev. D* **78**, 062002 (2008). DOI 10.1103/PhysRevD.78.062002
598. Roca-Maza, X., Centelles, M., Vinas, X., Warda, M.: Neutron skin of ^{208}Pb , nuclear symmetry energy, and the parity radius experiment. *Phys. Rev. Lett.* **106**, 252501 (2011). DOI 10.1103/PhysRevLett.106.252501
599. Rodriguez, C.L., Farr, B., Farr, W.M., Mandel, I.: Inadequacies of the Fisher Information Matrix in gravitational-wave parameter estimation. *Phys. Rev. D* **88**(8), 084013 (2013). DOI 10.1103/PhysRevD.88.084013
600. Rodriguez, C.L., Zevin, M., Pankow, C., Kalogera, V., Rasio, F.A.: Illuminating Black Hole Binary Formation Channels with Spins in Advanced LIGO. *ApJ***832**(1), L2 (2016). DOI 10.3847/2041-8205/832/1/L2
601. Romano, J.D., Cornish, N.J.: Detection methods for stochastic gravitational-wave backgrounds: a unified treatment. *Living Rev. Rel.* **20**(1), 2 (2017). DOI 10.1007/s41114-017-0004-1
602. Romero-Shaw, I.M., Thrane, E., Lasky, P.D.: When models fail: An introduction to posterior predictive checks and model misspecification in gravitational-wave astronomy. *PASA***39**, e025 (2022). DOI 10.1017/pasa.2022.24
603. Romero-Shaw, I.M., et al.: Bayesian inference for compact binary coalescences with bilby: validation and application to the first LIGO-Virgo gravitational-wave transient catalogue. *Mon. Not. Roy. Astron. Soc.* **499**(3), 3295–3319 (2020). DOI 10.1093/mnras/staa2850
604. Roulet, J., Chia, H.S., Olsen, S., Dai, L., Venumadhav, T., Zackay, B., Zaldarriaga, M.: Distribution of effective spins and masses of binary black holes from the LIGO and Virgo O1-O3a observing runs. *Phys. Rev. D***104**(8), 083010 (2021). DOI 10.1103/PhysRevD.104.083010
605. Roulet, J., Dai, L., Venumadhav, T., Zackay, B., Zaldarriaga, M.: Template Bank for Compact Binary Coalescence Searches in Gravitational Wave Data: A General Geometric Placement Algorithm. *Phys. Rev. D* **99**(12), 123022 (2019). DOI 10.1103/PhysRevD.99.123022
606. Roulet, J., Mushkin, J., Wadekar, D., Venumadhav, T., Zackay, B., Zaldarriaga, M.: Fast marginalization algorithm for optimizing gravitational wave detection, parameter estimation and sky localization (2024)
607. Roulet, J., Olsen, S., Mushkin, J., Islam, T., Venumadhav, T., Zackay, B., Zaldarriaga, M.: Removing degeneracy and multimodality in gravitational wave source parameters. *Phys. Rev. D* **106**(12), 123015 (2022). DOI 10.1103/PhysRevD.106.123015
608. Roulet, J., Zaldarriaga, M.: Constraints on binary black hole populations from LIGO-Virgo detections. *MNRAS***484**(3), 4216–4229 (2019). DOI 10.1093/mnras/stz226
609. Rover, C., Meyer, R., Christensen, N.: Modelling coloured residual noise in gravitational-wave signal processing. *Class. Quant. Grav.* **28**, 015010 (2011). DOI 10.1088/0264-9381/28/1/015010
610. Roy, S., Sengupta, A.S., Ajith, P.: Effectual template banks for upcoming compact binary searches in Advanced-LIGO and Virgo data. *Phys. Rev. D* **99**(2), 024048 (2019). DOI 10.1103/PhysRevD.99.024048
611. Roy, S., Sengupta, A.S., Thakor, N.: Hybrid geometric-random template-placement algorithm for gravitational wave searches from compact binary coalescences. *Phys. Rev. D* **95**(10), 104045 (2017). DOI 10.1103/PhysRevD.95.104045
612. Sachdev, S., Regimbau, T., Sathyaprakash, B.S.: Subtracting compact binary foreground sources to reveal primordial gravitational-wave backgrounds. *Phys. Rev. D* **102**(2), 024051 (2020). DOI 10.1103/PhysRevD.102.024051
613. Sachdev, S., et al.: The GstLAL Search Analysis Methods for Compact Binary Mergers in Advanced LIGO’s Second and Advanced Virgo’s First Observing Runs (2019)
614. Sachdev, S., et al.: An Early-warning System for Electromagnetic Follow-up of Gravitational-wave Events. *Astrophys. J. Lett.* **905**(2), L25 (2020). DOI 10.3847/2041-8213/abc753

615. Sadiq, J., Dent, T., Gieles, M.: Binary Vision: The Mass Distribution of Merging Binary Black Holes via Iterative Density Estimation. *Astrophys. J.* **960**(1), 65 (2024). DOI 10.3847/1538-4357/ad0ce6
616. Sadiq, J., Dent, T., Wysocki, D.: Flexible and fast estimation of binary merger population distributions with an adaptive kernel density estimator. *Phys. Rev. D* **105**(12), 123014 (2022). DOI 10.1103/PhysRevD.105.123014
617. Safarzadeh, M., Farr, W.M.: The Impact of Metallicity Evolution of the Universe on the Maximum Mass of LIGO Binary Black Holes. *ApJ* **883**(1), L24 (2019). DOI 10.3847/2041-8213/ab40bd
618. Safarzadeh, M., Farr, W.M., Ramirez-Ruiz, E.: A Trend in the Effective Spin Distribution of LIGO Binary Black Holes with Mass. *ApJ* **894**(2), 129 (2020). DOI 10.3847/1538-4357/ab80be
619. Saleem, M., Krishnendu, N.V., Ghosh, A., Gupta, A., Del Pozzo, W., Ghosh, A., Arun, K.G.: Population inference of spin-induced quadrupole moments as a probe for non-black hole compact binaries (2021)
620. Saleem, M., et al.: The science case for LIGO-India. *Class. Quant. Grav.* **39**(2), 025004 (2022). DOI 10.1088/1361-6382/ac3b99
621. Samajdar, A., Janquart, J., Van Den Broeck, C., Dietrich, T.: Biases in parameter estimation from overlapping gravitational-wave signals in the third-generation detector era. *Phys. Rev. D* **104**(4), 044003 (2021). DOI 10.1103/PhysRevD.104.044003
622. Sampson, L., Cornish, N., Yunes, N.: Gravitational Wave Tests of Strong Field General Relativity with Binary Inspirals: Realistic Injections and Optimal Model Selection. *Phys. Rev. D* **87**(10), 102001 (2013). DOI 10.1103/PhysRevD.87.102001
623. Sampson, L., Cornish, N., Yunes, N.: Mismodeling in gravitational-wave astronomy: The trouble with templates. *Phys. Rev. D* **89**(6), 064037 (2014). DOI 10.1103/PhysRevD.89.064037
624. Santamaria, L., et al.: Matching post-Newtonian and numerical relativity waveforms: systematic errors and a new phenomenological model for non-precessing black hole binaries. *Phys. Rev. D* **82**, 064016 (2010). DOI 10.1103/PhysRevD.82.064016
625. Sasaki, M., Tagoshi, H.: Analytic black hole perturbation approach to gravitational radiation. *Living Rev. Rel.* **6**, 6 (2003). DOI 10.12942/lrr-2003-6
626. Sathyaprakash, B.S., Dhurandhar, S.V.: Choice of filters for the detection of gravitational waves from coalescing binaries. *Phys. Rev. D* **44**, 3819–3834 (1991). DOI 10.1103/PhysRevD.44.3819
627. Sathyaprakash, B.S., Schutz, B.F.: Physics, Astrophysics and Cosmology with Gravitational Waves. *Living Rev. Rel.* **12**, 2 (2009). DOI 10.12942/lrr-2009-2
628. Schäfer, G., Jaranowski, P.: Hamiltonian formulation of general relativity and post-Newtonian dynamics of compact binaries. *Living Rev. Rel.* **21**(1), 7 (2018). DOI 10.1007/s41114-024-00048-7
629. Schäfer, M.B., Nitz, A.H.: From one to many: A deep learning coincident gravitational-wave search. *Phys. Rev. D* **105**(4), 043003 (2022). DOI 10.1103/PhysRevD.105.043003
630. Schmidt, P., Hannam, M., Husa, S., Ajith, P.: Tracking the precession of compact binaries from their gravitational-wave signal. *Phys. Rev. D* **84**, 024046 (2011). DOI 10.1103/PhysRevD.84.024046
631. Schmidt, P., Ohme, F., Hannam, M.: Towards models of gravitational waveforms from generic binaries II: Modelling precession effects with a single effective precession parameter. *Phys. Rev. D* **91**(2), 024043 (2015). DOI 10.1103/PhysRevD.91.024043
632. Schmidt, S., Breschi, M., Gamba, R., Pagano, G., Rettegno, P., Riemenschneider, G., Bernuzzi, S., Nagar, A., Del Pozzo, W.: Machine Learning Gravitational Waves from Binary Black Hole Mergers. *Phys. Rev. D* **103**(4), 043020 (2021). DOI 10.1103/PhysRevD.103.043020
633. Schutz, B.: *A First Course in General Relativity*. Cambridge University Press (2009)
634. Schutz, B.F.: Determining the Hubble constant from gravitational wave observations. *Nature* **323**(6086), 310–311 (1986). DOI 10.1038/323310a0
635. Schutz, B.F.: Gravitational Wave Sources and Their Detectability. *Class. Quant. Grav.* **6**, 1761–1780 (1989). DOI 10.1088/0264-9381/6/12/006
636. Schutz, B.F.: Networks of gravitational wave detectors and three figures of merit. *Class. Quant. Grav.* **28**, 125023 (2011). DOI 10.1088/0264-9381/28/12/125023

637. Schutz, B.F., Sathyaprakash, B.S.: Self-calibration of Networks of Gravitational Wave Detectors (2020)
638. Sesana, A.: Prospects for Multiband Gravitational-Wave Astronomy after GW150914. *Phys. Rev. Lett.* **116**(23), 231102 (2016). DOI 10.1103/PhysRevLett.116.231102
639. Setyawati, Y., Pürrer, M., Ohme, F.: Regression methods in waveform modeling: a comparative study. *Class. Quant. Grav.* **37**(7), 075012 (2020). DOI 10.1088/1361-6382/ab693b
640. Sigurdsson, S., Hernquist, L.: Primordial black holes in globular clusters. *Nature***364**(6436), 423–425 (1993). DOI 10.1038/364423a0
641. Singer, L.P., Price, L.R.: Rapid Bayesian position reconstruction for gravitational-wave transients. *Phys. Rev. D* **93**(2), 024013 (2016). DOI 10.1103/PhysRevD.93.024013
642. Singer, L.P., et al.: Going the Distance: Mapping Host Galaxies of LIGO and Virgo Sources in Three Dimensions Using Local Cosmography and Targeted Follow-up. *Astrophys. J. Lett.* **829**(1), L15 (2016). DOI 10.3847/2041-8205/829/1/L15
643. Sivia, D., Skilling, J.: *Data Analysis: A Bayesian Tutorial*. Oxford science publications. OUP Oxford (2006)
644. Skilling, J.: Nested sampling for general Bayesian computation. *Bayesian Analysis* **1**(4), 833–859 (2006). DOI 10.1214/06-BA127
645. van der Sluys, M., Raymond, V., Mandel, I., Rover, C., Christensen, N., Kalogera, V., Meyer, R., Vecchio, A.: Parameter estimation of spinning binary inspirals using Markov-chain Monte Carlo. *Class. Quant. Grav.* **25**, 184011 (2008). DOI 10.1088/0264-9381/25/18/184011
646. Smith, R., Field, S.E., Blackburn, K., Haster, C.J., Pürrer, M., Raymond, V., Schmidt, P.: Fast and accurate inference on gravitational waves from precessing compact binaries. *Phys. Rev. D* **94**(4), 044031 (2016). DOI 10.1103/PhysRevD.94.044031
647. Smith, R., Thrane, E.: Optimal Search for an Astrophysical Gravitational-Wave Background. *Phys. Rev. X* **8**(2), 021019 (2018). DOI 10.1103/PhysRevX.8.021019
648. Somasundaram, R., Tews, I., Margueron, J.: Perturbative QCD and the Neutron Star Equation of State (2022)
649. Soni, K., Gadre, B.U., Mitra, S., Dhurandhar, S.: Hierarchical search for compact binary coalescences in the Advanced LIGO’s first two observing runs. *Phys. Rev. D* **105**(6), 064005 (2022). DOI 10.1103/PhysRevD.105.064005
650. Soni, S., et al.: Reducing scattered light in LIGO’s third observing run. *Class. Quant. Grav.* **38**(2), 025016 (2020). DOI 10.1088/1361-6382/abc906
651. Soni, S., et al.: Discovering features in gravitational-wave data through detector characterization, citizen science and machine learning. *Class. Quant. Grav.* **38**(19), 195016 (2021). DOI 10.1088/1361-6382/ac1ccb
652. Speagle, J.S.: dynesty: a dynamic nested sampling package for estimating Bayesian posteriors and evidences. *Mon. Not. Roy. Astron. Soc.* **493**(3), 3132–3158 (2020). DOI 10.1093/mnras/staa278
653. Srivastava, V., Rajesh Nayak, K., Bose, S.: Toward low-latency coincident precessing and coherent aligned-spin gravitational-wave searches of compact binary coalescences with particle swarm optimization (2018)
654. Steinhoff, J., Hinderer, T., Buonanno, A., Taracchini, A.: Dynamical Tides in General Relativity: Effective Action and Effective-One-Body Hamiltonian. *Phys. Rev. D* **94**(10), 104028 (2016). DOI 10.1103/PhysRevD.94.104028
655. Stevenson, S., Clarke, T.A.: Constraints on the contributions to the observed binary black hole population from individual evolutionary pathways in isolated binary evolution. *MNRAS***517**(3), 4034–4053 (2022). DOI 10.1093/mnras/stac2936
656. Stevenson, S., Ohme, F., Fairhurst, S.: Distinguishing Compact Binary Population Synthesis Models Using Gravitational Wave Observations of Coalescing Binary Black Holes. *ApJ***810**(1), 58 (2015). DOI 10.1088/0004-637X/810/1/58
657. Sun, L., et al.: Characterization of systematic error in Advanced LIGO calibration. *Class. Quant. Grav.* **37**(22), 225008 (2020). DOI 10.1088/1361-6382/abb14e
658. Sutton, P.J.: A Rule of Thumb for the Detectability of Gravitational-Wave Bursts (2013)
659. Swendsen, R.H., Wang, J.S.: Replica monte carlo simulation of spin-glasses. *Phys. Rev. Lett.* **57**, 2607–2609 (1986). DOI 10.1103/PhysRevLett.57.2607. URL <https://link.aps.org/doi/10.1103/PhysRevLett.57.2607>

660. Tagawa, H., Haiman, Z., Bartos, I., Kocsis, B., Omukai, K.: Signatures of hierarchical mergers in black hole spin and mass distribution. *MNRAS***507**(3), 3362–3380 (2021). DOI 10.1093/mnras/stab2315
661. Talbot, C., Thrane, E.: Determining the population properties of spinning black holes. *Phys. Rev. D***96**(2), 023012 (2017). DOI 10.1103/PhysRevD.96.023012
662. Talbot, C., Thrane, E.: Measuring the Binary Black Hole Mass Spectrum with an Astrophysically Motivated Parameterization. *ApJ***856**(2), 173 (2018). DOI 10.3847/1538-4357/aab34c
663. Talbot, C., Thrane, E.: Gravitational-wave astronomy with an uncertain noise power spectral density. *Phys. Rev. Res.* **2**(4), 043298 (2020). DOI 10.1103/PhysRevResearch.2.043298
664. Talbot, C., Thrane, E.: Flexible and Accurate Evaluation of Gravitational-wave Malmquist Bias with Machine Learning. *ApJ***927**(1), 76 (2022). DOI 10.3847/1538-4357/ac4bc0
665. Talbot, C., Thrane, E., Biscoveanu, S., Smith, R.: Inference with finite time series: Observing the gravitational Universe through windows. *Phys. Rev. Res.* **3**(4), 043049 (2021). DOI 10.1103/PhysRevResearch.3.043049
666. Tanaka, T., Tagoshi, H.: The Use of new coordinates for the template space in hierarchical search for gravitational waves from inspiraling binaries. *Phys. Rev. D* **62**, 082001 (2000). DOI 10.1103/PhysRevD.62.082001
667. Taracchini, A., Pan, Y., Buonanno, A., Barausse, E., Boyle, M., Chu, T., Lovelace, G., Pfeiffer, H.P., Scheel, M.A.: Prototype effective-one-body model for nonprecessing spinning inspiral-merger-ringdown waveforms. *Phys. Rev. D* **86**, 024011 (2012). DOI 10.1103/PhysRevD.86.024011
668. Taracchini, A., et al.: Effective-one-body model for black-hole binaries with generic mass ratios and spins. *Phys. Rev. D* **89**(6), 061502 (2014). DOI 10.1103/PhysRevD.89.061502
669. Taylor, J.H., Weisberg, J.M.: A new test of general relativity: Gravitational radiation and the binary pulsar PS R 1913+16. *Astrophys. J.* **253**, 908–920 (1982). DOI 10.1086/159690
670. Taylor, S.R., Gair, J.R.: Cosmology with the lights off: Standard sirens in the Einstein Telescope era. *Phys. Rev. D***86**(2), 023502 (2012). DOI 10.1103/PhysRevD.86.023502
671. Taylor, S.R., Gerosa, D.: Mining gravitational-wave catalogs to understand binary stellar evolution: A new hierarchical Bayesian framework. *Phys. Rev. D***98**(8), 083017 (2018). DOI 10.1103/PhysRevD.98.083017
672. Tews, I., Carlson, J., Gandolfi, S., Reddy, S.: Constraining the speed of sound inside neutron stars with chiral effective field theory interactions and observations. *Astrophys. J.* **860**(2), 149 (2018). DOI 10.3847/1538-4357/aac267
673. Tews, I., Margueron, J., Reddy, S.: Confronting gravitational-wave observations with modern nuclear physics constraints. *Eur. Phys. J. A* **55**(6), 97 (2019). DOI 10.1140/epja/i2019-12774-6
674. Tews, I., Pang, P.T.H., Dietrich, T., Coughlin, M.W., Antier, S., Bulla, M., Heinzl, J., Issa, L.: On the Nature of GW190814 and Its Impact on the Understanding of Supranuclear Matter. *Astrophys. J. Lett.* **908**(1), L1 (2021). DOI 10.3847/2041-8213/abdaae
675. Thomas, L.M., Pratten, G., Schmidt, P.: Accelerating multimodal gravitational waveforms from precessing compact binaries with artificial neural networks. *Phys. Rev. D* **106**(10), 104029 (2022). DOI 10.1103/PhysRevD.106.104029
676. Thomas, L.M., Schmidt, P., Pratten, G.: New effective precession spin for modeling multimodal gravitational waveforms in the strong-field regime. *Phys. Rev. D* **103**(8), 083022 (2021). DOI 10.1103/PhysRevD.103.083022
677. Thompson, J.E., Fauchon-Jones, E., Khan, S., Nitoglia, E., Pannarale, F., Dietrich, T., Hannam, M.: Modeling the gravitational wave signature of neutron star black hole coalescences. *Phys. Rev. D* **101**(12), 124059 (2020). DOI 10.1103/PhysRevD.101.124059
678. Thompson, J.E., Hamilton, E., London, L., Ghosh, S., Kolitsidou, P., Hoy, C., Hannam, M.: Phenomenological gravitational-wave model for precessing black-hole binaries with higher multipoles and asymmetries. *Phys. Rev. D* **109**(6), 063012 (2024). DOI 10.1103/PhysRevD.109.063012

679. Thrane, E., Christensen, N., Schofield, R.: Correlated magnetic noise in global networks of gravitational-wave interferometers: observations and implications. *Phys. Rev. D* **87**, 123009 (2013). DOI 10.1103/PhysRevD.87.123009
680. Thrane, E., Talbot, C.: An introduction to Bayesian inference in gravitational-wave astronomy: Parameter estimation, model selection, and hierarchical models. *PASA* **36**, e010 (2019). DOI 10.1017/pasa.2019.2
681. Tiwari, V.: Estimation of the Sensitive Volume for Gravitational-wave Source Populations Using Weighted Monte Carlo Integration. *Class. Quant. Grav.* **35**(14), 145009 (2018). DOI 10.1088/1361-6382/aac89d
682. Tiwari, V.: VAMANA: modeling binary black hole population with minimal assumptions. *Class. Quant. Grav.* **38**(15), 155007 (2021). DOI 10.1088/1361-6382/ac0b54
683. Tiwari, V.: Exploring Features in the Binary Black Hole Population. *Astrophys. J.* **928**(2), 155 (2022). DOI 10.3847/1538-4357/ac589a
684. Tiwari, V., Fairhurst, S.: The Emergence of Structure in the Binary Black Hole Mass Distribution. *ApJ* **913**(2), L19 (2021). DOI 10.3847/2041-8213/abfb7
685. Tolley, A.E., Cabourn Davies, G.S., Harry, I.W., Lundgren, A.P.: ArchEnemy: removing scattered-light glitches from gravitational wave data. *Class. Quant. Grav.* **40**(16), 165005 (2023). DOI 10.1088/1361-6382/ace22f
686. Trozzo, L., Badaracco, F.: Seismic and Newtonian Noise in the GW Detectors. *Galaxies* **10**(1), 20 (2022). DOI 10.3390/galaxies10010020
687. Tsukada, L., Cannon, K., Hanna, C., Keppel, D., Meacher, D., Messick, C.: Application of a Zero-latency Whitening Filter to Compact Binary Coalescence Gravitational-wave Searches. *Phys. Rev. D* **97**(10), 103009 (2018). DOI 10.1103/PhysRevD.97.103009
688. Tsukada, L., et al.: Improved ranking statistics of the GstLAL inspiral search for compact binary coalescences. *Phys. Rev. D* **108**(4), 043004 (2023). DOI 10.1103/PhysRevD.108.043004
689. Turin, G.: An introduction to matched filters. *IRE Transactions on Information Theory* **6**(3), 311–329 (1960). DOI 10.1109/TIT.1960.1057571
690. Udall, R., Davis, D.: Bayesian modeling of scattered light in the LIGO interferometers. *Appl. Phys. Lett.* **122**(9), 094103 (2023). DOI 10.1063/5.0136896
691. Usman, S.A., et al.: The PyCBC search for gravitational waves from compact binary coalescence. *Class. Quant. Grav.* **33**(21), 215004 (2016). DOI 10.1088/0264-9381/33/21/215004
692. Vallisneri, M.: Use and abuse of the Fisher information matrix in the assessment of gravitational-wave parameter-estimation prospects. *Phys. Rev. D* **77**, 042001 (2008). DOI 10.1103/PhysRevD.77.042001
693. Van Den Broeck, C., Brown, D.A., Cokelaer, T., Harry, I., Jones, G., Sathyaprakash, B.S., Tagoshi, H., Takahashi, H.: Template banks to search for compact binaries with spinning components in gravitational wave data. *Phys. Rev. D* **80**, 024009 (2009). DOI 10.1103/PhysRevD.80.024009
694. Varma, V., Biscoveanu, S., Isi, M., Farr, W.M., Vitale, S.: Hints of Spin-Orbit Resonances in the Binary Black Hole Population. *Phys. Rev. Lett.* **128**(3), 031101 (2022). DOI 10.1103/PhysRevLett.128.031101
695. Varma, V., Field, S.E., Scheel, M.A., Blackman, J., Gerosa, D., Stein, L.C., Kidder, L.E., Pfeiffer, H.P.: Surrogate models for precessing binary black hole simulations with unequal masses. *Phys. Rev. Research.* **1**, 033015 (2019). DOI 10.1103/PhysRevResearch.1.033015
696. Varma, V., Field, S.E., Scheel, M.A., Blackman, J., Kidder, L.E., Pfeiffer, H.P.: Surrogate model of hybridized numerical relativity binary black hole waveforms. *Phys. Rev. D* **99**(6), 064045 (2019). DOI 10.1103/PhysRevD.99.064045
697. Varma, V., Gerosa, D., Stein, L.C., Hébert, F., Zhang, H.: High-accuracy mass, spin, and recoil predictions of generic black-hole merger remnants. *Phys. Rev. Lett.* **122**(1), 011101 (2019). DOI 10.1103/PhysRevLett.122.011101
698. Varma, V., Isi, M., Biscoveanu, S., Farr, W.M., Vitale, S.: Measuring binary black hole orbital-plane spin orientations. *Phys. Rev. D* **105**(2), 024045 (2022). DOI 10.1103/PhysRevD.105.024045
699. Veitch, J., Pürrer, M., Mandel, I.: Measuring intermediate mass black hole binaries with advanced gravitational wave detectors. *Phys. Rev. Lett.* **115**(14), 141101 (2015). DOI 10.1103/PhysRevLett.115.141101

700. Veitch, J., Raymond, V., Farr, B., Farr, W., Graff, P., Vitale, S., Aylott, B., Blackburn, K., Christensen, N., Coughlin, M., Del Pozzo, W., Feroz, F., Gair, J., Haster, C.J., Kalogera, V., Littenberg, T., Mandel, I., O'Shaughnessy, R., Pitkin, M., Rodriguez, C., Röver, C., Sidery, T., Smith, R., Van Der Sluys, M., Vecchio, A., Vousden, W., Wade, L.: Parameter estimation for compact binaries with ground-based gravitational-wave observations using the LALInference software library. *Phys. Rev. D* **91**(4), 042003 (2015). DOI 10.1103/PhysRevD.91.042003
701. Veitch, J., Vecchio, A.: Bayesian coherent analysis of in-spiral gravitational wave signals with a detector network. *Phys. Rev. D* **81**, 062003 (2010). DOI 10.1103/PhysRevD.81.062003
702. Venumadhav, T., Zackay, B., Roulet, J., Dai, L., Zaldarriaga, M.: New search pipeline for compact binary mergers: Results for binary black holes in the first observing run of Advanced LIGO. *Phys. Rev. D* **100**(2), 023011 (2019). DOI 10.1103/PhysRevD.100.023011
703. Vinciguerra, S., Veitch, J., Mandel, I.: Accelerating gravitational wave parameter estimation with multi-band template interpolation. *Class. Quant. Grav.* **34**(11), 115006 (2017). DOI 10.1088/1361-6382/aa6d44
704. Vitale, S., Biscoveanu, S., Talbot, C.: The orientations of the binary black holes in GWTC-3. arXiv e-prints arXiv:2204.00968 (2022). DOI 10.48550/arXiv.2204.00968
705. Vitale, S., Gerosa, D., Farr, W.M., Taylor, S.R.: Inferring the Properties of a Population of Compact Binaries in Presence of Selection Effects. In: *Handbook of Gravitational Wave Astronomy*, p. 45 (2022). DOI 10.1007/978-981-15-4702-7_45-1
706. Vitale, S., Zanolin, M.: Application of asymptotic expansions for maximum likelihood estimators' errors to gravitational waves from binary mergers: the network case. *Phys. Rev. D* **84**, 104020 (2011). DOI 10.1103/PhysRevD.84.104020
707. Wade, L., Creighton, J.D.E., Ochsner, E., Lackey, B.D., Farr, B.F., Littenberg, T.B., Raymond, V.: Systematic and statistical errors in a bayesian approach to the estimation of the neutron-star equation of state using advanced gravitational wave detectors. *Phys. Rev. D* **89**(10), 103012 (2014). DOI 10.1103/PhysRevD.89.103012
708. Wadekar, D., Roulet, J., Venumadhav, T., Mehta, A.K., Zackay, B., Mushkin, J., Olsen, S., Zaldarriaga, M.: New black hole mergers in the LIGO-Virgo O3 data from a gravitational wave search including higher-order harmonics (2023)
709. Wadekar, D., Venumadhav, T., Mehta, A.K., Roulet, J., Olsen, S., Mushkin, J., Zackay, B., Zaldarriaga, M.: A new approach to template banks of gravitational waves with higher harmonics: reducing matched-filtering cost by over an order of magnitude (2023)
710. Wagoner, R.V., Will, C.M.: PostNewtonian Gravitational Radiation from Orbiting Point Masses. *Astrophys. J.* **210**, 764–775 (1976). DOI 10.1086/154886. [Erratum: *Astrophys. J.* 215,984(1977)]
711. Wang, Y., Stebbins, A., Turner, E.L.: Gravitational lensing of gravitational waves from merging neutron star binaries. *Phys. Rev. Lett.* **77**, 2875–2878 (1996). DOI 10.1103/PhysRevLett.77.2875
712. Wang, Y.Z., Li, Y.J., Vink, J.S., Fan, Y.Z., Tang, S.P., Qin, Y., Wei, D.M.: Potential Subpopulations and Assembling Tendency of the Merging Black Holes. *Astrophys. J. Lett.* **941**(2), L39 (2022). DOI 10.3847/2041-8213/aca89f
713. Was, M., Bizouard, M.A., Brisson, V., Cavalier, F., Davier, M., Hello, P., Leroy, N., Robinet, F., Vavoulidis, M.: On the background estimation by time slides in a network of gravitational wave detectors. *Class. Quant. Grav.* **27**, 015005 (2010). DOI 10.1088/0264-9381/27/1/015005
714. Was, M., Gouaty, R., Bonnard, R.: End benches scattered light modelling and subtraction in advanced Virgo. *Class. Quant. Grav.* **38**(7), 075020 (2021). DOI 10.1088/1361-6382/abe759
715. Weerathunga, T.S., Mohanty, S.D.: Performance of Particle Swarm Optimization on the fully-coherent all-sky search for gravitational waves from compact binary coalescences. *Phys. Rev. D* **95**(12), 124030 (2017). DOI 10.1103/PhysRevD.95.124030
716. Wen, L., Chen, Y.: Geometrical Expression for the Angular Resolution of a Network of Gravitational-Wave Detectors. *Phys. Rev. D* **81**, 082001 (2010). DOI 10.1103/PhysRevD.81.082001

717. Whittle, P.: Curve and periodogram smoothing. *Journal of the Royal Statistical Society. Series B (Methodological)* **19**(1), 38–63 (1957). URL <http://www.jstor.org/stable/2983994>
718. Williams, D., Heng, I.S., Gair, J., Clark, J.A., Khamesra, B.: Precessing numerical relativity waveform surrogate model for binary black holes: A Gaussian process regression approach. *Phys. Rev. D* **101**(6), 063011 (2020). DOI 10.1103/PhysRevD.101.063011
719. Williams, M.: Gwviz. URL <https://github.com/mj-will/gwviz>
720. Williams, M.J., Veitch, J., Messenger, C.: Nested sampling with normalizing flows for gravitational-wave inference. *Phys. Rev. D* **103**(10), 103006 (2021). DOI 10.1103/PhysRevD.103.103006
721. Williamson, A.R., Biwer, C., Fairhurst, S., Harry, I.W., Macdonald, E., Macleod, D., Predoi, V.: Improved methods for detecting gravitational waves associated with short gamma-ray bursts. *Phys. Rev. D* **90**(12), 122004 (2014). DOI 10.1103/PhysRevD.90.122004
722. Wiseman, A.G.: Coalescing binary systems of compact objects to (post)5/2 Newtonian order. 2. Higher order wave forms and radiation recoil. *Phys. Rev. D* **46**, 1517–1539 (1992). DOI 10.1103/PhysRevD.46.1517
723. Wong, K.W.K., Isi, M., Edwards, T.D.P.: Fast gravitational wave parameter estimation without compromises (2023)
724. Wu, S., Nitz, A.H.: Mock data study for next-generation ground-based detectors: The performance loss of matched filtering due to correlated confusion noise. *Phys. Rev. D* **107**(6), 063022 (2023). DOI 10.1103/PhysRevD.107.063022
725. Wysocki, D., Lange, J., O’Shaughnessy, R.: Reconstructing phenomenological distributions of compact binaries via gravitational wave observations. *Phys. Rev. D* **100**(4), 043012 (2019). DOI 10.1103/PhysRevD.100.043012
726. Wysocki, D., Lange, J., O’Shaughnessy, R.: Reconstructing phenomenological distributions of compact binaries via gravitational wave observations. *Phys. Rev. D* **100**(4), 043012 (2019). DOI 10.1103/PhysRevD.100.043012
727. Wysocki, D., O’Shaughnessy, R., Wade, L., Lange, J.: Inferring the neutron star equation of state simultaneously with the population of merging neutron stars. *arXiv e-prints arXiv:2001.01747* (2020). DOI 10.48550/arXiv.2001.01747
728. Wysocki, D., O’Shaughnessy, R., Wade, L., Lange, J.: Inferring the neutron star equation of state simultaneously with the population of merging neutron stars (2020)
729. Yan, J., Avagyan, M., Colgan, R.E., Veske, D., Bartos, I., Wright, J., Márka, Z., Márka, S.: Generalized approach to matched filtering using neural networks. *Phys. Rev. D* **105**(4), 043006 (2022). DOI 10.1103/PhysRevD.105.043006
730. Yoo, J., Mitman, K., Varma, V., Boyle, M., Field, S.E., Deppe, N., Hébert, F., Kidder, L.E., Moxon, J., Pfeiffer, H.P., et al.: Numerical relativity surrogate model with memory effects and post-newtonian hybridization. *arXiv preprint arXiv:2306.03148* (2023)
731. Yunes, N., Pretorius, F.: Fundamental Theoretical Bias in Gravitational Wave Astrophysics and the Parameterized Post-Einsteinian Framework. *Phys. Rev. D* **80**, 122003 (2009). DOI 10.1103/PhysRevD.80.122003
732. Yunes, N., Siemens, X.: Gravitational-Wave Tests of General Relativity with Ground-Based Detectors and Pulsar Timing-Arrays. *Living Rev. Rel.* **16**, 9 (2013). DOI 10.12942/lrr-2013-9
733. Yunes, N., Yagi, K., Pretorius, F.: Theoretical Physics Implications of the Binary Black-Hole Mergers GW150914 and GW151226. *Phys. Rev. D* **94**(8), 084002 (2016). DOI 10.1103/PhysRevD.94.084002
734. Zackay, B., Dai, L., Venumadhav, T.: Relative Binning and Fast Likelihood Evaluation for Gravitational Wave Parameter Estimation (2018)
735. Zackay, B., Venumadhav, T., Roulet, J., Dai, L., Zaldarriaga, M.: Detecting gravitational waves in data with non-stationary and non-Gaussian noise. *Phys. Rev. D* **104**(6), 063034 (2021). DOI 10.1103/PhysRevD.104.063034
736. Zaldarriaga, M., Kushnir, D., Kollmeier, J.A.: The expected spins of gravitational wave sources with isolated field binary progenitors. *MNRAS* **473**(3), 4174–4178 (2018). DOI 10.1093/mnras/stx2577

-
737. Zevin, M., Bavera, S.S., Berry, C.P.L., Kalogera, V., Fragos, T., Marchant, P., Rodriguez, C.L., Antonini, F., Holz, D.E., Pankow, C.: One Channel to Rule Them All? Constraining the Origins of Binary Black Holes Using Multiple Formation Pathways. *ApJ***910**(2), 152 (2021). DOI 10.3847/1538-4357/abe40e
 738. Zevin, M., Pankow, C., Rodriguez, C.L., Sampson, L., Chase, E., Kalogera, V., Rasio, F.A.: Constraining Formation Models of Binary Black Holes with Gravitational-wave Observations. *ApJ***846**(1), 82 (2017). DOI 10.3847/1538-4357/aa8408
 739. Zevin, M., et al.: Gravity Spy: Integrating Advanced LIGO Detector Characterization, Machine Learning, and Citizen Science. *Class. Quant. Grav.* **34**(6), 064003 (2017). DOI 10.1088/1361-6382/aa5cea
 740. Zhao, X., Kesden, M., Gerosa, D.: Nutational resonances, transitional precession, and precession-averaged evolution in binary black-hole systems. *Phys. Rev. D* **96**(2), 024007 (2017). DOI 10.1103/PhysRevD.96.024007
 741. Zimmerman, A., Haster, C.J., Chatziioannou, K.: On combining information from multiple gravitational wave sources. *Phys. Rev. D* **99**(12), 124044 (2019). DOI 10.1103/PhysRevD.99.124044